HIGH-PERFORMANCE ELASTOMERIC MATERIALS REINFORCED BY NANO-CARBONS

MULTIFUNCTIONAL PROPERTIES AND INDUSTRIAL APPLICATIONS

EDITED BY
LUCA VALENTINI
MIGUEL ANGEL LOPEZ MANCHADO

ELSEVIER

HIGH-PERFORMANCE ELASTOMERIC MATERIALS REINFORCED BY NANO-CARBONS

This page intentionally left blank

HIGH-PERFORMANCE ELASTOMERIC MATERIALS REINFORCED BY NANO-CARBONS

Multifunctional Properties and Industrial Applications

Edited by

LUCA VALENTINI

MIGUEL ANGEL LOPEZ MANCHADO

ELSEVIER

Notices
Knowledge and best practice in this field are constantly changing. As new research and experience broaden our understanding, changes in research methods, professional practices, or medical treatment may become necessary.

Practitioners and researchers must always rely on their own experience and knowledge in evaluating and using any information, methods, compounds, or experiments described herein. In using such information or methods they should be mindful of their own safety and the safety of others, including parties for whom they have a professional responsibility.

To the fullest extent of the law, neither the Publisher nor the authors, contributors, or editors, assume any liability for any injury and/or damage to persons or property as a matter of products liability, negligence or otherwise, or from any use or operation of any methods, products, instructions, or ideas contained in the material herein.

Working together
to grow libraries in
developing countries

www.elsevier.com • www.bookaid.org

Contents

Contributors

Héctor Aguilar-Bolados
Faculty of Physical Sciences and Mathematics, University of Chile, Santiago, Chile

A. Alvino
SERMS srl, Terni, Italy

Vincenzina Barbera
Polytechnic of Milan, Department of Chemistry, Materials and Chemical Engineering "G. Natta", Milan, Italy

Claire Barrès
Univ Lyon, Université Lyon1, Laboratory of Polymer Materials Engineering, CNRS: UMR5223, Villeurbanne, France

Hasti Bizhani
Department of Polymer Engineering and Color Technology, Amirkabir University of Technology, Tehran, Iran; Institute of Polymer Science and Technology (ICTP-CSIC), Madrid, Spain

S. Borsini
SERMS srl, Terni, Italy

Maria V. Candal
Polymer Group USB, Mechanical Department, Universidad Simón Bolívar, Caracas, Venezuela

F. Carannante
Department of Structures for Engineering and Architecture, University of Napoli "Federico II", Napoli, Italy

A.R. Carotenuto
Department of Structures for Engineering and Architecture, University of Napoli "Federico II", Napoli, Italy

Philippe Cassagnau
Univ Lyon, Université Lyon1, Laboratory of Polymer Materials Engineering, CNRS: UMR5223, Villeurbanne, France

A. Cutolo
Department of Structures for Engineering and Architecture, University of Napoli "Federico II", Napoli, Italy

M. Fraldi
Department of Structures for Engineering and Architecture, University of Napoli "Federico II", Napoli; Laboratory of Bio-Inspired and Graphene Nanomechanics, University of Trento, Trento, Italy

Maurizio Galimberti
Polytechnic of Milan, Department of Chemistry, Materials and Chemical Engineering "G. Natta", Milan, Italy

Antonio Gordillo
Centre Català del Plàstic, Universidad Politècnica de Catalunya, Barcelona Tech
(UPC-EEBE), C/Colom, Terrassa, Spain

Ali Asghar Katbab
Department of Polymer Engineering and Color Technology, Amirkabir University of
Technology, Tehran, Iran

Miguel Angel Lopez–Manchado
Institute of Polymer Science and Technology, ICTP-CSIC, Madrid, Spain

N. Pugno
Laboratory of Bio-Inspired and Graphene Nanomechanics, University of Trento, Trento;
Ket Lab, Edoardo Amaldi Foundation, Rome; Department of Civil, Environmental and
Mechanical Engineering and Laboratory of Bio-inspired and Graphene Nanomechanics,
University of Trento, Trento, Italy; School of Engineering and Materials Science, Queen
Mary University of London, London, United Kingdom

Nicola Ranieri
Solvay Specialty Polymers, MiIan, Italy

Johan J. Sánchez
Polymer Group USB, Materials Department, Universidad Simón Bolívar, Caracas,
Venezuela

Orlando O. Santana
Centre Català del Plàstic, Universidad Politècnica de Catalunya Barcelona Tech
(UPC-EEBE), C/Colom, Terrassa, Spain

Annalisa Sironi
Eptatech SRL, Luisago, Italy

Graciela Terife
Centre Català del Plàstic, Universidad Politècnica de Catalunya Barcelona Tech
(UPC-EEBE), C/Colom, Terrassa, Spain

Luca Valentini
Civil and Environmental Engineering Department, University of Perugia, INSTM Research
Unit, Strada di Pentima, Terni, Italy

Raquel Verdejo
Institute of Polymer Science and Technology (ICTP-CSIC), Madrid, Spain

Mehrdad Yazdani–Pedram
Faculty of Chemical and Pharmaceutical Sciences, University of Chile, Santiago, Chile

CHAPTER 1

Classification of rubbers and components for harsh environmental systems

Luca Valentini[a], Miguel Angel Lopez-Manchado[b]
[a]Civil and Environmental Engineering Department, University of Perugia, INSTM Research Unit, Strada di Pentima, Terni, Italy
[b]Institute of Polymer Science and Technology, ICTP-CSIC, Madrid, Spain

Contents

1 Introduction

Elastomers are elastic materials that are characterized by large strain, high capability to recover the initial shape, nonlinear stress–strain curves and strain hardening [1–5]. The combinations of these properties make elastomers suitable for several industrial applications like those of oil and gas extraction. An oil exploration probe consists of various components, including sensors and a measurement instrument assembled in modules, in which sealants are essential to join adjacent modules. Among present sealant materials, rubbers are widely used in reservoir evaluation as well as in oil production under harsh conditions; they exhibit extreme hardness and strength with an appropriate flexibility as well as an excellent structural stability under temperatures and pressures such as $175\,°C$ and $135\,MPa$, typical conditions in present common wells. In the future, more wells will be drilled deeper, and the oil excavation environment will become much harsher. Since rubber is almost exclusively used as a sealing material and is essential in oil probing and excavation, rubber having the ability to withstand higher temperatures

and pressures has been a serious technological challenge in that field, although it is especially difficult to significantly increase the rubber resistance to high temperatures above 250 °C and high pressures above 200 MPa.

Most of the rubber applications are used as aircraft components, e.g., o-rings and gaskets, because they represent the interface between two environments: the internal one containing the functional fluid (gas or liquid) and the external one (air in most of the cases). Elastomers can be compressed and due to their excellent elasticity retain the original shape. Superior tear strength makes elastomers the most widely used material for high-performance aircraft tyres, and the high damping capacity of elastomers is exploited in space applications for the realization of shock absorbers and passive dampers installed on satellites.

2 Compounding

The vulcanization process invented in the year 1839 by Charles Goodyear made the rubber stronger and more elastic. The unvulcanized rubber is stiff when cold and soft when warm, hindering its utilization in products having a good level of elasticity. Vulcanization prevents the polymer chains from moving independently. As a result, when stress is applied the vulcanized rubber deforms, but upon release of the stress, the product reverts to its original shape.

Compounding is the process of mixing elastomers with various additives and/or nanofillers to improve the final properties, such as the mechanical resistance and electrical conductivity. Mixing machines include open two-roll mill and internal mixers. Internal mixers disperse the fillers by generating high shear forces, while the two-roll rubber mill disperses the fillers by repeated milling several times. The main types of mixing methods take into account three different technologies each of them in charge of a different partner (Fig. 1):

(1) **Traditional compression moulding technology** which is the *state of the art of the realization of the components like intake manifolds, O-rings and fuel filler neck protector*;
(2) **Extrusion manufacturing processes** for the production of fuel pipes.
(3) **Injection Molding technology** using Thermoplastic vulcanizates rubber **(TPV)**;
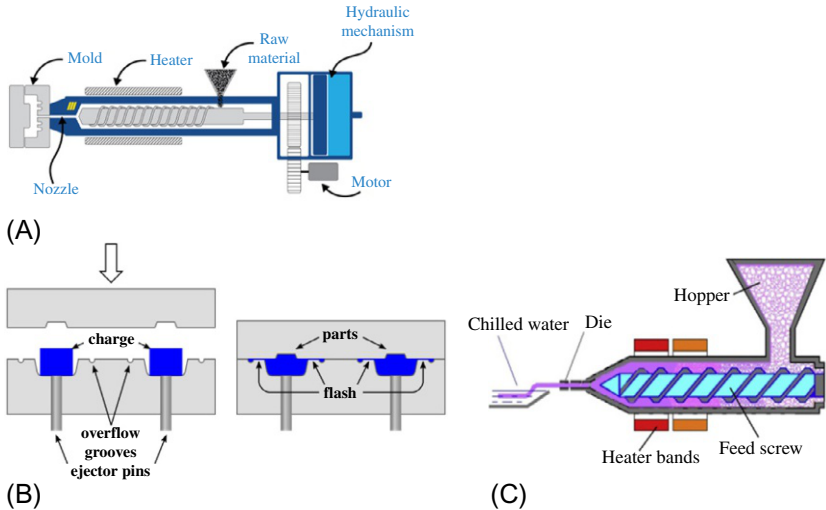
Fig. 1 (A) Injection moulding, (B) compression moulding, and (C) extrusion machines.

(4) Compounding ingredients may be categorized as:
- Base polymer (natural or synthetic rubber)
- Curing agents
- Stabilizer systems (antioxidants and antiozonants)
- Processing aids (plasticizers, etc.)
- Reinforcing fillers (carbon black, silica, mineral fillers) and/or nanofillers (grapheme, carbon nanotubes)
- Additives (abrasives, blowing agents, pigments, etc.).

The main advantages of the Injection moulding and extrusion technology respect to the compression moulding are reported in Wierseman Model of Fig. 2 and can be summarized as it follows:

(i) *Shortest cure times* (up to −50% compared to compression moulding) and cycle times (up to −40%)

(ii) *No preforms necessary*

(iii) *Increase in dimension quality* (up to +50%)

(iv) *Reduction in the use of materials* (up to −80% compared to compression moulding): precise volumes are injected into the mould

(v) *Better flowability* by friction heat of screw

(vi) *High homogeneity* of cross linking throughout the cross section

(vii) *Minimal waste and reworks*

(viii) *Welds reduction*

Baseline compression molding	Injection	Extrusion
Cycle time	-40%	-20%
Dimension quality	+50%	+15%
Material waste	-70%	-80%
Complexity	+	+++
Sustainability	+	+++
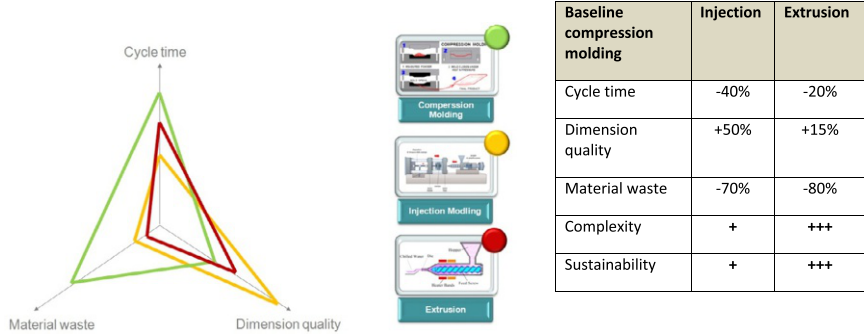
Fig. 2 Wierseman model: comparison between compression; extrusion and injection moulding.

2.1 Classifications of elastomers

Elastomers are classified according to ASTM D 1418 and are abbreviated as reported in Table 1.

In Table 2 the most common elastomers and their trade names are reported.

In the following section the most important elastomers are discussed [6–8].

2.1.1 Natural rubber

Natural rubber (NR) is the most important raw material used in the production of elastomers. Natural Rubber is obtained from the latex sap of trees, Hevea Brasiliensis, which is native to the tropical Americas. An incision

Table 1 Classifications of elastomers [6]

Last letter in the abbreviation: meaning	Examples
M: saturated chains of carbon atoms, no double bonds	EPDM, FKM, FFKM
R: double bonds in the carbon chain (unsaturated)	NR, CR, SR, SBR, IIR, NBR, HNBR
O: oxygen in the polymer chain	Epichlorohydrin rubber
Q: silicon and oxygen in the polymer chain	VMO, FVMQ
T: sulphur in the polymer chain	Polysulphide elastomer
U: carbon, oxygen, and nitrogen in the polymer chain	Polyurethane rubber

Table 2 Elastomers and trade names [7]

ASTM D 1418 abbreviation	Chemical names	Trade names
CR	Chloroprene	Neoprene, Skyprene, Butclor, Baypren, Denka
CSM	Chlorosulphonyl polyethylene (Chlorosulphonated polyethylene)	Hypalon, Noralon
EPD	Ethylene-propylene copolymer	Buna-AP, Dutral
EPDM	Ethylene propylene diene terpolymer	Epsyn, Nordel, Epcar, Keltan, Royalene, Polysar-EDM
FEPM	See TFE/P	Aflas, Epsyn
FFKM/ FFPM	Perfluoroelastomer	Perlast, Kalrez, Chemraz
FKM/FPM	Fluoroelastomer	Viton, Dai-el, Fluorel, Tecnoflon
FVMQ	Fluorosilicone	Silastic LS, FSE
HNBR	Hydrogenated nitrile	Therban, Tomac, Zetpol
IIR	Butyl rubber	Exxon Butyl, Polysar Butyl, Esso Butyl
IR	Isoprene	Shell Isoprene Rubber
NBR	Nitrile butadiene	Breon, Butakon, Chemigum, Hycar
XNBR	Carboxylated nitrile	Buna-N, Butacril, Paracil, Perbunan, Krynac, Europrene-N, Nipol
NR	Natural rubber	Nastsyn
SBR	Styrene butadiene (Buna-S)	Cariflex S, Plioflex, Europrene, Pliolite, Buna Huls, Carom, Solprene
TFE/P	Tetrafluoroethylene/ propylene	Alfas, Flourel, Fluoraz
VMQ PVMQ	Silicone	Silastic, Siloprene, Rhodorsil, Silplus

is made into the bark of the rubber tree and the latex sap is collected in cups. The solid grades are obtained by coagulation of the latex by adding an acid. Then, it is flattened and rolled into rubber sheets and hung out to dry. Natural rubber is available in many grades, but, the most important distinction is that between latex and solid grades.

The main properties of natural rubber are as follow:
–   Natural rubber combines high strength (tensile and tear) with outstanding resistance to fatigue.
–   It has excellent adhesion to brass–plated steel cord, which is ideal in the fabrication of tyres.
–   It has low hysteresis which leads to low heat generation, and this in turn maintains new tyre service integrity and extends retreadability.
–   Natural rubber has low rolling resistance with enhanced fuel economy.
–   It has high resistance to cutting, chipping and tearing.
–   It has moderate resistance to environmental damage by heat, light and ozone which is one of its drawback.

Thanks to these characteristics, natural rubber can be used in different applications. The main use of solid natural rubber is for the manufacture of tyres, but also, it is an excellent spring material. Latex natural rubber has good barrier properties against pathogens such as the AIDS virus (HIV), and so, it is used in condoms and surgical and medical examination gloves. Also, it is used in catheters, balloons, medical tubes, etc.

2.1.2 Styrene butadiene rubbers

Styrene butadiene rubber (SBR) is one of the cheaper and the highest volume general–purpose synthetic rubbers, that competes with natural rubber (NR). SBR is a highly random copolymer of butadiene and 10–25% styrene, produced by free–radical solution polymerization or by emulsion polymerization. The addition of styrene lowers the price and improves the abrasion and aging resistance, and blend properties of polybutadiene. For it, SBR is used in great quantities in automobile and truck tires, generally as an abrasion–resistant replacement for natural rubber.

Like natural rubber, SBR is swollen and weakened by hydrocarbon oils and is degraded over time by atmospheric oxygen and ozone. However, unlike natural rubber, it tends to harden with age instead of softening. The most important limitations of SBR are inferior mechanical properties (requires reinforcements), low resilience, low tear strength, and poor oil and ozone resistance. Thus, the proportion of SBR in tire treads decrease as increases the need for heat resistance. Hence, natural rubber is used in a 100% in the heaviest and most severe uses, such as tires for buses and aircraft. SBR is also used in footwear, conveyor belts, hoses, toys and moulded rubber goods, etc.

2.1.3 Butyl rubbers

Butyl rubber (IIR) is produced by low temperature cationic copolymerization of isobutylene and a small amount of isoprene, providing for a highly saturated backbone. It can be vulcanized with sulfur, but due to its low unsaturation requires more active accelerators, as dithiocarbamate and thiuram.

It has outstanding ozone and weathering resistance, thermal stability, vibration damping and higher coefficients of friction and good chemical resistance. IIR has exceptional low gas and moisture permeability which makes it ideal for inner tubes and high pressure/vacuum applications under demanding conditions. IIR elastomers are sometimes halogenated with chlorine or bromine to improve their resistance to certain chemical media.

Butyl rubber is a good choice for a wide variety of rubber goods. It is used for inner tubes of tires and other high pressure tubes, due to low permeability of air, automotive mechanical parts, insulations, vibration damping, liners, O-rings, sealant, adhesives, etc.

2.1.4 Butadiene rubbers

Polybutadiene is a synthetic rubber formed from the polymerization of the monomer 1,3-butadiene. It is the second largest volume synthetic rubber produced, next to styrene-butadiene rubber (SBR), with about a quarter global consumption of synthetic rubber. Polybutadiene has excellent abrasion resistance (good tread wear), low hysteresis loss, high elasticity, and low rolling resistance due to its low glass transition temperature (T_g), typically $< -90\,°C$. However, this also leads to a poor wet traction properties, so, usually, BR is blended with other elastomers like natural rubber or styrene–butadiene rubber for tread compounds. Its major use is in the manufacture of tires going into treads and sidewalls, which consumes about 70% of the production. Another 25% is used as an additive to improve the toughness (impact resistance) of plastics such as polystyrene and acrylonitrile butadiene styrene (ABS). It is also used to manufacture golf ball cores, various elastic objects and to coat or encapsulate electronic assemblies, offering high electrical resistivity.

2.1.5 Ethylene propylene diene rubber

Ethylene propylene diene monomer (EPDM) is a terpolymer of ethylene, propylene and a small amount of diene component (2.5–12 wt.%), which provides cross-linking sites for vulcanization. The diene is usually

dicyclopentadiene, ethylidene norbornene, or 1,4 hexadiene. The distribution of the propylene comonomer may vary from random to alternating. The ethylene content can vary from 45% to 85%. If the contents of ethylene and propylene are approximately equal, both monomers are distributed by equal within the polymer and the rubber is amorphous. If the ethylene content is above 65% by weight, the ethylene sequences are able of forming crystals. This results in improved tensile strength, hardness and compressive strength at low temperatures.

EPDM elastomers are valuable for their excellent resistance to heat, oxidation, ozone and weather aging due to their saturated backbone structure. They also exhibit excellent electrical insulation, compression set, and low temperature properties, but only fair physical strength properties. As non-polar elastomers, they have good electrical resistivity, as well as resistance to polar solvents, such as water, acids, alkalies, phosphate esters and many ketones and alcohols In fact, EPDMs are probably the most water resistant rubbers available. These rubbers respond well to high filler and plasticiser loading, providing economical compounds. They can develop high tensile and tear properties, excellent abrasion resistance, as well as improved oil swell resistance and flame retardance.

EPDM rubber is an extremely versatile material that can be used in a variety of applications, from automotive products to HVAC parts. Since EPDM rubber does not crack outdoors, it is widely used for seals in buildings and in the automotive industry. EPDM is used in other applications as steam hose, high temperature–resistant seals and roll covers. However, EPDM cannot be used in applications where a continual contact with petroleum based products is required. EPDM is not recommended for usage in food applications or those that expose it to aromatic hydrocarbons.

2.1.6 Nitrile rubbers

Nitrile rubbers (NBR) is a copolymer of acrylonitrile and butadiene rubber.

Nitrile rubber can be classified as three types based on the acrylonitrile (ACN) content (low, medium and high) as follows:
- High nitrile: >45% ACN content
- Medium nitrile: 30–45% ACN content
- Low nitrile: <30% ACN content

As the ACN content increases, NBRs show superior resistance to aromatic hydrocarbons. Hydrogenated (HNBR) compared to NBR shows higher physical strength and retention of properties after long-term exposure to heat and oil. HNBR compounds typically have tensile strengths of

20–31 MPa within a broad temperature range, −40 °C to 165 °C. HNBR elastomers have excellent resistance to common automotive fluids (e.g., engine oil, coolant, fuel, etc.) and many industrial chemicals. These unique properties make HNBR the most used elastomer in automotive, industrial, and performance-demanding applications. In the automotive market it is used for dynamic and static seals, hoses, and belts. HNBR has also been widely employed in industrial sealing for oil field exploration and processing.

2.1.7 Silicone elastomers

Silicones are synthetic polymers containing a silicon-oxygen backbone similar to that in silica, but with organic groups attached to the silicon atoms by C-Si bonds. Silicone rubber materials are readily available in a variety of forms, such as solids, open cell foams, closed cell sponges, thermally conductive, and electrically conductive. The most widely used silicones are those which have methyl groups along the backbone. However, some properties such as solubility in organic solvents, water-repellence and flexibility can be altered by substituting other organic groups for the methyls (Table 3). So, silicones with phenyl groups are more flexible polymers than those with methyl groups. Silicone rubber is generally non-reactive, non-toxic, stable at extreme temperatures, excellent resistant to extreme environments (ozone, UV, water, snow…), good resistance to compression set and low level of flammability. Due to these properties and its ease of manufacturing and shaping, silicone rubber can be found in a wide variety of products, including: voltage line insulators, automotive applications; cooking, sportswear, and footwear; electronics; medical devices and implants; and sealants.

Fluorocarbon elastomers (FKM or FPM)
The different types of FKM are reported in Table 4.

Table 3 Classification of silicone rubbers [9]

Class	Substituent in polymer chain	Applications
MQ	Methyl	Not commonly used
VMQ	Vinyl	General purpose
PMQ	Phenyl	Extremely low temperature
PVMQ	Methyl, phenyl and vinyl	Extremely low temperature
FVMQ	Trifluoropropyl	Fuel, oil and solvent resistance

Table 4 Classification of FKM [6]

Class: Fluorine content	Properties/applications
Copolymer of vinylidine fluoride (VF) and hexafluoropropylene (HFP): 65–65.5%	Good fluid and best compression set
Terpolymer of VF, HFP and tetrafluoroethylene (TFE): 67%	Better chemical resistance and inferior compression set
Tetrapolymer of VF, HFP, TFE and cure site monomer: 67–69%	Improved chemical resistance and compression set compared to terpolymers

2.1.8 Perfluoroelastomers

The chemical structure of perfluoroelastomers (FFKM) is sketched in Fig. 3; the absence of hydrogen atoms increases the heat and chemical resistance with the capability to withstand for a long-time to high temperatures up to 260 °C and, for a short–time, up to 310 °C.

Fluorinated elastomers FKM (typically containing 65% fluorine) and more recently perfluoroelastomers FFKM (typically containing 71% fluorine) provide materials with excellent high temperature and chemical resistance. FKM is of critical importance in solving problems in aerospace, automotive, chemical and petroleum industries. In particular FKM materials are noted for their high resistance to heat and a wide variety of chemicals (see Table 2) and they are usually extruded. Other key benefits include excellent resistance to aging and ozone, very low gas permeability and the fact that the materials are self–extinguishing. FKM materials are generally not resistant to hot water, steam, polar solvents, glycol–based brake fluids and low molecular weight organic acids. Also, they give low out–gassing under vacuum and have good high temperature compression set resistance. The major disadvantage is the poor low temperature flexibility. Fluorine containing thermoplastic vulcanizate (TPV) elastomers consist of a continuous thermoplastic fluorocarbon resin phase and a dispersed amorphous vulcanized fluorine containing elastomer phase, which is useful as a melt formable material having rubber elasticity and processable by injection moulding. Injection

$$-(CF_2-CF_2)_n-(CF_2-CF)_m-(CF_2-CF_2)_x-\overset{*}{C}S-$$
$$|$$
$$O$$
$$|$$
$$CF_3$$
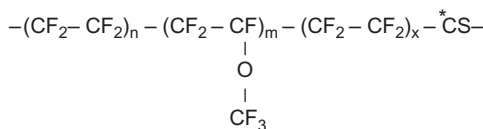
Fig. 3 Structure of FFKM.

moulded components can find use as seals and gaskets in applications where high temperatures and harsh chemical environments are common, for example in certain types of automotive applications.

3 Elastomer aerospace requirements

Energy absorption is an increasing important issue in the design of automobiles and aircraft. Mechanical damping is crucial for vibration controls, fatigue endurance, and impact resistance. Compared with metals, viscoelastic polymers are shown to be promising for damping materials and have attracted considerable attention recently [10–13]. Elastomers with their elasticity and elongation values from one hundred to several thousand percent, are ideal candidates to meet the requirements of enough rigidity and flexibility to give long flexural fatigue lives.

Current launch vehicle and payloads utilize numerous pyrotechnic devices that are generally used to separate structural subsystems (e.g., payloads from launch vehicles) and/or deploy appendages (e.g., solar panels). The initial pyroshock peak acceleration may be as high as 200,000 g with high frequency content as high as 1 MHz; because of the high frequency content, many hardware elements and small components are susceptible to pyroshock failure. The outstanding dynamic properties of elastomers make them suitable as shock absorbers and passive dampers in the space industry. Firstly, they were exploited to prevent damage due to shock loads and then they were used as passive damping equipment. In both cases the scope was always to limit shock level effects on equipment and devices.

In this regard the main properties that play a crucial role in aerospace applications are:

(i) Mechanical characteristics

The main mechanical characteristic of elastomers is the extreme elongation (more than 400%) and recovery of the original shape when relaxed. The extreme elongation can be attributed to the long molecular chains, while the networking of cross-links between such long molecular chains is responsible of the shape recovery.

(ii) Thermophysical aspects

The high mobility of the macromolecular chains is due to the glass transition temperature (T_g) of elastomers that is lower than room temperature, and it also depends on the chemical structure of the elastomer. Above T_g elastomers will be soft and flexible, while below the T_g they will be hard and

brittle. Thus, the elastomers are very elastic around T_g. This is the relaxation region where the damping of the elastomer is maximum.

(iii) Viscoelasticity

The Voigt model predicts the viscoelastic behavior of elastomers. This viscoelastic model predicts that the total stress (σ) is equal to the sum of the elastic and viscous stresses, as shown in Eq. (1):

$$\sigma = \gamma_0 [G'(\omega) \sin(\omega t) + G''(\omega) \cos(\omega t)] \tag{1}$$

Thus, the modulus can be expressed as the storage modulus (G'), which is the measure of the elastic behavior and loss modulus (G'') that measures the viscous behavior. The ratio of the loss to the storage modulus, is called the damping (φ).

The Voigt model predicts that G' and G'' depend on the frequency and temperature. When ω is low the molecular chains have enough time to flow and the viscous or liquid–like behavior predominates. Otherwise, when ω increases, the molecular chains behave like a rigid solid and hence the elasticity dominates and the material behaves in brittle fashion. The temperature has an opposite influence on elastomers: at very low temperatures the elastic modulus is very high and the elastomer is rigid and brittle, while at high temperatures the elastic moduli are low and the elastomer is elastic. At intermediate temperatures, near the glass transition temperature T_g, the elastomers are mostly viscous.

• Fluid resistance [14]

The O-ring is the most common elastomer sealing component based on Newton's Third Law, which states that "for every action, there is an equal and opposite reaction." When allocated in a dimensioned groove, elastomers act like a liquid and are incompressible; thus, the energy transmitted through the seal produces a sealing force against the faces of the groove. In extreme Oil and Gas applications, extreme performances are required, such as mechanical strength to withstand the pressures and strains without rupturing, good thermal stability and compression set properties, resistance to swelling, and resistance to explosive decompression. Many aerospace products such as seals, gaskets, and hoses encounter lubricating and hydraulic oils, greases, and fuels.Many liquids are good solvents for most elastomers; this causes swelling and thus the change of the physical properties and the housing of elastomeric seals. The fluid susceptibility test is the most reliable method for selecting an elastomer for use in the presence of specific fluids.

The fluid resistance of elastomers depends on the following factors:
- Elastomer cross–linking
- Compounding ingredients
- Temperature and time of exposure
- Dimensions of the elastomer part
- Chemical composition of fluid medium.

4 Aerospace applications of elastomers

Elastomers are essential materials for the following aerospace systems [15]:
- **(i)** *Airframe systems*
  - Structural system vibration damping elements
  - Pressurization system sealing parts
  - Control system power source, actuator, servo, and vibration damping parts
  - Chemical, thermal, and abrasion–resistant coatings and parts
  - Electrical system parts
  - Heating and cooling system parts.
- **(ii)** *Instrument, weapon, indicator and guidance systems*
  - Power source and transmission parts
  - Electrical insulation
  - Shock absorption and vibration damping parts
  - Chemical, thermal and abrasion resistant coatings and parts.
- **(iii)** *Landing gear systems*
  - Tyres
  - Shock absorption and vibration damping parts
  - Braking device parts
  - Retraction mechanism parts.
- **(iv)** *Propulsion systems*
  - Fuel containment and transfer element parts
  - Actuator and servo parts
  - Shock absorption and vibration damping parts
  - Electrical insulation
  - Solid propellant ingredients.

References

[1] E.P. De Garmo, J.T. Black, R.A. Kosher, Materials and Processes in Manufacturing, Macmillan Publishing Company, New York, 1988.
[2] M. Lancho, A. Fernandez, S. Kiryenko, Shock attenuation system for spacecraft and adaptor, in: European Conference on Spacecraft Structures, Materials & Mechanical Testing. ESA Publications Division, ESTEC, Noordwijk, The Netherlands, 2005.

[3] F.W. Barlow, Rubber Compounding: Principles: Materials and Techniques, Marcel Dekker Inc, New York, 1993.

[4] I. Franta, Elastomers and Rubber Compounding Materials, Elsevier Science Publishers Company, New York, 2012.

[5] M.P. Groover, Fundamentals of Modern Manufacturing Materials Processes and Systems, John Wiley & Sons, Hoboken, NJ, 2010.

[6] K. Nadgi, Rubber as an Engineering Material: Guideline for Users, Hanser Publishers, Munich, 1993.

[7] J.R. White, S.K. De (Eds.), Rapra Rubber Technology Handbook, Rapra Technology, Billingham, 2001.

[8] M. Morton, Rubber Technology, Van Nostrand Reinhold Company, New York, 1973.

[9] J.A. Brydson, Plastic Materials, Butterworth-Heinemann, Oxford, 1999.

[10] S. Ramakrishna, Microstructural design of composite materials for crashworthy structural applications, Mater. Des. 18 (1997) 167–173.

[11] V.R. Buravalla, C. Remillat, J.A. Rongong, G.R. Tomlinson, Advances in damping materials and technology, Smart Mater. Bull. 2001 (2001) 10–13.

[12] X. Zhou, E. Shin, K.W. Wang, C.E. Bakis, Interfacial damping characteristics of carbon nanotube-based composites, Compos. Sci. Technol. 64 (2004) 2425–2437.

[13] Y.T. Sung, C.K. Kum, H.S. Lee, N.S. Byon, H.G. Yoon, W.N. Kim, Dynamic mechanical and morphological properties of polycarbonate/multi–walled carbon nanotube composites, Polymer 46 (2005) 5656–5661.

[14] R.A. Shanks, I. Kong, General purpose elastomers: structure, chemistry, physics and performance, in: P.M. Visakh, S. Thomas, A.K. Chandra, A.P. Mathew (Eds.), Advances in Elastomers: Blends and Interpenetrating Networks, Springer-Verlag, Berlin, 2013.

[15] C.M. Bhuvaneswari, S.S. Kale, G. Gouda, P. Jayapal, K. Tamilmani, Elastomers and adhesives for aerospace applications, in: N. Eswara Prasad, R.J.H. Wanhill (Eds.), Aerospace Materials and Material Technologies, Springer, 2017.

CHAPTER 2

Elastomers in extreme environments applications

Nicola Ranieri
Solvay Specialty Polymers, MiIan, Italy

Contents

The purpose of this chapter is to help the reader in the choice of the correct rubber for applications in extreme environments. We will describe test methods simulating specific requirements which can be used in order to assess the behavior of elastomers under selected service conditions.

Elastomers are indeed the main component of a rubber, that is produced starting from a compound of elastomer, reinforcing filler, vulcanizing agents and processing aids. Because the elastomer is the most relevant ingredient in a rubber compound, both for its function and its quantity (usually above 60% in weight), the choice of the correct elastomer is a necessary condition to achieve high rubber performances.

The focus of this study will be therefore on the elastomers, even if the other ingredients of the rubber compound can also affect thermal- and chemical stability, though to a lesser extent; seen the variety of choice for the composition of the compounds, it would be anyhow not possible to cover all their possible combinations with respect to the effect they have on the overall performance of the rubber. Therefore each consideration about a given class of elastomers refers to the standard formulation as described in its available literature, that most often deals with carbon black as reinforcing filler.

Most of the rubbers applications is for use as seal elements such as e.g., o–rings, gaskets, shaft–seals or diaphragms, and all are key parts of any system,

15

because there they represent virtually the door between two environments: the internal one containing the functional fluid (gas or liquid), and the external one (air in most of the cases). Therefore the service life of a whole equipment is directly linked to the good service of the rubber part which is installed. Designing the right seal is a powerful tool to control the costs of service of an equipment (pumps, pipelines, engines, …), both because a seal failure can result in safety issues, as *worse-case scenario*, in loss of productivity, and because a longer seal lifetime means reduced maintenance with associated shut-downs.

The unfortunately famous Shuttle crash case in 1986 is an useful example of how important a sealing element can be. It was reported that the "*Challenger accident was caused by a failure in the o-rings sealing a joint on the right solid rocket booster*, which allowed pressurized hot gases and eventually flame to *blow by* the o-ring and make contact with the adjacent external tank, causing structural failure. The failure of the o-rings was attributed to a faulty design, whose performance could be too easily compromised by factors including the low temperature on the day of launch [1]". In this report the rubber element shows up in all its importance, where the *faulty design* apparently was not considering the lowest temperature possible faced by the o-ring in its lifetime. Such a disaster explains well the dimensions of the consequences linked to a rubber failure: beside the casualties, that are by far the most severe ones, and the economical damages, also the loss of the market name can add as long-lasting implication.

Fig. 1 shows schematically what a rubber part faces during its service life.

During its lifetime the rubber part can undergo several cycles of cooling/heating, can be stressed mechanically (reciprocating movements or pressure) and exposed to chemicals of various nature. Each of these aspects should not detriment the rubber performance nor compromise its service.

Extreme applications are meant herewith those where the rubber part, be that a seal, a hose or a membrane, must work at high temperatures, at low temperatures, or exposed to aggressive chemicals; often it deals with a combination of these cases. Even if the definition of the three conditions is quite arbitrary, herewith "high" temperatures are meant the ones above $150\,°C$ and "low temperatures" the ones below $-30\,°C$. The definition of "aggressive chemicals" is quite complicated given the variety of the chemistry of all possible media that can come in contact with rubber parts. Aggressive are generally meant the chemicals able to swell the rubber and/or to chemically degrade it.
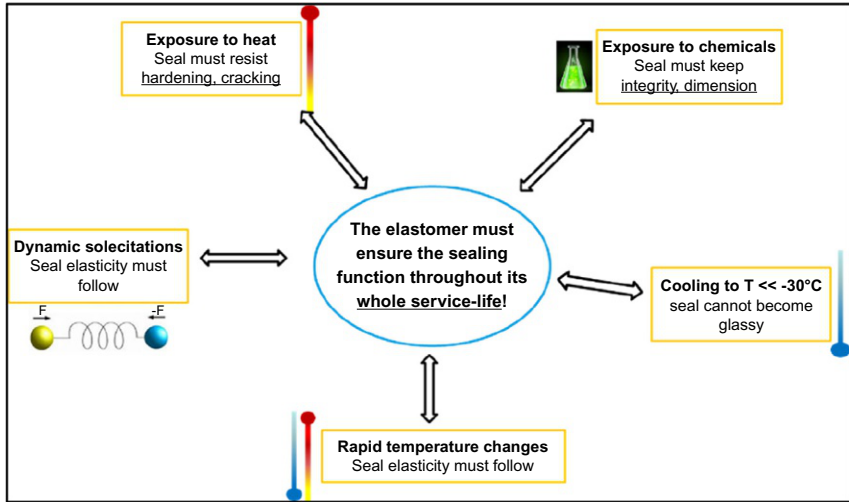
Fig. 1 The service challenges of rubber parts (scheme).

The chapter will focus on how to address the different requirements that an "extreme application" may need:

– resistance to temperatures higher than 150 °C
– cold flexibility below −30 °C
– resistance to complex fluids
– static or dynamic function[a]

It is usually the combination of all the four categories of requirements that makes the elastomer's choice challenging, and selected test methods are a valid support to find a suitable material able to face each given case.

Herewith the typical requirements that are met in *O&G, Aerospace* or *Industrial* applications, that are often referred to as "harsh environment cases", will be discussed.

Some of the most common chemical environments of such markets are listed in Table 1, along with their extreme service conditions.

Automotive applications are also demanding in terms of chemical and service temperatures, but these are not considered "extreme" because the consequences of a failure are not as dramatic as in *Aerospace*, *O&G* and *Industry processing*.

---

[a] Static: o–ring in a groove, gasket between two surfaces (e.g., flanges); dynamic: rotary shafts, reciprocating parts.

Table 1 Example of chemical environments for selected applications.

	Aerospace	O&G	Industry processing
Exposure to: (*examples*)	*Fuels*: blends of alifatic and aromatic hydrocarbons Turbine and engine *lubricants*: highly additivated oils with amine-based antioxidants *Oxidants*: oxygen and ozone *Radiations* (UV, X, γ)	*Fluids*: hydrocarbons, methanol, glycols, brines *Gas*: CO_2, CH_4, H_2S	*Oxidants*: nitric acid, peroxides, bleaches *Acids*: mineral and organic *Bases*: caustic, ammonia *Steam*
Max service T	250–300 °C	200 °C	250 °C
Lowest service T	−50/−60 °C	−40 °C	0 °C
Special requirements	–	RGD (rapid gas decompression) resistance	No metal corrosion

The review will consider first the thermal and chemical stability of elastomers, then their cold flexibility. Since cold flexibility is a necessary condition for extreme applications, the focus of the whole chapter will be on elastomers whose T_g by DSC is below 30 °C.

1 Elastomers for high temperature and harsh chemical environments

The resistance of a rubber part to high temperatures is related to the resistance of the rubber compound primarily to oxidation. Since oxidation is also the mechanism of many chemical degradation patterns, the choice of a compound that resists to oxidation is one of the main criteria for its use in extreme environments.

ASTM D2000 standard classifies the most common elastomer classes according to their volume swell in a reference oil (IRM 903), and to their highest service temperature, defined as the highest temperature at which changes of original mechanical properties after 70 h aging are kept within defined limits.
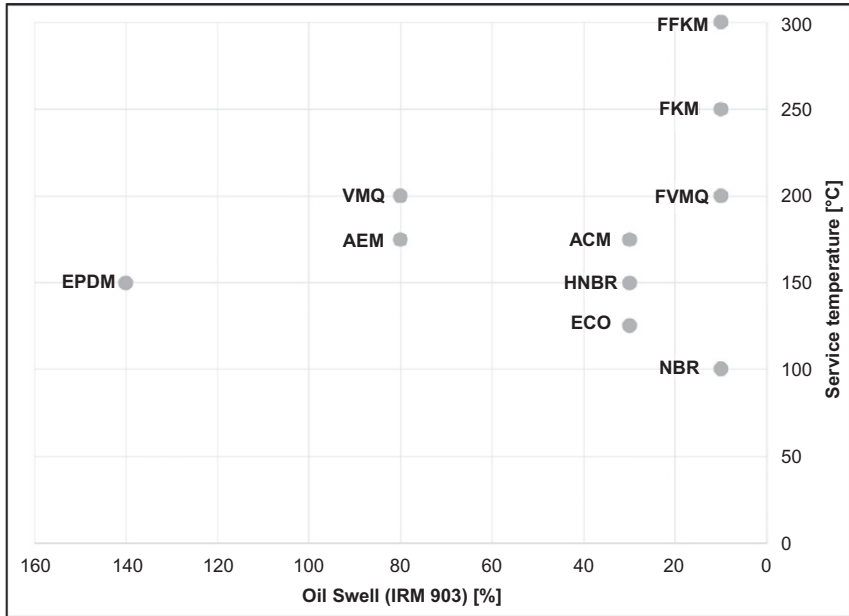
Fig. 2 Relative performance of elastomers according to ASTM D2000.

Fig. 2 shows such elastomers ranking according to *ASTM D2000*, focusing here on the ones for mid- to high-end applications, such as the ones in the *Automotive, Aerospace, O&G* or *Processing Industry* markets, where the rubber part faces high temperatures during service, with often exposure to aggressive chemicals.

Table 2 describes the main features of the elastomers that are discussed herewith.

The nature of the elastomer's polymer chain is the main driver for the resistance to both oxidation (thermal, chemical) and UV/light degradation (yellowing, brittleness); the most important polymer functionalities with this respect are summarized schematically below, in an increasing order of resistance:

  i. *unsaturations on polymer main chain*
 ii. *unsaturations on side chains*
iii. *saturated hydrocarbon main chain*
 iv. *siloxane-based main chain*
  v. *fluorinated polymer main- or side chain*
 vi. *perfluorinated polymer main chain*

Table 2 Short description of selected elastomers composition, main curing technology, and T_g measured on tested samples.

Tested elastomers	Description	Composition/ curing	Grades	T_g (DSC)
HNBR (hydrogenated acrylonitrile– butadiene)	Low T_g elastomer + improved chemical resistance vs NBR	49% ACN perox. cure 34% ACN 19% ACN	HNBR high ACN HNBR mid ACN HNBR low ACN	−6 °C −24 °C −37 °C
AEM (methylacrylate ethylene)	Low T_g elastomer with high thermal- and chemical resistance	55% MA diamine cure	AEM G.P. AEM high res AEM high T	−29 °C −32 °C −30 °C
ECO (epichlorydrin– ethylene oxide)	Low T_g elastomer with good hydrocarbon resistance	EC/EO diamine cure	ECO	−31 °C
VMQ (silicone)	Very low T_g elastomer	PDMS peroxide cure	VMQ	−39 °C (Tm)
FVMQ (fluorosilicone)	Very low T_g elastomer + good chemical resistance	TFPS/DMS peroxide cure	FVMQ	−67 °C
Tecnoflon VPLs FKM (fluoroelastomer)	Very low T_g FKM family + high chemical resistance	VDF/TFE/ MVE/ MOVE peroxide cure	VPL 85730 VPL 88540 VPL 75545 VPL 65455	−31 °C −41 °C −46 °C −55 °C

This simplified assessment can be confirmed if one looks at the thermal rating as to *ASTM D2000*, where at same 10% oil swell, the thermal rating is NBR ≪ VMQ and FVMQ < FKM < FFKM, which is in accordance the considerations above (Figs. 3 and 4).

The usual tests that are part of every material specification of rubbers are the compression set (*ASTM D395*): duration and temperature of such tests depend on the given specification, and for an *extreme application* compression

Fig. 3 Chemical structure of high-end hydrogenated elastomers.

Fig. 4 Chemical structure of silicone and fluorinated elastomers.

Fig. 5 Compression set of selected elastomer samples.

set is usually measured after 70 h at 200 °C, to assess the "thermal fit" of an elastomer for heat–resistance demanding applications.

Fig. 5 shows c-set values of representative high–end elastomers and clearly sets FKMs way ahead in terms of heat resistance, as expected.

It is worth noting that "HNBR low ACN" and "FKM 66% F" in Fig. 5 refer to the copolymer composition of HNBR and FKM, respectively; indeed, the properties of such elastomers can be further tuned by the comonomers choice and level, that influence the polymer chemical resistance and cold flexibility:

– in the case of HNBR and NBR families, the ACN monomer content can be varied, tuning so the chemical resistance to hydrocarbons (higher with high ACN levels) vs the cold flexibility (better with low ACN levels).

–   for FKMs, the monomers drive in an analogue way the chemical resistance (directly linked to the polymer Fluorine content) vs the cold flexibility (better at low F contents; more details in Section 2.)

It is therefore useful to describe which compositions of NBR, HNBR and FKM polymers are considered when describing their performance.

Also the measurement of the mechanical properties after an heat aging in an oven at defined time/temperature conditions is an useful tool to assess the suitability of a rubber element for long heat exposures: their change compared to the original values tells how stable the rubber (mainly the elastomer) is to oxidation or thermal decomposition.

Figs. 6 and 7 show that best heat stability is obtained with fluorinated elastomer, FVMQ and *VPL 88540,*[b] whereas many of hydrogenated elastomers are not even tested at temperatures exceeding 150 °C.

The change of mechanical properties upon thermal aging can give interesting information:

(a) when *elongation at break decreases upon heat aging*, usually the degradation reaction has led to additional interchain bonds created by radical activated mechanism (e.g., VMQ or FVMQ), that reduce chains mobility and hence the elongation at break

(b) when instead *elongation increases significantly*, either a chain cleavage reaction has occurred, or the crosslinking agent failed, because it was decomposed, leaving behind a loose rubber network

Fig. 8 shows a radical activated crosslinking of PDMS chains in a silicone rubber [2]: it is interesting to notice that when this mechanism occurs in a controlled manner, such as via organic peroxides in a silicone compound, it leads to rubber vulcanization, while instead it is the result of uncontrolled oxidation, it leads to rubber hardening.

If no oxidative patterns are likely, thermal degradation can still occur when temperatures exceed the *ceiling temperature* of the polymer, i.e., the polymer decomposition into low molecular weight species. Still taking silicone as example (one of most heat stable elastomers), such temperature is 339 °C in air and it leads to its decomposition into cyclic oligomers (D3, D4, D5, …) [3].

Both mechanisms (a) and (b) represent a rubber failure: the former, because the rubber hardens and behaves more and more like a glass with time; the latter because the resistance to mechanical stress or the recovering ability from deformation worsens significantly. In all cases the primary criterium of the rubber selection—*elasticity*—has failed.

---

[b] VPL FKMs are special FKM polymers supplied by *Solvay Specialty Polymers* under the tradename *Tecnoflon*; see later on in Section 2.
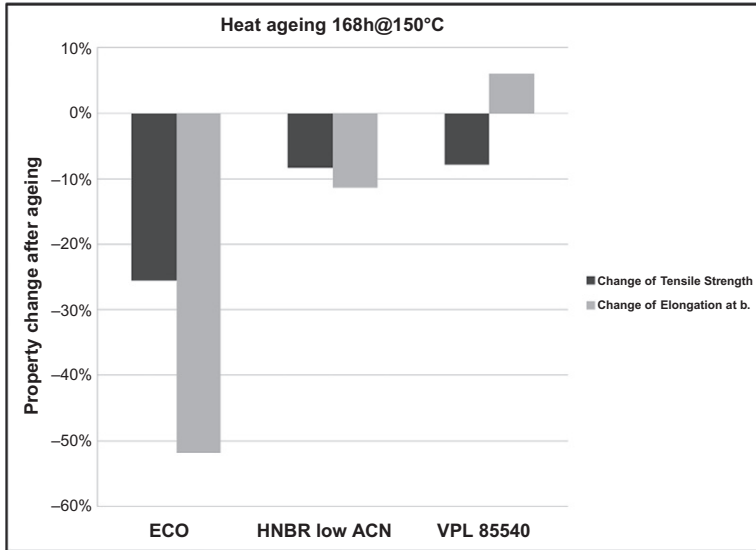
Fig. 6 Heat aging at 150 °C.
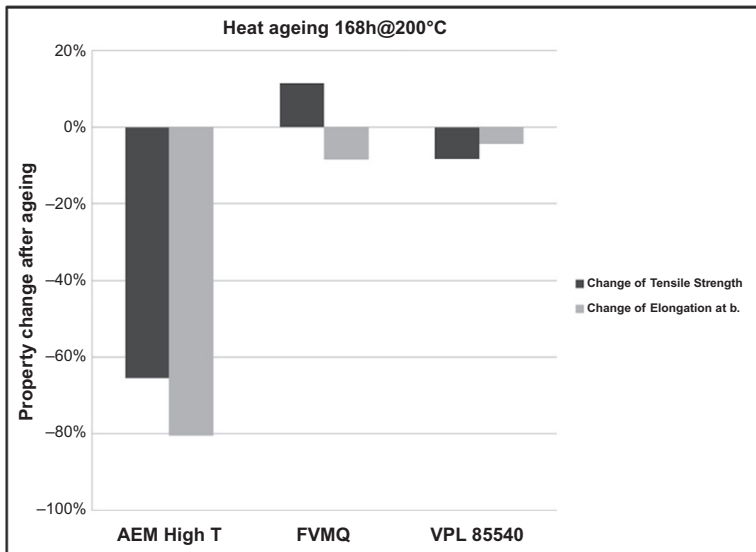
Fig. 7 Heat aging at 200 °C.

For FKM and FFKM, the heat resistance is actually driven by the cross–linking agent used, since this is the weak point of the rubber network, being it a hydrogenated moiety hence more rapidly oxidized than the fluorinated main chain.
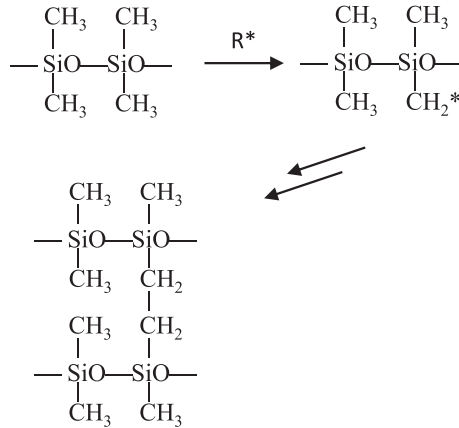
Fig. 8 VMQ oxidation scheme.

2 Elastomers resistant to harsh chemical environments

Considering the chemical resistance that a rubber element must provide, the immersion tests in the target media (gas or fluid) are usually performed at a temperature higher than the real service one, in order to have a conservative approach on the assessment of the service life of the part, and the variation of mechanical properties vs the original sample is taken as the indication of the rubber suitability for contact with that media.

A simple experiment can serve well to show the negative effect of the solvent swelling on a sealing material such as an o-ring: Fig. 9 show o-rings made of 4 different rubbers in their groove after 24h immersion in toluene at room temperature.

Dimensional stability was compromised for not fluorinated rubbers (VMQ, HNBR) and as swelling lowers as well the mechanical resistance of the o-ring, this is likely to be extruded off its groove in a pressurized system.
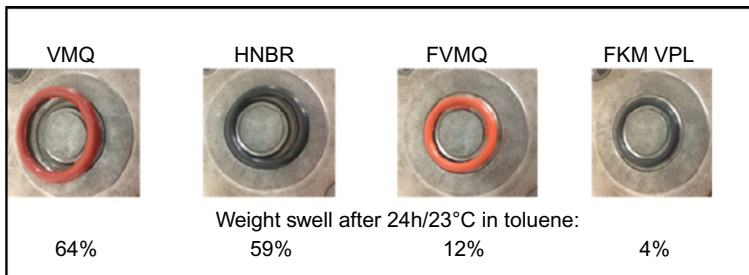
Fig. 9 Toluene swelling of selected o-rings.

According to a general rule of thumb, the more the chemical composition of the elastomer and the liquid to which it is exposed is similar, the higher their mutual compatibility and hence the easier the elastomer will be swollen. The IRM 903 oil of Fig. 2 is useful as such example: it is made of hydrocarbons, and the elastomer that swells the most in it is EPDM, that is indeed a polyolefin. Therefore the choice of an elastomer to be facing a given chemical environment should focus on those polymers whose composition does not allow for significant interactions with that chemical class.

In addition to swelling, additives often present in service fluids can cause two different degradation phenomena on the elastomer:

(a) hydrolysis- or oxidative reactions lead to an increase of elongation at break with concomitant tensile strength decrease, as consequence of the cleavage of intrachain- or/and crosslinking bonds

(b) undesired reactions can lead to an increase of the interchain bonds (additional crosslinks), hence the chain mobility is reduced and the rubber hardens. This pattern is very similar as observed in case of thermal degradative phenomena

Since any chemical attack first starts with a physical diffusion of the chemical species into the rubber (diffusion-driven swelling), hence by limiting physical diffusion, also chemical interactions are limited, including degradative reactions.

Considering the same example of IRM 903, NBR elastomers swell in a much minor way than EPDM, and this behavior relates directly to the presence in the NBR polymer chain of the polar monomer ACN (Fig. 3). For same reason, ACN presence lowers the NBR/HNBR resistance to polar fluids.

Therefore, if an additive was present in a IRM 903 solution and it was able of a chemical degradation of the elastomer chain, its negative effect onto NBR would be much less than onto EPDM, because the "transportation" of that additive inside the NBR rubber would be at a minor extent than in EPDM: chemical resistance would be improved just by increasing "diffusion resistance".

At the high-end of the chemical resistance of elastomers as to *ASTM D2000* we find the fluorinated elastomers such as FVMQ, FKM and FFKM. These elastomers, whose polymer chain is described in Fig., are the least compatible polymers with many chemicals. They all contain a C—F bond in some part of their repeating units, that is among the most resistant single bonds of organic chemistry (some examples in Table 3 [4]); the Fluorine atom is also responsible of the very low intermolecular forces between

Table 3 Bond energies of representative bonds.

Bond	Energy [KJ/mol]
C—H	337
C—F	536
C—O—C	335
Si—O	798
Si—C	435

fluorinated groups. These two features combined together make fluorinated polymers difficult to swell by many polar and unpolar fluids (the solvent–polymer interactions are not favored vs solvent-solvent ones), and very resistant to thermal degradation or oxidation. The relatively low chemical affinity of fluorinated polymers with the most classes of chemicals (e.g., hydrocarbons, alcohols, water, …) can explain why such elastomers are considered for demanding chemical applications.

Hereafter, representative cases of difficult chemical environments are listed, together with the basic criteria that can help the correct elastomer choice.

- *Additives based on amines*

A class of fluid additives that can lead to both mechanisms *(a)* and *(b)* are organic amines, that are used mainly as antioxidant protection of lubricants or coolants. Usually, the higher the service temperature of the lubricant, such as e.g., in *Aerospace* or in the latest developed car engines, the higher the level of the amine present therein and its antioxidative activity. It is worth suggesting to perform immersion tests with this kind of fluids in a closed vessel, to prevent atmospheric Oxygen to diffuse in and consume the amine, leading to false positive results.

For elastomers that crosslink via nucleophilic reactions, such as e.g., acrylic rubbers (AEM or ACM), ad–hoc selected amines are actually the crosslinking agent: therefore when an extra amine is present in the service fluid too, this can form additional undesired bonds, hardening the rubber. The magnitude of the effects depends on the additive chemical composition (i.e., number and type of substitutions of the amine), beside concentration and temperature.

Even the polymer mainchain of VMQ, FVMQ and FKMs can be broken by amine attack, though with different mechanism, with consequent drop of mechanical properties. Indeed, VDF monomer represents the only significant weak point in FKMs, for basic attack due to its inherent acidity, driven

by the high electron withdrawing effect of the perfluorinated proximity (the HFP and TFE monomers). A way to tackle that is the use of a special alternate copolymer of TFE and propylene, FEPM, marketed as *Aflas* by *Asahi Glass Co Ltd*: the Hydrogens do not display an acidic character because of the relative longer distance from TFE, and are more protected sterically by the side methyl than in VDF (Fig. 10).

On the other side, having a hydrogenated monomer in the polymer mainchain increases TFE/P's affinity to hydrocarbons, hence decreasing the elastomer resistance in e.g., fuels and crude oil.

This is explicative of how the chemistry of the polymer backbone is the most useful knowledge to understand and drive chemical resistance.

- *Highly concentrated amines*

Desulfurization or carbon dioxide removal, as required in the *O&G* industry, is often performed by a water solution of amines whose concentration can be as high as 50% *w*/w. Not many polymers survive such conditions: EPDM is one of those, because the polymer backbone is apolar (= very limited swelling by aqueous solutions), there are no acidic moieties, and there is no site for the nucleophilic attack of an amine. As the gas removal is promoted by low temperatures, anyway lower than 100°C, the use of EPDM is suggested, and limited only if other gases like methane are present.

For similar applications where temperature exceeds 120–130°C, TFE/P elastomers work well. Their upgrade becomes necessary only if heat stability is required beyond 200°C or cold flexibility below −10°C: in these cases, FFKMs are the only sure solution. Their perfluorinated chain is unaffected by amines, they can work up to 230–250°C, and a special FFKM grade down to −30°C (see Section 3).

- *Inorganic acids*

Inorganic or mineral acids are water based solutions of highly dissociated acids (in protons and the respective anion), such as sulfuric and nitric acid, Hydrogen sulfide (H_2S, see later) and Hydrogen halides (HF, HCl, HBr, HI), that are of main concern especially in the *Industry Processing* market.
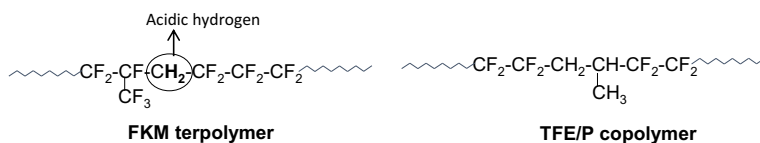
Fig. 10 Main differences between FKM and FEPM polymers.

There are mainly two negative effects that acids can show on an elastomer, oxidation and hydrolysis:

– *oxidation* can be played by nitric or perchloric acids, and the rules that apply to protect a polymer from thermal oxidation are valid for oxidizing acids too (see Section 2)
– *hydrolysis* can work on inter–chain bonds and on main–chain ones: acrylic rubbers vulcanized by amines form amide-type of crosslink, that can be hydrolyzed by acid catalysis; siloxane-based elastomers such as VMQ and FVMQ can have their mainchain hydrolyzed, because the Si—O—Si bond is highly reactive towards acid catalyzed hydrolysis. In both cases, the rubber network becomes inconsistent, with the strength of the effect driven by acid concentration and temperature

Even water itself can be considered with respect to hydrolysis: even if its action in a neutral solution is much slower, it can become important at high temperatures, or when water is present as steam

• H_2S

Hydrogen sulfide, or sour gas, can work both as an acid and as a nucleophile. This "versatility" in attack possibilities make the application of many elastomers in contact with sour gas difficult; here some examples:

– amine-cured acrylic elastomers (ACM, AEM) may be added of Sulfur on the cure–site monomers (usually carboxylic moieties) leading to additional interchain links, i.e., to rubber hardening
– same effect is observed with HNBR and EPDM, but through a different route, that is the H_2S addition on the residual double bonds; only grades with very low residual unsaturations are suggested for use
– the siloxane main chain of VMQ and FVMQ can also be hydrolysed by H_2S, making these elastomers unsuited for the application
– even FKMs should be chosen with care, because ionic curing technology of these elastomers proceed via the formation of mainchain unsaturations [5], hence same as seen for HNBR and EPDM can happen, though higher temperatures are needed

• *Compounding ingredients*

Ingredients of the rubber compound are also affecting its chemical resistance, but to a minor extent: it can be stated that the right polymer choice is a necessary condition for the longest rubber service, while the wrong compounding is a sufficient condition for it to fail. Among the most common examples useful to address chemical resistance through compounding, we can name following:

– *UV stabilizers* help reducing the detrimental effects of UV light especially, but not only, on unsaturated polymers. In case these are not

selected with care, they can turn out to be reactive towards the polymer through chemical routes, like in the case of amine-based stabilizers. They can be also stripped off during service, therefore good UV-stability is achieved with a saturated elastomer or, even better, with a fluorinated one

- *ZnO* has been claimed to work to enhance the elastomer heat rating and the adhesion of rubbers to metals, but it absorbs water at high temperature and reacts with acids, leading to rubber swelling. In the example of the acid H_2S, the addition of ZnO to the compound would make therefore the correct elastomer choice useless

- *Calcium carbonate (dolomite) or silicate (wollastonite)* are often the fillers of choice when the rubber cannot be black. Beside their different reinforcing character, both fillers have in common that they can be considered as salts of very weak acids, therefore in concentrated acids, and especially at high temperatures, they can be hydrolyzed back to CO_2 and water (*dolomite*) or SiO_2 and water (*wollastonite*). Such hydrolysis swells significantly the rubber networks, determining the mechanical resistance dramatically

While it is not possible here to cover all possible chemical environments of high-end applications with examples and data, general selection guides provided by suppliers of elastomers or rubber compounds are an useful tool as first criterium to assess the feasibility of a given elastomer for the main categories of chemicals.

3 High-end elastomers for cold temperature environments

We have seen in Section 1 that the high-end elastomers of choice when service temperatures approach or exceed 150 °C, and/or when in contact with aggressive chemicals, are HNBR, VMQ and fluorinated elastomers, such as FVMQ, FKM and FFKM (Fig. 4), that represent an upgrade with respect to common hydrogenated rubbers. Herewith we will focus on an additional level of performance that is required: the low temperature flexibility. Indeed, *Aerospace* and *O&G* applications are examples of markets where many rubber parts (gaskets, membranes, packers, hoses) are expected to work not only at very high T, but also in very cold environments, such as at T < − 30 °C. Here, the elastomer is expected to never reach its glassy state ("freeze"), that would resemble what happens by heat hardening. Indeed, even if "freezing" is a reversible phenomenon, this can lead to

dramatic part failure if happening at the wrong moment, such as e.g. when the glassy o-ring is supposed to seal the space and instead shrinks, or when the glassy hose is fragile towards mechanical stresses. The visit card of each elastomer is its Tg as defined by DSC (metodo …), either via on-set or mid-point. Glass transition defined by DSC is very helpful to assess the sealing behavior in static applications, such as for o-rings: the direct correlation between the ability to seal at $-40\,°C$ and the T_g of the elastomer is clearly summarized in Table 4.

Hence DSC is very useful to assess good isolation performances (seal-ability) of a static seal or gasket. DSC method measures glass transition according to change of specific heat in a static regime, therefore it cannot say much about how the seal responds to dynamic environments, i.e. when the temperature changes cyclically and the rubber part must follow, by pro-viding elastic recovery from deformation, such as strain or compression.

The "temperature of retraction test" ("*TR-test*" hereafter) as defined in ASTM D1329 can be helpful to have a look at the mechanical behavior of a rubber responding to temperature changes. Here, the specimen is strained of 50% of its original length and frozen in this constrained status well below the elastomer T_g; then, the rubber is left free to move and the temperature is increased slowly. The instrument measures how much of its original length the rubber recovers during the temperature increase. TR–test assesses TR10 as the temperature at which the rubber recovers 10% of its original dimen-sion, TR30 at 30% of recovery, and the like for TR50 and TR70: a simple curve is obtained connecting such recovery temperatures. T_g by DSC and TR10 are correlated, as expected, being TR10 usually a couple of degrees higher than T_g, because T_g is measured usually on the polymer itself, and TR10 on a crosslinked rubber hence with restricted chain mobility. An ideal elastomer is expected to show one single "TR100" temperature, close to its

Table 4 Compression set measured at $-40\,°C$.

Elastomer	c-set after 60 min at $-40\,°C$[a]	T_g DSC (mid-point) [°C]
FVMQ	37	−60
VMQ	40	−41
VPL 88540	38	−40
HNBR low ACN	65	−37
AEM	97	−32
ECO	97	−31

[a]ISO 815; specimen compressed of 25% 1 h at $-40\,°C$, then c-set measured at $-40\,°C$ 1 h after releasing from compression.

T_g, above which the elastic recovery is full, as a kind of temperature switch. Since this cannot be the case with polymers, the steeper the TR–curve measured, the closer is the elastomer behavior to the ideal one. For an application, the temperature span of elastic recovery should be the narrowest, indicating that the rubber part would recover back its elastic function soon after being warmed up slightly beyond its glass transition temperature; or, the other way around (cooling), that the rubber part does not stop being elastic before the T_g is reached. Indeed, it is tolerable in principle to have a frozen rubber element, when it rests at very low temperatures during function pauses, provided that it can go back fast to full service as soon as the system requires it increases, i.e. the warming caused by the part function should be used as quick as possible to recover full elasticity. Also, when the rubber part faces cooling down to temperature values close to-, but not yet lower than T_g, its elastic function should be still guaranteed.

Fig. 11 shows TR curves of elastomers with a T_g between $-40\,°C$ and $-20\,°C$: the information gathered by the sole TR10 value is not very different than T_g by DSC, as already stated. The shape of the curves instead describes that the EPDM sample takes more that $30\,°C$-span to recover full elastic behavior, whereas the HNBR samples and especially the *VPL 85540* need less warming to be back to a fully elastic rubber: VPL needs slightly more than $10\,°C$ above its TR10.

Following this model, flexibility at $-15\,°C$ is granted for "HNBR low T" and *VPL 85540* samples, but not for EPDM or "HNBR high ACN", despite what expected from their nominal T_g values.
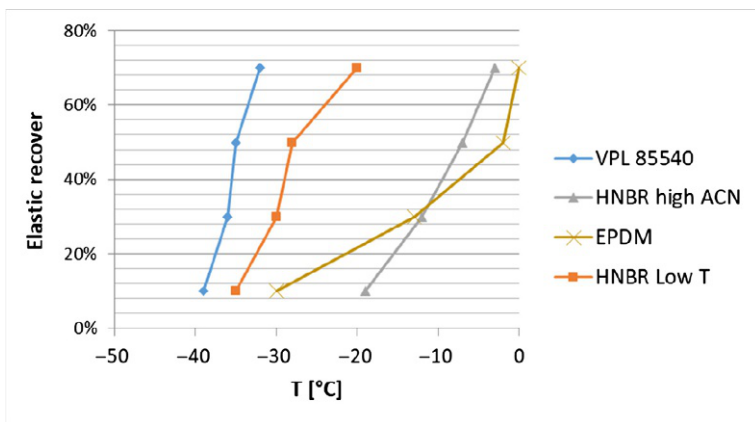
Fig. 11 TR-test of selected elastomers.

The TR curves recorded for polymers with T_g below $-40\,°C$ (Fig. 12) show interesting features:

– FVMQ represents an upgrade of VMQ concerning chemical resistance, still resembling a very low T_g (around $-60\,°C$). The TR-curve shows that its elastic recovery is quite slow i.e., the rubber starts to lose free chain mobility at T below $-30\,°C$ already

– *VPL X65455* is the FKM with the lowest T_g know in the market: even if its T_g is higher than FVMQ, the TR curve shows a higher chain mobility in the temperature range above $-40\,°C$, where instead FVMQ is not yet "completely elastic"

– VMQ is the elastomer with the lowest T_g (around $-110\,°C$), but the TR-test show an unusual steep line at $-43\,°C$: this transition is due to crystallization of PDMS chains, which have a melting point around $-40\,°C$. Being this a 1st order transition and being VMQ polymer chains highly flexible, the TR-test shows a kind of switch-like transition that happens much before the expected glass–rubber one

TR-test was also performed on aged samples, and the curves obtained after heat- or chemical aging were compared with the ones measured on the original samples. Indeed, for some applications it might be more important to keep flexibility at low temperatures during service rather than retaining decent mechanical properties, which are instead usually the data used to assess the suitability of a material, as seen earlier in Section 1 for the thermal rating tests. With this respect, it is important that the rubber element shows its characteristic elastic behavior all along its service life: measuring the
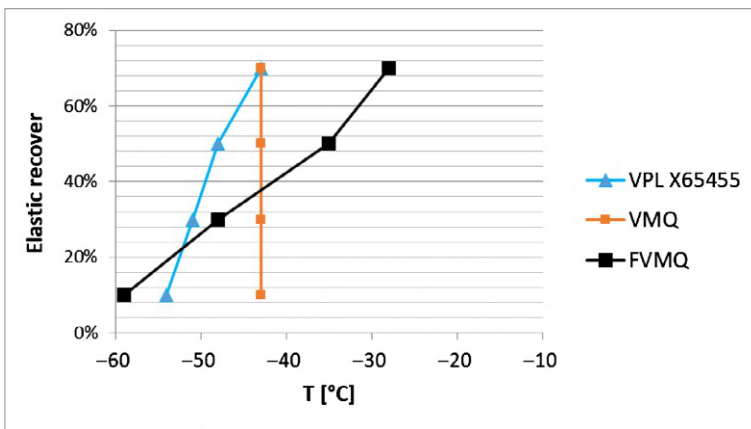
Fig. 12 TR-test of very low T_g elastomers.

change of TR-curve after an aging is as helpful as measuring the change of mechanical properties. Analogue to the common practice of measuring the change of mechanical performance after chemical or heat aging, also checking the elastomer behavior upon "cooling" or "warming" on aged samples is key to assess that the elastic behavior shown in the *as-delivered* status is kept during the entire service.

Fig. 13 shows TR-test performed on selected, high performance elastomers after heat aging for 1 week at 150 °C.

All heat aged samples but *VPL 85540* show a TR-curve shifted to higher temperatures: this can be interpreted as an heat hardening that has reduced chain mobility. After 1 week at 150 °C the ECO and HNBR samples tested did not show anymore the same flexibility *as-delivered*, and especially the ECO sample showed a shift of about 10 °C to recover full elasticity (aged TR70 at −2 °C vs −11 °C original).

Fig. 14 shows same experiment run at 200 °C with elastomers more suited to withstand such high temperature.

The curves obtained after 1 week at 200 °C show similar trend, with the TR-curves shifted to higher temperatures due to the heat hardening, for all elastomers but the FKM *VPL 88540*. The magnitude of the shift is proportional to the resistance to oxidation of the polymers. It is interesting to note that VMQ's straight line corresponding to Tm is also shifted, therefore even the melting process looks affected by some heat-driven hardening.
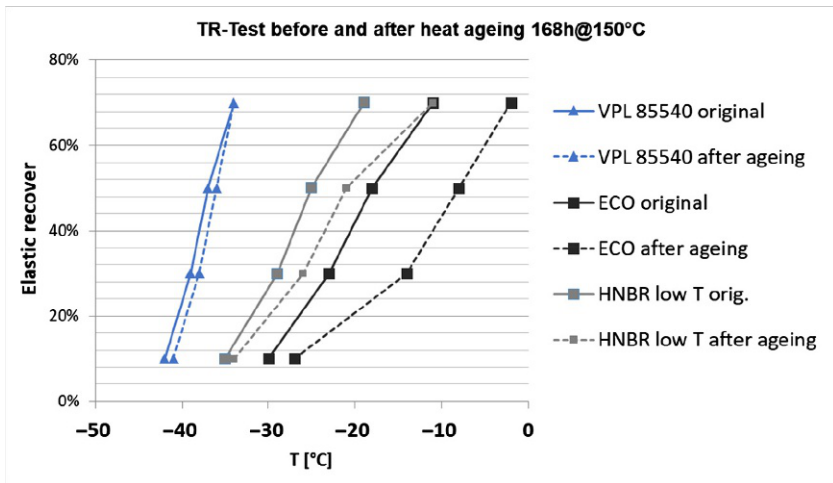
Fig. 13 TR-test curves before- and after heat aging at 150 °C.
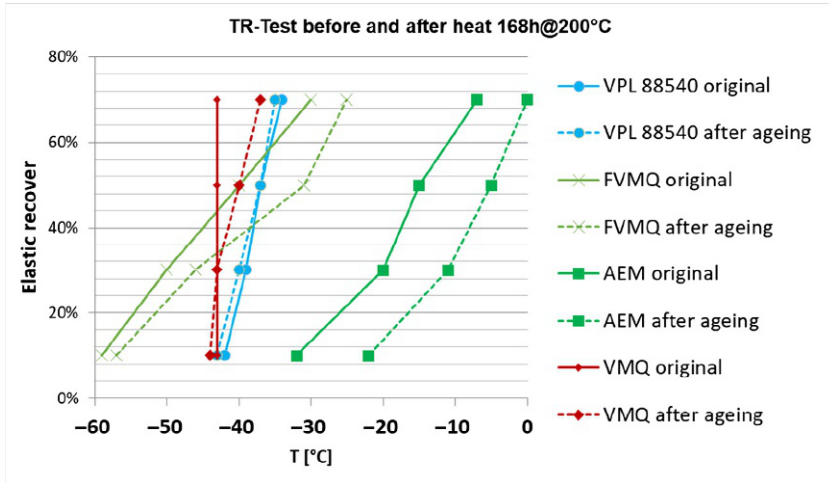
Fig. 14 TR-test curves before- and after heat aging at 200 °C.

As worse–case scenario we can look at the AEM sample that after aging at 200 °C shows a TR10 at −22 °C vs −32 °C (Fig. 14) of the original status, that is it becomes glassy and brittle already at −25 °C if thermally aged. On the opposite, a FKM such as *VPL 88540* retains its original cold flexibility because it is not thermally degraded.

Same kind of experiment was carried out after a chemical aging of selected elastomers samples: the comparison of TR-curves obtained after the condition of Table 5 to the original ones (Fig. 15) could give an idea how cold flexibility is affected by chemical degradation.

These TR–curves add a piece of information that was not shown by the results from the usual chemical resistance test (Table 5): indeed, whereas the

Table 5 Change of mechanical properties and weight after chemical aging of selected elastomers.

Change of mechanical properties after 168 h@100 °C in *Fuel C + 1% benzylamine +* dry-out 168 h@150 °C				
		VPL X75545	FVMQ	HNBR high ACN	AEM
Tensile strength	%	−4.5	−6.6	−26.5	12
Elongation @ break	%	−6.4	−24.7	−62.4	−13
Hardness	ShA	3	2	12	−17
Weight increase	%	0	−0.6	−4.2	−8.5
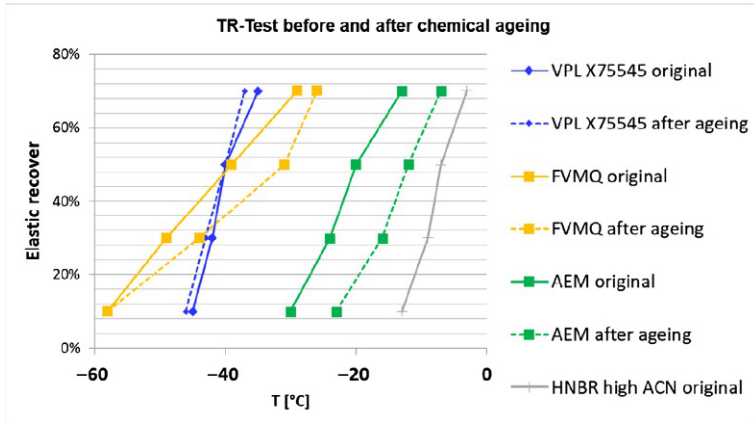
Fig. 15 TR-test curves before- and after chemical aging in Fuel C+benzylamine.

TR–curves after aging reflect the poor stability of HNBR and AEM elastomers in the selected fluid (likely also because of the hard dry–out conditions for such polymers), and the good stability of the FKM *VPL X75545*, for FVMQ the TR-curve is helpful to assess that its elastic behavior at cold temperatures is still good, despite what instead the significant change of elongation as in Table 5 could indicate.

   The tests above suggest that elastomers that are not sufficiently resistance to thermal or chemical degradation may underperform in cold temperature applications because of the loss over time of their intrinsic elastic behavior, i.e., the key reason for their selection.

   The excellent chemical resistance of the FKM type VPL is an additional attribute to the cold flexibility that this type of fluoroelastomers can offer. Indeed, most common FKM elastomers have been known for decades to work up to $-30\,°C$ at the lowest, whereas it was also known that at such temperatures the chemical resistance of low T_g FKMs must compromise. Indeed, the viable technology to lower the T_g of a FKM polymer has been the synthesis of terpolymers of TFE, VDF and MVE as depicted in Fig. 16, where the higher the VDF content the lower the T_g.
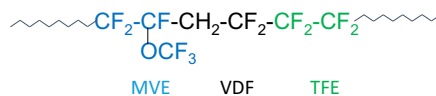
Fig. 16 Low temperature FKM composition.

By increasing the VDF content, the Fluorine content of the main chain decreases too and hence the polymer becomes more readily swollen by polar solvents (alcohols, esters, …), lowering so the chemical resistance.

The fact that the FKM VPL types show instead outstanding resistance combined with flexibility, exceeding the limit of T_g at $-30\,°C$ down to approximately $-55\,°C$, is due to the proprietary technology exploited to build the VPL polymer chains, that uses the perfluorinated monomer methoxy methyl vinyl ether (also known as MOVE, Fig. 17) to decrease T_g without decreasing the Fluorine content of the main chain.

The benefit of the MOVE technology of achieving very low T_g's while keeping outstanding chemical resistance typical of FKM polymers is described in Fig. 18, where the volume swell in M15 test fluid (Fuel C: methanol 85:15 w/w) is plotted vs the TR10 of FKM elastomers and FVMQ, to compare another fluorinated elastomer with close TR10.

The high chemical resistance available at temperatures as low as $-55\,°C$ makes VPL type of FKM engineered specialties, that are the ultimate solution to face extreme conditions. MOVE monomer was exploited for FFKM technology too, achieving with PFR LT supplied by *Solvay Specialty*
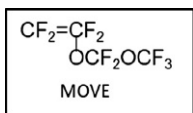
Fig. 17 Perfluoro methoxy methyl vinyl ether.
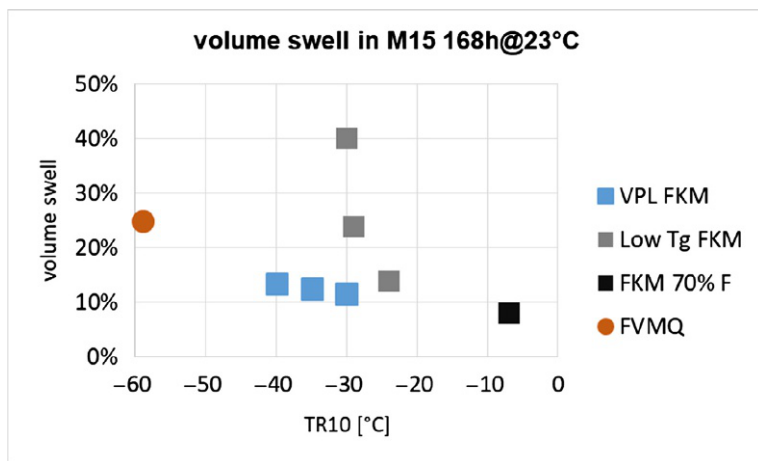
Fig. 18 Volume swell in M15 of low T_g FKMs compared to VPL FKMs and FVMQ.

Polymers under the trademark *Tecnoflon PFR,* the unique solution available of a perfluoroelastomer working up to −30 °C (Fig. 19). Such a perfluoroelastomer is virtually the best-in-class in the high-end options for harsh applications, because its main chain is practically undestroyable by any chemical and the polymer shows flexibility 30 °C below common FFKMs. This set of properties are of significant importance in O&G and Aerospace applications.

Dynamic Mechanical Analysis (DMA) is a characterization technique that is able to investigate separately the viscous and the elastic response of a polymer to external mechanical stimulus, as function of the temperature. Such peculiar characteristics of every polymer are extremely interesting for elastomers too, where especially the elastic component is per definition the key feature for the application of the rubber, as it drives deformation- and recovery ability. Plotting the elastic modulus of elastomers vs temperature is also a method to record the glass–rubber transition, defining the "T_g by DMA"; for the purpose of this study it is not important to define where such T_g value is taken along the curve, but to observe the range of temperature in which such transition takes place. This information is very analogue, but more accurate, than what is gathered by the TR-test, because the elastic component of the response to a stress is recorded continuously from the glassy to the rubber state, hence it is possible to understand in which range of temperatures a rubber element is able to oppose elastic, reversible deformation to a stress, or when it will be irreversibly modified. The transition range can vary of tens of degrees depending on the elastomer (and its
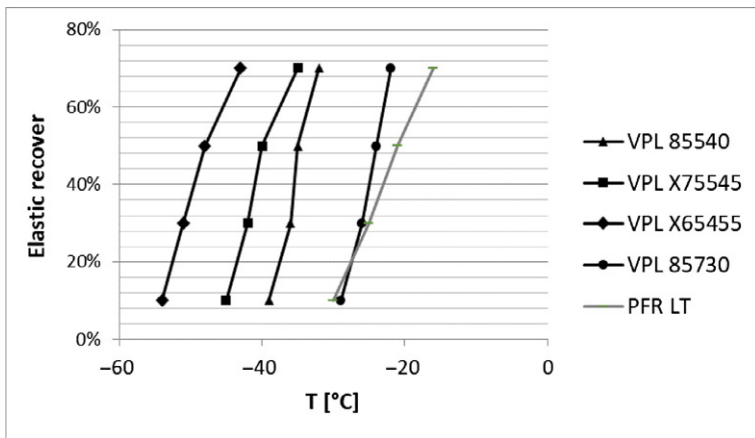
Fig. 19 Comparison of TR curves of FKMs and FFKM based on MOVE technology.

compounding recipe at a second level), and the narrower the transition the more ideally elastic the behavior of the rubber.

Fig. 20 shows the elastic modulus recorded for the three high–end elastomers with the lowest T_g:

-   by comparing the curves of VMQ and FKM *VPL X65455,* it looks like the two elastomers have a glass–rubber transition very close, disregarding their respective T_g (and T_m for VMQ) values as per DSC. The much shorter transition for VMQ can be correlated well to the steep TR–curve seen earlier
-   the DMA curve of FVMQ confirmed what observed with the TR–test: this elastomer needs to be warmed well above its T_g in order to achieve the rubber plateau typical of an elastic behavior. It looks like the "chemical upgrade" of VMQ to FVMQ achieves higher chemical/thermal resistance of the latter at the expenses of the better elasticity behavior known for silicone backbones.

For cold temperatures applications it is important that the glass–rubber transition does not shift upwards significantly as consequence of chemical- or heat aging during service, that can drive changes of the elastomer structure and hence of its part function. Therefore it is interesting to perform the DMA also on aged samples and to compare those curves to the original ones.
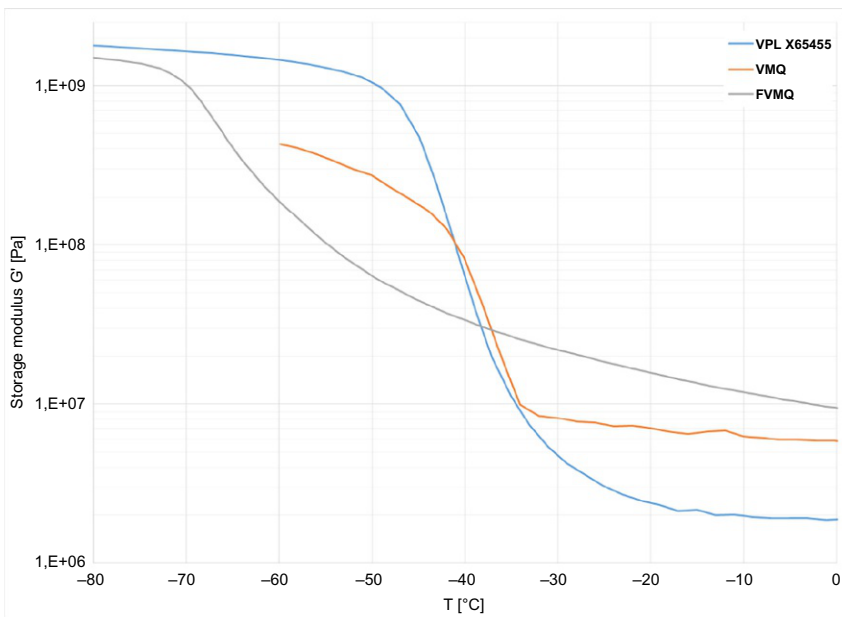
Fig. 20 DMA curves (storage modulus) of low T_g elastomers.

This experiment was carried out with the FKM *VPL 85730* and the AEM samples, that have both a glass transition around −30 °C as delivered. DMA specimen of both were tested in a highly additivated transmission fluid of proprietary composition ("ATF oil") for 96 h at 150 °C, which changed mechanical properties of both as in Table 6.

The curve of the VPL elastomer keeps its original shape after testing, as expected from the minor changes of mechanical properties recorded. On the opposite, AEM shows a shift upwards of the glass transition and of the elastic modulus, both elements indicating an hardening phenomenon occurred during chemical aging, affecting the performance of the AEM elastomer when approaching its nominal T_g at −30 °C (Fig. 21).

Table 6 Change of mechanical properties after chemical aging of selected elastomers.

Change of properties after 96 h@150 °C in *ATF oil* + dry out at 150°		
	VPL 85730	**AEM**
Tensile strength [MPa]	−11%	+3%
Elongation @ break [%]	+2%	+10%
Hardness [ShA]	0	−1
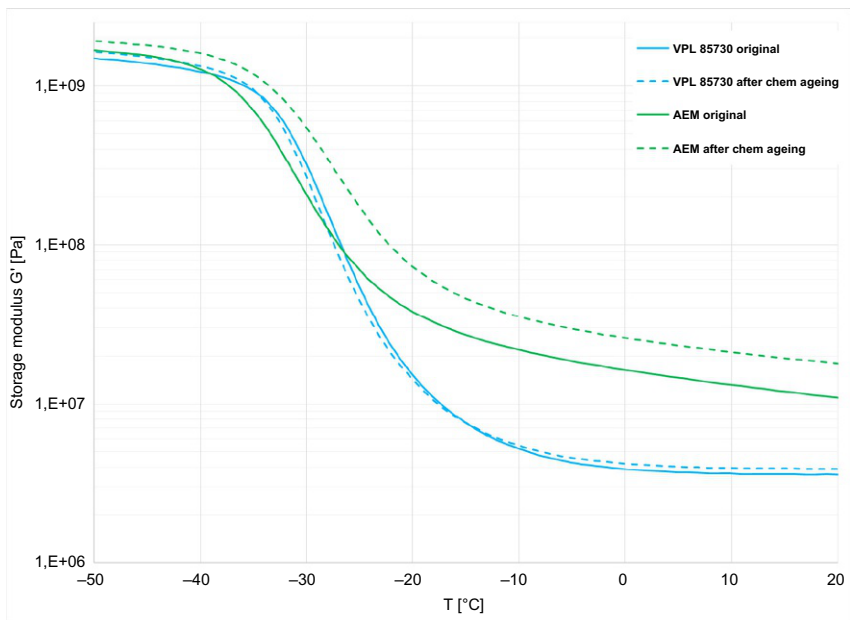
Fig. 21 DMA curves before- and after chemical aging.

4 Outlook

There can be different further developments of elastomers for harsh applications, where delivering a solution able to provide a long-lasting service is surely a value worth all the development efforts. The most common demands are targeting to widen the service temperature range:

– flexibility at even lower temperatures, whereas the synthesis of new monomers looks like the only way to achieve such "almost cryogenic" performance, since VMQ, FVMQ and FKM VPL work already beyond $-50\,°C$

– ceramic-like resistance to high temperatures: nitrilic cure FFKMs are nowadays able to work beyond $300\,°C$; this rating can be further increased by developing innovative crosslinking agents, that are the weak point in such a rubber network made of perfluorinated chains, where even ad-hoc compounding cannot add significant step increase

Beside developments involving the elastomer polymer or its vulcanization chemistry, innovative fillers can improve too rubber performance significantly. Improving conductivity has been always a topic in the rubber industry, despite the apparent contradiction of aiming at a property that cannot belong to the chemistry of saturated polymers. Indeed, polymers with conjugated insaturations do show electrical conductivity, but their elastic modules and T_g are so high to be more fibers-like than elastomers. Therefore compounding is the only way to improve electrical conductivity of a rubber element, otherwise born as insulator. Dissipative surface conductivity can be achieved by increasing the ionic content of the compound or by having surfactant-like additives, able to accumulate a water layer sufficient to dissipate electrostatic charges. To further improve electrical conductivity, innovative rubber compounds are described using graphene: the electron transportation through this graphite-like filler beyond its percolation threshold, shows electrical conductivities in the range of 0.1–1 S/m [6], that is comparable to that of salty water solutions and tens of orders of magnitude higher than usual rubber values (10^{-14}–10^{-16} S/m). This is an interesting example of how technology of compounding can help in designing high added-value rubber parts.

Acknowledgment

References

[1] J. Atkinson, Researcher News—Langley Research Center, May 10, (2012).
[2] N.S. Tomer, F. Delor-Jestin, L. Frezet, J. Lacoste, Open J. Org. Polym. Mater. 2 (2012) 13–22.
[3] M. Zeldin, B.-R.Q. Sung, J. Choi, Polym. Chem. 21 (5) (1983).
[4] J.A. Dean, Lange's Handbook of Chemistry, fifteenth ed., McGraw-Hill, Inc., 1998, p. 4.41
[5] A.L. Logothetis, Prog. Polym. Sci. 14 (1989) 251.
[6] J. Wang, K. Zhang, Q. Bu, M. Lavorgna, H. Xia, Carbon-Related Materials in Recognition of Nobel Lectures by Prof. Akira Suzuki in ICCE, vol. 175, (2017).

This page intentionally left blank

CHAPTER 3

Functionalized sp^2 carbon allotropes as fillers for rubber nanocomposites

Maurizio Galimberti[a], Vincenzina Barbera[a], Annalisa Sironi[b]
[a]Polytechnic of Milan, Department of Chemistry, Materials and Chemical Engineering "G. Natta", Milan, Italy
[b]Eptatech SRL, Luisago, Italy

Contents

43

1 sp² carbon allotropes as reinforcing fillers for rubbers

1.1 Families of sp² carbon allotropes

Reinforcing fillers [1, 2] are used in rubber compounds to impart the physical–mechanical properties required by the applications. Among them, sp^2 carbon allotropes are well known for their efficient reinforcing action.

CB [1–3] is one of the ten most important chemical products nowadays and is used since the beginning of the last century, though the consumer resistance to the black color [4] delayed its large scale application. HR-TEM (high resolution transmission electron microscopy) micrographs of Carbon Black N326 from Cabot Corporation are in Fig. 1.

As it was written [5], the discovery of fullerenes [6] "stimulated the creativity and imagination of scientists and paved the way to a whole new chemistry and physics of nanocarbons". Hence, over the last decades, new generations of sp^2 carbon allotropes have become available: carbon nanotubes (both single [7, 8] and multi-walled [9, 10]), graphene [11–14] or graphitic nanofillers made by few layers of graphene [15–18]. The quest for other members of this family is not over: "many exciting challenges remain. There are various new allotropes to be synthesized, and there are major challenges in combining our basic low-dimensional forms into more complex 3D architectures" [19].

Most of new generation sp^2 carbon allotropes are represented in Fig. 2.

The behavior of all these potential fillers and of some hybrid systems (in particular based on CB) in rubber compounds has been studied [1–3, 20–31].
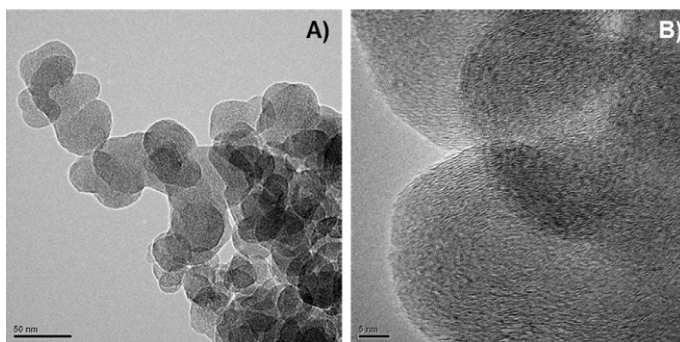
Fig. 1 HR-TEM micrographs of carbon black at low (A) and higher (B) magnifications.
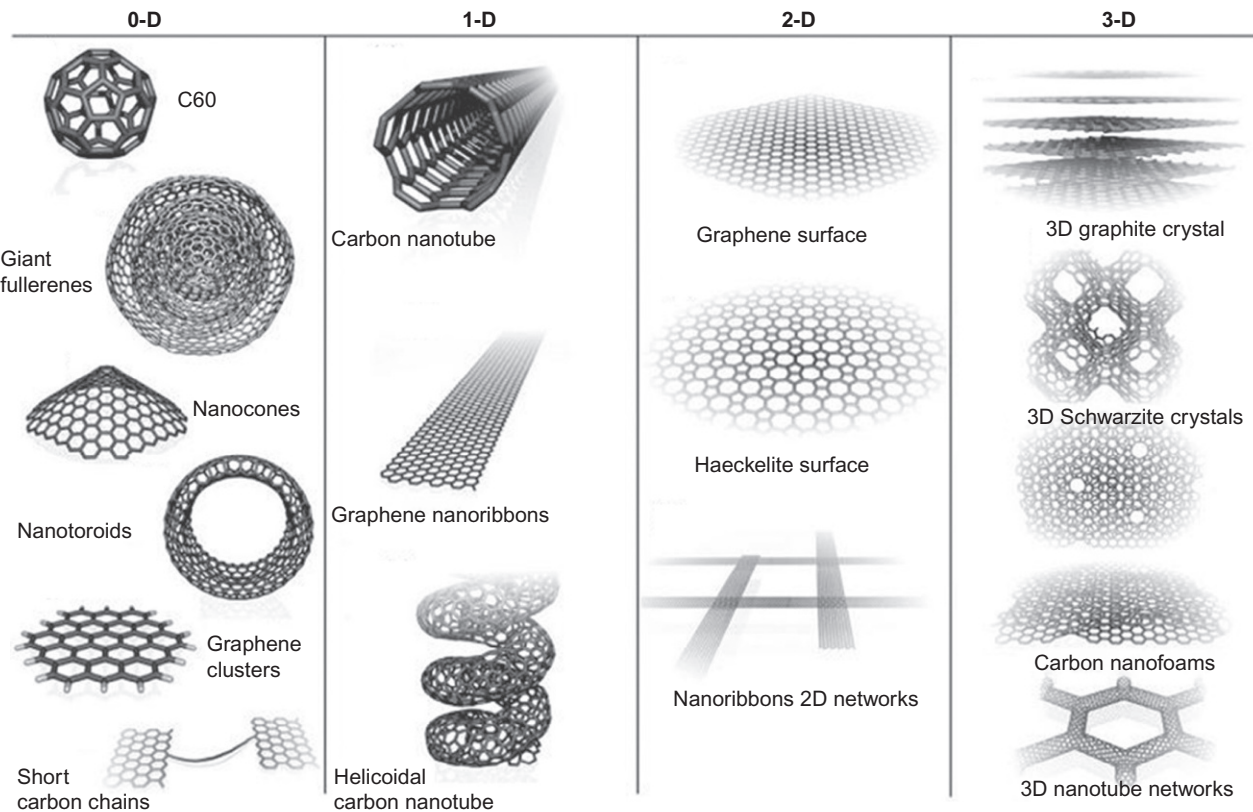
Fig. 2 sp² carbon allotropes. *(From J. Zhang, M. Terrones, C.R. Park, R. Mukherjee, M. Monthioux, N. Koratkar, Y.S. Kim, R. Hurt, E. Frackowiak, T. Enoki, Y. Chen, Y. Chen, A. Bianco, "Carbon science in 2016: status, challenges and perspectives", Carbon 98 (2016) 708–732).*

1.2 sp^2 carbon allotropes as nanomaterials

On a size basis, sp^2 carbon allotropes reported so far can be classified as nano-materials. Indeed, according to the standard definition [32], the nanoscale ranges approximately from 1 to 100 nm and a nanomaterial should have any external dimension, internal structure or surface structure in the nano-scale. As a consequence, sp^2 carbon allotropes are usually defined as nano-structured or nanometric materials. For example, CB is a nanostructured filler: as it can be seen in Fig. 1, it is made by primary particles which have at least one dimension below 100 nm and are joined together to form aggre-gates at least 200 nm long. Silica is a nanostructured filler as well [1, 2]. CNT, GRM and the allotropes in Fig. 2 are nanometric fillers: their nanosized pri-mary particles can be separated and individually dispersed in the polymer matrix.

The importance of nanosize can be easily explained as follows: particles have large surface area (s.a.) and are in large number per unit volume, at lower interparticle distance. In particular, a larger s.a. means a larger filler–polymer interfacial area (i.a.), that is the surface made available by the filler per unit volume of composite; it can be calculated through Eq. (1):

$$i.a. = s.a.*\rho*\phi \tag{1}$$

where r is the density and f is the filler volume fraction.

Nanometric fillers such as CNT and GRM are characterized by a high ratio between the largest and the smallest dimension, called aspect ratio. Hence, thanks to nanosize and high aspect ratio, they have very large surface area and are able to establish significant interactions with the polymer matrix, promoting dramatic effects on the properties of the rubber compound. Nanometric fillers can lend rubber compounds the same mechanical rein-forcement as nanostructured fillers at much lower content: so, lightweight materials can be envisaged [29].

2 Functionalization of sp^2 carbon allotropes

2.1 The need for functionalization

In a rubber compound, is the interaction between a reinforcing filler and polymer chains stable?

As reported above, CB and silica are nanostructured fillers: aggregates contain voids, which are able to occlude and immobilize polymer chains, giving rise to a fundamental contribution to the mechanical reinforcement

[1, 2]. Nanometric fillers such as GRM and CNT are not nanostructured and immobilization of polymer chains has not been clearly demonstrated. In fact: (i) polymer chains cannot be accommodated between layers of a graphitic aggregate, (ii) entangled CNT could trap the chains, but the tubes are broken during melt blending [33], even when a so called wet melt blending is used [34]. Also the other nanometric carbon allotropes in Fig. 2 do not reveal a structure suitable to occlude polymer chains. Moreover, since carbon fillers do not have functional groups able to react with rubber chains and with other compound ingredients, they can only establish Van der Waals interactions with the polymer matrix.

On the contrary, silica has a polar surface, rich of oxygen atoms which are involved in siloxane and silanol functional groups [35]. The so called precipitated silica [35, 36] is able to give rise to chemical reactions, for example with organosilanes containing sulfur atoms, which are used to shield the silica surface and as coupling agents with the polymer chains [36, 37]. Compatibilization and chemical linkage between silica and the polymer are thus obtained.

A stable filler-polymer interaction is of the outmost importance. Indeed, a labile interaction leads to substantial decrease of the dynamic-mechanical modulus with the increase of the strain amplitude. The network established by the filler, either directly or through a layer of absorbed polymer, is continuously formed and disrupted. Such a phenomenon of filler networking is known as Payne effect [38] and is explained with filler agglomeration-de-agglomeration [39–41] and/or filler-matrix bonding and debonding [42–51]. Thanks to its chemical modification with silanes, silica is the best filler for low filler networking and, as a consequence, for low dissipation of energy and fuel consumption [1, 2, 52].

As previously remarked, nanometric fillers, such as CNT and GRM, have large interfacial area but are not able to establish chemical links with the polymer, just large and labile interactions between filler particles and between filler and polymer chains. This leads to high values of modulus at minimum strain and to remarkable modulus decrease with the increase of the strain amplitude, so rubber compounds based on CNT [33] and nano-sized graphitic fillers [26] are characterized by a large Payne effect.

In the light of such recollection, it is clear that the functionalization of sp^2 carbon allotropes is a basic need for the compatibilization with polymer chains, in particular in the case of nanometric fillers. Reactive carbon fillers would lead to substantial mechanical reinforcement and to dramatic reduction of energy dissipation and hence, for example, of rolling resistance of a tyre compound.

Moreover, a modification allowing to tune the solubility parameter of sp^2 carbon allotropes would be highly desirable, in order to steer both the compatibility with different polymer matrices and the ability to interact with compound important ingredients, namely the vulcanizers.

2.2 Prior art

A brief summary of the prior art on the functionalization of CB, CNT and GRM as the carbon allotropes is reported in Section 4 and 5. As mentioned in the summary, some aspects are in particular considered:

  (i)   chemicals and procedures used for the functionalization
 (ii)   main features of the functionalized products
(iii)   properties and applications of the rubber composites based on the func-
        tionalized carbon allotropes

In particular, recent advancements are taken into consideration. Attention is focused on what appeared in the scientific and patent literature in the last 3 years.

3 Functionalized graphite and graphene related materials in rubber compounds

3.1 Functionalization of graphite and graphene related materials

A brief sum–up of prior art and present status of functionalization of graphitic materials, in view of their application in rubber compounds, can be attempted as follows.

The first approach for the functionalization of graphite was oxidation, which dates back to XIX century. Over the last decades, the interest in the oxidation of graphitic materials has largely increased, with the aim to prepare graphite and graphene oxide (GO) and then, through thermal or chemical reduction, graphene and GRM. GO and its derivatives have been and are used in rubber compounds. The introduction of functional groups is exploited to improve the compatibility either with rubber latexes or with rubber matrices.

Fuming HNO_3 and $KClO_3$ were used by Brodie [53] in the late 1850s: the adopted multi–cycle process had major drawbacks as the production of toxic and explosive gases such as NO_2/N_2O_4 and ClO_2. Explosions indeed have been documented [54, 55]. A blend of H_2SO_4 and HNO_3 (2:1) with $KClO_3$ as oxidant was used by Staudenmeier, toward the end of the XIX century. The one–step process yet generated explosive ClO_2 [56]. In the late

60's of the last century, Hummers chose $H_2SO_4/NaNO_3$ and $KMnO_4$ [57] for the intercalation and oxidation of graphite. $KMnO_4$ has high efficiency and only few hours are required for the reaction, though only partial oxidation is obtained [58–61]. Explosive products are not formed and acidic smokes are removed by replacing HNO_3 with $NaNO_3$. For all these reasons, Hummers' method is considered as one of the best, if not the best method for large scale production of GO. However, toxic NO_2/N_2O_4 are still obtained and manganese ions need to be removed by using strong acids such as HCl, which remains adsorbed on the graphitic substrate. Improvement of the Hummers' method [60–63] has been performed by excluding $NaNO_3$ and by increasing the amount of $KMnO_4$, with a H_2SO_4/H_3PO_4 mixture [60]. The exclusive use of potassium permanganate did not cause negative effects on the reaction [61], but only an incomplete conversion of graphite to GO was obtained. Also the residence times have been modified [61]. Pre-oxidation of graphite was carried out with P_2O_5 and $K_2S_2O_8$ in H_2SO_4 [63]. The adoption of graphite flakes with sizes in the 3–20 μm range has allowed the complete conversion to GO [62]. GO could also be obtained through solvent-free mechano–chemical oxidation of graphite [64]. However, such a method can be hardly employed for large scale production.

All the aspects of graphene oxide chemistry (preparation, structural features, reduction and functionalization) are rationalized in the open literature [65, 66].

Focus of this chapter is on functionalized carbon allotropes, for rubber composites. However, it is worth to make a quick *detour* on the reduction step which is crucial in order to obtain layers with the expected graphene properties. It is well known that hydrazine [67–70] and hydrogen plasma [69] can be used. A stabilizing agent is added to avoid re-aggregation of graphitic flakes [71, 72]. Quick deoxygenation of graphite oxide in the presence of a base (NaOH 0.1 M) has been carried out at moderate temperatures (80 °C) [73]. Ascorbic acid has been used [74]. Thermal [75] and flash [76] reductions have been performed. However, it is known that reduction is incomplete and that the ideal graphene structure is not restored [77, 78]. As regards the papers appeared in the scientific literature, GO used as a filler in rubber compounds has been in most cases produced through (modified) Hummers' method [65, 79, 80]. This chemical form allowed to achieve the best dispersion of the graphene layers in the rubber composites. For example [81], after dispersing GO in NR latex, in situ chemical reduction to RGO was performed, followed by stirring and sonication. Coalescence and freeze-dry approach led to a templated array, with graphene platelets confined around

NR globules. After hot molding, a segregated interconnected network of graphite in NR matrix was obtained. The scheme of this approach is shown in Fig. 3.

Thanks to this procedure, percolation is obtained with the minimum amount of graphene platelets, even though, as reported by the authors, some restacking of graphene layers can be expected. GO has also been used as a carbon framework for the preparation of many derivatives [65, 82, 83].

In this chapter, the GO derivatives used for the preparation of rubber composites are considered. What appeared both in the scientific and patent literature has been examined, with emphasis on the last few years. Table 1 lists the chemical modification of GRM, the polymer matrix used, the objective of functionalization and the main result(s) obtained. In brief, the polar groups introduced onto the graphitic layers lead to:

 (i) stronger interfacial interaction, also via covalent bonding, with a polar rubber
 (ii) formation of hybrid system with a polar filler, such as silica
(iii) loading of polar functional molecules, such as the antioxidants, on the filler
(iv) self-assembly and self-healing materials
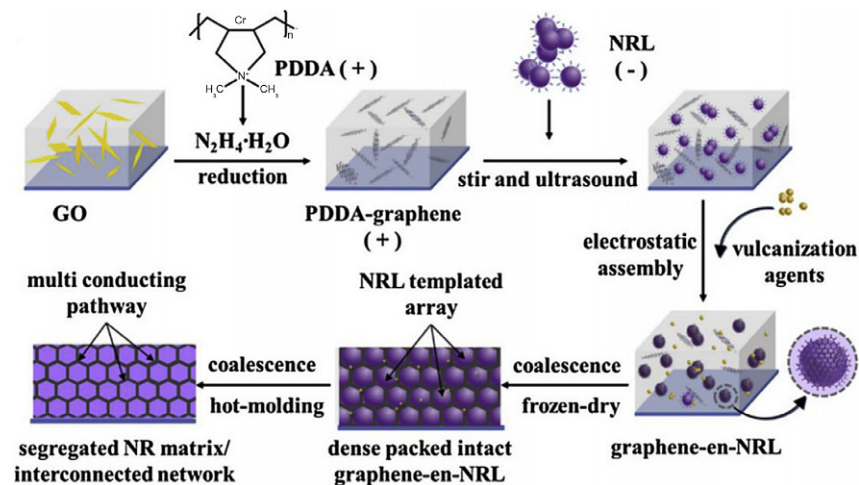
Fig. 3 Interconnection of graphene platelets in NR matrix. *(From Y. Luo, P. Zhao, Q. Yang, D. He, L. Kong, Z. Peng, "Fabrication of conductive elastic nanocomposites via framing intact interconnected graphene networks", Compos. Sci. Technol. 100 (2014) 143–151).*

Table 1 Functionalized GRM in rubber composites

Chemical modification	Rubber matrix	Objective/main achievement(s)	Ref.
3-Mercaptopropyltrimethoxy silane (MPTMS)[a]	Nitrile–butadiene rubber	Elaboration of a one–pot procedure to simultaneously modify and reduce GO; a stronger interfacial interaction via covalent bonding between filler and matrix; superior mechanical properties and higher storage modulus	[84]
Glycerol and fatty acid (molar ratio 2:1)[b]	Styrene–butadiene rubber/silica	Remarkable improvement in mechanical, thermal and electrical properties; enhanced dry and wet braking and rolling resistance	[85]
Plant polyphenol-tannic acid; mixture with primary amine-containing silane coupling agent modified SiO$_2$ to obtain a hybrid[b]	Natural rubber	A new efficient strategy of constructing graphene–SiO$_2$ hybrid fillers established; evenly distribution of the filler in the matrix with improved interfacial interaction; high tensile and tear strength; good thermal conductivity; excellent abrasive resistance capacity	[86]
—OH, —COOH	Maleinated polystyrene-b-poly(ethylene-r-butylene)-b-polystyrene thermoplastic elastomer	Superior mechanical properties, higher hardness, higher electrical conductivity at a lower percolation threshold and enhanced gas barrier resistance with respect to analogous composites with non-functionalized graphene	[87]

Table 1 Functionalized GRM in rubber composites—cont'd

Chemical modification	Rubber matrix	Objective/main achievement(s)	Ref.
2-Tert-butyl-6-(3-tertbutyl-2-hydroxy-5-methylphenyl) methyl-4-methylphenyl acrylate[a]	Natural rubber	Improvement of thermo-oxidative aging resistance	[88]
2,6-Di-tert-butyl-4-hydroxymethyl phenol[a]	Natural rubber	Enhancement of thermal stability and thermo-oxidative aging resistance of vulcanized composite	[89]
Polystyrene-*block*-poly(2-hydroxyethyl methacrylate)[a]	Styrene-butadiene rubber	Strong interfacial interaction between filler and matrix; continuous filler networks; enhancement of thermal conductivity and mechanical properties of vulcanized composite	[90]
AMPTES and GPTMS (silanes)[a]	Polypropylene/ethylene-propylene rubber	Improvement of tensile strength, Young's modulus and thermal stability; elongation and Izod impact strength adversely affected	[91]
Silica decoration[a]	Styrene-butadiene rubber	Tensile strength and thermal stability increased; possible various high-performance rubber composites	[92]
Hexadecylamine[a]	Carboxylated nitrile rubber	Improvement in tensile strength and in elongation at break; reduction of Young's modulus; enhancement of thermal stability and dielectrical constant; possible application as flexible dielectric materials in electronic devices	[93]

Fluoridric acid[a]	Styrene–butadiene and butadiene rubber	Mechanical properties substantially improved; decrease of antiwear properties since layered graphene promotes to tear and peel off	[94]
—OH, —COOH	Bromobutyl rubber	Significant enhancement of the barrier properties at low levels of nanofiller loading and exceptionally low value of electrical percolation threshold for a composite with a segregated morphology	[95]
4,4′-Methylenedianiline and polypropylene chains[a]	Polypropylene/ethylene-propylene diene	Lower damping behavior and intensity of the loss factor	[96]
N-1,3-dimethylbutyl-N′-phenyl-p-phenylenediamine[a]	Styrene–butadiene rubber	Immobilization of the antioxidant leads to a much better antimigratory efficiency and to exceptionally high long-term thermo-oxidative aging resistance; potentially a promising strategy for the eco-friendly reduction and functionalization of GO	[97]
Phenylene ethynylene oligomer[a]	Diene—based elastomer	Promotion of low rolling resistance and tread wear resistance for a tire tread rubber composition as well as of the thermal conductivity for the rubber composition (tread, sidewall, other internal components)	[98]
1-Allyl-3-methyl-imidazolium chloride[a]	Styrene–butadiene rubber	Great enhancement of tensile strength, tear strength, thermal conductivity and solvent resistance	[99]

Table 1 Functionalized GRM in rubber composites—cont'd

Chemical modification	Rubber matrix	Objective/main achievement(s)	Ref.
Polyethylene terminated with —SH groups brushes[b]	Poly(styrene-b-ethylene-*co*-butylene-b-styrene) triblock copolymer	modification of polymer domains morphology; retention of high elongation at break; percolation threshold for electrical conductivity slightly above 0.7 vol%; promising new class of flexible conductors for applications like actuators or bodily motion sensors	[100]
3-Aminopropyltriethoxysilane (APTES)[b]	Polyurethane	Enhancement of anti-corrosion properties attributed to the hydrophobicity and barrier effect which not only reduce the contact and interaction between water and the surfaces, but also increase the tortuosity of the corrosive medium diffusion pathway	[101]
p-Phenylenediamine[a]	Bromobutyl rubber	remarkable enhancement in tensile strength, storage modulus, thermal stability and permittivity; drastic improvement in gas impermeability; nanocomposite developed for tyre inner liner application	[102]
3-Aminopropyl triethoxysilane (APTES)[a]	Nitrile-butadiene rubber	Relatively high dielectric constant and a small loss factor at 1.0 kHz, combining with a good insulating property; potential applications in resistive and capacitive field grading materials	[103]

[a]From graphite/graphene oxide.
[b]From graphitic materials.

4 Functionalized carbon nanotubes in rubber compounds

CNT, both single- [7, 8] and multi-walled [9, 10] are nanofillers of great potentialities to improve the properties of rubber composites. The main objective of the many functionalization methods reported in the scientific literature is to convert CNT bundles into dispersible tubes, able to establish a strong interaction with the matrix. It is fulfilled by performing:

 (i) endohedral or exohedral functionalization
(ii) covalent or non–covalent functionalization

The endohedral functionalization occurs in the internal part of the tubes, is hindered by the size of the tube diameter (up to about 2 nm), and has minor effect on the compatibilization with the matrix. The exohedral functionalization, involving the external area of CNT, has been mainly attempted and both non-covalent and covalent approaches have been developed.

Reviews are available to describe covalent [104–110] and non-covalent [107–109] chemical modifications. A very concise summary is proposed as follows.

Non-covalent functionalization. Non-covalent functionalization is based on (i) anionic, cationic, and non-ionic surfactants, (ii) polymers wrapped around the tubes, such as for example polyurethanes, poly(phenylenevinylene), poly(styrene)–*block*–poly(acrylic acid), (iii) biomacromolecules such as proteins. This approach has been used also in the last years, for the preparation of rubber composites. Examples appeared in the scientific literature are in Table 2. In brief:

 (i) cation–pi interaction is exploited, thanks to the use of ionic salts
 (ii) ionic surfactants typically have long hydrophobic chains and a salt as the functional group
(iii) non-ionic surfactants typically are poly(oxyalkylene)
(iv) the increased compatibility with the elastomer matrix and the better dispersion lead to the reduction of polymer phases size in a blend, to the improvement of thermal and electrical properties and to the effect on rheological properties

Covalent functionalization. Covalent chemical functionalization of CNT can be divided in:

 (i) direct functionalization (see Fig. 4)
(ii) derivatization of oxidized CNT (see Fig. 5).

As it can be seen, oxidation is the first step for the introduction of many functional groups. Oxidized CNT have been also used, in many elastomer nanocomposites, to obtain ultimate dispersion in rubber latex. Procedures to obtain such dispersions are summarized in Table 3.

Table 2 Non-covalent functionalization of CNT and their use in rubber composites

Chemical modification	Rubber matrix	Objective/main achievement(s)	Ref.
Ionic liquids	Thermoplastic, thermosetting and elastomer matrixes	Development of new materials with EMI shielding, supercapacitors, energy storage, sensors applications	[111]
Compatible furan groups	Thermoreversibly crosslinked ethylene propylene rubbers grafted with furan groups	Crack-healing by welding; design of novel strain-sensors based on recyclable rubbers	[112]
Surfactants (lithium dodecyl sulfate, sodium dodecyl sulfate, Na + K Soap, Zn-Soap)	SBR latex	Composites with outstanding mechanical, thermal, and electrical properties at low loadings; tread compounds of a pneumatic tyre with enhanced abrasion, wet grip, and rolling resistance performance	[113]
Polystyrene brushes	Polystyrene-*block*-poly (ethylene-butylene)-*block*-polystyrene (SEBS)	Decrease of the block *co*-polymer microphase separation temperature; significant promoting effect on microstructural development, comparable to that of annealing	[114]
Poly(ethylene glycol) monomethylether; dodecyl groups	Epoxy resin or chloroprene rubber	Electrical conductive nanocomposite adhesive containing also polyaniline	[115]
Surfactants (sodium dodecyl sulfate, cetyl tri-Me ammonium bromide, Tween 20)	Natural rubber latex	Finding a correlation between the dispersion of CNT and the rheological properties of nanocomposites	[116]
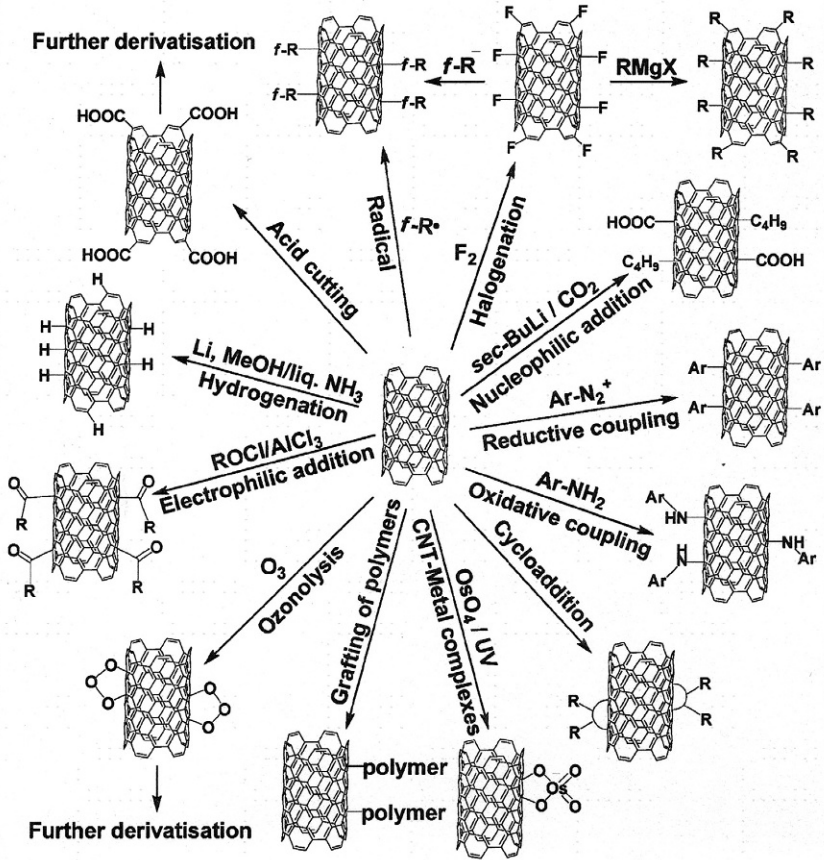
Fig. 4 Direct functionalization of CNT. *(From H.-C. Wu, X. Chang, L. Liu, F. Zhao, Y. Zhao, "Chemistry of carbon nanotubes in biomedical applications", J. Mater. Chem. 20(6) (2010) 1036–1052).*

In brief:
- **(i)** —OH and —COOH groups are preferentially introduced, with oxidation techniques
- **(ii)** CNT with polar groups are preferentially mixed with rubber latexes or polar rubbers
- **(iii)** lower permeation to oil, better mechanical and electrical properties, better properties under stretching are obtained.

Functionalized CNT are steadily used for the preparation of rubber composites. In this chapter, focus is on what has appeared in the scientific literature between 2014 and 2018. Chemical modification, rubber matrix, objective and main results are indicated in Table 4.
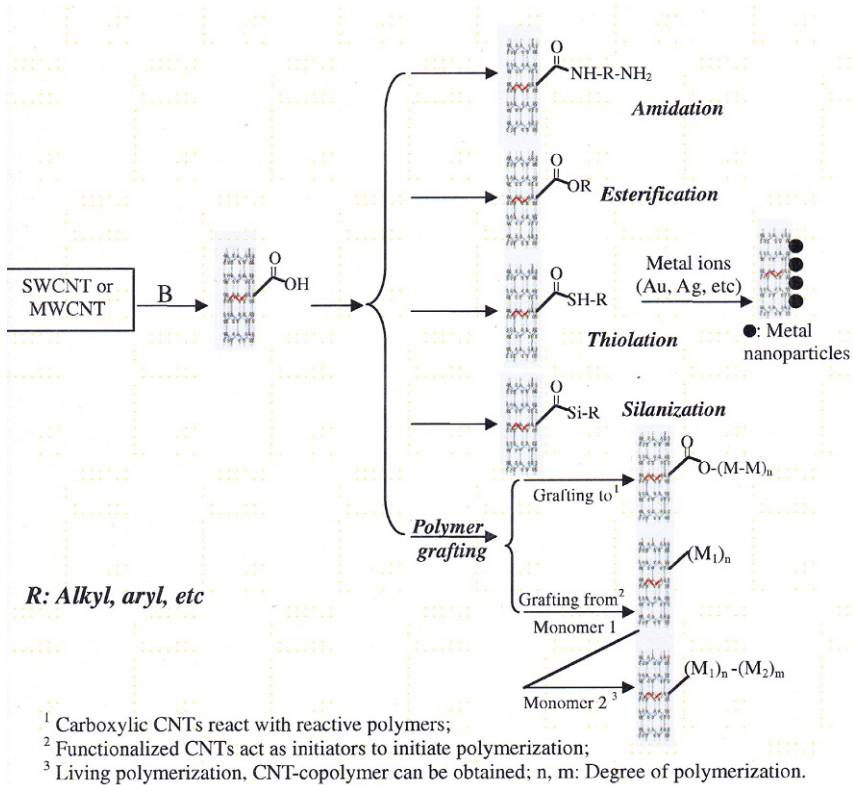
Fig. 5 CNT functionalization through derivatization of carboxylic groups. (From P.-C. Ma, N.A. Siddiqui, G. Marom, J.-K. Kim, Dispersion and functionalization of carbon nanotubes for polymer-based nanocomposites: a review. Comp. Part A Appl. Sci. Manuf. 41 (10) (2010) 1345–1367).

5 Functionalized carbon black

CB can be functionalized in many ways, as reported in the scientific literature and in the industrial practice [3]. Examples are the CB treatment with ozone [127–131], plasma [132], triazole [133], polysulfide [134]. Carbon-silicon dual phase was obtained with the so called cofuming technology [135, 136]. Research on the functionalization of CB has been active also over the last years. In Table 5, examples appeared in the scientific and patent literature in the year period 2016–2018 are shown.

In brief:

  (i) both non–covalent and covalent functionalization have been performed
 (ii) hydroxy, carboxy and silanol groups have been preferentially introduced
(iii) improvement of mechanical, thermal, electrical properties have been achieved

Table 3 Covalent functionalization of CNT and their use in rubber composites

CNT treatment	Blending procedure	Results: CNT dispersion	Ref.
1. HCl 2. HNO_3	1. Dispersion in water with SDS, 1/1 wt ratio; bath sonicator for 15 min 2. Dispersion added to ammonia solution of prevulcanized natural rubber 3. Magnetic stirring for 24 h, sonication for 15 min 4. Poured into a Petri dish, dried at 60 °C for 24 h	– CNT strongly adhered to latex particle surface – Latex spheres: exclusion volume for CNT – The available space for CNT is reduced: lower percolation threshold and formation of networks at the "grain boundaries" – No aggregates. CNT are properly embedded in the films and do not impede latex spheres coagulation.	[117]
H_2SO_4/HNO_3	1. Dispersion in water with sodium dodecyl sulfate (SDS; SDS/CNT $= 1/1.5$ wt ratio); bath sonicator for 2 h 2. Addition of natural rubber latex, magnetic stirring 3. Sonication 1 h (to remove bubbles): thick slurries 4. Cast onto a flat plastic mold, dried in an oven under air, 50 °C, 24 h	– High concentration of oxygen and sulfur around CNT: surfactant molecules remain adhered to CNT surface and act as a bridge between the CNT and the polymer – CNT covered by a layer of polymer: good adhesion between the two components – The polymer is "softer" around the boundaries of CNT than in other regions: dissipative interfacial layer	[118]

Continued

Table 3 Covalent functionalization of CNT and their use in rubber composites—cont'd

CNT treatment	Blending procedure	Results: CNT dispersion	Ref.
1. SDS (CNT/SDS = 2/1) 2. KOH (pH = 10, negatively charged CNT) 3. Poly(diallylmethyl ammonium) chloride (PDDA; CNT/PDDA = 10/1)	1. Prevulcanized NR latex (addition of curing system for 2 h at 60 °C). Total solid 50% 2. CNT-PDDA water suspension dropped into negatively charged natural rubber latex. Gentle magnetic stirring, room temperature, 24 h 3. Cast onto glass plates, dried at 50 °C for 24 h	– Untreated CNT severely aggregated in the matrix (twisting): uncompatible – PDDA: used as a bridge, to enhance the interfacial adhesion with the polymer – CNT–PDDA: more intimate with the matrix, individually attached to the NR particles like a little worm. Much improved dispersion. Interface with NR very smooth – With CNT content <3 wt%, almost all CNT homogeneously distributed throughout the matrix as individual tubes. A further increase of CNT content had an unfavorable effect on dispersion in the latex	[119]

Table 4 Chemical modification of CNT

Chemical modification	Polymeric matrix	Objective/main achievement	Ref.
Compatible furan groups	Thermoreversibly crosslinked ethylene propylene rubbers grafted with furan groups	Crack–healing by welding; design of novel strain sensors based on recyclable rubbers	[112]
Polystyrene brushes	Polystyrene-*block*-poly (ethylene-butylene)-*block*-polystyrene (SEBS)	Decrease of the block *co*-polymer microphase separation temperature; significant promoting effect on microstructural development, comparable to that of annealing	[114]
—OH groups	Fluoroelastomer	Resistance to oil based drilling mud; use as sealing rubbers (for example o-rings) in this application field	[120]
3-Aminopropyltriethoxy silane (APTES)	Epoxidized natural rubber	Composites with good electrical conductivity achieved with a very low content (0.5 phr) of CNT	[121]
Bis(triethoxysilylpropyl)tetrasulfide (TESPT)	Natural rubber	Composites prepd. by latex mixing with better tensile properties and electric conductivities	[122]
—COOH groups	Polyethylene-octene copolymer (E38)	Increase of the stiffness, mechanical strength and of UV resistance	[123]

Continued

Table 4 Chemical modification of CNT—cont'd

Chemical modification	Polymeric matrix	Objective/main achievement	Ref.
—COOH groups	Polyurethane	all-printed, inexpensive, highly stretchable electrochemical sensor and biofuel cell array with negligible impact on structural integrity, electrical performances and electrochemical properties upon repeated stretching, torsional twisting, indenting stress	[124]
Acid treatment and silanization reaction with bis(triethoxysilylpropyl)tetrasulfide	Natural rubber	High rubber reinforcement and crosslink density; retardation of vulcanization reaction	[125]
Covalent functionalization with styrene groups; non-covalent functionalization with $C_6H_5CH{=}CH_2$ or $CH_2{=}CH{-}CH{=}CH_2$	SBS thermoplastic elastomer	Electro-mechanical composites suitable for large deformation sensor applications	[126]

Table 5 Functionalization of carbon black

Chemical modification	Polymeric matrix	Objective/main achievement	Ref.
Ferrocene aldehyde, ketone or carboxylic acid compound	Natural rubber	Improvement of thermal aging; significant toughening and reinforcing effects	[137]
—OH, —COOH	Non-functionalized diene-based elastomer	Pneumatic tyre	[138]
Acrylic acid	Synthetic rubber; automobile tire leftovers	Fender; recycling economy: minimization, recycling and reclamation	[139]
Long-chain alkylsilane	Natural rubber	Method with simple equipment and gentle reaction conditions; is adapted to industrialized production	[140]
Maleic anhydride	Isocyanate-modified vinylchloride-vinyl acetate copolymer; maleic anhydride grafted ethylene-1-octene copolymer elastomer, linear low density polyethylene	Super-smooth semiconductive shielding cable with high volume resistivity stability, good dispersion uniformity of the conductive filler, high pressure and temperature resistance, good mechanical performance and long service life	[141]
1-Hexadecyl-3-methylimidazolium bromide	Silicone rubber	Polymer-based flexible piezoresistive composite for future fabrication of sensors and wearable electronic devices	[142]
Ampholytic surfactant	Natural rubber	Wet-process masterbatch with homodispersed filler; the obtained tire prepared using the vulcanized rubber can reduce compression heat generation and oil consumption	[143]

6 Sustainable functionalization of sp² carbon allotropes. Objectives

All the methods reported in previous paragraphs are characterized by the use of a specific chemistry, sometimes with harsh conditions and hazardous chemicals. In most cases, the functionalization methods lack of versatility. There is still room for investigating innovative, more sustainable and versatile procedure.

Starting from the present paragraph, functionalization methods developed by the authors are discussed. They were inspired by the following objectives:

(i) sustainability

(ii) preservation of bulk structure and sp² hybridization of the carbon substrate

(iii) introduction of different types of functional groups.

In particular, the adopted sustainable functionalization methods rely on the absence of solvents and catalysts and avoid the production of wastes. Reagents are available on the market and associated to acceptable phrases of risk.

To what extent such objectives were achieved with the developed functionalization methods will be discussed in the following.

7 Sustainable functionalization of sp² carbon allotropes. Methods

Reactions on carbon allotropes were performed with:

(i) potassium hydroxide

(ii) hydrogen peroxide

(iii) serinol derivatives: pyrrole compounds obtained by means of Paal–Knorr reaction between a primary amine and a dicarbonyl compound.

sp² carbon allotropes were: CB, nanosized graphite with high surface area (HSAG), MWCNT.

In this section, the experimental procedures adopted for performing the functionalization reactions (Par. 7.1, 7.2, 7.3), a comparison between the methods (Par. 7.4) and the effect of functionalization reactions on the structure of the graphitic substrate (Par. 7.5) are presented and discussed in order to evaluate the sustainability of the methods and the preservation of the molecular structure of the carbon allotropes.

All the presented methods allowed to introduce heteroatoms such as oxygen and nitrogen in the chosen substrate.

7.1 Functionalization of sp^2 carbon allotropes with KOH

Reactions of carbon allotropes (CA) with KOH were carried out as shown in Fig. 6 and described in detail in the experimental part of published papers [144–146].

In brief, KOH powder was mixed with the selected carbon allotrope and energy was given to the mixture, by simply heating or by using a ball mill. The product (CA-OH) was carefully washed and then isolated, upon verifying a neutral pH. KOH/CA mass ratio was in the range from 1:5 to 20:1. In particular, this paragraph will be focused on samples obtained with 1:1 as the mass ratio.

The functionalization method with KOH appears to be simple indeed. The critical step is the achievement of a neutral pH after the reaction, although such a procedure is not that troublesome when a little amount of KOH is used.

The efficiency of the functionalization method was investigated by estimating the amount of acidic groups in CA-OH by means of Boehm titration, as described further below in Table 10 (see also the experimental part in Ref. 145).

7.2 Functionalization of sp^2 carbon allotropes with H$_2$O$_2$

Reactions of CA with H$_2$O$_2$ were carried out as shown in Fig. 7 and described in detail in the experimental part of a published paper [145].

In brief, mixtures of CA and H$_2$O$_2$ were formed in the absence of catalysts and solvents (other than water) and stirred either at room temperature or at 70 °C, for either 3 or 24 h. The functionalized carbon allotropes (CA-Ox) were isolated by washing with H$_2$O until neutral pH.
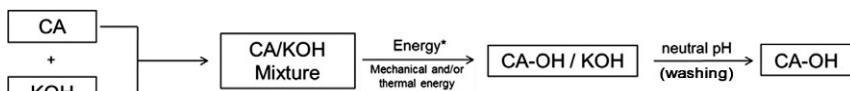
Fig. 6 Block diagram for the preparation of hydroxylated carbon allotropes (CA-OH).
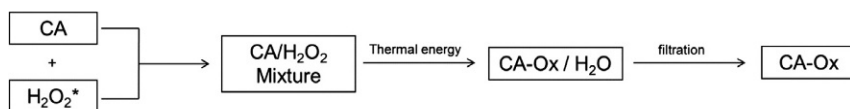
* 30 % (w/w) in H$_2$O

Fig. 7 Block diagram for the preparation of oxidated carbon allotropes (CA-Ox).

Also the functionalization method with H_2O_2 appears to be simple and the washing procedure is easier than in the case of the reaction with KOH. Even on these samples the amount of acidic functional groups was estimated by means of Boehm titration (vide infra).

7.3 Functionalization of sp² carbon allotropes with pyrrole compounds

Various pyrrole compounds (PyCs) were synthesized through the Paal–Knorr reaction of 2,5-hexanedione with primary amines, as reported in previous publications. Different types of primary amines were considered. The synthesis was performed in the absence of solvents and catalysts, as reported in detail elsewhere [147–154], and is summarized in Fig. 8.

All the reactions are characterized by a high atom economy and just one by-product, that is water. A high yield was obtained for all the syntheses. Atom economy (AE) and yield of the reactions are reported in Table 6.

Some of the authors have in particular reported the synthesis of 2-(2,5-dimethyl-1H-pyrrol-1-yl)-1,3-propanediol (serinolpyrrole, SP), whose structure is in Fig. 9, from 2-amino-1,3-propandiol (serinol) as the primary amine (Run 6 in Table 6) [147–151].

Such synthesis is characterized by a yield larger than 95% and by an 83% AE. The reaction mass efficiency [150–155] is thus of about 80%. However, the yield of most reactions of Table 6 was at least 70% and the yield of some of them exceeds 80%. All these data allow to comment that the PyCs were obtained with a sustainable process.

The functionalization of CA was performed as schematically shown in Fig. 10 and as reported in detail in previous publications. The reagents were simply mixed in a low boiling solvent such as acetone, optionally with the help of sonication. Upon solvent removal, either thermal or mechanical energy was given. The thermal treatment was from 80°C to 150°C, for 2–4 h. The mechanical treatment was performed with a ball milling, at 300 rpm for 6 h.
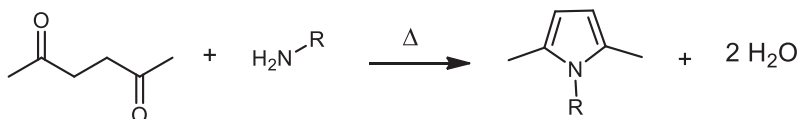
Fig. 8 Reaction of 2,5-hexanedione with primary amines to give pyrrole compounds (PyCs).

Table 6 Reactions of 2,5-hexanedione with different primary amines[a]

Run	Amine	AE (%)	Yield (%)	Product Acronym	Structure
1	H₃C–NH₂	75	86.9	TMP	
2	~NH₂	84	73	HP	
3	H₂N–(CH₂)₁₁	88	62	DDcP	
4	H₂N–(CH₂)₁₇	90	73	ODcP	
5	H₂N–CH₂–C(O)OH	81	80	GlyP	
6	HO–CH₂–CH(NH₂)–CH₂–OH	83	96	SP	
7	(EtO)₃Si–(CH₂)₃–NH₂	89	80	APTESP	

[a]Temperature: 130 °C, time = 3h. For Run 1 and 5: $T = 150$ °C.
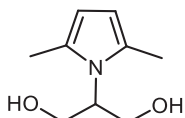
Fig. 9 2-(2,5-dimethyl-1*H*-pyrrol-1-yl)-1,3-propanediol (serinolpyrrole, SP).
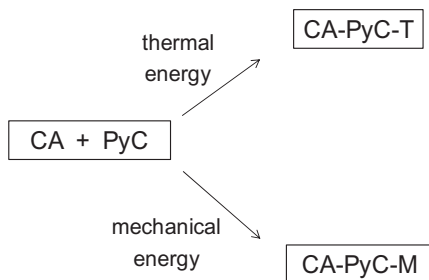
Fig. 10 Block diagram for the preparation of CA-PyC adducts with the help of either thermal or mechanical energy.

Adducts were rinsed with acetone, until it was not possible to detect any organic substance in the washing solvent. After drying in air, thermogravimetric analysis (TGA) was performed on the obtained powder, determining the amount of PyC.

The yield of functionalization was evaluated, through the following equation (Eq. 2):

$$\text{Functionalization Yield}\,(\%) = \frac{PyC_{after\ washing}}{PyC_{before\ washing}} \times 100 \qquad (2)$$

In the following, adducts prepared through the thermal treatment will be discussed. The yield of functionalization will be compared for the reaction of HSAG, CNT and CB with SP as the pyrrole compound. Then, the efficiency of functionalization reaction of HSAG with various PyC will be discussed. Results from TGA analysis of CA reacted with SP are listed in Table 7.

Three main steps were detected for the mass loss in the TGA thermograph at various temperatures and were attributed [150] as follows:

- at $T < 150\,°C$ loss of absorbed low molar mass substances, namely water;
- from $150\,°C$ to $700\,°C$ decomposition of PyC and alkenylic groups, defects in CA
- at $T > 700\,°C$ combustion with oxygen.

The yields of functionalization are summarized in Table 8.

Table 7 Mass loss for CA-SP adducts from TGA analysis

Carbon allotrope	Mass loss [%]			
	$T < 150\,°C$	$150\,°C$ $<T < 400\,°C$	$400\,°C$ $<T < 700\,°C$	$T > 700\,°C$
HSAG[a]	0.0	0.1	0.4	99.5
HSAG[b]	0.4	4.1	6.0	89.5
CB[b]	0.2	2.9	5.3	91.6
CNT[b]	0.4	2.4	6.8	90.4

[a] Pristine sample.
[b] After the reaction.

Table 8 Yield of functionalization of CA with SP from TGA analysis and Eq. (2)

Carbon allotrope	Surface area (m²/g)	Yield of functionalization
HSAG	330	96%
CNT	275	92%
CB	77	82%

High functionalization yield was obtained with all the CA and was almost quantitative for HSAG. The amount of functional groups in the adducts was again determined by means of Boehm titration (vide infra). Functionalization yields of HSAG with various PyCs are compared in Table 9. Data reveal that the functionalization was efficient whatever pyrrole compound was used.

7.4 Comparison of the functionalization methods

As previously anticipated, the amount of functional groups in CA reacted with KOH, H_2O_2 or PyC has been determined by means of Boehm titration. It was performed to quantitatively determine the content of oxygenated surface groups. In a typical experiment, $0.05\,g$ of the carbon allotrope were dispersed in $50\,mL$ of a $0.05\,M$ NaOH solution. After stirring at room temperature for $24\,h$, the mixture was filtered. $10\,mL$ of solution were mixed with an aqueous solution of HCl ($0.05\,M$, $20\,mL$). The obtained mixture was titrated using a $0.05\,M$ solution of NaOH. The results are summarized in Table 10.

In the case of the reaction with KOH, a certain correlation between the amount of functional groups and the surface area of the carbon allotrope can

Table 9 Yield of functionalization of HSAG with various PyCs from TGA analysis and Eq. (2)

Product		
Acronym	**Structure**	**Functionalization yield (%)**
TMP		73
HP		87
DDcP		80
ODcP		98
GlyP		82
SP		96
APTESP		78

Table 10 Amount of functional groups (mmol/g) in functionalized CA determined by means of Boehm titration

		Functionalization method		
	Surface area	KOH	H$_2$O$_2$[a]	SP
Carbon allotrope	m^2/g		mmol/g	
HSAG	300	5.0	3.1	6.3
CNT	275	3.0	3.2	2.6
CB	77	2.0	5.8	7.7

[a]Sample prepared at 70 °C.

be noted. Indeed, HSAG has larger surface area than CB. However, why do CNT, in spite of their large surface area, reveal a low amount of functional groups? The functionalization of graphene layers by means of KOH has been hypothesized to occur through a nucleophilic substitution on the edge benzene rings [144]. In the light of such mechanism, HSAG could be more reactive, as it has a larger amount of reactive edges.

As regards the functionalization of CA with H_2O_2, a higher number of functional groups was found on samples prepared at higher temperature, though in a shorter time. Data in Table 10 refer to a reaction performed at 70 °C. The efficiency of the functionalization reaction appears to depend on the type of CA, differently from what observed in the case of KOH. In particular, the larger amount of functional groups in CB-Ox could be explained taking into account that CB contains alkenylic and oxygenated groups, which easily react with H_2O_2.

Considering the functionalization of CA with SP, the reaction was efficient indeed, particularly for CB and HSAG. By observing the values in Table 8, the yield of functionalization seems to depend on the surface area of the carbon allotrope as well as on the available reactive sites, such as the edges, which are more abundant in CB and HSAG than in CNT.

7.5 Effect of functionalization reaction on the graphitic substrate structure

The effect of the reaction with KOH, H_2O_2 and PyC on the bulk structure of the graphitic substrate was studied by means of wide angle X-ray diffraction (WAXD) and Raman spectroscopy. HSAG was chosen as the carbon allotrope. SP was selected as the pyrrole compound.

In Fig. 11 WAXD patterns taken on powders of pristine HSAG and of HSAG functionalized in different ways are shown.

In pristine HSAG (a), two reflections reveal the crystalline order in the direction orthogonal to structural layers: (002) at 26.6 degrees, which corresponds to an interlayer distance of 0.338 nm, and (004) at 54.3 degrees. (100) and (110) reflections indicate the in-plane order: at 42.5 and 77.6 degrees, respectively. WAXD spectra of functionalized HSAGs in Fig. 11 reveal that the (002) peak remains at the same 2θ value, allowing to exclude any intercalation. Peak shape analysis of (002) reflection permitted to evaluate the size of crystallites orthogonal to the layers, by applying the Scherrer
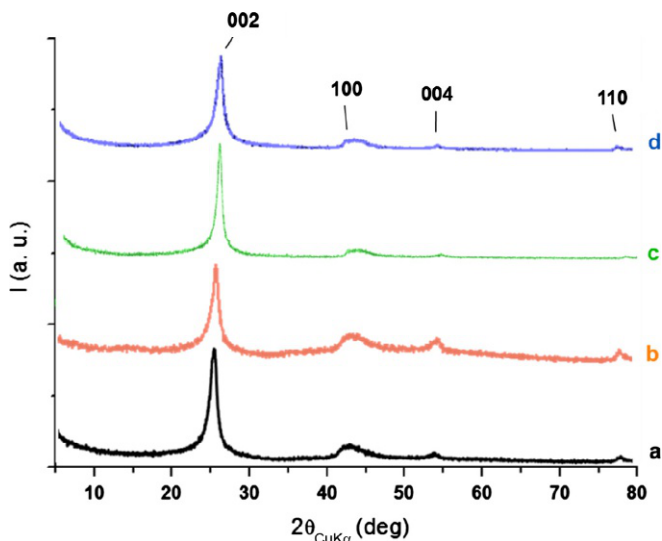
Fig. 11 WAXD patterns of: HSAG (a), HSAG-SP (b), G-Ox (c), and G-OH (d).

Equation [144, 147]. Taking into consideration the interlayer distance, the number of stacked layers was then estimated: 35 in HSAG, 24 in HSAG-SP, 28 in G-Ox and 23 in G-OH. Peak shape analysis of (100) and (110) reflections, clearly visible in each pattern, allows to estimate the dimension of crystallites also inside the structural layers. Almost the same value was found, in particular for HSAG, G-OH and HSAG-SP.

From these findings, it can be commented that the reaction with SP, H_2O_2 and KOH promotes the partial exfoliation of HSAG without altering the in-plane order.

In Fig. 12 Raman spectra (recorded with the laser excitation at 632.8 nm) of HSAG, pristine and functionalized, are shown.

Two main peaks located at 1580 and 1350 cm^{-1}, named G and D respectively, indicate the presence of graphitic sp^2-phase in the Raman spectra [144, 145]. The high intensity of the D band has been attributed [156, 157] to different types of molecular disorder, in particular to the relative large amount of edges in such a nanosized graphite, prepared via ball milling. However, G and D bands are present in all spectra in similar relative amount and there are no indications that the reaction of HSAG with each modifying agent appreciably affect the structure of the graphitic layers.
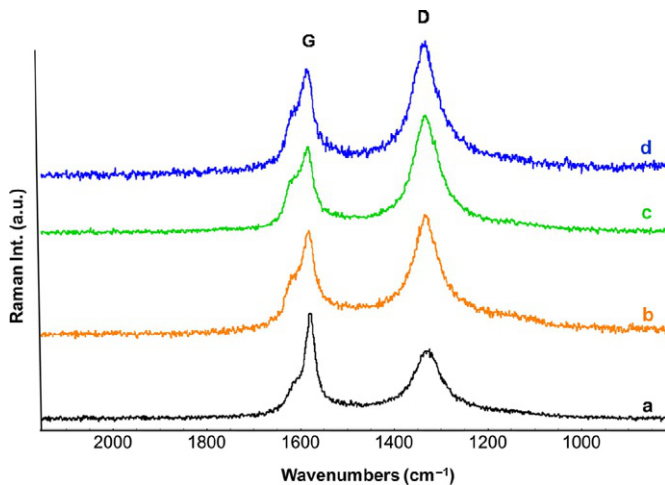
Fig. 12 Raman spectra with normalized intensities of HSAG (a), HSAG-SP (b), G-Ox (c), and G-OH (d).

8 Functionalized carbon allotropes. Structure of functional groups

Qualitative investigation of functional groups was performed by means of Fourier transform infrared (FT-IR) spectroscopy. Absorption spectra were recorded in transmission mode using a diamond anvil cell.

In the following, the functional groups introduced onto the carbon allotrope by using the different functionalization methods are examined. Spectra of HSAG and HSAG functionalized with oxygenated groups are compared in Fig. 13. Oxygenated HSAG samples were obtained with SP, H_2O_2 and KOH.

The diffusion/reflection phenomena of the IR light caused by the particles of the samples led to an increasing background toward high wavenumbers, clearly visible in all the spectra. In the HSAG spectrum (Fig. 13a), the band at $1590\,cm^{-1}$, typical of graphene and GRM, is assigned to E_{1u} IR active mode of collective C=C stretching vibration. Bands which cannot be attributed to HSAG are found in the spectrum of HSAG-SP (Fig. 13b): the broad band at $3370\,cm^{-1}$ is due to hydrogen bonded OH groups, the bands centered at about $2900\,cm^{-1}$ are due to sp^3 C—H stretching and the band at $1383\,cm^{-1}$ is due to diol vibration. Stretching of the amidic C=O is at $1652\,cm^{-1}$ and vibration of the alkenyl groups is at $802\,cm^{-1}$.
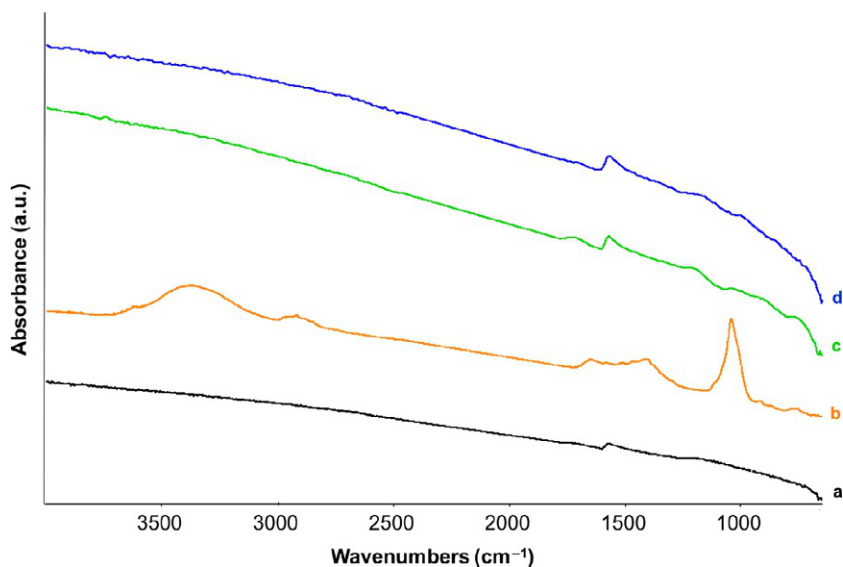
Fig. 13 FT-IR spectra of HSAG (a), HSAG-SP (b), G-Ox (c), and G-OH (d).

Bands in the region of C—C bonds, at 1590 and 1470 cm^{-1}, could arise from the aromatic rings.

The C=C peak is visible also in the spectrum of G-Ox sample (HSAG reacted with H_2O_2) (Fig. 13c), as well as broad bands, which were not visible in the spectrum of pristine HSAG. They are at: 3400 cm^{-1}, due to stretching vibration of —OH; 1388 cm^{-1}, attributed to the out of plane vibration of —OH groups; 1724 cm^{-1}, assigned to C=O stretching vibration. Strong and broad features at 1202 and 1044 cm^{-1} are assigned to the C—O—C bond stretching of ester and epoxide groups respectively, together with other vibrations of C—O–C and —OH functionalities.

In the spectrum of G-OH (HSAG reacted with KOH) (Fig. 13d) bands are present which can be assigned to the absorption of different —OH groups. Peaks are located at: 3400 cm^{-1}, attributed to stretching vibrations of hydrogen bonded hydroxyl groups; 1388 cm^{-1}, assigned to the out of plane vibration; 1110 cm^{-1}, attributed to C—O stretching vibration; 970 cm^{-1}, assigned to the in–plane phenyl—O—H bending.

The functionalization with PyCs led to decoration of the graphene layers with a variety of functional groups. FT–IR spectra (recorded in attenuated total reflectance mode) of HSAG and HSAG functionalized with various
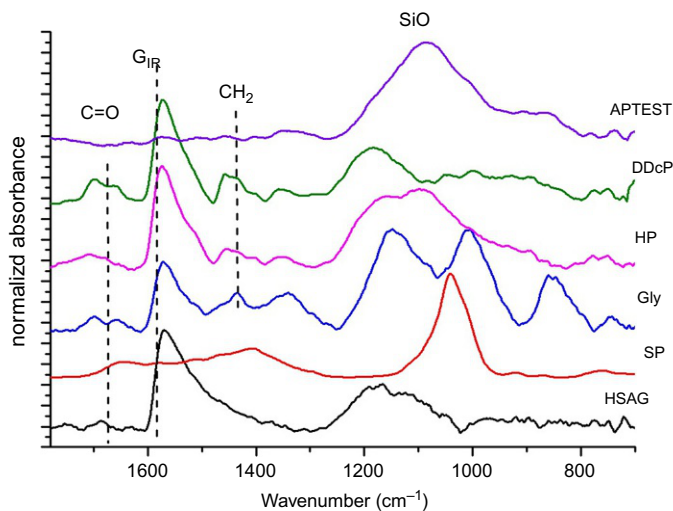
Fig. 14 FT-IR spectra in the fingerprint region 700–1800 cm^{-1}, after baseline correction, of HSAG and HSAG functionalized with SP, Gly, HP, DDcP, APTESP (see Tables 6 and 9 for the acronym reference).

PyC are shown in Fig. 14. Each PyC used for the functionalization is indicated by the acronyms already reported in Tables 6 and 9.

Some absorptions appear to be common for all the spectra. They are close to 1700 cm^{-1}, compatible with the presence of C=O stretching vibrations, and in the 1100–1200 cm^{-1} range, most likely due to the stretching vibrations of C—O—C and C—OH functional groups. A strong feature is present at 1590 cm^{-1} in most of the spectra of Fig. 14, is typical of graphitic materials and is assigned to E$_{1u}$ IR active mode of the collective C=C stretching vibration. Such band is hardly visible in the spectra of HSAG-SP and HSAG-APTESP, because of the strong absorption of the functional groups.

Indeed, the spectrum of HSAG-SP is characterized by i) the strong absorption assigned to the stretching of C—O—R groups at about 1040 cm^{-1} and ii) the strong and broad bands due to the C=C stretching of the pyrrole ring, at 1650 and 1400 cm^{-1}. The spectrum of HSAG-APTESP reveals a very strong absorption at about 1100 cm^{-1}, typical of Si—O stretching vibration. In the spectra of HSAG-HP and HSAG-DDcP, the bands close to 1450 cm^{-1} (assigned to CH$_3$ and CH$_2$ bending vibrations) can be attributed to the alkyl residues present in PyCs. The strong and broad bands at 855 and 1005 cm^{-1} could be tentatively assigned to aliphatic ether.

9 The mechanisms and the products of the functionalization reactions

Mechanisms for the functionalization of CA with KOH, PyCs and H_2O_2 have been investigated, by using graphitic substrates [144, 145, 158]. A two–step mechanism has been reported for the functionalization of graphene layers with KOH. Such mechanism is shown in Fig. 15.

In brief: (i) hydroxide anions give rise to a nucleophilic addition to peripheral aromatic rings and a negatively charged intermediate is formed, favored by a considerable number of resonance hybrids; (ii) a re–aromatization process occurs. The large stabilization of the charged intermediate in step (i) could be considered as a sort of "wave effect" and the driving force of the whole process could be the aromatization of the graphene layer. Poly(hydroxylated) graphene layers are formed, shown in Fig. 16.

A domino reaction has been proposed [158] for the functionalization of graphene layers with PyCs. The mechanism is shown in Fig. 17.

In brief: (i) one PyC undergoes oxidation, catalyzed by the graphitic substrate and an oxidized lateral substituent (the aldehyde in Fig. 17) is formed; (ii) the activated double bond in PyC performs a cycloaddition reaction on peripheral positions of the graphene layers. It is worth underlying that the PyC can be formed in situ on the CA. The structure of the product of such reaction is in Fig. 18.
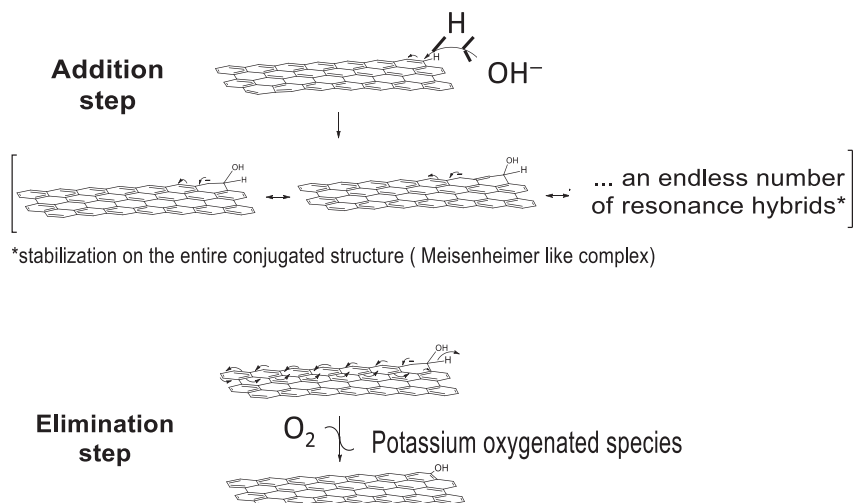
Fig. 15 Proposed two step mechanism for the functionalization of graphene layers with KOH (addition-elimination reaction).
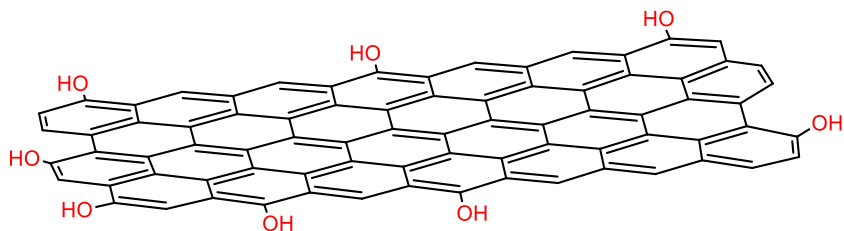
Fig. 16 Poly(hydroxylated) graphene layers from the functionalization with KOH.
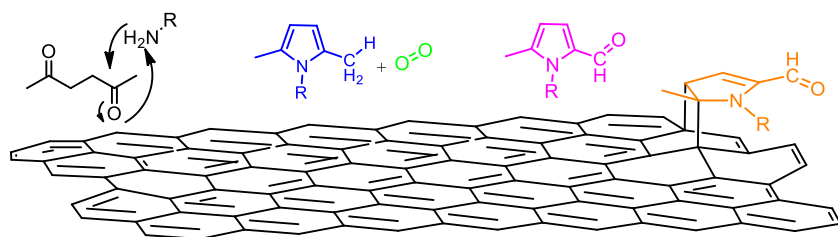
Fig. 17 Proposed domino reaction for the functionalization of graphene layers with PyCs.
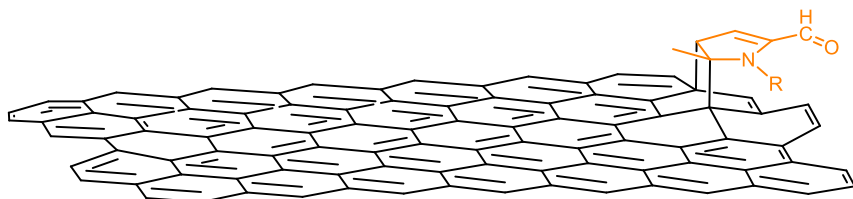
Fig. 18 Product from the reaction of graphene layers with PyCs.

Mechanism for the oxidation of graphitic materials with H_2O_2 is currently under investigation.

10 Comparative evaluation of the functionalization techniques

In the previous paragraphs, the functionalization of graphene layers with KOH, H_2O_2 and PyC has been discussed. Is it possible to identify some criteria on the basis of which such methods can be conveniently compared? An answer is schematized in Fig. 19.

Reaction sustainability and product compatibility in various environments have been considered. As far as the functionalization method is concerned, sustainability and the possibility to use it in the frame of the existing technology, adopting the so called "drop-in" approach, are of great
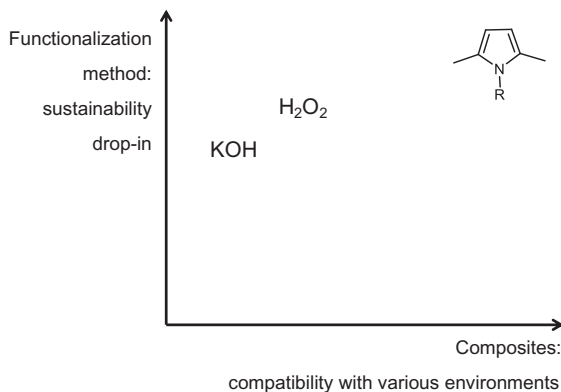
Fig. 19 Comparative evaluation of functionalization methods.

importance. All the methods appear to be sustainable. In particular, the very high yield of the functionalization with PyC and the negligible amount of substances other than the functionalized CA at the end of the process, indicate that it is the most efficient and sustainable one. Moreover, the reaction of CA with PyC can be performed in the frame of existing plants. The compatibility with various environments of functionalized CA emerges as the main criterion for evaluating the versatility of a functionalization method. Once again, functionalization with PyC seems to be the best method since it is the only one able to modify the chemical nature of the graphitic substrates over a wide range of solubility parameters, whereas KOH and H_2O_2 allow to introduce only oxygenated groups.

In conclusion, functionalization of CA with PyC appears a very interesting and promising method to enlarge their properties and applications. Composites based on functionalized CA, prepared either via latex or melt blending, with natural rubber, polyisoprene and polybutadiene as the rubbers (NR, IR and BR respectively) and CB and silica as the fillers are reported in the following paragraph. In particular, G-OH was used as the only filler in composites based on NR, prepared via latex blending. CB-SP was used in composites based on IR and BR with CB and silica as the filler system.

11 Elastomer nanocomposites with functionalized carbon allotropes

Elastomer nanocomposites were prepared with either G-OH or CB-SP. Purpose of the research was to investigate the effect of a better compatibilization of CA with polar surroundings.

11.1 Elastomer nanocomposites with G-OH

Nanocomposites were based on NR and G–OH. Preparation is described in the experimental part of previously published papers. Recipes are in Table 11, all the amounts are expressed in phr.

Structure of the composites was investigated by means of TEM and WAXD analyses.

WAXD patterns of HSAG and crosslinked G–OH–15 composite, in Fig. 20A, reveal that (002) reflection remains at the same 2θ value, indicating that the preparation of the composite from the latex did not lead to any inter-calation. The number of graphene layers stacked in G–OH, in the powder isolated after the functionalization reaction and in the crosslinked composite, was estimated by applying the Scherrer equation (as reported above in the text) to (001) peak, estimating the dimension of crystallites orthogonal to structural layers and dividing the values by the interlayer distance. Values are shown in Table 12.

The number of stacked layers increases from the powder to the cross-linked composite. Such a finding was already observed in the case of HSAG. In Table 12, the values of layers stacked in HSAG as powder and in the NR crosslinked composite are reported. Some of the authors already commented

Table 11 Formulations of elastomer nanocomposites based on NR and G-OH[a]

	Nanocomposite						
Ingredient	G-OH-0	G-OH-4	G-OH-7	G-OH-10	G-OH-12	G-OH-15	G-OH-25
NR	100	100	100	100	100	100	100
G-OH	0	3.7	6.5	9.5	12.3	15.1	25

[a]Other ingredients: ZnO 4 phr, Stearic acid 2 phr, 6PPD 2 phr, S 3 phr, TBBS 1.8 phr.
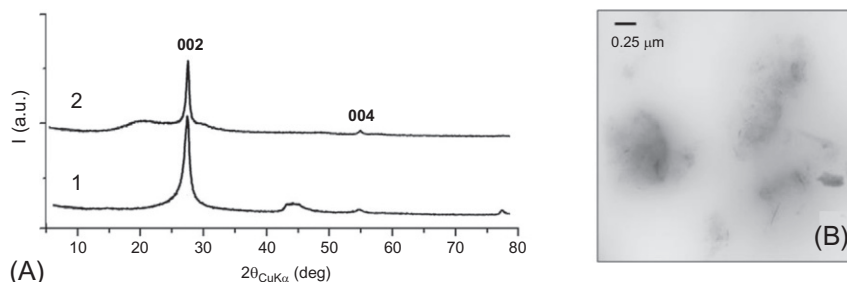
Fig. 20 (A) WAXD pattern of HSAG (1) and G-OH-15 crosslinked composite (2) (see Table 11); (B) TEM micrograph of G-OH-9 composite as precipitated from the NR latex.

Table 12 Number of stacked graphene layers in HSAG and G-OH

Compound	Number of stacked graphene layers	Ref
G–OH	23	[144]
G–OH in G–OH–15 NR composite	70	
Pristine HSAG	35	[22, 26]
HSAG in IR composite	70	

[22, 26] that the energy given to the composite during processing and vulcanization favors re-aggregation of the graphitic layers (both G–OH and HSAG) into a crystalline graphite: indeed, the crystalline organization corresponds to the minimum of energy.

Fig. 20B shows the TEM micrographs of the composite G–OH–9, precipitated from the NR latex. TEM analysis revealed that G–OH is evenly distributed. Sub-micrometric size aggregates and few agglomerates not larger than 3 μm were present in the micrographs; very few isolated graphene layers and stacks of layers, of different dimensions, are visible.

Rheometric tests have been performed on all the composites. G–OH had an impact on the sulfur-based crosslinking, causing the decrease of t_{s1} (induction time of vulcanization) and the increase of both M_H (highest torque value) and M_H-M_L (difference between highest and lowest torque value) as it can be seen in Fig. 21A and B respectively.

Hence, all the data from rheometric tests can be correlated with the G–OH content in the composites. The consistent trends and in particular the linearity of correlations in Fig. 21B seems to confirm that G–OH was evenly distributed and dispersed in the rubber matrix. It is worth commenting that the reduction of induction time with the content of the graphitic filler is in line with what reported by some of the authors [159]: the increase of surface area of the CA led to faster vulcanizations.

Uniaxial stretching was applied to the nanocomposites of Table 11 and tensile measurements were taken. The dependence of nominal stress on nominal strain is in Fig. 22.

Neat NR (G–OH–0) gave the lowest values of stress at every deformation and the largest elongation. Increase of stresses and reduction of strain at break were obtained with G–OH. Presence of agglomerates of G–OH could be hypothesized to explain the worse ultimate properties of G–OH–15, with respect to G–OH–12.

In conclusion, it can be commented that even distribution and dispersion of a nanosized high surface area graphite were achieved thanks to the
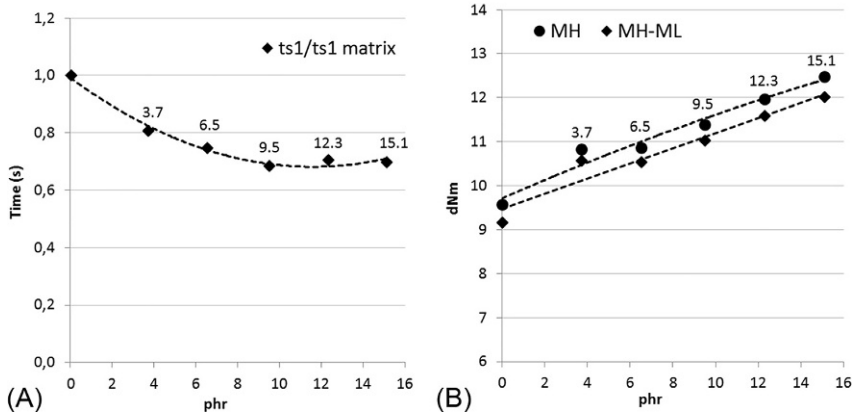
Fig. 21 $t_{s1}/t_{s1matrix}$ (A), M_H and $(M_H - M_L)$ (B) as a function of G-OH content for the vulcanization reactions of composites of Table 11. The amount of G-OH in the composites is indicated.
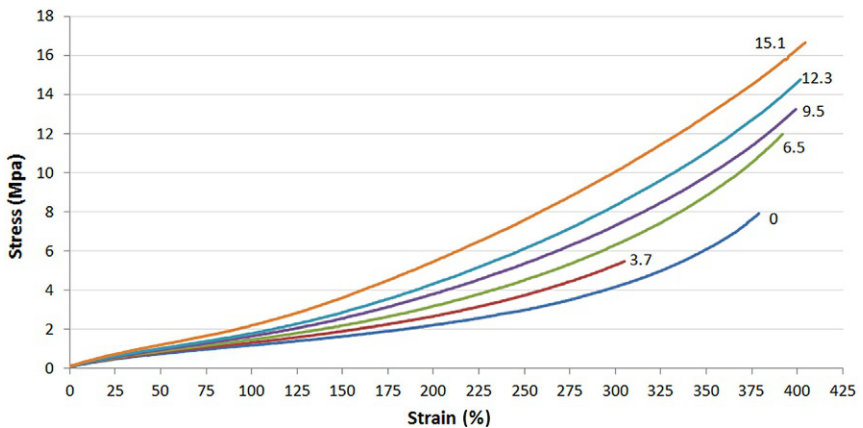
Fig. 22 Nominal stress-nominal strain curves, with standard deviations for crosslinked G-OH composites of Table 11. The amount of G-OH in the composites is indicated.

functionalization with KOH. As a consequence, consistent effects were observed on the nanocomposite properties: faster vulcanization, large reinforcement.

11.2 Elastomer nanocomposites with CB-SP

Nanocomposites were based on IR and BR as the rubbers and CB and silica as the fillers. A furnace carbon black (CB N326) was functionalized with serinol pyrrole (10% by mass of functionalization). Objective of the research was the reduction of the silica networking, thanks to the affinity of silica for

the functionalized CB. Recipes are in Table 13, all the amounts are expressed in phr.

Both the nanocomposites contained the same amount of CB; SP was an extra-ingredient in composite (2). Also in this case, crosslinking was performed with a sulfur-based system. It was found that functionalization had no effect on the vulcanization behaviors, as it is shown by the curves in Fig. 23.

Silica networking was investigated by performing strain sweep experiments at 50 °C, on crosslinked samples. The dependence of shear storage modulus G' on strain amplitude and the dependence of loss module G'' on G' are in Fig. 24.

Table 13 Formulations of elastomer nanocomposites based on IR, BR as the rubber and CB and silica as the fillers. CB-SP as the functionalized CA[a,b]

Ingredient	Composite	
	(1)	(2)
IR	50.0	50.0
BR	50.0	50.0
CB N326	25.0	20.0
CB–SP	0.0	5.5
Silica	25.0	25.0
TESPT	2.0	2.0

[a]Other ingredients: ZnO 4.0, Stearic acid 2.0, 6PPD 2.0, S 1.5, TBBS 1.8.
[b]Amount of SP on CB 1:10 mass.
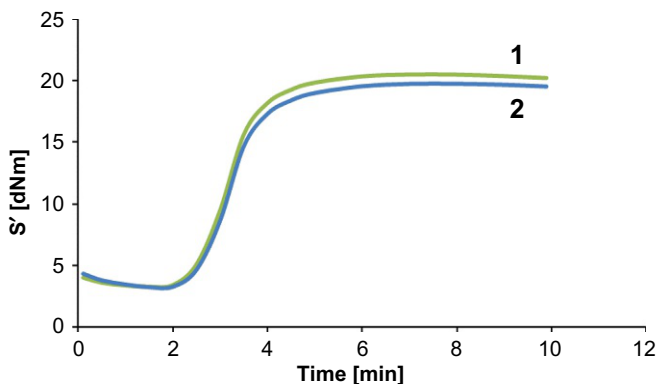
Fig. 23 Rheometric curves taken at 170 °C for composites of Table 13. Content of CB–SP: (1) 0 phr; (2) 5.5 phr.
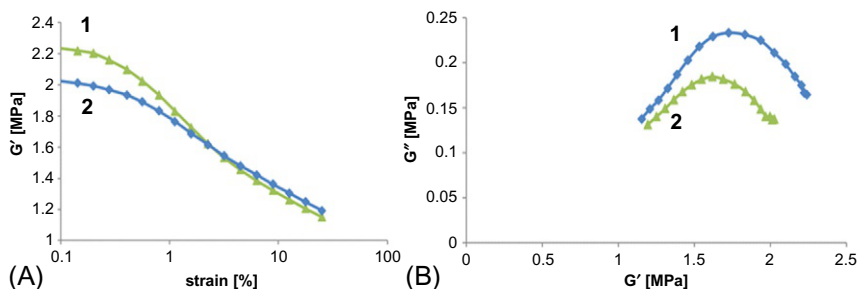
Fig. 24 Storage modulus G′ versus strain amplitude (A); loss modulus G″ versus storage modulus G′, for crosslinked composites of Table 13. Content of CB–SP: (1) 0 phr; (2) 5.5 phr.

From the graphs of Fig. 24 it is clear that the addition of CB-SP led to the reduction of the G′ modulus non linearity, i.e. of the Payne Effect [46]. More interestingly, crossover of the curves can be seen. This is usually taken as indication that a chemical bond was established between the filler and the polymer chains. Most likely, CB is able to establish a stable interaction with silica and such a "hybrid filler system" reacts with the polymer, through the sulfur-based silane. Indeed, as it appears from the Cole-Cole plot in Fig. 24B, for a given level of dynamic stiffness, the use of CB-SP allows to have lower loss modulus.

In conclusion, functionalization of CB with SP leaves the vulcanization behavior substantially unaltered but leads to larger moduli at large strain and to lower dissipation of energy.

References

[1] A.I. Medalia, G. Kraus, in: J.E. Mark, B. Erman, F.R. Eirich (Eds.), The Science and Technology of Rubber, second ed., Elsevier Academic Press, 1994, pp. 387–418 (Chapter 8).

[2] J.B. Donnet, E. Custodero, in: J.E. Mark, B. Erman, F.R. Eirich (Eds.), The Science and Technology of Rubber, third ed., Elsevier Academic Press, 2005, pp. 367–400 (Chapter 8).

[3] J.-B. Donnet, Carbon Black: Science and Technology, second ed., CRC Press, 1993.

[4] P. Schidrowitz, T.R. Dawson, History of the Rubber Industry, Heffer, Cambridge, 1952, pp. 71–72.

[5] M. Terrones, A.R. Botello-Méndez, J. Campos-Delgado, F. López-Urías, Y.I. Vega-Cantú, F.J. Rodríguez-Macías, A.L. Elías, E. Muñoz-Sandoval, A.G. Cano-Márquez, J.-C. Charlier, H. Terrones, Graphene and graphite nanoribbons: morphology, properties, synthesis, defects and applications, Nano Today 5 (4) (2010) 351–372.

[6] H.W. Kroto, K. McKay, The formation of quasi-icosahedral spiral shell carbon particles, Nature 331 (1988) 328–331.

[7] S. Iijima, T. Ichihashi, Single-shell carbon nanotubes of 1-nm diameter, Nature 363 (1993) 603–605.

[8] D.S. Bethune, C.H. Kiang, M.S. de Vries, G. Gorman, R. Savoy, J. Vazquez, R. Beyers, Cobalt-catalysed growth of carbon nanotubes with single-atomic-layer walls, Nature 363 (1993) 605–607.

[9] S. Iijima, Helical microtubules of graphitic carbon, Nature 354 (1991) 56–58.

[10] M. Monthioux, V.L. Kuznetsov, Who should be given the credit for the discovery of carbon nanotubes? Carbon 44 (9) (2006) 1621–1623.

[11] K.S. Novoselov, A.K. Geim, S.V. Morozov, D. Jiang, Y. Zhang, S.V. Dubonos, I. V. Grigorieva, A.A. Firsov, Electric field effect in atomically thin carbon films, Science 306 (2004) 666–669.

[12] A.K. Geim, K.S. Novoselov, The rise of graphene, Nat. Mater. 6 (3) (2007) 183–191.

[13] M.J. Allen, V.C. Tung, R.B. Kaner, Honeycomb carbon: a review of graphene, Chem. Rev. 110 (1) (2010) 132–145.

[14] Y.W. Zhu, S. Murali, W. Cai, X. Li, J.W. Suk, J.R. Potts, R.S. Ruoff, Graphene and graphene oxide: synthesis, properties, and applications, Adv. Mater. 22 (2010) 3906–3924.

[15] Y. Geng, S.J. Wang, J.-K. Kim, Preparation of graphite nanoplatelets and graphene sheets, J. Colloid Interface Sci. 336 (2) (2009) 592–598.

[16] L. Kavan, J.H. Yum, M. Gratzel, Optically transparent cathode for dye-sensitized solar cells based on graphene nanoplatelets, ACS Nano 5 (1) (2011) 165–172.

[17] A. Nieto, D. Lahiri, A. Agarwal, Synthesis and properties of bulk graphene nanoplatelets consolidated by spark plasma sintering, Carbon 50 (11) (2012) 4068–4070.

[18] K.R. Paton, E. Varrla, C. Backes, R.J. Smith, U. Khan, A. O'Neill, C. Boland, M. Lotya, O.M. Istrate, P. King, T. Higgins, S. Barwich, P. May, P. Puczkarski, I. Ahmed, M. Moebius, H. Pettersson, E. Long, J. Coelho, S.E. O'Brien, E. K. McGuire, B. Mendoza Sanchez, G.S. Duesberg, N. McEvoy, T.J. Pennycook, Scalable production of large quantities of defect-free few-layer graphene by shear exfoliation in liquids, Nat. Mater. 13 (2014) 624–630.

[19] J. Zhang, M. Terrones, C.R. Park, R. Mukherjee, M. Monthioux, N. Koratkar, Y. S. Kim, R. Hurt, E. Frackowiak, T. Enoki, Y. Chen, Y. Chen, A. Bianco, Carbon science in 2016: status, challenges and perspectives, Carbon 98 (2016) 708–732.

[20] L. Bokobza, Multiwall carbon nanotube elastomeric composites: a review, Polymer 48 (17) (2007) 4907–4920.

[21] M. Maiti, M. Bhattacharya, A.K. Bhowmick, Elastomer nanocomposites, Rubber Chem. Technol. 81 (3) (2008) 384–469.

[22] M. Galimberti, V. Cipolletti, S. Musto, S. Cioppa, G. Peli, M. Mauro, G. Guerra, S. Agnelli, T. Riccò, V. Kumar, Recent advancements in rubber nanocomposites, Rubber Chem. Technol. 87 (3) (2014) 417–442.

[23] M. Bhattacharya, M. Maiti, A.K. Bhowmick, Tailoring properties of styrene butadiene rubber nanocomposite by various nanofillers and their dispersion, Polym. Eng. Sci. 49 (2009) 81–98.

[24] A.K. Bhowmick, M. Bhattacharya, S. Mitra, Exfoliation of nanolayer assemblies for improved natural rubber properties: methods and theory, J. Elastom. Plast. 42 (2010) 517–537.

[25] F.R. Al-Solamya, A.A. Al-Ghamdib, W.E. Mahmou, Piezoresistive behavior of graphite nanoplatelets based rubber nanocomposites, Polym. Adv. Technol. 23 (2012) 478–482.

[26] M. Galimberti, V. Kumar, M. Coombs, V. Cipolletti, S. Agnelli, S. Pandini, L. Conzatti, Filler networking of a nanographite with a high shape anisotropy and synergism with carbon black in poly(1,4-cis-isoprene)-based nanocomposites, Rubber Chem. Technol. 87 (2) (2014) 197–218.

[27] S. Agnelli, V. Cipolletti, S. Musto, M. Coombs, L. Conzatti, S. Pandini, T. Riccò, M. Galimberti, Interactive effects between carbon allotrope fillers on the mechanical

reinforcement of polyisoprene based nanocomposites, eXPRESS Polym. Lett. 8 (6) (2014) 436–449.

[28] M. Galimberti, V. Cipolletti, S. Agnelli, S. Pandini, Hybrid filler systems for the mechanical reinforcement of isoprene rubber, Rubber World (2017) 28–37.

[29] M. Galimberti, G. Infortuna, S. Guerra, V. Barbera, S. Agnelli, S. Pandini, sp^2 carbon allotropes in elastomer matrix: from master curves for the mechanical reinforcement to lightweight materials, eXPRESS Polym. Lett. 12 (3) (2018) 265–283.

[30] M. Galimberti, S. Agnelli, V. Cipolletti, Hybrid filler systems in rubber nanocomposites, in: T. Sabu, M. Hanna (Eds.), Progress in Rubber Nanocomposites, first ed., Woodhead Publishing, 2016, p. 596.

[31] M. Galimberti, G. Infortuna, V. Barbera, S. Guerra, A. Bernardi, S. Agnelli, S. Pandini, Mechanical reinforcement of rubber by sp^2 carbon allotropes such as carbon black and carbon nanotubes: the role of interfacial area and filler orientation, Rubber World 257 (5) (2018) 24–30.

[32] ISO/TS 80004-1:2015, *Nanotechnologies Vocabulary Pt 1: Core terms*.

[33] M. Galimberti, M. Coombs, P. Riccio, T. Riccò, S. Passera, S. Pandini, L. Conzatti, A. Ravasio, I. Tritto, The role of CNTs in promoting hybrid filler networking and synergism with carbon black in the mechanical behavior of filled polyisoprene, Macromol. Mater. Eng. 298 (2012) 241–251.

[34] A. Das, K.W. Stöckelhuber, R. Jurk, M. Saphiannikova, J. Fritzsche, H. Lorenz, M. Klüppel, G. Heinrich, Modified and unmodified multiwalled carbon nanotubes in high performance solution-styrene–butadiene and butadiene rubber blends, Polymer 49 (24) (2008) 5276–5283.

[35] A.P. Legrand, On the silica edge, in: A.P. Legrand (Ed.), The Surface Properties of Silicas, Wiley and Sons, 1998, pp. 1–20.

[36] Y. Chevalier, J.C. Morawski, Precipitated Silica With Morphological Properties, Process for Producing it and its Application, Especially as a Filler, EP 0157703, 1984.

[37] J.L. Leblanc, Rubber-filler interactions and rheological properties in filled compounds, Prog. Polym. Sci. 27 (4) (2002) 627–687.

[38] A.R. Payne, R.E. Whittaker, Low strain dynamic properties of filled rubbers, Rubber Chem. Technol. 44 (1971) 440–478.

[39] C.G. Robertson, C.M. Roland, Glass transition and interfacial segmental dynamics in polymer-particle composites, Rubber Chem. Technol. 81 (2008) 506–522.

[40] G.A. Bohm, W. Tomaszewski, W. Cole, T. Hogan, Furthering the understanding of the non linear response of filler reinforced elastomers, Polymer 51 (2010) 2057–2068.

[41] N. Warasitthinon, C.G. Robertson, Interpretation of the tan δ peak height for particle-filled rubber and polymer nanocomposites with relevance to tire tread performance balance, Rubber Chem. Technol. 91 (3) (2018) 577–594.

[42] G. Heinrich, M. Kluppel, Recent advances in the theory of filler networking in elastomers, Adv. Polym. Sci. 160 (2002) 1–44.

[43] P.G. Maier, D. Goritz, Molecular interpretation of the Payne effect, Kautschuk Gummi Kunstoffe 49 (1996) 18–21.

[44] L. Chazeau, J.D. Brown, L.C. Yanyo, S.S. Sternstein, Modulus recovery kinetics and other insights into the Payne effect for filled elastomers, Polym. Compos. 21 (2000) 202–222.

[45] S.S. Sternstein, A.J. Zhu, Reinforcement mechanism of nanofilled polymer melts as elucidated by nonlinear viscoelastic behavior, Macromolecules 35 (2002) 7262–7273.

[46] H. Montes, F. Lequeux, J. Berriot, Influence of the glass transition temperature gradient on the nonlinear viscoelastic behavior in reinforced elastomers, Macromolecules 36 (2003) 8107–8118.

[47] Z. Zhu, T. Thompson, S.Q. Wang, E.D. von Meerwall, A. Halasa, Investigating linear and nonlinear viscoelastic behavior using model silica-particle-filled polybutadiene, Macromolecules 38 (2005) 8816–8824.

[48] J. Kalfus, J. Jancar, Elastic response of nanocomposite poly(vinylacetate)-hydroxyapatite with varying particle shape, Polym. Compos. 28 (2007) 365–371.

[49] J. Jancar, J.F. Douglas, F.W. Starr, S.K. Kumar, P. Cassagnau, A.J. Lesser, S. S. Sternsteinh, M.J. Buehler, Current issues in research on structure–property relationships in polymer nanocomposites, Polymer 51 (2010) 3321–3343.

[50] J.M. Funt, Dynamic testing and reinforcement of rubber, Rubber Chem. Technol. 61 (1988) 842–865.

[51] C. Gauthier, E. Reynaud, R. Vassoille, L. Ladouce-Stelandre, Analysis of the non-linear viscoelastic behaviour of silica filled styrene butadiene rubber, Polymer 45 (2004) 2761–2771.

[52] J. Fröhlich, W. Niedermeier, H.D. Luginsland, The effect of filler-filler and filler-elastomer interaction on rubber reinforcement, Compos. Part A Appl. Sci. Manuf. 36 (4) (2005) 449–460.

[53] B.C. Brodie, On the atomic weight of graphite, Philos. Trans. R. Soc. Lond. 14 (1859) 249–259.

[54] M.I. Lopez, A.E. Croce, J.E. Sicre, Explosive decomposition of gaseous chlorine dioxide, J. Chem. Soc. Faraday Trans. 90 (22) (1994) 3391–3396.

[55] H.L. Poh, F. Sanek, A. Ambrosi, G. Zhao, Z. Sofer, M. Pumera, Graphenes prepared by Staudenmaier, Hofmann and Hummers methods with consequent thermal exfoliation exhibit very different electrochemical properties, Nanoscale 4 (11) (2012) 3515–3522.

[56] L. Staudenmaier, Verfahren zur Darstellung der Graphitsäure, Ber. Dtsch. Chem. Ges. 31 (1898) 1481–1487.

[57] W.S. Hummers, R.E. Offeman, Preparation of graphitic oxide, J. Am. Chem. Soc. 80 (1958) 1339.

[58] P.K. Ang, S. Wang, Q. Bao, J.T.L. Thong, K.P. Loh, High-throughput synthesis of graphene by intercalation–exfoliation of graphite oxide and study of ionic screening in graphene transistor, ACS Nano 3 (11) (2009) 3587–3594.

[59] D.C. Marcano, D.V. Kosynkin, J.M. Berlin, A. Sinitskii, Z. Sun, A. Slesarev, L. B. Alemany, W. Lu, J.M. Tour, Improved synthesis of graphene, ACS Nano 4 (8) (2010) 4806–4814.

[60] J. Chen, B. Yao, C. Li, G. Shi, An improved Hummers method for eco-friendly synthesis of graphene oxide, Carbon 64 (2013) 225–229.

[61] J. Guerrero-Contreras, F. Caballero-Briones, Graphene oxide powders with different oxidation degree, prepared by synthesis variations of the Hummers method, Mater. Chem. Phys. 153 (2015) 209–220.

[62] J. Chen, Y. Li, L. Huang, C. Li, G. Shi, High-yield preparation of graphene oxide from small graphite flakes via an improved Hummers method with a simple purification process, Carbon 81 (2015) 826–834.

[63] N.I. Kovtyukhova, P.J. Ollivier, B.R. Martin, T.E. Mallouk, S.A. Chizhik, E. V. Buzaneva, A.D. Gorchinskiy, Layer-by-layer assembly of ultrathin composite films from micron-sized graphite oxide sheets and polycations, Chem. Mater. 11 (3) (1999) 771–778.

[64] O.Y. Posudievsky, O.A. Khazieieva, V.G. Koshechko, V.D. Pokhodenko, Preparation of graphene oxide by solvent-free mechanochemical oxidation of graphite, J. Mater. Chem. 22 (2012) 12465–12467.

[65] D.R. Dreyer, S. Park, C.W. Bielawski, R.S. Ruoff, The chemistry of graphene oxide, Chem. Soc. Rev. 39 (2010) 228–240.

[66] D.R. Dreyer, A.D. Todd, C.,.W. Bielawski, Harnessing the chemistry of graphene oxide, Chem. Soc. Rev. 43 (2014) 5288–5301.

[67] H.P. Boehm, A. Clauss, G.O. Fischer, U. Hofmann, Dünnste Kohlenstoff-Folien, Z. Naturforsch Pt. B 17 (3) (1962) 150–153.

[68] G. Eda, G. Fanchini, M. Chhowalla, Large-area ultrathin films of reduced graphene oxide as a transparent and flexible electronic material, Nat. Nanotechnol. 3 (5) (2008) 270–274.

[69] C. Gomez-Navarro, R.T. Weitz, A.M. Bittner, M. Scolari, A. Mews, M. Burghard, K. Kern, Electronic transport properties of individual chemically reduced graphene oxide sheets, Nano Lett. 7 (11) (2007) 3499–3503.

[70] S. Stankovich, D.A. Dikin, R.D. Piner, K.A. Kohlhaas, A. Kleinhammes, Y. Jia, Y. Wu, S.T. Nguyen, R.S. Ruoff, Synthesis of graphene-based nanosheets via chemical reduction of exfoliated graphite oxide, Carbon 45 (2007) 1558−−1565.

[71] D. Li, M.B. Muller, S. Gilje, R.B. Kaner, G.G. Wallace, Processable aqueous dispersions of graphene nanosheets, Nat. Nanotechnol. 3 (2) (2008) 101–105.

[72] S. Stankovich, D.A. Dikin, G.H.B. Dommett, K.M. Kohlhaas, E.J. Zimney, E. A. Stach, R.D. Piner, S.T. Nguyen, R.S. Ruoff, Graphene-based composite materials, Nature 442 (2006) 282–286.

[73] X.B. Fan, W. Peng, Y. Li, X. Li, S. Wang, G. Zhang, F. Zhang, Deoxygenation of exfoliated graphite oxide under alkaline conditions: a green route to graphene preparation, Adv. Mater. 20 (23) (2008) 4490–4493.

[74] S. Abdolhosseinzadeh, H. Asgharzadeh, H.S. Kimb, Fast and fully-scalable synthesis of reduced graphene oxide, Sci. Rep. 5 (2015) 10160–10166.

[75] F. You, D. Wang, J. Cao, X. Li, Z.-M. Dang, G.-H. Hu, In situ thermal reduction of graphene oxide in a styrene–ethylene/butylene–styrene triblock copolymer via melt blending, Polym. Int. 63 (2014) 93–99.

[76] L.J. Cote, R. Cruz-Silva, J. Huang, Flash reduction and patterning of graphite oxide and its polymer composite, J. Am. Chem. Soc. 131 (2009) 11027–11032.

[77] Y. Hernandez, S. Pang, X. Feng, K. Müllen, Graphene and its synthesis, Polym. Sci. A Compr. Ref. 8 (2012) 415–438.

[78] M. Mauro, V. Cipolletti, M. Galimberti, P. Longo, G. Guerra, Chemically reduced graphite oxide with improved shape anisotropy, J. Phys. Chem. C 116 (46) (2012) 24809–24813.

[79] J.R. Potts, O. Shankar, S. Murali, L. Dub, R.S. Ruoff, Latex and two-roll mill processing of thermally-exfoliated graphite oxide/natural rubber nanocomposites, Compos. Sci. Technol. 74 (2013) 166–172.

[80] M. Galimberti, V. Cipolletti, M. Mauro, L. Conzatti, Nanocomposites of Poly(1,4-cis-Isoprene) with graphite oxide intercalation compounds, Macromol. Chem. Phys. 214 (17) (2013) 1931–1939.

[81] Y. Luo, P. Zhao, Q. Yang, D. He, L. Kong, Z. Peng, Fabrication of conductive elastic nanocomposites via framing intact interconnected graphene networks, Compos. Sci. Technol. 100 (2014) 143–151.

[82] S. Eigler, S. Grimm, F. Hof, A. Hirsch, Graphene oxide: a stable carbon framework for functionalization, J. Mater. Chem. A 1 (2013) 11559–11562.

[83] W.R. Collins, W. Lewandowski, E. Schmois, J. Walish, T.M. Swager, Claisen rearrangement of graphite oxide: a route to covalently functionalized graphenes, Angew. Chem. Int. Ed. 50 (2011) 8848–8852.

[84] Y. Zhang, U.R. Cho, Enhanced thermo-physical properties of nitrile-butadiene rubber nanocomposites filled with simultaneously reduced and functionalized graphene oxide, Polym. Compos. 39 (9) (2018) 3227–3235.

[85] J.G. Seo, C.K. Lee, D. Lee, S.H. Song, High-performance tires based on graphene coated with Zn-free coupling agents, J. Ind. Eng. Chem. 66 (2018) 78–85.

[86] S. Zhao, S. Xie, P. Sun, Z. Zhao, L. Li, X. Shao, X. Liu, Z. Xin, Synergistic effect of graphene and silicon dioxide hybrids through hydrogen bonding self-assembly in elastomer composites, RSC Adv. 8 (32) (2018) 17813–17825.

[87] D. Hofmann, R. Thomann, R. Muelhaupt, Thermoplastic SEBS elastomer nanocomposites reinforced with functionalized graphene dispersions, Macromol. Mater. Eng. 303 (1) (2018). 1700324.

[88] L. Zhang, H. Li, X. Lai, X. Liao, J. Wang, X. Su, H. Liu, W. Wu, X. Zeng, Functionalized graphene as an effective antioxidant in natural rubber, Compos. Part A Appl. Sci. Manuf. 107 (2018) 47–54.

[89] L. Zhang, H. Li, X. Lai, W. Wu, X. Zeng, Hindered phenol functionalized graphene oxide for natural rubber, Mater. Lett. 210 (2018) 239–242.

[90] S. Song, Y. Zhang, Carbon nanotube/reduced graphene oxide hybrid for simultaneously enhancing the thermal conductivity and mechanical properties of styrene-butadiene rubber, Carbon 123 (2017) 158–167.

[91] Z. Guezzout, R. Doufnoune, N. Haddaoui, Effect of graphene oxide on the properties of compatibilized polypropylene/ethylene-propylene-rubber blend, J. Polym. Res. 24 (8) (2017) 1–15.

[92] Z. Liu, Y. Zhang, Enhanced mechanical and thermal properties of SBR composites by introducing graphene oxide nanosheets decorated with silica particles, Compos. Part A Appl. Sci. Manuf. 102 (2017) 236–242.

[93] R. Manna, S.K. Srivastava, Fabrication of functionalized graphene filled carboxylated nitrile rubber nanocomposites as flexible dielectric materials, Mater. Chem. Front. 1 (4) (2017) 780–788.

[94] Y. Wu, L. Chen, S. Qin, J. Li, H. Zhou, J. Chen, Functionalized graphene-reinforced rubber composite: mechanical and tribological behavior study, J. Appl. Polym. Sci. 134 (25) (2017). 44970.

[95] F. He, G. Mensitieri, M. Lavorgna, M. Salzano de Luna, G. Filippone, H. Xia, R. Esposito, G. Scherillo, Tailoring gas permeation and dielectric properties of bromobutyl rubber—graphene oxide nanocomposites by inducing an ordered nanofiller microstructure, Compos. Part B 116 (2017) 361–368.

[96] M. Haghnegahdar, G. Naderi, M.H.R. Ghoreishy, Microstructure and mechanical properties of nanocomposite based on polypropylene/ethylene propylene diene monomer/graphene, Int. Polym. Process. XXXII (1) (2017) 72.

[97] B. Zhong, H. Dong, Y. Luo, D. Zhang, Z. Jia, D. Jia, F. Liu, Simultaneous reduction and functionalization of graphene oxide via antioxidant for highly aging resistant and thermal conductive elastomer composites, Compos. Sci. Technol. 151 (2017) 156–163.

[98] L. Du, X. Yang, C.T.R. Pulford, Tire with Rubber Component Containing Reinforcement Comprised of Precipitated Silica and Functionalized Graphene, (2017) US 9757983B1.

[99] B. Yin, X. Zhang, X. Zhang, J. Wang, Y. Wen, H. Jia, Q. Ji, L. Ding, Ionic liquid functionalized graphene oxide for enhancement of styrene-butadiene rubber nanocomposites, Polym. Adv. Technol. 28 (3) (2016) 293–302.

[100] H.J. Salavagione, S. Quiles-Díaz, P. Enrique-Jimenez, G. Martínez, F. Ania, A. Flores, M.A. Gómez-Fatou, Development of advanced elastomeric conductive nanocomposites by selective chemical affinity of modified graphene, Macromolecules 49 (2016) 4948–4956.

[101] M. Mo, W. Zhao, Z. Chen, E. Liu, Q. Xue, Corrosion inhibition of functional graphene reinforced polyurethane nanocomposite coatings with regular textures, RSC Adv. 6 (2016) 7780–7790.

[102] M. Kotal, S. Shankar Banerjee, A.K. Bhowmick, Functionalized graphene with polymer as unique strategy in tailoring the properties of bromobutyl rubber nanocomposites, Polymer 82 (2016) 121–132.

[103] X. Zhi, Y. Mao, Z. Yu, S. Wen, Y. Li, L. Zhang, T.W. Chan, L. Liu, γ-Aminopropyl triethoxysilane functionalized graphene oxide for composites with high dielectric constant and low dielectric loss, Compos Part A 76 (2015) 194–202.

[104] C.A. Dyke, J.M. Tour, Covalent functionalization of single-walled carbon nanotubes for materials applications, J. Phys. Chem. B 108 (51) (2004) 11151–11159.

[105] D. Tasis, N. Tagmatarchis, A. Bianco, M. Prato, Chemistry of carbon nanotubes, Chem. Rev. 106 (3) (2006) 1105–1136.

[106] P. Singh, S. Campidelli, S. Giordani, D. Bonifazi, A. Bianco, M. Prato, Organic functionalisation and characterisation of single-walled carbon nanotubes, Chem. Soc. Rev. 38 (8) (2009) 2214–2230.

[107] N. Karousis, N. Tagmatarchis, D. Tasis, Current progress on the chemical modification of carbon nanotubes, Chem. Rev. 110 (9) (2010) 5366–5397.

[108] N.G. Sahoo, S. Rana, J.W. Cho, L. Li, S.H. Chan, Polymer nanocomposites based on functionalized carbon nanotubes, Prog. Polym. Sci. 35 (1) (2010) 837–867.

[109] P.-C. Ma, N.A. Siddiqui, G. Marom, J.-K. Kim, Dispersion and functionalization of carbon nanotubes for polymer-based nanocomposites: a review, Compos. Part A Appl. Sci. Manuf. 41 (10) (2010) 1345–1367.

[110] A. Setaro, Advanced carbon nanotubes functionalization, J. Phys. Condens. Matter 29 (2017)423003.

[111] B.G. Soares, Ionic liquid: a smart approach for developing conducting polymer composites, J. Mol. Liq. 262 (2018) 8–18 (a review).

[112] L.M. Polgar, F. Criscitiello, M. van Essen, R. Araya-Hermosilla, N. Migliore, M. Lenti, P. Raffa, F. Picchioni, A. Pucci, Thermoreversibly cross-linked EPM rubber nanocomposites with carbon nanotubes, Nanomaterials 8 (2) (2018) 58/1–58/18.

[113] S.H. Song, Effect of surfactants on MWNT filled elastomer composites by latex mixing, Polym. Eng. Sci. 58 (10) (2018) 1843–1848.

[114] N. Hasanabadi, H. Nazockdast, B. Gajewska, S. Balog, I. Gunkel, N. Bruns, M. Lattuada, Structural behavior of cylindrical polystyrene-block-poly(ethylene-butylene)-block-polystyrene (SEBS) triblock copolymer containing MWCNTs: on the influence of nanoparticle surface modification, Macromol. Chem. Phys. 218 (22) (2017). 1700231.

[115] B. Massoumi, M. Hosseinzadeh, M. Jaymand, Electrically conductive nanocomposite adhesives based on epoxy or chloroprene containing polyaniline, and carbon nanotubes, J. Mater. Sci. Mater. Electron. 26 (8) (2015) 6057–6067.

[116] D. Ponnamma, S.H. Sung, J.S. Hong, K.H. Ahn, K.T. Varughese, S. Thomas, Influence of non-covalent functionalization of carbon nanotubes on the rheological behavior of natural rubber latex nanocomposites, Eur. Polym. J. 53 (2014) 147–159.

[117] S. Bhattacharyya, C. Sinturel, O. Bahloul, M.-L. Saboungi, S. Thomas, J.-P. Salvetat, Improving reinforcement of natural rubber by networking of activated carbon nanotubes, Carbon 46 (2008) 1037–1045.

[118] C.F. Matos, F. Galembeck, A.J.G. Zarbin, Multifunctional materials based on iron/ iron oxide-filled carbon nanotubes/natural rubber composites, Carbon 50 (12) (2012) 4685–4695.

[119] P.M. Ajayan, L.S. Schadler, C. Giannaris, A. Rubio, Single-walled carbon nanotube–polymer composites: strength and weakness, Adv. Mater. 12 (2000) 750–753.

[120] J. Heidarian, OH-functionalized carbon nanotube filled fluoroelastomers aging test in oil based drilling fluids, J. Pet. Sci. Eng. 158 (2017) 11–28.

[121] Y. Nakaramontri, C. Nakason, C. Kummerlowe, N. Vennemann, Enhancement of electrical conductivity and other related properties of epoxidized natural rubber/carbon nanotube composites by optimizing concentration of 3-aminopropyltriethoxy silane, Polym. Eng. Sci. 57 (4) (2017) 381–391.

[122] Y. Nakaramontri, C. Nakason, C. Kummerlowe, N. Vennemann, Enhancement of electrical conductivity and filler dispersion of carbon nanotube filled natural rubber composites by latex mixing and *in situ* silanization, Rubber Chem. Technol. 89 (2) (2016) 272–291.

[123] R. Merijs Meri, J. Zicans, T. Ivanova, J. Bitenieks, I. Reinholds, A. Abele, Z. Roja, Elastic properties of UV irradiated polyethylene-octene copolymer composites with functionalized multi-walled carbon nanotubes, Integr. Ferroelectr. 173 (1) (2016) 147–152.

[124] A.J. Bandodkar, I. Jeerapan, J.-M. You, R. Nunez-Flores, J. Wang, Highly stretchable fully-printed CNT-based electrochemical sensors and biofuel cells: Combining intrinsic and design-induced stretchability, Nano Lett. 16 (1) (2016) 721–727.

[125] Y. Nakaramontri, C. Kummerlowe, C. Nakason, N. Vennemann, The effect of surface functionalization of carbon nanotubes on properties of natural rubber/carbon nanotube composites, Polym. Compos. 36 (11) (2015) 2113–2122.

[126] P. Costa, J. Silva, A. Anson-Casaos, M.T. Martinez, M.J. Abad, J. Viana, S. Lanceros-Mendez, Effect of carbon nanotube type and functionalization on the electrical, thermal, mechanical and electromechanical properties of carbon nanotube/styrene–butadiene–styrene composites for large strain sensor applications, Compos. Part B Eng. 61 (2014) 136–146.

[127] W. Wang, A. Vidal, J.B. Donnet, M.J. Wang, Study of surface activity of carbon black by inverse gas chromatography, part III. Superficial plasma treatment of carbon black and its surface activity, Kautschuk Gummi Kunststoffe 46 (12) (1993) 933–934 936, 938–940.

[128] C.R. Kinney, L.D. Friedman, Ozonization studies of coal constitution, J. Am. Chem. Soc. 74 (1) (1952) 57–61.

[129] M.R. Cines, Treatment of Furnace Blacks, (1956) CA531569.

[130] J. Rodriguez, R. Ghosal, S.K. Narayanan, An Improved Process for the Production of Carbon Black, (2013) WO 2013098838 A3.

[131] C. Herd, C. Edwards, J. Curtis, S. Crossley, K.C. Schomberg, T. Gross, N. Steinhauser, H. Kloppenberg, D. Hardy, A. Lucassen, Use of Surface-Treated Carbon Blacks in an Elastomer to Reduce Compound Hysteresis and Tire Rolling Resistance and Improve Wet Traction, (2013) US20130046064A1.

[132] S.J. Park, K.S. Cho, S.K. Ryu, Filler–elastomer interactions: influence of oxygen plasma treatment on surface and mechanical properties of carbon black/rubber composites, Carbon 41 (7) (2003) 1437–1442.

[133] J.A. Belmont, V.R. Tirumala, P. Zhang, Elastomeric Composites Containing Modified Fillers and Functionalized Elastomers, (2013) WO 2013130099.

[134] W. Wampler, B.M. Jacobsson, L. Nikiel, P.D. Cameron, J. Neilsen, Polysulfide Treatment of Carbon Black Filler and Elastomeric Compositions with Polysulfide Treated Carbon Black, (2015) US20150191579.

[135] M.J. Wang, Y. Kutsovsky, P. Zhang, L.J. Murphy, S. Laube, K. Mahmud, New generation carbon-silica dual phase filler, part I. Characterization and application to passenger tire, Rubber Chem. Technol. 75 (2) (2002) 247–263.

[136] M.J. Wang, K. Mahmud, L.J. Murphy, W.J. Patterson, Carbon-silica dual phase filler, a new generation reinforcing agent for rubber—part I. Characterization, Kautschuk Gummi Kunststoffe 51 (1998) 348.

[137] Y. Wang, Y. Wang, Y. Cheng, Ferrocenyl Hydrophobically Modified Carbon Black and Preparation Method Thereof, Faming Zhuanli Shenqing, CN 107778532 A 20180309 (2018).

[138] Y. Jiang, M.P.C.J. Klinkenberg, L. Forciniti, W.J. Busch, P.H. Sandstrom, T.D. Martter, Rubber Composition and Pneumatic Tire, (2018) US 20180171114 A1 20180621.

[139] Y. Zhang, Rubber Fender Produced by Utilizing Leftover Material of Automobile Tire and Production Method of Rubber Fender, Faming Zhuanli Shenqing, *CN 107540906 A 20180105* (2018).

[140] C. Wang, J. Jin, Y. Tang, J. Gan, S. Chen, S. Gan, Modified Rubber Auxiliary and Preparation Method Thereof, Faming Zhuanli Shenqing, CN 107474313 A 20171215 (2017).

[141] H. Hou, X. Hou, Super-Smooth Semiconductive Shield Cable Special Material and Shield Cable Made of Super-Smooth Semiconductive Shield Cable Special Material-semiconductive shield cable special material, Faming Zhuanli Shenqing, CN 106046638 A 20161026 (2016).

[142] P. Xu, X. Wang, Y. Hu, X. Luo, Y. Ding, Piezoresistive properties of nanocomposites based on silicone rubber and ionic liquid-functionalized carbon black, Mater. Lett. 182 (2016) 218–222.

[143] Y. Zhang, D. Jiang, X. Zhang, M. Zhu, S. Qu, P. Qi, Wet-Processed Carbon Masterbatch, as well as Preparation Method and Application Thereof, Faming Zhuanli Shenqing, CN 106084336 A 20161109 (2016).

[144] V. Barbera, A. Porta, L. Brambilla, S. Guerra, A. Serafini, A.M. Valerio, A. Vitale, M. Galimberti, Polyhydroxylated few layer graphene for the preparation of flexible conductive carbon paper, RSC Adv. 6 (90) (2016) 87767–87777.

[145] V. Barbera, A. Bernardi, G. Torrisi, A. Porta, M. Galimberti, Controlled functionalization of sp^2 carbon allotropes for the reinforcement of diene elastomers, Elastomery, 2017, p. 21.

[146] V. Barbera, L. Brambilla, A. Porta, R. Bongiovanni, A. Vitale, G. Torrisi, M. Galimberti, Selective edge functionalization of graphene layers with oxygenated groups by means of Reimer–Tiemann and domino Reimer–Tiemann/Cannizzaro reactions, J. Mater. Chem. A 6 (17) (2018) 7749–7761.

[147] M. Galimberti, V. Barbera, S. Guerra, L. Conzatti, C. Castiglioni, L. Brambilla, A. Serafini, Biobased Janus molecule for the facile preparation of water solutions of few layer graphene sheets, RSC Adv. 5 (99) (2015) 81142–81152.

[148] M. Galimberti, V. Barbera, A. Citterio, R. Sebastiano, A. Truscello, A.M. Valerio, L. Conzarri, R. Mendichi, Supramolecular interactions of carbon nanotubes with biosourced polyurethanes from 2-(2, 5-dimethyl-1H-pyrrol-1-yl)-1, 3-propanediol, Polymer 63 (2015) 62–70.

[149] V. Barbera, S. Musto, A. Citterio, L. Conzatti, M. Galimberti, Polyether from a biobased Janus molecule as surfactant for carbon nanotubes, eXPRESS Polym. Lett. 10 (7) (2016) 548–558.

[150] V. Barbera, A. Bernardi, A. Palazzolo, A. Rosengart, L. Brambilla, M. Galimberti, Facile and sustainable functionalization of graphene layers with pyrrole compounds, Pure Appl. Chem. 90 (2) (2018) 253–270.

[151] V. Barbera, A. Citterio, M. Galimberti, G. Leonardi, R. Sebastiano, S. Shisodia, A. M. Valerio, Process for the synthesis of 2-(2,5-dimethyl-1h-pyrrol-1-yl)-1,3-propanediol and its substituted derivatives, US20170101376A1 (2015).

[152] M. Galimberti, V. Barbera, Adducts Formed From Primary Amines, Dicarbonyl Derivatives, Inorganic Oxide Hydroxydes and sp^2-Hybridized Carbon Allotropes, WO2018087688A1 (2018).

[153] M. Galimberti, V. Barbera, Adducts of Pyrrole Derivatives to Carbon Allotropes, WO2018087685A1 (2018).

[154] M. Galimberti, V. Barbera, S. Guerra, A. Bernardi, Facile functionalization of sp^2 carbon allotropes with a biobased Janus molecule, Rubber Chem. Technol. 90 (2) (2017) 285–307.

[155] D.J. Constable, A.D. Curzons, V.L. Cunningham, Metrics to 'green' chemistry—which are the best? Green Chem. 4 (2002) 521.

[156] A.C. Ferrari, J.C. Meyer, V. Scardaci, C. Casiraghi, M. Lazzeri, F. Mauri, A.K. Geim, Raman spectrum of graphene and graphene layers, Phys. Rev. Lett. 97 (2006). 187401.

[157] C. Castiglioni, M. Tommasini, G. Zerbi, Raman spectroscopy of polyconjugated molecules and materials: confinement effect in one and two dimensions, Philos. Trans. R. Soc. A 362 (2004) 2425.

[158] V. Barbera, L. Brambilla, A. Milani, A. Palazzolo, C. Castiglioni, A. Vitale, R. Bongiovanni, M. Galimberti, Domino reaction for the sustainable functionalization of few-layer graphene, Nanomaterials 9 (2019) 44–67.

[159] S. Musto, V. Barbera, V. Cipolletti, A. Citterio, M. Galimberti, Master curves for the sulphur assisted crosslinking reaction of natural rubber in the presence of nano- and nano-structured sp^2 carbon allotropes, eXPRESS Polym. Lett. 11 (6) (2017) 435–448.

Further reading

[160] J.R. Potts, O. Shankar, L. Du, R.S. Ruoff, Processing−morphology−property relationships and composite theory analysis of reduced graphene oxide/natural rubber nanocomposites, Macromolecules 45 (2012) 6045–6055.

[161] H.-C. Wu, X. Chang, L. Liu, F. Zhao, Y. Zhao, Chemistry of carbon nanotubes in biomedical applications, J. Mater. Chem. 20 (6) (2010) 1036–1052.

CHAPTER 4

Rheological study of elastomeric nanocomposites

Philippe Cassagnau, Claire Barrès
Univ Lyon, Université Lyon1, Laboratory of Polymer Materials Engineering, CNRS: UMR5223, Villeurbanne, France

Contents

1 Introduction

From a rheological point of view, a direct consequence of incorporation of nano-particles in molten polymers is the significant change in the viscoelastic properties. For example, the effect of strain-dependence (non-linearity effect) of the dynamic viscoelastic properties of filled polymers, often referred to as the Payne effect [1, 2], has been well known in elastomers and rubbers for 40 years. The filler dispersion (scales of dispersion and aggregation), their nature (silica, carbon and clay particles for example) and aspect ratio (sphere, lamella, nano-tubes, etc.…) are expected to play a major role in determining the filler effects on non-linear responses of nanocomposites. Generally speaking, elastomers filled with nano-particles show a solid-like behavior response which includes a non-terminal zone of relaxation, apparent yield stress and a shear-thinning dependence of viscosity on particle concentration and dispersion [3]. Specifically to rubbers applications, the compression set (mechanisms of relaxation at long times) could depend also on the nanocomposite structures. All these particular rheological behaviors arise from the presence of a network structure.

The present work is dedicated to the review of the current knowledge on rheology of rubber composites filled with nanofillers (carbon and silica particles). As the structure of nanoparticles is of importance in the viscoelastic behavior of nanocomposites, a brief description of structure of the carbon nanofillers, for example, is addressed in this introductive part.

Carbon nanoparticles (carbon black, carbon nanotube and graphene derivatives) have been extensively studied due their ability to improve the mechanical and electrical conductive properties of polymer nanocomposites. Fig. 1 shows the morphology from Transmission Electronic Microscopy (TEM) of carbon nanoparticles. The Fig. 1A shows that the carbon black CB primary particles are structured at different scale (aggregation) due to strong interaction among the particles which results in chain-like structures. Note that fumed silica has similar structures at the different scales. This type of strong interaction of particles leads to apparent elongated particles which have larger interacting volume than spheres with the same particle volume in weakly structured carbon blacks. From Fig. 1B, CNT are expected to achieve their percolation threshold at low filler volume fractions due to the high aspect ratio (generally $L/D \gg 100$). Indeed, percolation thresholds as low as 0.06 wt% have been reported in the literature for CNT–polymer systems. Regarding graphene nano–particles in Fig. 1C, it can be observed like in carbon black, an aggregation of the graphene sheets at different scales. From a physic point of view the percolation threshold, the transition between liquid-solid (or between insulator-conductor), depends on the nature of these carbon nano-particles. It can be then expected the following classification in terms of the percolation threshold concentration: CNT < Graphene < CB from the lowest to the highest value. However, the dispersion and the control of the aggregation at different scales are of importance to control this percolation threshold and the final properties.
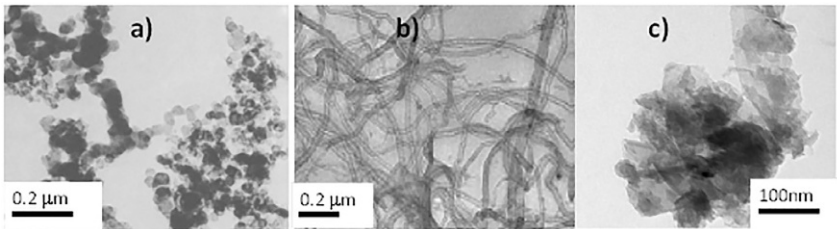
Fig. 1 TEM observation of carbon nanoparticles: (A) carbon black, (B) carbon nanotubes, (C) graphene.

2 Linear viscoelasticity

Due to the small size and the high specific surface, nano-fillers are prone to self-aggregation and consequently easily form three-dimensional network in molten polymer matrix. For example Fig. 2A and B shows the variation of

(A)

(B)
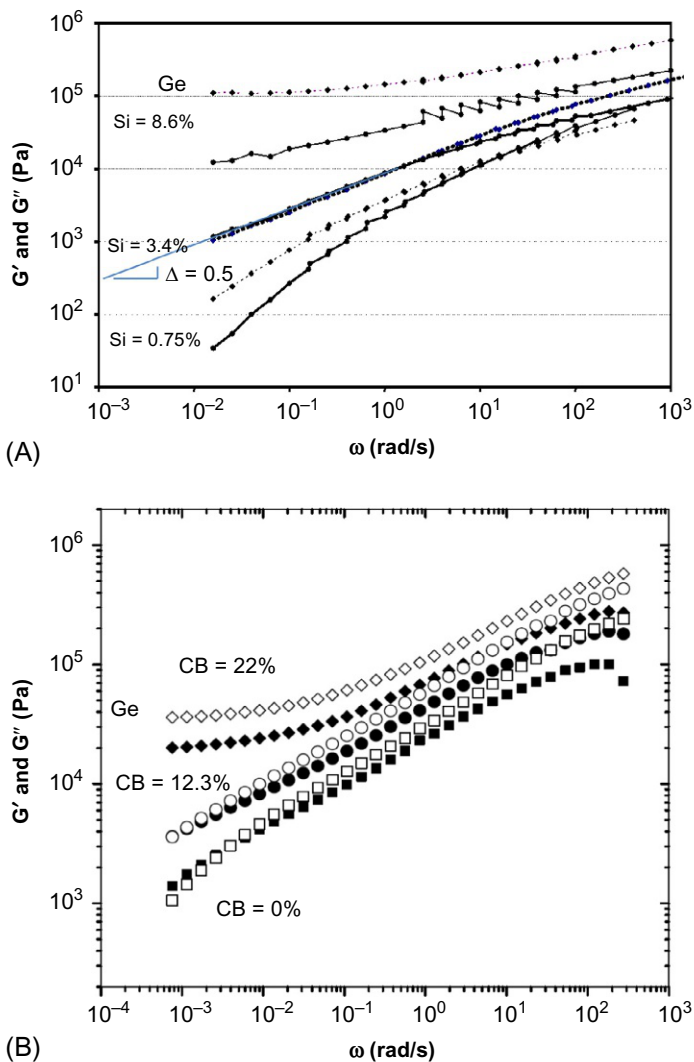
Fig. 2 Variation of the complex shear modulus of nanocomposites at different nanofiller concentrations: (A) EVA copolymers filled with fumed silica. (B) SBR filled with carbon black. (A) Reprinted with permission from P. Cassagnau, Polymer 44 (2003) 2455–2462; (B) Reprinted with permission from A. Mongruel, M. Cartault, J. Rheol. 50 (2006) 115–135.

the linear complex shear modulus $(G^*(\omega) = G'(\omega) + jG''(\omega))$ at different nanofiller concentrations for respectively: (a) copolymers of ethylene and vinyl acetate (EVA) filled with hydrophilic silica [4], Styrene butadiene rubber (SBR) filled with carbon black [5]. Therefore, the general rheological trend for nanocomposites reported in most of the works is the appearance of a transition from a liquid–like behavior ($G' \alpha \omega^2$ and $G'' \propto \omega^1$) to a solid-like behavior ($G' \propto \omega^0 = Ge$), i.e. the apparition of a plateau (second plateau modulus) of the storage modulus at low frequency which is higher than the loss modulus ($\tan\delta < 1$). Actually, it is admitted that the increase in nanofiller concentration is driving this transition. However, the state of dispersion and/or the surface modification of nanofillers is another parameter driving this transition. Since the filler-matrix interactions dictate the nature of shell formation, they play a direct role in the filler agglomeration process. It is evident that poor compatibility, for example untreated silica particles (hydrophilic) in hydrophobic polymer such as polybutadiene or SBR makes the dispersion difficult.

The sol–gel transition (liquid to solid-like behavior) occurs during a random aggregation process of subunits into larger and larger aggregates at the macroscopic scale. From a practical point of view, the increase in the effective particle volume fraction due to particle swelling or clustering from inter–particle interaction leads to a drastic decrease in ϕ_c. Scaling relations have been developed to provide the divergence of the properties at the percolation threshold arising from physical interactions. Actually, the sol–gel transition for nanocomposites in which the filler particle aggregates has the same features as chemical gelation, namely the divergence of the longest relaxation time and power law spectrum with negative exponent [6]. As a result, at the percolation threshold, storage and loss moduli have the same power law frequency dependency (Eq. 1):

$$G'(\omega) \propto G''(\omega) \propto \omega^\Delta \tag{1}$$

where Δ is the relaxation exponent. Moreover, the loss tangent $\tan\delta$ ($\tan\delta = G''/G'$) is independent on the frequency and is given by: $\tan\delta = \tan(\Delta\pi/2)$. For example, Fig. 2A shows that the silica concentration at the percolation threshold and the relaxation exponent on complex shear modulus are observed to be $\phi_c \approx 0.034$ and $\Delta = 0.5$, respectively. Furthermore, Transmission Electronic Microscopy (TEM) allowed the author [4] to visualize the scale of segregation of silica particles at different concentration in EVA samples. As shown in Fig. 3, the fumed silica is aggregated in clusters of elementary silica particles, these clusters at high concentrations lead to the formation a percolation–like filler network.
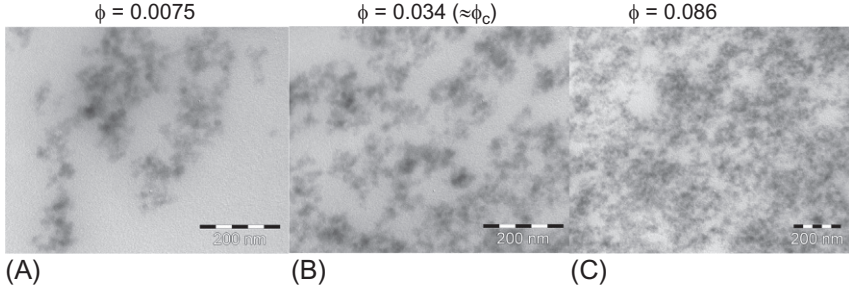
Fig. 3 TEM pictures for different silica concentrations in EVA nanocomposites: (A) $\phi = 0.0075$ ($<\phi_c$), (B) $\phi = 0.034$ ($\approx \phi_c$), (C) $\phi = 0.086$. *Reprinted with permission from P. Cassagnau, Polymer 44 (2003) 2455–2462.*

Regarding carbon black-filled SBR, Mongruel and Cartault [5] and Leboeuf et al. [6a] observed a percolation threshold situated between $\phi = 0.12$ and $\phi = 0.18$ with $\Delta \approx 0.5$. However, It must be pointed out that the viscoelastic behaviors of the elastomers, and even more so for the rubbers, are far from a viscoelastic Maxwell behavior due to the fact that that these polymer systems do not exhibit any clear and well defined terminal relaxation zone. Therefore, the liquid-solid transition cannot be clearly determined unlike thermoplastics.

Above the percolation threshold, the growth of the equilibrium elastic modulus can be described as a function of the volume concentration ϕ by:

$$G_e \propto \Phi^m \tag{2}$$

It is expected that this power-law exponent depends on particle-particle interaction. From a modeling point of view, Heinrich and Klüppel [7] have considered a network structure that refers to a space filling configuration of kinetically aggregated filler clusters: the Cluster-Cluster Aggregation (CCA) model. This model is based upon the assumption that the particles can fluctuate around their mean position in a polymer matrix. Depending on the concentration of filler particles, a flocculation process of particles or clusters leads to a filler network that can be considered as space-filling configuration of fractal CCA-clusters. From the calculation of the solid fraction of the fractal CCA-clusters and assuming a rigidity condition for reinforcement of the polymer matrix, the authors derived the concentration dependence of the equilibrium elastic modulus:

$$G_e \propto \Phi^{\frac{3 + d_{f,B}}{3 - d_f}} \tag{3}$$

where $d_{f,B} \approx 1.3$ is the fractal dimension of the CCA–cluster backbone and $d_f \approx 1.8$ is the fractal dimension due to the characteristic self-similar structure of the CCA Clusters. The Eq. (3) predicts a power law $G_e \propto \Phi^{3.5}$ which has been confirmed [7, 8] by viscoelastic data obtained for carbon black filled rubbers.

On the other hand, the elasticity should increase more rapidly and the network become more resistive for elastomers filled with hydrophilic silica than for the hydrophobic ones. For example, Cassagnau [4] observed m = 4.5 for nanocomposites of hydrophilic silica in EVA copolymer. Zhu et al. [8a] observed the scaling law $G_e \propto \Phi^{3.4}$ for polybutadiene filled with silica particles. More recently, Majesté and Vincent [9] showed a direct link between the bound rubber (Styrene-butadiene rubber, SBR) amount (more precisely the covering rate of the surface of aggregates by physically adsorbed rubber, a more detailed analysis of the bound rubber concept is given by Leblanc [9a]) and the modulus G_e. Then, they derived a power-law, $G_e \propto \Phi^{4.5}$, by introducing an effective interacting surface between filler (effective filler concentration: $\frac{(d+2\Delta)^3 - 6d\Delta^2}{d^3}\Phi$, d: diameter of particles, Δ: bound rubber thickness) as postulated by Klüppel and Heinrich [7].

3 Non-linear viscoelasticity

The famous effect of strain amplitude dependence of the dynamic viscoelastic properties of filled polymers is often referred to as the Payne [1] effect. Actually, the Payne effect was first reported for carbon black reinforced rubbers and extensively studied on filled elastomers [7, 10]. Nowadays a lot of papers deal with rubber filled with silica particles with the objective to study the influence of silica dispersion and silica surface treatment (from hydrophilic to hydrophobic behavior). For an illustrative purpose, the Fig. 4 shows the Payne effect (Variation of G' versus strain) for hydrophilic and hydrophobic silica particles at different concentrations.

The concept of filler networking yields a good interpretation of the Payne effect for filled elastomers. For example, common features between the phenomenological agglomeration–disagglomeration and recent microscopic networking approaches (particle-particle interaction) were discussed by Heinrich and Klüppel [7]. The excess of dissipated energy is attributed to the breakdown of particle structure. Consequently, filled elastomers can be drastically modified under large deformation and the viscoelastic properties are then governed by filler–structure breakdown and build-up.
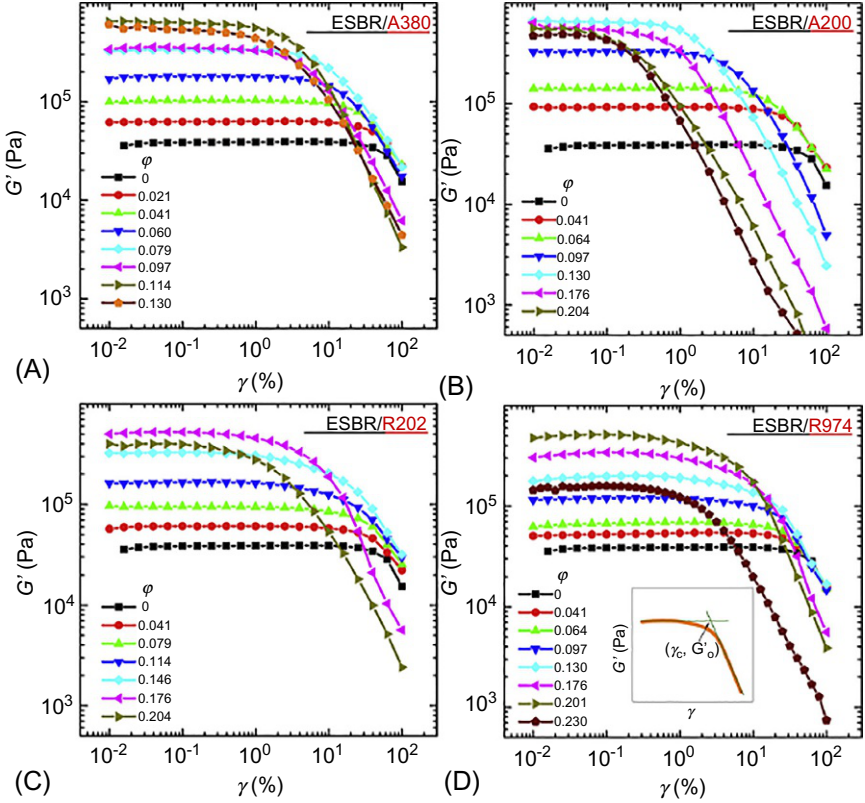
Fig. 4 Non-linear rheology of ESBR filled with A380 (A), A200 (B), R202 (C), R974 (D) at 100 °C. A380 and A200 are hydrophilic silica. R202 and R974 are hydrophobic silica. *From R. Yang, Y. Song, Q. Zheng, Polymer 116 (2017) 304–313, reprinted with permission from Elsevier.*

As a consequence of the Payne effect, the limit of linearity γ_c decreases with increasing the volume fraction of particles according to the following power-law:

$$\gamma_c \propto \phi^{-\nu} \qquad (4)$$

Actually, Shih et al. [10a] developed a scaling theory for this limit of linearity γ_c:

$$\gamma_c \propto \phi^{\frac{-\left(1 + d_{f,B}\right)}{3 - d_f}} \qquad (5)$$

The fractal dimension $d_f \approx 2$ is universal for gel aggregate systems whereas $d_{f,b}$, which depends on the number of particles per aggregates, strongly depends on the shape of fillers (spherical or tactoids).

According to the works from Zhu and Sternstein [11] and Sternstein and Zhu [12] we found $\nu = 2.4$ and $\nu = 3.0$ for hydrophobic and hydrophilic silica, respectively. According to our previous work [13] we calculated $\nu = 1.7$ for hydrophilic silica and Clement et al. [14] showed that the amplitude of the Payne effect is reduced by introducing a permanent treatment of the silica surface or a processing aid.

According to the paper of Yurekli et al. [15] on carbon black–filled elastomer composites, we derived from their work the power law $\gamma_c \propto \phi^{-1.8}$. Finally, Chatterjee and Krishnamoorti [16] reported $\gamma_c \propto \phi^{-2.3}$ for nanotube–poly(ethylene oxide) nanocomposites. The authors concluded that the weak and relatively short range interactions between nanotubes and the pathways between percolating paths dominate the network properties. This conclusion is consistent with the mechanism of particle-particle interaction between fillers to explain the non-linearity effect in nanocomposites.

4 Shear rheology

From a practical point of view, polymer processing tools create steady state or transient flow conditions in which the material experiences large deformations and large deformation rates. In such situations, filled polymers and more specifically nanocomposites exhibit complex rheological properties, so the description of their flow behavior is still a challenge. From a fundamental point of view, this requires to understand how the nanofiller particles modify the properties of the polymer matrix. Due to the different natures of the flow conditions, the influence of the nano-filler nature or concentration on the shear viscosity, measured either in steady state or in transient conditions like those met in start-up experiments, is expected to be different from the effects described previously on viscoelastic properties measured in oscillatory shear.

Unlike thermoplastic polymers or soft elastomers (thermoplastic elastomers for example) that have been the subject of extensive research, relatively few rheological studies are devoted to rubbers. This is due to several experimental problems met during rheological characterization of this class of materials, such as high viscosities, wall slippage and long-time evolution of properties. Due to their industrial history, carbon black–filled rubbers have been studied for long, and they induced the development of some specific rheological devices, for the reasons cited above. Thus, prototype instruments such as a sandwich rheometer for low stress creep tests [17], a modified Mooney-viscometer [17a] or modified Weissenberg rheometer [18], or a sliding cylinder rheometer [19], were built to offer new experimental capacities.

As pointed out by Leblanc [9a], the reinforcing fillers most commonly used with elastomers, namely carbon blacks and high-structure silane-treated silicas, are very different, specifically with regard to their interactions with the polymer, but induce the same qualitative trends of the flow properties, though (see for example the work carried out in parallel with carbon black and silica by Mongruel and Cartault [5]). Data published by Montes et al. (1988), displayed in Fig. 5, illustrate these features which can be summarized as follows:

- at low shear rates (or stresses), the compounds with low filler fractions exhibit a Newtonian plateau and the dependence of the zero-shear viscosity on the volume concentration of particles can be described satisfactorily by hydrodynamic models as those used in suspension rheology. When increasing the filler concentration, the Newtonian plateau is no longer observed and yield behavior occurs (Fig. 5A).
- at large strain rates or stresses, a shear-thinning behavior is observed, and the viscosity is much less sensitive to the filler volume fraction than in the low shear rate range.
- the increase of carbon black surface area (decrease of particle size) at constant loading has qualitatively similar effects as the increase of particle concentration, as shown in Fig. 5B: increase of viscosity, and transition towards yielding behavior as particle size decreases.

As mentioned above, the incorporation of solid particles strongly influences the low shear rate viscosity. Elastomers filled with carbon blacks comprising large, structureless and roughly spherical aggregates, at volume fractions below the percolation threshold, exhibit Newtonian behavior at low shear rates, and their zero-shear viscosity agrees well to the Guth and Gold relation [20]:

$$\eta_0(\phi) = \eta_{0,polymer} \cdot F(\phi) \quad with \quad F(\phi) = 1 + 2.5\,\phi + 14.1\,\phi^2 \quad (6)$$

However, this equation does not hold for small particle structure blacks, even in Newtonian polymeric medium. Kraus [21], reviews some attempts to improve the description of viscosity increase in polymers filled with highly reinforcing carbon blacks, by introducing shape factors for example, but also mainly by introducing the concept of effective filler volume concentration, which takes into account the combined volumes of the filler particles and of the unextractible polymer fraction. This concept was extensively developed by Pliskin and Tokita [22], and involves the notion of bound rubber, which is viewed by these authors as a layer of polymer strongly adsorbed on the particle surface and covering the latter as a rigid
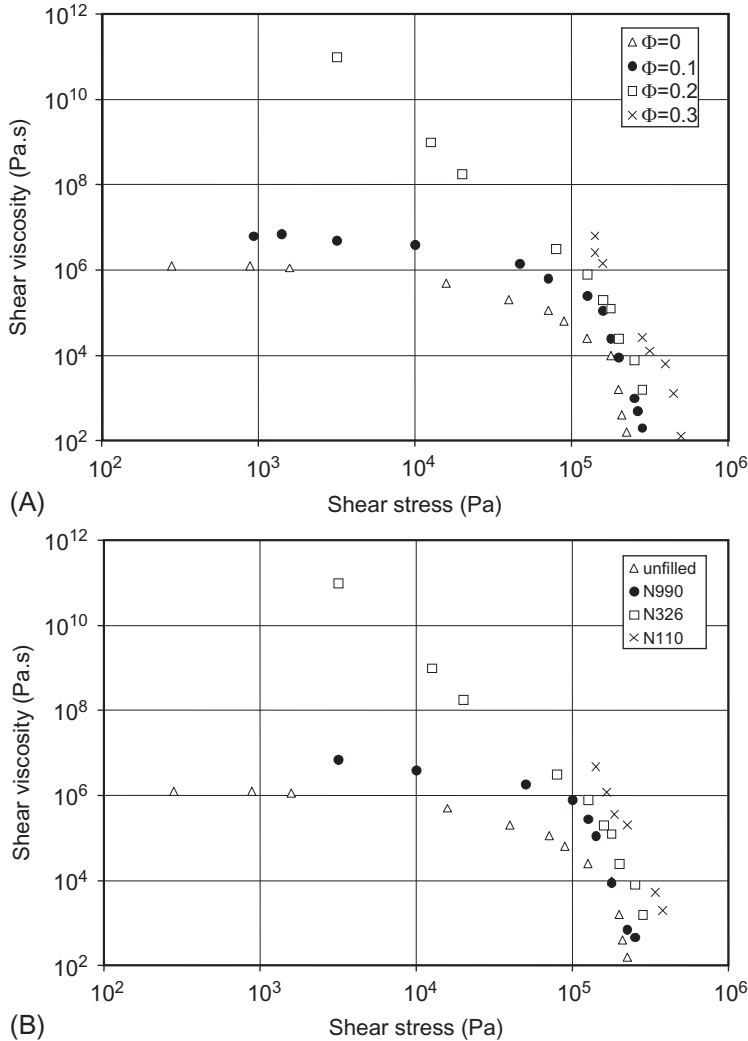
Fig. 5 Variation of shear viscosity of natural rubber (NR) compounds vs. shear stress, at 100°C. (A) Unfilled NR and filled NR compounds with different volume fractions Φ of N326 carbon black (surface area = 80 m^2/g). (B) Unfilled NR and filled NR compounds with $\Phi = 0.2$ of carbon blacks with increasing surface area, from 8 m^2/g (N990) to 140 m^2/g (N110). *Plotted with data from S. Montes, J.L. White, N. Nakajima, J. Non-Newtonian Fluid Mech. 28 (1988) 183–212.*

layer of uniform thickness. The "filler" volume fraction can now be considered as the sum of the respective fractions of the particles and bound rubber, which yields the so-called effective volume fraction. White and Crowder [23] give a general form of the concentration-related factor that they

introduce in their continuum mechanics analysis of suspensions of particles (carbon black) in viscoelastic media (synthetic rubbers):

$$F(\phi) = \left(1 + \alpha_1 f \phi_e + \alpha_2 f \phi_e^2 + \ldots \right) \qquad (7)$$

where ϕ_e is the effective volume fraction, f an anisotropy factor, α_1 and α_2 empirical coefficients depending on the system under study.

Such relations fail for filler volume fractions increasing beyond the percolation threshold of the particles, because at low shear rates the effects of particles become dominant over those of the matrix: the dynamics of the latter is modified by increasing interparticle forces, and solid-like behavior occurs.

In contrast to the preceding statement, when strain rates are high enough, highly filled polymers demonstrate usual viscoelastic behavior as unfilled polymeric liquids. Several authors illustrate the effects of increasing carbon black or silica concentration on the steady state, shear thinning viscosity of elastomers, for example (this list is not exhaustive): White and Crowder [23], Ertong et al. [18], Bandyopadhyay et al. [24], Mongruel and Cartault [5]. The general pattern of the plots for different concentrations remain similar, which demonstrates that not qualitative change of rheological behavior occurs. Shifting of the plots over one another is possible. In this respect, the work by Mongruel and Cartault is worth examining in more details, since it proposes an original analysis of the "concentration scaling" in the non-linear viscoelastic domain, and more specifically of the flow curves.

The authors deal with carbon black and silica-filled SBR compounds with filler volume fractions ranging between 0.05 and 0.23 (the volume fraction at percolation, ϕ_p, for these fillers lays between 0.12 and 0.16). They first introduce a concentration shift factor $f(\phi)$ defined as the ratio $[G'(\omega, \phi)]/[G'(\omega, \phi=0)]$, where $G'(\omega, \phi)$ is the storage modulus measured in the linear viscoelastic domain for a compound with filler volume fraction ϕ. They demonstrate that $f(\phi)$ is also equal to $[G''(\omega, \phi)]/[G''(\omega, \phi=0)]$ and remains independent upon angular frequency ω. The Guth and Gold equation fails in modeling the evolution of f for $\phi > \phi_p$ whereas the Krieger-type relation $f(\phi) = \left(1 - \dfrac{\phi}{\phi_m}\right)^{-2}$ [25], used in the framework of suspension rheology, succeeds in fitting the data over the whole range of ϕ. This concentration shift factor is then used to rescale the viscosity curves in the non-linear domain (Fig. 6A). Interestingly, when plotting $\eta(\dot{\gamma}, \phi, T)/f(\phi)$ vs. $\dot{\gamma} \cdot f(\phi)$, a reasonable master-curve is obtained over

the whole range of shear rates for filler volume fractions ϕ below the percolation threshold, whereas for the most filled compounds ($\phi > \phi_p$), the superposition only holds in the low to medium shear rate range. The plots separate in the highest shear rate domain. When plotting the graph of the shear stress vs. $\dot{\gamma} \cdot f(\phi)$ (Fig. 6B), again the superposition fails for the most filled materials at highest shear rates, which correspond to stress values beyond a critical value of about $0.3\,\text{MPa}$. The explanation proposed as most probable is that the data collected for compounds containing filler fractions beyond percolation have been obtained under slip conditions.

Finally, the same shift factor is shown to rescale satisfactorily the damping function $h(\gamma, \phi)$ which is derived from the factorization of the relaxation modulus measured in the non-linear domain (principle of time strain separability: $G(t, \gamma, \phi) = G_0(t, \phi) \cdot h(\gamma)$). The authors' conclusions can be summarized as follows:

– at large strain or strain rates, the rheological behavior shows qualitatively the same trends as for unfilled rubber, suggesting that the particles do not alter qualitatively the dynamics of the polymer chains.
– a single concentration shift factor, analogous to the one used for Newtonian suspensions, can rescale different viscoelastic functions of filled materials
– in practice, this concentration scaling factor can be used to assess the presence or not of slip in capillary rheometer data.

Nevertheless, comparisons between different systems must be carried out with care, though, since variations in rubber–filler interaction influence structure and properties via very complex mechanisms. The work of Kim and White [26] typically illustrates this statement. The authors compare untreated silica-filled EPDM with compounds of EPDM and the same silica treated with silanes of different chemical nature or chain length, at the same filler volume fraction and submitted to the same mixing procedure. The viscosity is measured over the $0.1–1\,\text{s}^{-1}$ decade and exhibits strong shear thinning. The very clear effect of silanization is to reduce significantly the viscosity with respect to untreated silica. Nevertheless, since all parameters vary simultaneously, especially the size of the agglomerates, the state of dispersion, the interparticle interactions and the physicochemical nature of the particle-polymer interactions, no straightforward conclusion regarding the mechanisms of such reduction can be drawn.
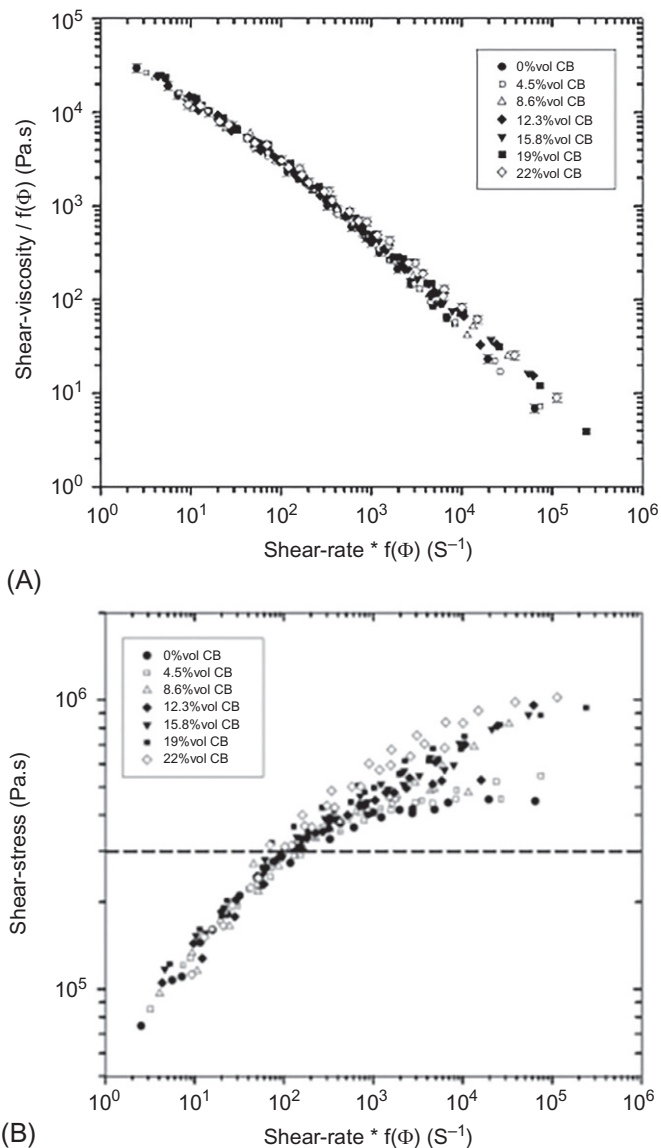
Fig. 6 Rescaling of time-temperature master curves at 100 °C obtained for SBR1500 compounds with different N330 carbon black volume fractions Φ, using the concentration shift factor $f(\Phi)$: (A) shear viscosity vs. shear rate. (B) shear stress vs. shear rate. *Reprinted with permission from A. Mongruel, M. Cartault, J. Rheol. 50 (2006) 115–135.*

5 Wall slip and extrudate swell

A more effective impact is expected from wall slip than from yielding on the flow of filled rubbers. Indeed, wall slippage is often observed with industrial rubber compounds. Ma et al. [27] demonstrated with colored markers the occurrence of slip above a critical shear rate. Slip is induced by the presence of filler (above 10 wt% carbon black for example) but can also result from the release of some components like plasticizers, lubricants and processing aids that enter these complex formulations.

It was already mentioned that any rheological characterization of such materials should assess first whether slip is present or not, in order to ensure significance of rheological data. Then, the quantification of slip is a key issue. In the framework of classical assumptions for viscometric measurements, the assessment of a master–curve for the true wall shear stress σ_w (corrected for entry effects following Bagley's method) vs. apparent shear rate $\dot{\gamma}_{app}$, upon variation of the measuring geometry (radius or gap), is a proof of no–slip conditions. By assuming that slip velocity V_s only depended on σ_w, Mooney [28] proposed a method to quantify V_s which is still the most widely used, since it can be applied to most geometries (capillary and slit dies, rotational systems…). However, Mooney's method fails in a number of situations and provides slip velocity values with no physical meaning (V_s greater than mean flow velocity $\overline{V}$), which led authors to introduce a dependence of V_s upon the local geometry in addition to σ_w [29, 30].

Other approaches rely on the use of rheological tools with smooth and grooved surfaces. The latter allow to determine slip-free behavior, and comparison with the former leads to the values of slip velocity [31, 32].

Mourniac et al. [33] addressed the wall slip velocity of SBR compounds by revisiting Mooney's technique. The first step was to assess the real, slip-free behavior of the material with grooved, non–slippery die surfaces. Then, experimental data collected in the current die provided pressure drop measurements ΔP with corresponding actual flow rate Q. If Q^* represents the theoretical flow rate that would be obtained with the same pressure drop in no–slip conditions, then the wall slip velocity V_s is given by $V_s = (Q-Q^*)/S$ where S is the cross–sectional area of the die. V_s was found to follow a power law upon shear stress in the form $\sigma_w = \alpha K V_s^n$, where K and n are the power-law coefficients of the true viscous behavior and α is a slip parameter that depends on the material characteristics and on the local geometry. With this method, physically sound values of slip velocities were obtained in all cases, and an additional interesting observations could be made: a critical

shear stress appeared, showing that the onset of wall slippage was located above 0.1 MPa, which is in good agreement with data published by other authors (except for EPDM compounds).

As a modification to Mooney's method, the consideration for the geometry dependence of the slip velocity gave rise to different expressions (see for example [34, 35]). Similarly, varied interpretations for the increase of $V_s/\overline{V}$ upon gap decrease, all other conditions remaining constant, were given. Mourniac et al. suggest that this could result from the increasing weight of surface effects at the expense of volume effects. Migration of some components is also frequently conjectured.

Reinforcing fillers, in general, reduce the extrudate swell of elastomeric materials. This has been studied for long with carbon black-filled rubbers and was reviewed by Leblanc [9a]. Therefore, no exhaustive reporting on extrudate swell is carried out here, but only some complementary aspects, especially dealing with nanoclay or nanosilica-filled rubbers, are addressed.

Generally admitted mechanisms for extrudate swell combine rearrangement of velocity profile at die exit, partial relaxation of entry tensile stress and recovery of strains associated with normal stress difference within the die. Upon addition of solid filler particles, die swell is reduced not only due to their hydrodynamic effect and the reduction of polymer volume fraction, but also because of the polymer-filler interactions which develop generally higher viscosities at the expense of elasticity.

This point can be illustrated by the variation of the first normal stress difference N_1, which characterizes the elasticity of viscoelastic materials. For example, Bandyopadhyay et al. [24], who prepared nanocomposites of epoxydized natural rubber and in-situ generated nanosilica by a sol–gel technique, observed a remarkable drop of N_1 when the concentration of nanofiller increased. Similarly, Gupta et al. [36] examined the effect of dispersed organo-bentonite on the melt elasticity of exfoliated EVA–nanocomposites by monitoring the dependence of N_1 on the organo–clay concentration. The addition of the nanofiller decreases N_1 at high shear stresses (above 2000 Pa), whereas at low shear stress N_1 appears almost independent on silicate concentration. This behavior offers contrast with published data concerning intercalated nanocomposites, whose N_1 was independent of silicate concentration. It shows that strong interactions between clay layers and polymer chains are responsible for the reduced mobility of the latter and thus, reduced elasticity which has direct consequences in decreasing extrudate swell. The effect of dispersion (exfoliation vs. intercalation) was confirmed by Sadhu and Bhowmick [37] or Ibarra et al. [38], with different polymer matrices like (carboxylated or not) acrylonitrile butadiene, styrene

butadiene and butadiene rubbers. All these studies, along with the work by Kader et al. [39] on fluoroelastomer/layered clay nanocomposites, demonstrate that the die swell reduces when fillers are added, like in traditional rubber compounds.

6 Compression set

The compression set test aims to measure the ability of rubber compounds to retain elastic properties after prolonged action of compressed stresses. Tests are frequently conducted at elevated temperatures ($T = 100\,°C$), so that crosslink samples are placed between two heating plates. Usually the samples have the shape of a disk having a thickness l_o of a few millimeters. A nominal deformation of $\varepsilon_{o,n} = 0.25$ is usually applied to the sample for few hours, generally 24 h. After this loading time, the sample is removed out of the plates and cooled down at the room temperature by placing it on a poor thermally conducting surface for 30 min before making the measure of the final thickness l_1. From Fig. 7, which schematically defines the different size parameters, the compression set is then expressed as:

$$Cs = \frac{l_0 - l_1}{l_0 - l_2} \cdot 100 \text{ with } \varepsilon_{0,n} = \frac{l_0 - l_2}{l_0} \tag{8}$$

which implies the following limits of the compression set data under the experimental conditions (temperature and loading time):

$Cs = 0\%$, as $l_1 = l_o$, the sample shows a perfect elastic recovery.

$Cs = 100\%$, as $l_1 = l_2$, the sample shows no elastic recovery.

From a viscoelastic point of view, the compression set experiment is a stress relaxation test under compression followed by an elastic recovery test. It can be then modeled [40] from the superposition principle of Boltzmann (linear viscoelasticity).

However, there is actually few works in the literature that report the compression set of rubber nanocomposites. Kim et al. [41] showed the
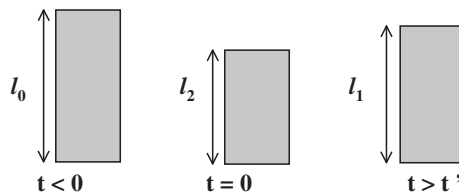
Fig. 7 Size parameters of an elastomer sample submitted *t* a compression set experiment.

compression set of butadiene rubber (BR) decreases (from 27% to 15%) with the presence of nanofillers (3 phr of organo–clays and 10 phr carbon black). Rattanasom et al. [42] reported a slight variation of the compression set with the concentration of different fillers (organo–clays, carbon black and silica). Varghese et al. [43] studied the compression set of acrylonitrile butadiene rubber using pristine few layer graphene (FLG). They showed that the compression set slightly increases (from 16% to 20%) at the concentration of 5 phr of FLG. However, the compression set decreases to 12% at the same concentration of 5 phr of fillers based on 2.5 phr of FLG and 2.5 phr of carbon black. In the case of natural rubbers, Chaichua et al. [44] observed a significant increase (from 34% to 62%) of the compression set with the addition of 30 phr of silica. Finally, Ziraki et al. [45] measured a decrease of the compression set of silicone rubber from 16% to 9% with the addition of 2% of silica particles.

From these results, obtained with different rubbers and fillers systems, it is quite difficult to have a clear trend of the influence of nanofillers on the compression set variations. However, it can be observed that the compression set decreases at low concentrations of fillers. In other works, the elastic recovery is better with the presence of nanofillers. Actually this behavior is reversed at high concentration (typically >10%) as it is observed that the compression set significantly increases. It must be remind that the applied strain in the compression set is 25% so that we generally do not know if the test is performed in the linear or non–linear regimes. As the transition between linear and non–linear regimes (Payne effect) strongly depends on the nature and concentration of nano–fillers, it can be then imagine that the trend in the variation of the compression set depends on these viscoelastic regimes. Therefore, we can assume that at low concentration of fillers the viscoelastic regime is still linear and the fillers contribute to a better elasticity recovery. On the contrary at high concentrations, the linear domain of the nanocomposite is lower than 25% so that the compression set experiment is carried out in the non–linear regime resulting in worse properties. However, this speculative discussion would require more controlled experiments in terms of viscoelastic regimes and more fundamentals approaches.

7 Conclusions

From an historical point of view, the determination of the viscoelastic properties of industrial rubber nanocomposites, i.e. basically carbon black and silica–filled compounds, has been considered for decades in the purposes

of quality control and of predicting behavior in processing conditions. The appearance of a novel class of rubber nanocomposites, based on nanoparticles such as carbon nanotubes and graphene in very low concentrations, has not reached yet this stage of industrial concern. The studies on these new classes of polymer materials are much more focused on microstructural analysis through linear and non-linear viscoelastic properties (Payne effect). Determining sound rheological data in processing conditions still remains a challenge with elastomeric materials [9], because fundamental knowledge on the influence of filler particles, the strongly viscoelastic behavior and slip phenomena, which are inherent to the flow of rubber materials, is only partial. Furthermore, in spite of the progress made in computational rheometry of thermoplastic polymers, the rheology of elastomeric materials still presents enhanced difficulties, which explains that comparatively rather few data are published in literature. On the other hand, the compression set, which is a simple way to measure the elasticity recovery of rubbers, needs to be more deeply investigated for rubber filled with nanoparticles.

References

[1] A.R. Payne, J. Appl. Polym. Sci. 6 (1962) 57.
[2] A.R. Payne, Reinforcement of Elastomers, Interscience, New York, 1965, pp. 69–123 (Chapter 3).
[3] P. Cassagnau, Polymer 49 (2008) 2183–2196.
[4] P. Cassagnau, Polymer 44 (2003) 2455–2462.
[5] A. Mongruel, M. Cartault, J. Rheol. 50 (2006) 115–135.
[6] H.H. Winter, M. Mours, Adv. Polym. Sci. 134 (1997) 165–234.
[6a] M. Leboeuf, N. Ghamri, B. Brulé, T. Coupez, B. Vergnes, Rheol. Acta 47 (2008) 201–212.
[7] G. Heinrich, M. Klüppel, Adv. Polym. Sci. 160 (2002) 1–44.
[8] M. Klüppel, Macromol. Symp. 194 (2003) 39–45.
[8a] Z. Zhu, T. Thompson, S.Q. Wang, E.D. von Meerwall, A. Halasa, Macromolecules 38 (2005) 8816–8824.
[9] J.C. Majesté, F. Vincent, J. Rheol. 59 (2015) 405–427.
[9a] J.L. Leblanc, Prog. Polym. Sci. 27 (2002) 627–687.
[10] A.I. Medalia, Rubber Chem. Technol. 51 (1978) 437.
[10a] W.H. Shih, W.Y. Shi, S.I. Kim, A.I. Aksay, Phys. Rev. A 42 (1990) 4772–4779.
[11] A.J. Zhu, S.S. Sternstein, Compos. Sci. Technol. 63 (2003) 1113–1126.
[12] S.S. Sternstein, A.J. Zhu, Macromolecules 35 (2002) 7262–7273.
[13] P. Cassagnau, F. Mélis, Polymer 44 (2003) 6607–6615.
[14] F. Clement, L. Bokobza, L. Monnerie, Rubber Chem. Technol. 78 (2005) 211–231.
[15] K. Yurekli, R. Krishnamoorti, M.F. Tse, K.O. Mcelrath, A.H. Tsou, H.C. Wang, J. Polym. Sci. Polym. Phys. 39 (2001) 256–275.
[16] T. Chatterjee, R. Krishnamoorti, Phys. Rev. E (2007) 1–4. 050403.
[17] S. Toki, J.L. White, J. Appl. Polym. Sci. 27 (1982) 3171–3184.
[17a] S. Montes, J.L. White, N. Nakajima, J. Non-Newtonian Fluid Mech. 28 (1988) 183–212.

[18] S. Ertong, H. Eggers, P. Schümmer, Rubber Chem. Technol. 67 (1994) 207–216.
[19] C. Barrès, J.L. Leblanc, Polym. Test. 19 (2000) 177–191.
[20] E. Guth, O. Gold, Phys. Rev. 53 (1938) 322.
[21] G. Kraus, Adv. Polym. Sci. 8 (1971) 155–231.
[22] I. Pliskin, N. Tokita, J. Appl. Polym. Sci. 16 (1972) 473–492.
[23] J.L. White, J.W. Crowder, J. Appl. Polym. Sci. 18 (1974) 1013–1038.
[24] A. Bandyopadhyay, M. De Sarkar, A.K. Bhowmick, Rubber Chem. Technol. 78 (2005) 806–826.
[25] I.M. Krieger, T.J. Dougherty, Trans. Soc. Rheol. 3 (1959) 137–152.
[26] K.J. Kim, J.L. White, Compos. Interfaces 9 (2002) 541–556.
[27] C.Y. Ma, J.L. White, F.C. Weissert, A. Isayev, N. Nakajima, K. Min, Rubber Chem. Technol. 58 (1985) 815–829.
[28] M. Mooney, J. Rheol. 2 (1931) 210–222.
[29] K. Geiger, Kautsch. Gummi Kunstst. 42 (1989) 273–283.
[30] S. Wiegreffe, Kautsch. Gummi Kunstst. 44 (1991) 216–221.
[31] D.M. Turner, M.D. Moore, Plast. Rubber Proc. 5 (1980) 81–84.
[32] J.L. White, M.H. Han, N. Nakajima, R. Brzoskowski, J. Rheol. 35 (1991) 167–189.
[33] P. Mourniac, J.F. Agassant, B. Vergnes, Rheol. Acta 31 (1992) 565–574.
[34] B. Crawford, J.K. Watterson, P.L. Spedding, S. Raghunathan, W. Herron, M. Proctor, J. Nonnewton Fluid Mech. 129 (2005) 38–45.
[35] A.Y. Malkin, A.V. Baranov, M.E. Vickulenkova, Rheol. Acta 32 (1993) 150–155.
[36] R.K. Gupta, V. Pasanovic-Zujo, S.N. Bhattacharya, J. Nonnewton Fluid Mech. 128 (2005) 116–125.
[37] S. Sadhu, A.K. Bhowmick, J. Polym. Sci. B Polym. Phys. 43 (2005) 1854–1864.
[38] L. Ibarra, A. Rodriguez, I. Mora, Eur. Polym. J. 43 (2007) 753–761.
[39] M.A. Kader, M.Y. Lyu, C. Nah, Comp. Sci. Technol. 66 (2006) 1431–1443.
[40] C. Joubert, A. Michel, L. Choplin, P. Cassagnau, J. Polym. Sci. B Polym. Phys. 41 (2003) 1779–1790.
[41] M.S. Kim, D.W. Kim, S.R. Chowdhury, G.H. Kim, J. Appl. Polym. Sci. 102 (2006) 2062–2066.
[42] N. Rattanasom, S. Prasertsri, T. Ruangritnumchai, Polym. Test. 28 (2009) 8–12.
[43] T.V. Varghese, H.A. Kumar, S. Anitha, S. Ratheesh, R.S. Rajeev, R.V. Lakshmana, Carbon 6 (2013) 476–486.
[44] B. Chaichua, P. Prasassarakich, S. Poompradub, J. Sol-Gel Sci. Technol. 52 (2009) 219–227.
[45] S. Ziraki, S.M. Zebarjad, M.J. Hadianfard, Polym.-Plast. Technol. Eng. 55 (2016) 1693–1699.

Further reading

[46] J. Clarke, J. Petera, J. Appl. Polym. Sci. 66 (1997) 1139–1150.
[47] C.R. Lin, D. Lee, Macromol. Theory Simul. 6 (1997) 339–347.
[48] C.A. Mitchell, J.L. Bahr, S. Arepalli, J.M. Tour, R. Krishnamoorti, Macromolecules 35 (2002) 8825–8830.
[49] R. Yang, Y. Song, Q. Zheng, Polymer 116 (2017) 304–313.

This page intentionally left blank

CHAPTER 5

Hard/soft combinations based on thermoplastic elastomer and a rigid thermoplastic polymer: Study of the adhesion strength

Maria V. Candal[a], Orlando O. Santana[b], Johan J. Sánchez[c], Graciela Terife[b], Antonio Gordillo[b]
[a]Polymer Group USB, Mechanical Department, Universidad Simón Bolívar, Caracas, Venezuela
[b]Centre Català del Plàstic, Universidad Politécnica de Catalunya Barcelona Tech (UPC-EEBE), C/Colom, Terrassa, Spain
[c]Polymer Group USB, Materials Department, Universidad Simón Bolívar, Caracas, Venezuela

Contents

113

1 Introduction

Among the current processing techniques used to produce polymeric parts and components, injection molding is one of the most widely used due to its high versatility and productivity: it allows the production of high quality parts in less time. In the latest years several variations of the conventional injection molding process have been developed; one of them is Overmolding or Multicomponent Injection Molding, which has been extensively used and has a lot of growing potential [1]. The development of more complex molds, which are capable of joining different materials into one part, has been very important in making this possible. The overmolding process is used in the fabrication of parts for several industrial sectors such as automotive, medical and packaging. Some of its products commonly seen in the market are: tooth brushes, razors and tools, among others.

In spite of this, there are still some difficulties associated to the overmolding process during the design and production stages. First, when designing a multicomponent part, the only information available to perform material selection are qualitative tables, which only indicate if adhesion may be achieved for some material pairs. Also, the lack of quantitative information about adhesion strength makes it impossible to predict if the part under a certain load state will fail by an adhesive or cohesive mechanism. In other words, the designer does not know what is going to occur first: the separation of the two materials or the failure of one of them. Furthermore, there is insufficient information correlating the processing conditions with the adhesion strength.

Therefore, the main objective of the present work is to compare experimental test methods to quantify the adhesion strength between two overmolded polymers, and to choose the best method to measure the adhesion strength between these materials. For this study, tensile test, peeling test and essential work of interfacial fracture (EWIF) are explored and compared as potential testing methods to quantify the adhesion strength between Overmolded materials.

1.1 Overmolding

Overmolding is a variation of the conventional injection molding process; it can be seen as consecutive injections because the principle of this process is to inject another melted polymer over a previously molded plastic part, using one or several molds. Some of the techniques currently in use are: Rotatory

Table, Indexing Plate, Stack Mold, Slide–Cam and Transfer Molding [1–4]. The applications of this process could be divided in three groups [3]:

- Multicomponent one step assembly: if two similar materials are selected, it is possible to produce a strong joint in a single step, without using screws, welding or adhesives.
- Multicolor injection molding: it allows injecting parts of the same material but with different colors, improving the visual aspect of the final product.
- Hard-soft combinations: by molding a suitable thermoplastic elastomer (TPE) or thermoplastic vulcanized elastomer (TPV) on top of a rigid polymer it is possible to improve the tactile properties of the finished part.

When two or more materials are overmolded, it is important to understand the adhesion mechanism by which a strong bond is formed. This mechanism can be divided into three stages [5–7] as long as physical (roughness) or chemical (reaction between both materials) anchorages are neglected:

1. *Wetting of the substrate*: during the first stage of the overmolding process, a polymer is injected and solidifies inside the mold cavity. Then, this part becomes the substrate as it is used as an insert in the cavity during the next injection step. Wetting the substrate by the melted material is very important, because it is in this stage where intimate contact between the two materials is generated, assuring the absence of interfacial defects that could act as stress concentration factors that will decrease the adhesion strength of the part.

2. *Interdiffusion of the polymer chains*: the diffusion process takes place as soon as the melted material has wetted the substrate. Once the interface is formed, by intimate contact between the two materials, the polymer chains will diffuse through them. The chains of both materials will thus tend to entangle forming a strong union. Both wettability and diffusion strongly depend on the compatibility between the materials being overmolded. Hence, it is very important that the materials have similar solubility parameters (δ) in order to bond them, because both the wettability and the diffusion will be favored. In addition to diffusion of the melted polymer, the migration of the additives or some other compounds present in the elastomer could affect the adhesion strength.

3. *Solidification of melted material*: once the melted material solidifies, an interphase with a concentration gradient of both materials is formed as a result of the diffusion process.

1.2 Adhesion strength measurement

The adhesion strength is a measure of how strong the bond between two materials is. This can be done in terms of load, stress, energy or work required to break the interphase. In the present work, the adhesion strength was evaluated by:

(a) *Tensile test*: a conventional mechanical test which measures the resistance of a material to the gradual application of uniaxial strain. In the present case, a dumbell specimen where the interphase of the overmolded polymers was located at the center of the gage length had to be prepared in order to measure the adhesion strength.

(b) *Peeling test*: it is a technique frequently used today to measure the adhesion strength between two materials. Different configurations of peeling test may be used by changing the crack opening angle [8–12].

(c) *Essential Work of Interfacial Fracture (EWIF)*: it is a method that derived from the Essential Work of Fracture (EWF) methodology [13, 14] which has been used satisfactorily to determine the fracture behavior of many ductile polymeric systems [15, 16]. It has been proposed that when a ductile solid material is subjected to a uniaxial load, its failure can be studied applying the EWF technique if the crack propagation starts after the fracture process zone (FPZ) has completely yielded (full plastic collapse, implying pure plane stress). In this case, the total work of fracture (W_F) may be divided into two components:

$$W_F = W_e + W_p \tag{1}$$

where W_e is the essential work of fracture (i.e. work done to generate the fracture surfaces), and W_p is the non-essential work of fracture associated with the energy consumed during any dissipative deformation process (usually plastic) of the material that surrounds the FPZ (i.e. crack propagation plane).

Since the W_e is proportional to the size of the FPZ and W_p is proportional to the deformed volume around FPZ (i.e. outer process zone, OPZ), then Eq. (1) may be rewritten using specific terms by taking into account the thickness (B) and width (usually, ligament length, L) of the FPZ and the volume of OPZ [14]:

$$w_F \left(L \times B \right) = w_e \left(L \times B \right) + \beta\, w_p \left(L^2 \times B \right) \tag{2}$$

$$w_F = w_e + \beta\, w_p\, L \tag{3}$$

where w_e is the specific essential work of fracture and it may be considered as a property of the material under evaluation, w_p is the non-essential work of fracture by the volume of deformed material in the OPZ and β is a geometrical factor with a value <1 that quantifies how much the volume of OPZ deviates from its ideal volume (i.e. $L^2 \times B$). Experimentally, the EWF parameters are determined from load-displacement (P-d) curves of test specimens with different L values. The double edge-notched tension (DENT) and single edge-notched tension (SENT) are the geometries mostly used for this test [15], although a center-notched tension (CNT) geometry has also been used [17] (Fig. 1).

Knowing the basic principles of the EWF method, it is possible to study the adhesion strength of polymer-polymer interphases [13, 14]. The total work of interfacial fracture (w_{IF}) of two materials (1 and 2) that, during the test, display plastic deformation around the interphase can be described according to the following expression:

$$w_{IF} = w_I + (\beta_1 \, w_{NI,1} + \beta_2 \, w_{NI,2}) \, L \tag{4}$$

where w_I is the specific essential work of interfacial fracture, β_1 and β_2 are the geometrical factors associated with the shape of the plastic zone of materials 1 and 2, respectively, and $w_{NI,1}$ and $w_{NI,2}$ correspond to specific non-essential work of interfacial fracture of each material. Then it is assumed that w_I is a measure of the strength of the joint; a higher w_I value indicates higher adhesion strength (see [13] for more details).

1.3 Adhesion strength measurement of overmolded materials

Weng et al. [6] determined the adhesion force through peeling tests for several pairs of overmolded materials. They studied the adhesion between a styrene based TPE overmolded with PP, PC, PMMA and PA6. The authors observed good adhesion only with PP because both materials have similar δ values, but in the cases where the compatibility was poor (PC, PMMA and PA6), the TPE was modified to obtain similar δ values or to generate specific interactions with the substrate.

On the other hand, Carella et al. [18] used the 180 degrees peeling test to determine the optimal melt and mold temperatures to obtain a good adhesion between two overmolded materials. In that case, two polyolefin based TPEs with different hardness were overmolded. They concluded that if the melt temperature was low, the holding/packing pressure was insufficient to achieve good adhesion between both materials.
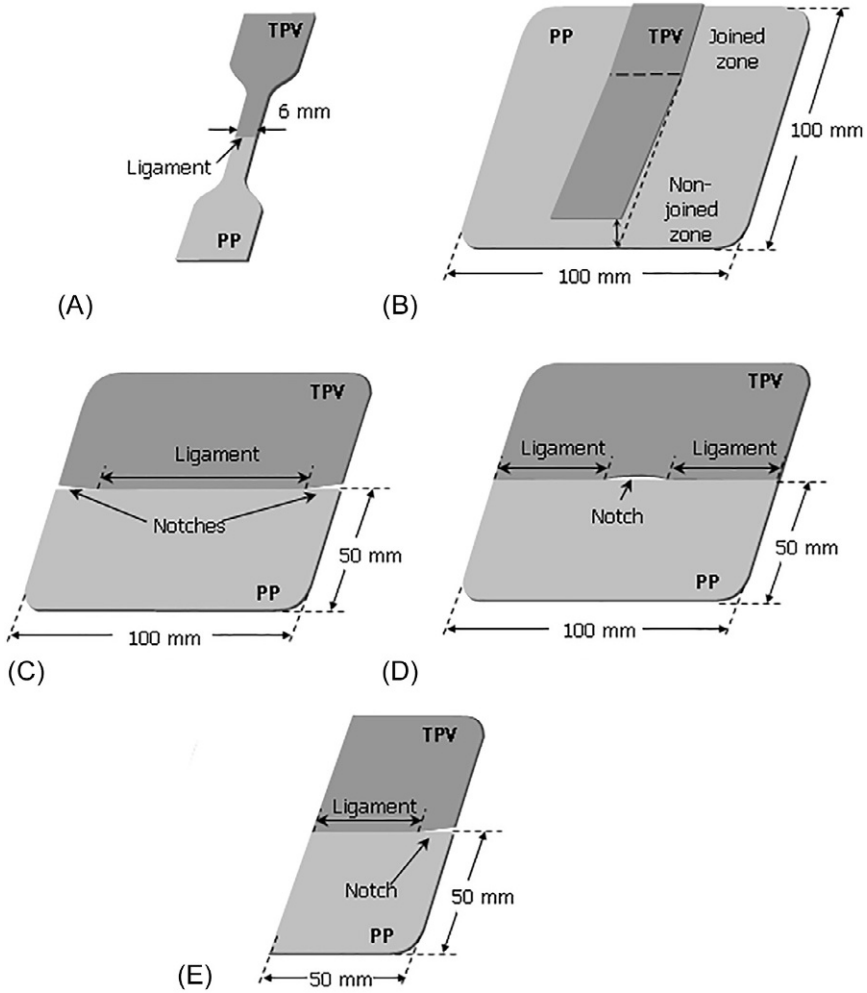
Fig. 1 Schematic illustration of a specimen used. (A) Tensile (dumbbell) specimen, (B) peeling specimen, (C) DENT specimen, (D) CNT specimen, and (E) SENT specimen.

Arzondo et al. [2] studied the influence of the melt temperature and other factors in the adhesion strength of PP overmolded with an ethylene/1-octene copolymer (EOC) and low–density polyethylene (LDPE), using the 180 degrees peeling test. The adhesion force reached by PP/LDPE was much smaller than that the reached by PP/EOC, because the compatibility between EOC and PP is higher than that the PP/LDPE pair. They concluded that the strength of the union depends mainly on the

temperature of the interface and the mobility of the EOC. The peeling force tended to be higher as the melt temperature increases.

As it has been stated before, the adhesion strength was measured for three melt temperatures to evaluate the accuracy of the different test methods. In Candal et al. [13, 19] previous works, it was shown that as the TPV's melt temperature is increased, the tensile load required to break the interphase is also higher; in other words, the adhesion between the two materials is improved. This effect is probably produced by an improvement of the substrate wettability and of the diffusion of the melted material (TPV) through the PP, and as a consequence, the molecular entanglement of the polymeric chains of both materials is enhanced. It is important to point out that both wettability and diffusion are favored at higher melt temperatures, producing a stronger link.

2 Experimental part

2.1 Materials

The materials used in this study were a Polypropylene (PP) homopolymer *Moplen HP501H* from Basell Polyolefins and a TPV *Santoprene 8211-55* from Advanced Elastomer Systems (Table 1).

It is important to know that the morphology of the TPV used depends on two phases (PP and elastomer), the nature of the blend before the cross-linking and the mechanism of cross-linking. For uncured EPDM-PP blends, depending on the composition, three morphologies can be obtained: (a) Dispersed elastomer particles in a continuous PP matrix, (b) Co-continuous PP in the elastomeric phase and (c) Dispersed PP particles in the continuous phase of the elastomer. For the EPDM-PP blend,

Table 1 Properties of PP and TPV

Properties	Unit	PP	TPV
Density	g/cm^3	0.90	0.93
Melt flow index (230/2.16)[a]	dg/min	2.1	–
Hardness	Shore	D: 70	A: 55
Young modulus	MPa	1450	–
Tensile stress at 100%	MPa	–	2.1
Elongation at break	%	700	480

[a]ASTM D1238-04c.

with PP as a major component, the dynamic vulcanization preserves the morphology by dispersing the EPDM in the PP matrix. However, for the EPDM–PP blend in the intermediate composition two co-continuous phases are generated before the dynamic vulcanization process. As the cross-linking occurs, the inversion of phases takes place, and at the end of the process, vulcanized elastomer particles dispersed in the PP matrix are obtained. The morphological characteristic of having a continuous phase of PP with particles of cross-linked elastomer is the key to obtain a blend that exhibits physical properties comparable to that of a cross-linked elastomer but with the processability of a thermoplastic.

2.2 Solubility parameter (δ)

The δ of the TPV was determined using chloroform, hexane, benzene, formic acid, acetone and THF. The same procedure was used for all the solvents; first, several pellets were weighted in an *Ohaus* balance with a precision of $0.01\,g$. Then, they were immersed in the different solvents for 24 h. Afterwards, the weight difference was calculated. The solvent that caused the biggest difference between initial and the final weights of the pellets; in other words, the solvent that induced the greater swelling of the pellets was used to determine the δ of the TPV. The δ obtained for the TPV was $19.0\,MPa^{1/2}$ and that δ of the PP was taken as $18.8\,MPa^{1/2}$ [20].

2.3 Overmolding procedure

All test specimens where molded with an injection molding machine Mateu & Solé *Meteor 440/90*, and molds for plates of $100 \times 100\,mm$ were used. In all cases, the PP plates of 1 mm thickness were molded first, and the TPV was overmolded on the PP. All the PP plates had the same surface roughness. The process conditions used for both materials are presented in Table 2. All the variables were held constant except for the TPV's melt temperatures which were $190\,°C$, $210\,°C$ and $230\,°C$.

Table 2 Molding conditions

Variable	Unit	PP	TPV
Melt temperature	°C	220	–
Injection velocity	cm/s	21	11
Holding/packing pressure	MPa	50	35
Holding/packing pressure time	s	8	8
Mold temperature	°C	40	40

Three different techniques were used to measure the adhesion strength: Tensile, Peeling and EWIF testing. For EWIF testing, three geometries were used: DENT, CNT and SENT. The test specimen preparation details will follow:

- Tensile (dumbell) specimens

In order to mold the dumbell specimens, PP plates of $100 \times 50 \times 1$ mm were molded first, and then used as mold inserts, where TPV was overmolded. Finally, the test specimens were cut from the center of the bimaterial plates, according to ASTM D638 standard Type IV test specimens (Fig. 1A). For each melt temperature, 10 specimens were molded and tested.

- Peeling specimens

The first step to produce the peeling test specimens was to mold PP plates of $100 \times 100 \times 1$ mm. Then, their sides were partially wrapped with aluminum foil (thickness $= 0.015 \pm 0.001$ mm), so no TPV will adhere on that area. Then, the section of the plates not covered with the foil was overmolded with the TPV forming a bimaterial plate (Fig. 1B). For each melt temperature, 10 specimens were molded and tested.

- Double edge-notched tension (DENT) specimens

The DENT specimens were molded following a similar procedure to that for obtaining peeling test probes. In this case, PP plates of $100 \times 50 \times 1$ mm were molded. Then, the edges of the PP plates were partially wrapped with aluminum foil in order to generate edge notches inside the mold cavity. Finally, using PP plates as mold inserts, the TPV was overmolded. The bimaterial test specimens were plates of $100 \times 100 \times 1$ mm (Fig. 1C). The ligament length was varied between 6 and 32 mm.

- Center notched tension (CNT) specimens

As it was done in the DENT test specimens preparation, the CNT specimens were obtained molding PP plates of $100 \times 50 \times 1$ mm. Then, the center of them was wrapped with aluminum foil so the crack will be generated inside the mold cavity during the overmolding process (Fig. 1D). The crack lengths were varied between 6 and 32 mm.

- Single edge-notched tension (SENT) specimens

The SENT test specimens were made by cutting the DENT specimens in half (Fig. 1E). The study was done with 14 different ligament lengths ranging between 3 and 16 mm.

2.4 Mechanical testing

The five specimen types were tested in a Lloyd universal testing machine, with a crosshead speed of 20 mm/min and at a temperature of 23 ± 1 °C.

The dumbell specimens were tested according to ASTM D638 standard. The distance between grips was 75 mm and the adhesion strength was determined from load–displacement (P-d) curves.

The P-d curves of the Peeling Test were obtained with a crack opening angle of 180 degrees, applying the principles of ASTM D903 standard. In addition, looking for better results, the specimens were also tested using the 90 degrees configuration and additional crosshead speeds of 2 and 200 mm/min. In all cases, the distance between grips was 90 mm.

Finally, the EWIF methodology was applied using CNT, DENT and SENT specimens in Mode I, which consists of crack opening under tensile stress, applied normal to the crack plane. For each ligament length, P-d curves were used to calculate the EWIF parameter [13]. The distance between grips was 50 mm. The real ligament length was measured after fracture for all test specimens using a Medilab optical microscope with a precision of $\pm 10^{-4}$ mm.

3 Results and discussion

3.1 Peeling tests

Typical P-d curves of the 180 degrees peeling test (performed at 20 mm/min) for different melt temperatures are compared in Fig. 2 (see Fig. 3A and B for a visual description of test setup and Fig. 3C and D for a visual description of the rupture of the polymer). All the curves have similar behavior at the beginning of the test (d < 15 mm), associated to the deformation of the TPV. After
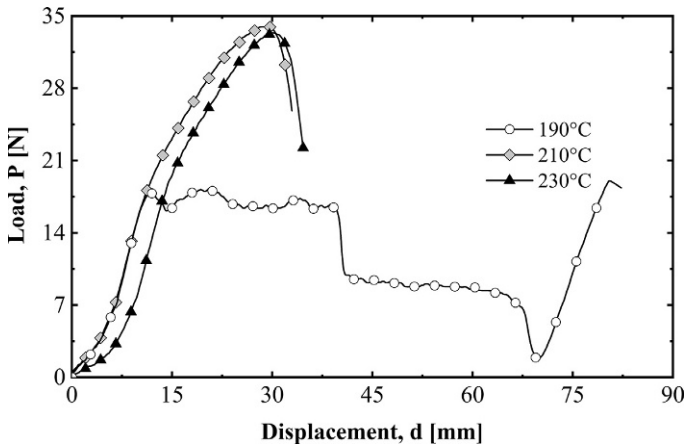
Fig. 2 Typical P-d curves for the 180 degrees peeling testing for different melt temperatures at 20 mm/min.

Visual description of peeling testing:

(A)   (B)

(C)   (D)

Fracture mechanisms:

(E)   (F)
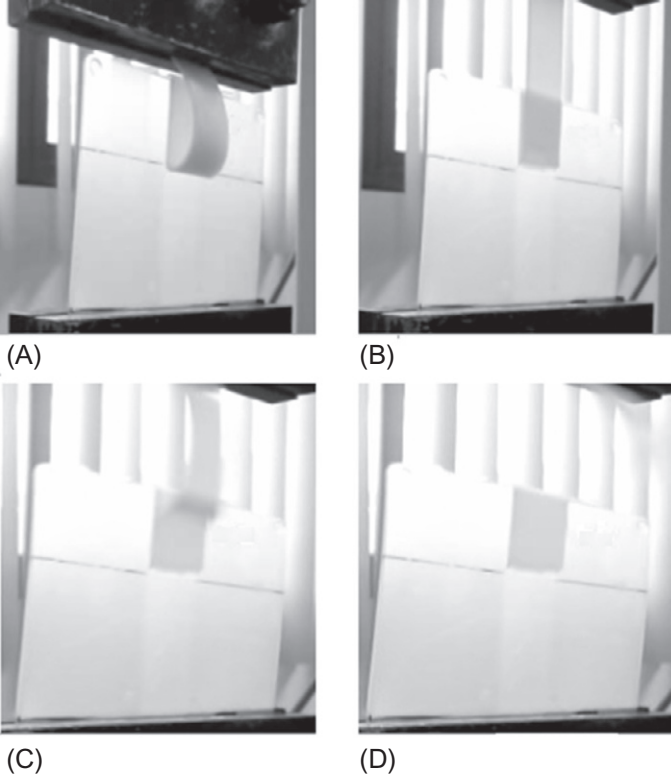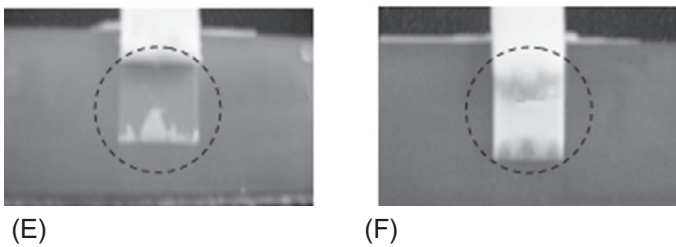
Fig. 3 Sequential pictures taken during the loading of peeling test specimen (A–D) and fracture mechanism observed: Fracture surface shown evidences of adhesive mechanisms (E) adhesive and (F) cohesive mechanisms.

that, the shape of the curve depends on the fracture mechanism. The curve for 190 °C shows a maximum load, when the fracture of the interface starts, and then the load reaches a first plateau during adhesive failure. On the other hand, at the melt temperatures of 210 °C and 230 °C the load does not reach a

plateau because adhesive and cohesive failures are taking place simultaneously. This is evidenced in Fig. 3E and F, where the fracture surfaces of the PP after conducting the 180 degrees peeling test are shown. It is clear that at the lower melt temperature (190 °C) the fracture is adhesive (Fig. 3E), whereas in the fracture surface of the specimens molded at higher melt temperatures (210 °C and 230 °C) the two fracture mechanisms (cohesive and adhesive) are present simultaneously (Fig. 3F).

After analyzing the fracture surfaces, it can be concluded that the adhesion improves with the melt temperature, as predicted, because substrate wetting and TPV diffusion are enhanced at the higher melt temperatures [13, 18, 20]. However, since the two fracture mechanisms (adhesive and cohesive) occurred at the same time it is impossible to obtain a quantitative measure of the adhesion strength using this method for the higher melt temperatures.

The results obtained from the 90 degrees peeling test were very similar to those at 180 degrees. At the lowest melt temperature the test gives good results, but at 210 °C and 230 °C the cohesive fracture mechanism takes place. Hence, it is not possible to measure the adhesion strength by this method either. Analogous results were obtained using other crosshead speeds (2 and 200 mm/min).

Based on all the above it can be concluded that the Peeling Testing is not a good test method to measure the adhesion strength of overmolded materials; variations in the fracture mechanism do not allow to quantitatively compare the adhesion strengths at different injection temperatures.

3.2 EWIF tests using DENT geometry

Lauke and Schüller [14] applied the EWIF methodology to determine the adhesive strength between two overmolded polymers. Their work was left at a very early phase; only three ligament lengths were studied using DENT geometry. However, they pre-established a technique for the application of this methodology in overmolded materials. The authors concluded that it is possible to study the adhesion strength of the interface by using EWIF parameters. At the end of the study, they recommended using more ligament lengths to obtain satisfactory results.

However, in the present work, the P-d curves of DENT specimens, presented in Fig. 4, show poor correlation between the shape of the curves and the ligament lengths (low autosimilarity). Based on experimental observations, this low autosimilarity is attributed to asymmetric crack propagation,
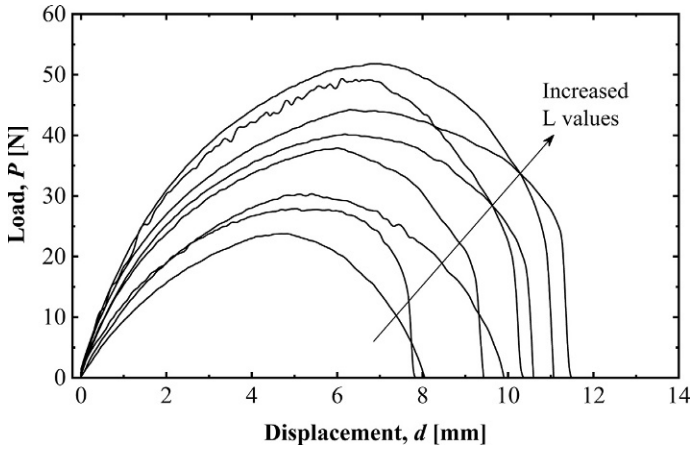
Fig. 4 Typical P-d curves of DENT test specimens at different ligament lengths (*L*). Condition: M1.

caused by aleatory irregularities in the specimen preparation (i.e. movement of the aluminum foil from its original position before or during overmolding). The poor correlation between the shape of the curves and the ligament lengths observed in Fig. 4 is also reflected in Fig. 5, where high data dispersion can be clearly observed when plotting the total work of fracture as a function of the ligament length. As a consequence, the errors associated with w_I determinations are too big to establish a clear correlation between w_I
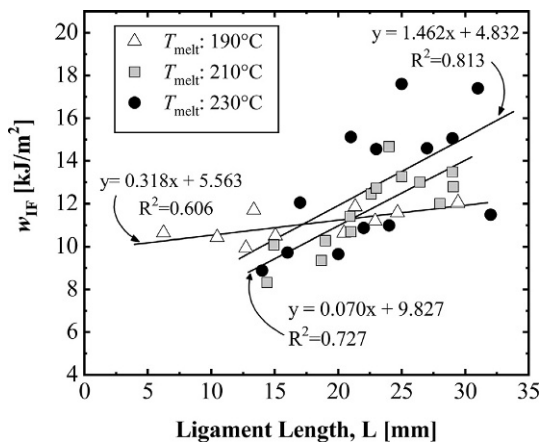
Fig. 5 Total work of interfacial fracture vs. ligament length at different melt temperatures used DENT geometry.

and the melt temperature for this geometry. Therefore, using the DENT geometry to apply EWIF is not the most recommended test method for determining the adhesion strength of overmolded materials (at least using the specimen preparation procedure described here).

3.3 EWIF tests using CNT geometry

As it is shown in Fig. 6, the crack propagation in CNT test specimens exhibits the same problem than that in the DENT specimens. It was completely asymmetric due to the difficulty to guarantee the correct position of the aluminum foil during overmolding, which results in low autosimilarity of the P–d curves obtained (not shown here). In other words, the P–d curves do not follow any trend with respect to the ligament length. Since this behavior is very similar to the one observed with the DENT specimens, at this point it is possible to conclude that this test method is not accurate either.

(A)   (B)

(C)
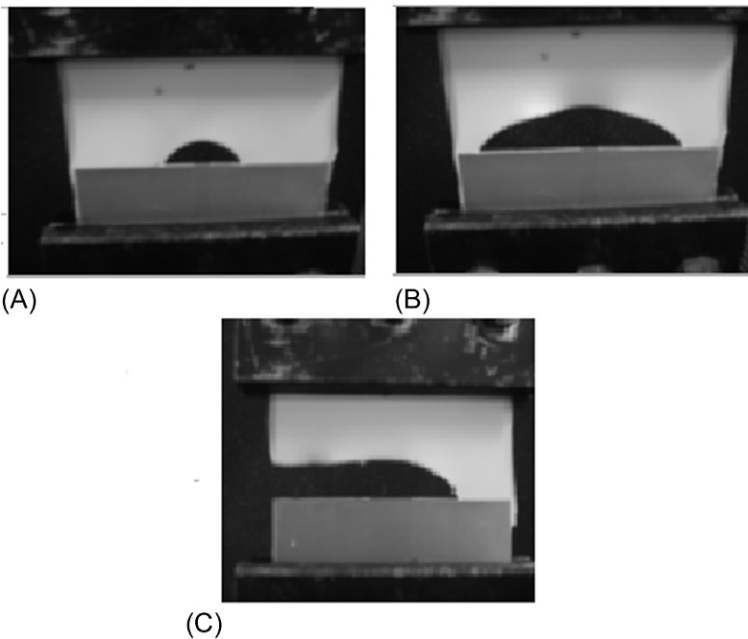
Fig. 6 Crack propagation during the EWIF-CCT testing. (A) Notch of the CNT specimen, (B) Asymmetry of the notch, and (C) Asymmetric notch rupture.

3.4 EWIF tests using SENT geometry

Due to the problems encountered using the DENT and the CNT geome-
tries (i.e. asymmetric crack growth), the SENT geometry was tested for the
EWIF measurements. This geometry has a single crack propagation front,
and in a previous work, the authors showed that it is possible to use it in
the evaluation of the adhesion strength of overmolding polymeric
systems [13].

Typical P–d curves for different ligament lengths of the SENT specimens
were presented elsewhere [13]: In contrast to the DENT specimens, SENT
specimens showed good correlation between shape of the curves and the
ligament length (high autosimilarity) for all the melt temperatures studied
(see [13] for more details about the results obtained). Also, when the EWIF
parameters are determined, the data distribution is much better than the
results obtained with the DENT specimens.

In agreement to the ESIS protocol [15], when applying conventional
EWF methodology in polymers (evaluation of bulk material), the crack
propagation must start after the ligament is fully yielded to assure failure
under pure plane stress state. In general, when DENT specimens are used,
this is favored due to symmetrical stress concentration along the ligament, a
consequence of two aligned notches. In addition, DENT specimens avoid
possible edge effects like those in the case of the SENT specimens along the
un–notched side.

However, in a previous work using SENT specimens [13] it was estab-
lished that, in overmolded materials, it is possible to use the essential param-
eter (w_I) as a quantitative adhesion energetic parameter for comparison
purposes between processing conditions, even though the aforementioned
requirement is not fulfilled in the overmolded material. Both SENT and
DENT specimens showed no-plastic deformation along the outer process
zone (surrounding the interphase) before or when crack propagation was
initiated. Furthermore, the greater amount of deformation corresponds to
the nonlinear elastic (highly recoverable and time dependant) response of
the TPV half; no plastic or even elastic deformation was observed in the
PP substrate.

Therefore, the limitations found in the evaluation of the adhesion
strength using the DENT specimens are overcome by using the SENT
geometry. So far, the measurement of the adhesion strength with SENT test
specimens applying EWIF methodology seems to be the most accurate
test method.

Barany et al. [21] mentioned in a state of art related with applications of the EWF concept for polymers, related blends and composites, that it is successfully adapted also for the qualification of welded joints of polymer/polymer systems.

3.5 Tensile tests

Another technique that has been applied to study the adhesion strength between two overmolded materials is the tensile testing. Applying this technique, Extrand and Bhatt [22] found that when the test specimen is deformed, the crack always grows normal to the applied force. In addition, the stress at break obtained for overmolded specimens is always lower than those of each material individually tested.

The adhesion strength measured with dumbell specimens was analyzed in terms of force at break. First of all, by comparing a typical P–d curve of the TPV with one of an overmolded (190 °C) test specimen (Fig. 7), it is clear that the shape of the curves are very similar, but the values of the stress and strain at break are much lower for the overmolded material, in agreement with Extrand and Bhatt [22] observations. This behavior is the result of two factors: (1) the interphase is less resistant than the bulk material, and (2) the deformation of the TPV is restricted by the interphase.

Fig. 8 shows that the force at break of the interface increases with the overmolding melt temperature. In other words, the adhesion strength of the test specimen is improved. Based on these results, the adhesion strength
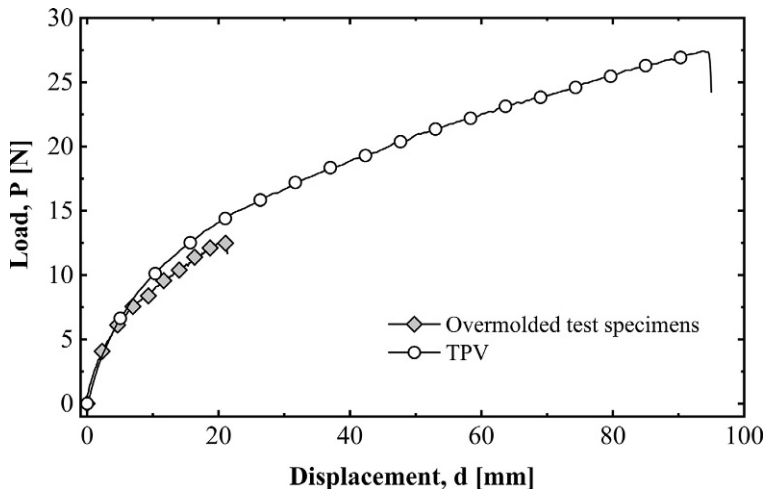
Fig. 7 Typical P-d curves of tensile testing for TPV and overmolded test specimens.
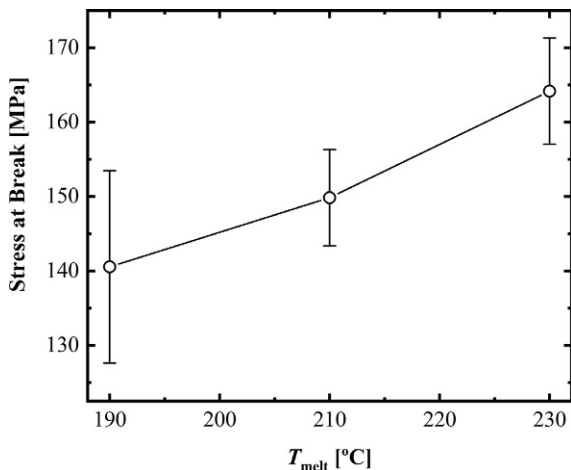
Fig. 8 Variation of the force at break (σ_b) with the TPV melt temperature (T_{melt}).

could also be measured by conventional tensile test. However, when using dumbell specimens, it is not possible to assure that the fracture occurs along the interphase, while with the SENT test specimens, the notch guarantees that the fracture takes place along the interphase rather than through the less resistant material.

In addition, when the adhesion strength is measured in terms of EWIF parameters using the SENT geometry, the results are an actual measurement of the resistance of the interphase. On the other hand, in the tensile test, the measured force at break is related not only to the interphase but also to the properties of the material being deformed, in this case the TPV.

4 Conclusions

Neither the 180 degrees nor the 90 degrees peeling testing method can be used to determine the adhesion strength of overmolded materials because at high melt temperatures the two fracture mechanisms (cohesive and adhesive) take place simultaneously. In the case of the EWIF methodology, when the test specimen has two fronts of crack propagation, the results have very high variability caused by asymmetric crack growth, so it is not possible to measure the adhesion strength with DENT or CNT specimens either (under the conditions of specimens preparation employed in this work). In future work, DENT and CNT specimens should be manufactured with symmetric crack growth, but the manufacturing would be more

complicated than the SENT specimens. The potential methods to measure the adhesion strength according to the results obtained in this work are: EWIF method using SENT specimens or tensile testing. Although, it would be interesting, in future works, to verify the accuracy of these tests using other pairs of overmolded materials.

Acknowledgments

References

[1] L. Turng, Special and emerging injection molding processes, J. Injec. Mold. Technol. 3 (5) (2001) 160–179.

[2] L.M. Arzondo, N. Pino, J.M. Carella, J.M. Pastor, J.C. Merino, J. Poveda, C. Alonso, Sequential injection overmolding of an elastomeric ethylene-octene copolymer on a polypropylene homopolymer core, Polym. Eng. Sci. 44 (11) (2004) 2110–2116.

[3] Battenfeld, HM Multipart, 2006. United States: Battenfeld Injection Technology.

[4] H. Plank, Horizontal turntable and Stackmold Technologies-Innovative Technologies in Multipart Injection Molding, SPE ANTEC Proceedings, 2002. w/p.

[5] A. Pocius, Adhesion and Adhesives Technology. An Introduction, Hanser Publishers, Cincinnati, 2002.

[6] D. Weng, J. Andries, P. Morin, K. Sauders, J. Politis, Fundamentals and material development for thermoplastic elastomer (TPE) overmolding, J. Injec. Mold. Technol. 4 (1) (2000) 22–28.

[7] S. Wu, Polymer Interface and Adhesion, Marcel Dekker, New York, 1982.

[8] V. Altstädt,in: W. Grellmann, S. Seidler (Eds.), Polymer Testing, Carl Hanser Verlag, 2007, pp. 552–554.

[9] M. Dondero, J.M. Pastor, J.M. Carella, C. Pérez, Adhesion control for injection overmolding of polypropylene with elastomeric ethylene copolymers, Polym. Eng. Sci. 49 (10) (2009) 1886–1893.

[10] A.J. Kinloch, C.C. Lau, J.G. Williams, The peeling of flexible laminates, Int. J. Fract. 66 (1) (1994) 45–70.

[11] D.R. Moore, J.G. Williams,in: D.R. Moore, A. Pavan, J.G. Williams (Eds.), Fracture Mechanics Testing Methods for Polymers, Adhesives and Composites, ESIS Publication 28, Elsevier Science, 2001, pp. 203–224.

[12] S. Nguyen, C.J. Pérez, P.M. Desimone, J.M. Pastor, J.P. Tomba, J.M. Carella, Adhesion control for injection overmolding of elastomeric propylene copolymers on polypropylene. Effects of block and random microstructures, Int. J. Adhes. Adhes. 46 (2013) 44–55.

[13] M.V. Candal, A. Gordillo, O.O. Santana, J.J. Sánchez, Study of the adhesion strength on overmoulded plastic materials using the essential work of interfacial fracture (EWIF) concept, J. Mater. Sci. 43 (15) (2008) 5052–5060.
[14] B. Lauke, T. Schüller, Essential work of interfacial fracture: a method to characterize adhesion at polymer-polymer interfaces, Int. J. Adhes. Adhes. 21 (2) (2001) 55–58.
[15] E.Q. Clutton,in: D.R. Moore, A. Pavan, J.G. Williams (Eds.), Fracture Mechanics Testing Methods for Polymers, Adhesives and Composites, ESIS Publication-28, Elsevier Science, 2001, pp. 177–195.
[16] D. Mousikus, J. Karger-Kcosis, E. Moskala, Interrelation between partitioned work of fracture parameters and the crack tip opening displacement in amorphous polyester films, J. Mater. Sci. Lett. 19 (18) (2000) 1615–1619.
[17] E.C.Y. Ching, W.K.Y. Poon, R.K.Y. Li, Y.-W. Mai, Effect of strain rate on the fracture toughness of some ductile polymers using the essential work of fracture (EWF) approach, Polym. Eng. Sci. 40 (12) (2004) 2558–2568.
[18] A.R. Carella, C. Alonso, J.C. Merino, J.M. Pastor, Sequential injection molding of thermoplastic polymers. Analysis of processing parameters for optimal bonding conditions, Polym. Eng. Sci. 42 (11) (2002) 2172–2181.
[19] Candal, M.V., Gordillo, A., Terife, G., Santana, O.O. (2007). In: Proceedings of the 65th Annual SPE Conference (PP. 620–624). Cincinnati: ANTEC.
[20] R.A. Orwoll, P.A. Arnold,in: J. Mark (Ed.), Physical properties of polymers handbook, 2007. Springer, EEUU.
[21] T. Barany, T. Czigány, J. Karger-Kocsis, Application of the essential work of fracture (EWF) concept for polymers, related blends and composites: a review, Prog. Polym. Sci. 35 (2010) 1257–1287.
[22] C.W. Extrand, S. Bhatt, The mechanical properties of insert-molded bimaterial composites, Polym. Eng. Sci. 41 (3) (2001) 373–379.

This page intentionally left blank

CHAPTER 6

Elastomeric nanocomposite foams with improved properties for extreme conditions

Hasti Bizhani[a,b], Ali Asghar Katbab[a], Raquel Verdejo[b]
[a]Department of Polymer Engineering and Color Technology, Amirkabir University of Technology, Tehran, Iran
[b]Institute of Polymer Science and Technology (ICTP-CSIC), Madrid, Spain

Contents

1 Introduction

Elastomers have found myriad uses in the industrial, transport, biomedical and electrical sectors, to name but a few. Their elasticity, resistance to abrasion and high tensile strength have made them a key material in our everyday life and, as technology improves, their uses have encountered ever more extreme conditions, such as high/low temperatures and pressures, frequency of vibration, radiation or chemical levels. Among their many applications, elastomers are the choice material in gaskets, sealants, or damping elements. However, there are countless sealing and damping jobs where solid rubber is often unable to perform effectively. For these, foamed rubber is selected because it is extremely soft and elastic, ensuring an airtight and durable seal in extreme conditions and under heavy loads. Additionally, foams strength-to-weight ratio, impact, and sound absorbing capabilities have ensured their widespread use in the transport and aeronautical sectors for improved fuel efficiency.

Foams are two–phase materials: a solid matrix, with a cellular structure, in which is dispersed a gas phase [1]. Foamed rubber, also known as cellular rubber or sponge, can be produced in a continuous extrusion process or a discontinuous molding process using traditional rubber formulations, where a blowing agent is also introduced. Foaming and vulcanization reactions have to be well adjusted to obtain either an open or closed cell system [2]. Fillers are introduced into solid and foamed rubbers to reduce cost or to modify the properties of the cured system. However, foamed rubbers usually present a considerably lower amount of reinforcing fillers than solid rubbers since they would retard, or even prevent, the expansion. Hence, the use of nanofillers can represent an advantage over traditional fillers since they require low loading fractions (less than 10 vol%) to provide comparable property enhancements than micrometer-scale fillers. Additionally, the nanofiller size represents a further advantage for the reinforcement of fine structures in which conventional fillers cannot be readily accommodated (Fig. 1).

Elastomer nanocomposites have already proved their value to improve further the initial performance of the matrix, enabling them to endure harsh environments and severe uses [3]. Even though nanocomposite foams have not been so extensively studied as solid elastomer nanocomposites, there are a number of interesting reports in the literature that have already highlighted the potential benefits of nanofillers on the foaming process, cellular structure, and properties of the final nanocomposite foams. Research on
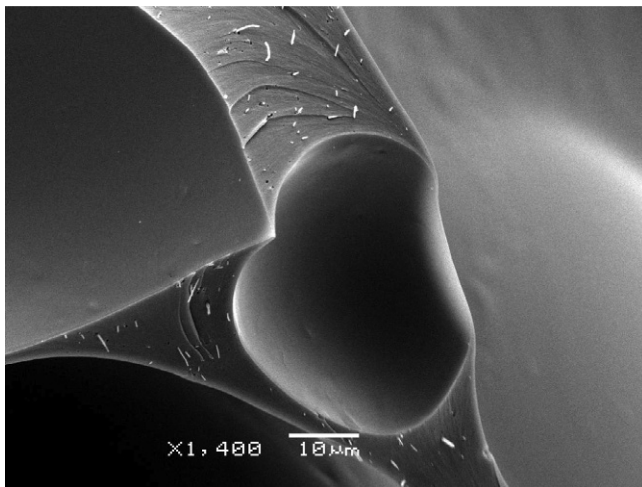
Fig. 1 Carbon nanotube reinforcement of the foam's cellular structure.

nanocomposite foams has taken advantage of the versatility of foam manufacturing and several methodologies have been pursued from the use of chemical blowing agents (CBAs) to foam high-performance thermoplastics [4], to physical foaming by supercritical carbon dioxide [5], and reactive foaming of polyurethanes and silicones [6, 7]. Nevertheless, there still are fundamental questions to be answered concerning the interaction of nanofillers with the foaming process, the resulting cellular structure, and final properties. For example, nanofiller-polymer interactions can give rise to significant changes in polymer morphology and, hence, to its rheological behavior and foaming dynamics. Research in this field should lead to fundamental knowledge and to a number of applications.

This chapter discusses two exemplary cases of rubber foams, in particular ethylene-propylene-diene terpolymer (EPDM) and silicone, since they provide an overview of the foaming processes, and they are both used in extreme environmental conditions.

2 Nanofillers

There are three major types of nanofillers, nanoparticles, rod-like, and plate-like nanofillers. The first type of nanofillers, nanoparticles, has all three dimensions at the nanometer scale, such as carbon black, silica, and quantum dots, among others. These nanofillers have been traditionally used in the composite industry; however, the current means to individually dispersed, control and modified their structure have stimulated further investigation. Rod-like nanofillers have two dimensions at the nanometer scale; examples include carbon nanofibers (CNFs) and nanotubes (CNTs), metallic nanorods, and whiskers. Arguably, CNFs and CNTs are the most widely used rod-like nanofillers in polymer nanocomposites due to their remarkable properties [8]. CNTs are cylindrical shells of one or more co-axial graphitic sheets, with diameters in the range 1–100 nm, and lengths typically on the order of tens of microns. Individual CNTs have been predicted and observed to have remarkable properties. Axial stiffness and strength are of the order of 1 TPa and 50 GPa, respectively, and densities are low (less than 2 g/cm^3). A variety of synthesis methods exist to produce CNTs that lead to a wide range of structural differences, such as their diameter, aspect ratio, crystallinity, purity, and entanglement, among others. Finally, the last nanofillers are platelet-like systems where only one of their dimensions, the thickness, is on the nanometer scale while the lateral dimensions could be in the range of several hundred nanometers to microns [9]. Smectite clay minerals,

in particular montmorillonites (MMTs), are the most representative group of this type of nanofillers. One of the strategies to improve the silicate compatibility with the polymer chains is by the organophilic modification of the internal and external cations. A second example is graphene. Graphene is a one-atom-thick planar single sheet of sp^2-bonded carbon atoms obtained in 2004 from graphite by micromechanical cleavage [10, 11]. Graphene was successfully synthesized from graphite and started to receive considerable attention [12–14]. Current strategies use traditional chemical processes [15–17] to produce graphene materials and have open new opportunities for this variety of carbons.

3 Foamed rubbers

Foams are basically produced when a gas is blown into a low viscosity matrix. Foaming reaction is commonly achieved through the thermal decomposition of CBAs, reactive foaming, or expansion of gas dissolved in the matrix. This evolution involves the interplay of several physical phenomena such as surface tension, diffusion, and viscosity. Thus, this reaction has to be well controlled in order to balance the rates of both the evolution of the gas and the increase in viscosity [18], if not, the foam will collapse. The selection of the blowing agents determines the cellular structure of the foam and, thus, its application. Closed cell foams are the preferred material for thermal insulation, seals and gaskets that protect against moisture, chemicals, UV light or ozone, dynamic shock absorbers, and packaging. Meanwhile, open cells are employed in seating, automotive trim, filters, and acoustic applications.

3.1 EPDM foams

Ethylene-propylene-diene terpolymer (EPDM) is a nonpolar synthetic rubber, which is produced by copolymerizing ethylene (45–75%) and propylene monomers (13–45%) and non-conjugated dienes [(ethylidene norbornene, dicyclopentadiene and 1,4 hexadiene), (1–11%)]. The ethylene monomer, propylene monomer, and non-conjugated diene are responsible for the load bearing, prevention of crystallinity, and providing sites for crosslinking (vulcanization), respectively. The schematic chemical structure of EPDM is shown in Fig. 2. Owing to its great resistance to ozone,

$$\left[CH_2-CH_2\right]_n\left[CH_2-\underset{CH_3}{CH}\right]_m\left[Diene\right]_o$$
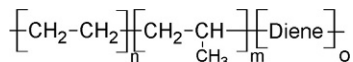
Fig. 2 Chemical structure of EPDM.

weathering, heat, water, and chemicals (acids, alkalis, polar fluids, and hot water) and excellent electrical insulation properties, EPDM has attracted considerable attention in different industries, such as gaskets, acoustic insulation, seals, weather-stripping, and pipe insulation in automotive, electric-electronic, marine and construction industries, and is a polymer of choice to withstand harsh conditions. It is worth mentioning that EPDM is the most water resistant elastomer, which makes it a great candidate for maritime applications. However, they are not compatible with mineral and synthetic di-ester lubricants, and hydrocarbon fuels and solvents.

EPDM foams are mostly prepared by the thermal decomposition of CBAs added to the formulations. Since the cellular structure is formed due to the decomposition of the blowing agent, many parameters like its content, dispersion state, and its particles size have a great impact on the foam properties. The principal CBAs are organic compounds, such as azo compounds, mostly azodicarbonamide (ADC) that decomposes between 150 °C and 210 °C, and sulfonyl hydrazide compounds, such as 4,4′-oxy-bis(benzene sulfonyl hydrazide) (OBSH) that decomposes between 95 °C and 100 °C.

The final properties of foams are greatly dependent on the achieved cellular structure, which in turns depends on the matrix characteristics, processing conditions, and dispersion and decomposition of the blowing agent. Michaeli et al. [19] fabricated foam samples based on EPDM rubber with different viscosities and ADC (as a blowing agent), and explored the effect of EPDM viscosity on the average cells size and cell density of the foams. They found that as the viscosity of EPDM rubber increased, the average cell diameter decreased. Meanwhile, Yamsaengsung et al. [20] analyzed two types of OBSH blowing agent [neat OBSH and ethylene–propylene modified OBSH (EPR-b-OBSH)] to prepare EPDM foams with closed–cell structure and investigated their effects on the cell morphology and mechanical properties. They observed that using EPR–b-OBSH increased the porosity and cell number (Fig. 3A), which was ascribed to a better dispersion within the EPDM matrix. This higher porosity led to a decrease of the tensile modulus (Fig. 3B) and an increase of the compression set with blowing agent content (Fig. 3C). Similar results have been reported by other researchers [21–23] on the effect of blowing agent loading on EPDM foams.

Wang et al. investigated the effect of foaming process temperature on the morphology of closed–cell foams. Their results revealed that increasing temperature resulted in bigger cells and decrease the foam density (See Fig. 4) [24].
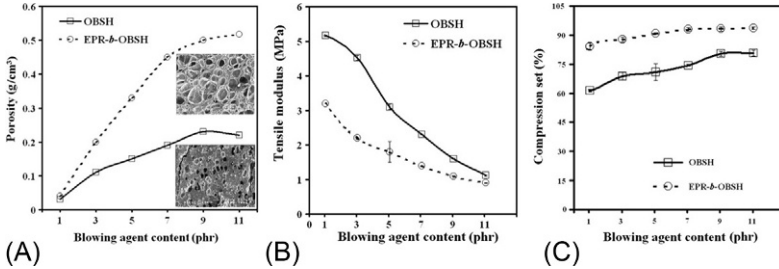
Fig. 3 Effect of blowing agent (OBSH and EPR-b-OBSH) content on: (A) porosity, (B) tensile modulus, and (C) compression set- of EPDM foams [20]. *(Reprinted from W. Yamsaengsung, N. Sombatsompop, Effect of chemical blowing agent on cell structure and mechanical properties of EPDM foam, and peel strength and thermal conductivity of wood/NR composite–EPDM foam laminates. Compos. Part B 40(7) (2009) 594–600, Copyright (2009), with permission from Elsevier.)*
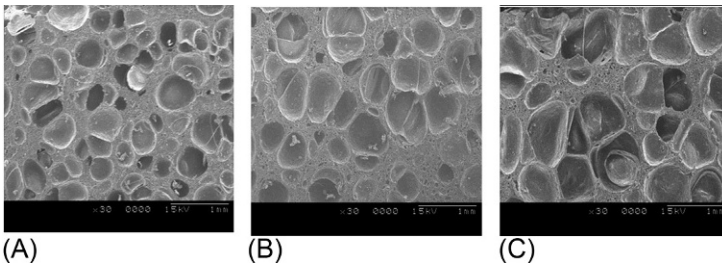
Fig. 4 Scanning electron microscope (SEM) micrographs of EPDM foams prepared at different temperatures: (A) 175 °C; (B) 185 °C; (C) 195 °C [24]. *(Reprinted from Wang, Z. Peng, Y. Zhang, Zhang Y. Study on foaming kinetics and preparation of EPDM foams. Plast. Rubber Compos. 35(9) (2006) 360–367, with permission from Taylor & Francis.)*

An effective method to control the cell size and distribution is using the pre–curing approach. Pre–curing results in higher viscosity and consequently alters the foam structure. Wang et al. studied the effect of pre–curing on the EPDM foams using ADC as a blowing agent and found that it leads to smaller cell size and more uniform cell distribution, and also increase the foam density (Fig. 5) [25].

The addition of nanofillers into EPDM foams has already shown to affect the cellular structure and enhance their final properties. Chang et al. [26] produced EPDM/organoclay foams observing a heterogeneous nucleating effect of the clay and a reduction of the cell size. Similar nucleating effect has been reported with halloysite [27] but not with carbon black [22, 23, 28]. Furthermore, Dindarloo et al. [29] studied the effect of nanofiller
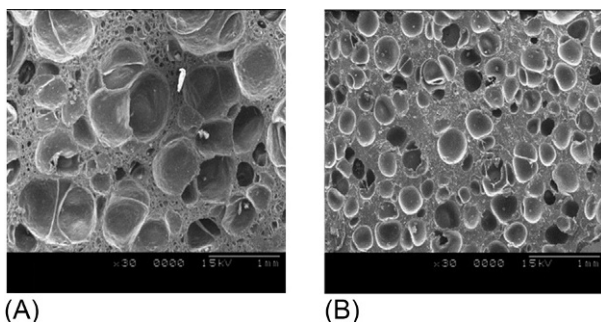
Fig. 5 Effect of pre-curing on the morphology and cell structure of EPDM foams: (A) without pre-curing and (B) with pre-curing in a HAAKE Rheometer at 80 rpm at 80°C for 15 min [25]. *(Reprinted from B. Wang, Z. Peng, Y. Zhang, Y. Zhang, Compressive response and energy absorption of foam EPDM. J. Appl. Polym. Sci. 105(6) (2007) 3462–3469, with permission of Wiley.)*

geometry on the cell structure and mechanical properties of EPDM foams. They observed that foams loaded with nanosilica (0D) had a sharp cell size distribution and larger cell size compared to CNT (1D) and nanoclay (2D). Additionally, CNT resulted in higher compression strength, modulus, and hysteresis loss (compared to nanosilica and nanoclay), which was attributed to the higher aspect ratio of CNT and more flexural restriction of it.

Recent studies have analyzed blends of EPDM with other elastomers [30–32] and blends with nanofillers [33–35]. For example, Ma et al. [32] prepared EPDM foams containing silicone rubber (SR). The addition of SR resulted in higher crosslink density of EPDM/SR blend, which improved the compression set, wear resistance, and tensile strength. Ding et al. [35] prepared EPDM/chloroprene rubber (CR) foams containing expandable graphite (EG), organic montmorillonite (OMMT), and magnesium hydrate (MH) and studied their effect on the flame-retardancy behavior. Their results indicated that thermostability and flame-retardancy performance of the EPDM foams are improved by combining all three fillers due to the formation of a rigid layer of EG particles embedded within the OMMT honeycomb structure [35].

3.2 Silicone foams

Silicone, or polyorganosiloxane, consists of alternating silicon and oxygen atoms, or siloxane units, with hydrocarbon side radicals combined directly with silicon. Thus, silicones are considered as intermediate compounds between inorganic materials, in particular silicates, and organic polymers.

The characteristics of the Si—O—Si bond, large bond length (0.163 nm) and angle (130 degrees), and bond energy (445 kJ/mol), provides silicones with high elasticity, high thermal and UV radiation stability, high weathering resistance, and good dielectric properties, as well as low temperature dependence of their physical properties and very low glass transition temperature ($T_g \approx -120\,°C$) [36–38]. The most common silicone polymer is polydimethylsiloxane (PDMS) (Fig. 6).

Silicone foams are commonly produced through reactive foaming, which involves the simultaneous foaming and polymerization of liquid reactants, presenting a liquid-solid phase transition. The foaming is driven by a gas generated as a by-product of the polymerization reaction [7]. Reactive foaming is a versatile manufacturing process as the control of parameters such as functionality, chemical composition, and molecular weight of the different reactants, produces a wide set of materials with significantly different properties [39–41]. Here, we briefly explain the basic reactions taking place during the reactive foaming of silicones. A detailed recount can be found elsewhere [2, 40, 42]. Silicone foaming is based on two simultaneous reactions, a polyaddition and a polycondensation. Foaming is the result of a condensation reaction that takes place between ≡SiOH-containing and ≡SiH-containing components in the presence of platinum, as the catalyst, with the evolution of hydrogen. The crosslinking takes place by the addition-cure reaction of vinyl-endblocked groups with Si—H groups (Fig. 7) [2]. Commercially available silicone foam reactants are generally supplied as a two-part system; one component consists of the ≡SiH- plus cross-linker and the second component consist of the ≡SiOH- plus catalyst. One practical way in which to improve the stability of reactive foams is to increase the bulk viscosity of the reactants or the surface viscosity of the gas-liquid interface through a colloidal suspension of solid particles [43]. These dispersed (nano)particles can also act as nucleation sites for bubbles in the early stages of the process and as functional fillers for the final foam.

Additionally, physical foaming methods are also used minority to produce silicone foams such as phase separation, supercritical carbon dioxide,
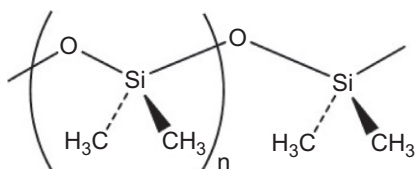
Fig. 6 Chemical structure of PDMS.

$$R_1 - \begin{bmatrix} H \\ | \\ Si - O \\ | \\ CH_3 \end{bmatrix}_n - R_3 + OH - \begin{bmatrix} CH_3 \\ | \\ Si - O \\ | \\ CH_3 \end{bmatrix}_m - H \xrightarrow{Pt} R_1 - Si - O - \begin{bmatrix} H \\ | \\ Si - O \\ | \\ CH_3 \end{bmatrix}_{n-1} - R_2 + H_2 \uparrow \quad (1)$$

where the top substituent is $O - \begin{bmatrix} CH_3 \\ | \\ Si - O \\ | \\ CH_3 \end{bmatrix}_m - H$ and the central Si bears CH_3.

$$R_1 - \begin{bmatrix} H \\ | \\ Si - O \\ | \\ R_2 \end{bmatrix}_x - R_3 + CH_2 = CH - \begin{bmatrix} R_4 \\ | \\ Si - O \\ | \\ R_5 \end{bmatrix}_y CH = CH_2 \xrightarrow{Pt}$$

$$CH_2 - CH_2 - \begin{bmatrix} R_4 \\ | \\ Si - O \\ | \\ R_5 \end{bmatrix}_y - CH = CH_2$$

$$R_1 - \begin{bmatrix} Si - O \\ | \\ R_2 \end{bmatrix}_x - R_3 \quad (2)$$
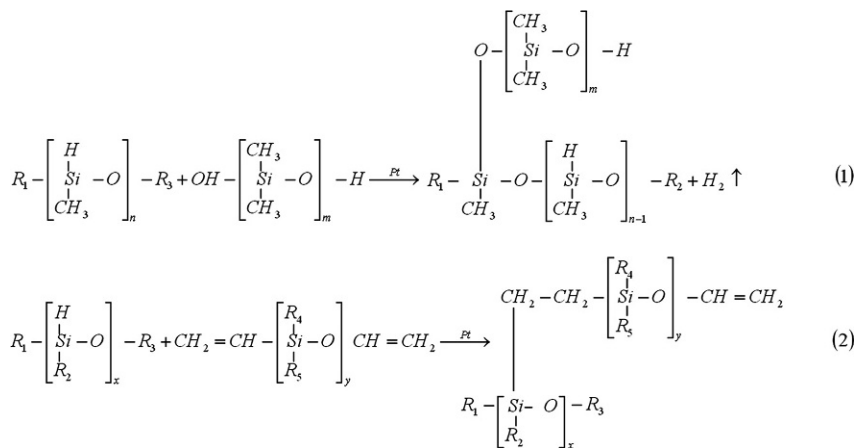
Fig. 7 Basic chemistry of reactive silicone foams: blowing (1) and gelling (2) reactions. *(Reproduced from R. Verdejo, F. Barroso-Bujans, M.A. Rodriguez-Perez, J.A. de Saja, M.A. Lopez-Manchado. Functionalized graphene sheet filled silicone foam nanocomposites. J. Mater. Chem. 18(19) (2008) 2221–2226, with permission of The Royal Society of Chemistry.)*

emulsions and sacrificial models, and syntactic balloons [44–50]. The reader can find further information on the manufacturing processes used in the development of cellular silicone in a recent review [42].

Verdejo et al. [12, 51–53] were among the first authors to use carbon-based nanoparticles, particularly CNTs and functionalized graphene sheets, which are now termed thermally reduced graphene oxide, in reactive silicone foams. The authors studied the effect of the nanoparticles on the foaming, cellular structure, and thermal and flammability characteristics of the developed systems.

The use of nanoparticles has shown to improve thermal degradation by delaying the onset of degradation and shifting the degradation temperature to higher temperatures [54]. Verdejo et al. [12, 51, 52] reported a noticeable increase of the decomposition temperature of more than 50 °C, the thermal conductivity by up to 6% and the normalized modulus of more than 200%. Vertical fire conditions indicated that the CNT filled silicone foams may be classified as self-extinguishing, as the limiting oxygen index increased from 20.5 ± 0.5 for the control sample to 30 ± 0.5 oxygen content for the 1 wt% CNT sample [51]. These results were attributed to the formation of a CNT network throughout the sample (Fig. 8) via non–covalent CH-π interactions and to the surface tension of the gas–polymer interface during foaming.
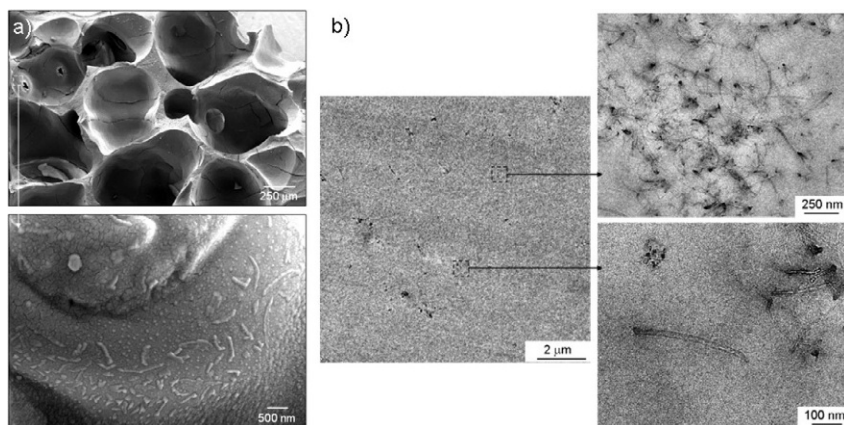
Fig. 8 (A) SEM images of silica residue after thermogravimetric analysis (TGA) with CNTs lying on the gas-polymer interface and (B) transmission electron microscope (TEM) images of the CNT network formed in CNT/silicone foams [51]. *(Reproduced R. Verdejo, F. Barroso-Bujans, M.A. Rodriguez-Perez, J.A. de Saja, M. Arroyo, M.A. Lopez-Manchado, Carbon nanotubes provide self-extinguishing grade to silicone-based foams. J. Mater. Chem. 18(33) (2008) 3933–3939, with permission of The Royal Society of Chemistry.)*

Recently, a thermally and electrically conductive graphene foam was produced through filtration of low viscosity PDMS in a commercially available graphene foam (Fig. 9) [55]. The authors reported a highly efficient – current–induced heating and de-icing capabilities, with improvements of 477% de-icing efficiency as compared to previously reported high carbon-based nanofiller containing systems. Additionally, they reported a good reproducibility of the electrothermal behavior after 100 cycles of loading-unloading current.

Piperopoulos et al. [56, 57] have looked at oil recovery performance of reactive silicone foams filled with CNT of four commonly used oils (kerosene, pump oil, naphtha, and crude oil). They reported comparable results of sorption capacity of their system but a better reusability (up to 10 times).

Several authors have studied the sensing capabilities of these silicone nanocomposites foams [58–63]. Among them, Dusek et al. [59] reported the sensing capacities of a reactive foam filled with carbon black for marine vehicles where there is a need for saline waterproof, and conformal system. The response of the sensor array was characterized underwater using periodic hydrodynamic pressure stimuli from vertical plunging and surface water waves and observed a pressure sensitivity on the order of 5 Pa and dynamic range of 50–500 Pa.
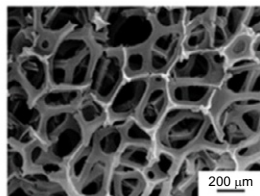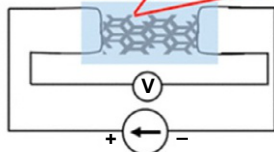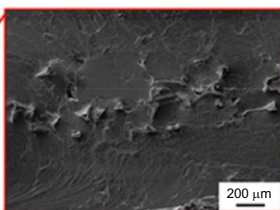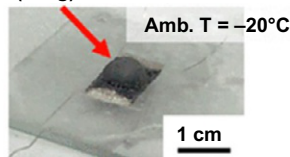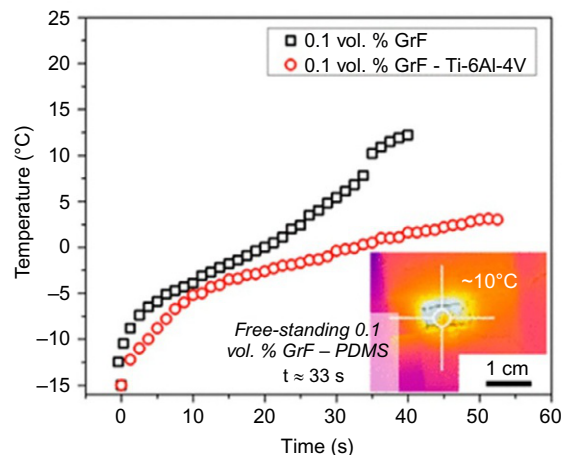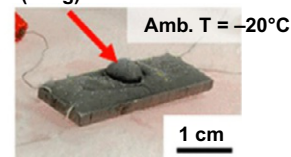
Fig. 9 (Left) Schematic representation of the preparation of multifunctional graphene foam-PDMS composite. The inset shows fracture surface morphology of GrF-PDMS. (Right) Photograph of current induced de-icing experiments at −20 °C on free-standing GrF-PDMS composite and GrF-PDMS composite as a coating on a Ti-6Al-4V substrate. Heating profiles of 0.1 vol% GrF composites during de-icing experiments with a thermal image at $t = 33$ s [55]. *(Reprinted with permission from J. Bustillos, C. Zhang, B. Boesl, A. Agarwal, Three-Dimensional Graphene Foam-Polymer Composite with Superior Deicing Efficiency and Strength. ACS Appl. Mater. Interfaces 10(5) (2018) 5022–5029. Copyright (2018) American Chemical Society.)*

4 Conclusions

The reviewed literature has clearly established the potential of elastomeric nanocomposite foams for an ever increasing range of applications and conditions. Significant progress has been made in understanding the property-morphology correlations, but there are still many fundamental issues to be explored. The development of new products would be of great benefit to both industry and, of course, to the public who would have access to improved products.

Acknowledgments

References

[1] D. Klempner, V. Sendijarevic, Handbook of Polymeric Foams and Foam Technology, second ed., Hanser Publishers, Munich, 2004.

[2] R.F. Mausser, Latex foam and sponge, in: D. Klempner, V. Sendijarevic (Eds.), Handbook of Polymeric Foams and Foam Technology, second ed., Hanser Publishers, 2004, pp. 367–378.

[3] L. Valentini, M.A. Lopez-Manchado, Rubber nanocomposites for extreme environments: critics and counterintuitive solutions, Front. Mater. 5 (49) (2018).

[4] P. Werner, R. Verdejo, F. Wollecke, V. Altstadt, J. Sandler, M.S.P. Shaffer, Carbon nanofibers allow foaming of semicrystalline poly(ether ether ketone), Adv. Mater. 17 (23) (2005) 2864–2869.

[5] J.M. Thomassin, C. Pagnoulle, L. Bednarz, I. Huynen, R. Jerome, C. Detrembleur, Foams of polycaprolactone/MWNT nanocomposites for efficient EMI reduction, J. Mater. Chem. 18 (7) (2008) 792–796.

[6] X. Cao, L.J. Lee, T. Widya, C. Macosko, Polyurethane/clay nanocomposites foams: processing, structure and properties, Polymer 46 (3) (2005) 775–783.

[7] R. Verdejo, M.M. Bernal, L.J. Romasanta, F.J. Tapiador, M.A. Lopez-Manchado, Reactive nanocomposite foams, Cell. Polym. 30 (2) (2011) 45–62.

[8] V.N. Popov, Carbon nanotubes: properties and application, Mater. Sci. Eng. R 43 (2004) 61–102.

[9] A. Okada, A. Usuki, Twenty years of polymer–clay nanocomposites, Macromol. Mater. Eng. 291 (2006) 1449–1476.

[10] N.A. Kotov, Carbon sheet solutions, Nature 442 (2006) 254.

[11] K.S. Novoselov, A.K. Geim, S.V. Morozov, D. Jiang, Y. Zhang, S.V. Dubonos, et al., Electric field effect in atomically thin carbon films, Science 306 (5696) (2004) 666–669.

[12] R. Verdejo, F. Barroso-Bujans, M.A. Rodriguez-Perez, J.A. de Saja, M.A. Lopez-Manchado, Functionalized graphene sheet filled silicone foam nanocomposites, J. Mater. Chem. 18 (19) (2008) 2221–2226.

[13] T. Ramanathan, A.A. Abdala, S. Stankovich, D.A. Dikin, M. Herrera-Alonso, R. D. Piner, et al., Functionalized graphene sheets for polymer nanocomposites, Nat. Nanotechnol. 3 (6) (2008) 327–331.

[14] O.C. Compton, S.T. Nguyen, Graphene oxide, highly reduced graphene oxide, and graphene: versatile building blocks for carbon-based materials, Small 6 (6) (2010) 711–723.

[15] B.C. Brodie, On the atomic weight of graphite, Philos. Trans. R. Soc. Lond. (1776–1886) 149 (1) (1859) 249–259.

[16] L. Staudenmaier, Verfahren zur darstellung der graphitsaure, Ber. Dtsch. Chem. Ges. 31 (1898) 1481–1499.

[17] W.S. Hummers Jr., R.E. Offeman, Preparation of graphitic oxide, J. Am. Chem. Soc. 80 (6) (1958) 1339.

[18] J.H. Saunders, R.H. Hansen, The mechanism of foam formation, in: K.C. Frisch, J. H. Saunders (Eds.), Plastics Foams, Marcel Dekker, New York, 1972.

[19] W. Michaeli, C. Hopmann, U. Masberg, S. Sitz, Determination of the expansion process of cellular rubber materials, Cell. Polym. 30 (4) (2011) 215.

[20] W. Yamsaengsung, N. Sombatsompop, Effect of chemical blowing agent on cell structure and mechanical properties of EPDM foam, and peel strength and thermal conductivity of wood/NR composite–EPDM foam laminates, Compos. Part B 40 (7) (2009) 594–600.

[21] B. Wang, Z. Peng, Y. Zhang, Y. Zhang, Rheological properties and foam processibility of precured EPDM, J. Appl. Polym. Sci. 101 (5) (2006) 3387–3394.

[22] K. Guriya, D. Tripathy, Morphology and physical properties of closed-cell microcellular ethylene–propylene–diene terpolymer (EPDM) rubber vulcanizates: effect of blowing agent and carbon black loading, J. Appl. Polym. Sci. 62 (1) (1996) 117–127.

[23] K. Guriya, D. Tripathy, Dynamic viscoelastic properties of carbon black loaded closed-cell microcellular ethylene-propylene-diene rubber vulcanizates: effect of blowing agent, temperature frequency, and strain, J. Appl. Polym. Sci. 61 (5) (1996) 805–813.

[24] B. Wang, Z. Peng, Y. Zhang, Y. Zhang, Study on foaming kinetics and preparation of EPDM foams, Plast. Rubber Compos. 35 (9) (2006) 360–367.

[25] B. Wang, Z. Peng, Y. Zhang, Y. Zhang, Compressive response and energy absorption of foam EPDM, J. Appl. Polym. Sci. 105 (6) (2007) 3462–3469.

[26] Y.-W. Chang, S. Kim, S.C. Kang, S.-Y. Bae, Thermomechanical properties of ethylene-propylene-diene terpolymer/organoclay nanocomposites and foam processing in supercritical carbon dioxide, Korean J. Chem. Eng. 28 (8) (2011) 1779–1784.

[27] K. Lee, Y.W. Chang, S.W. Kim, Ethylene–propylene-diene terpolymer/halloysite nanocomposites: thermal, mechanical properties, and foam processing, J. Appl. Polym. Sci. 131 (11) (2014).

[28] S. Mahapatra, D. Tripathy, Morphology and physico-mechanical properties of closed cell microcellular EPDM rubber vulcanizates: effect of conductive carbon black and blowing agent, Cell. Polym. 23 (3) (2004) 127–144.

[29] A.S. Dindarloo, M. Karrabi, H.R. Ghoreishy, Effect of different types of nanoparticles on the morphology and mechanical properties of EPDM foam, Cell. Polym. 36 (3) (2017).

[30] C. Lewis, Y. Rodlum, B. Misaen, S. Changchum, G. Sims, Effect of compound formulation and processing conditions on properties of extruded EPDM and NR/EPDM foams, Cell. Polym. 22 (1) (2003) 43–56.

[31] X. Zhang, D. Tian, W. Zhang, J. Zhu, C. Lu, Morphology, foaming rheology and physical properties of ethylene–propylene diene rubber/ground tyre rubber (GTR) composite foams: effect of mechanochemical devulcanisation of GTR, Prog. Rubber Plast. Recycl. Technol. 29 (2) (2013) 81.

[32] J. Ma, C. Bian, C. Xue, F. Deng, Wear-resistant EPDM/silicone rubber foam materials, J. Porous. Mater. 23 (1) (2016) 201–209.

[33] M. Keramati, I. Ghasemi, M. Karrabi, H. Azizi, Production of microcellular foam based on PP/EPDM: the effects of processing parameters and nanoclay using response surface methodology, E-Polymers 12 (1) (2012).

[34] M. Keramati, I. Ghasemi, M. Karrabi, H. Azizi, Microcellular foaming of PP/EPDM/organoclay nanocomposites: the effect of the distribution of nanoclay on foam morphology, Polym. J. 44 (5) (2012) 433.

[35] Z. Ding, Y. Li, M. He, W. Wang, C. Wang, The combination of expandable graphite, organic montmorillonite, and magnesium hydrate as fire-retardant additives for ethylene–propylene–diene monomer/chloroprene rubber foams, J. Appl. Polym. Sci. 134 (23) (2017).

[36] E. Yilgör, I. Yilgör, Silicone containing copolymers: synthesis, properties and applications, Prog. Polym. Sci. 39 (2014) 1165–1195.

[37] S.K. Srivastava, B. Pradhan, Developments and properties of reinforced silicone rubber nanocomposites, in: A. Tiwari, M.D. Soucek (Eds.), Concise Encyclopedia of High Performance Silicones, Wiley-Scrivener, Hoboken, NJ, 2014, , pp. 85–110.

[38] H.-H. Moretto, M. Schulze, W.G. Silicones, Ullmann's Encyclopedia of Industrial Chemistry, Wiley-VCH, Weinheim, 2005.

[39] J.H. Saunders, D. Klempner, Fundamentals of Foam Formation, second ed., Hanser Publishers, Munich, 2004.

[40] R. Herrington, R. Broos, P. Knaub, Flexible Polyurethane Foams, second ed., Hanser Publishers, Munich, 2004.

[41] J.K. Backus, Rigid Polyurethane Foams, second ed., Hanser Publishers, Munich, 2004.

[42] T. Métivier, P. Cassagnau, New trends in cellular silicone: innovations and applications, J. Cell. Plast. (2018).

[43] D.L. Schmidt, Nonaqueous foams, in: R.K. Prud'homme, S.A. Khan (Eds.), Foams: Theory, Measurements and Applications, CRC Press, New York, 1996, , pp. 287–314.

[44] I.K. Hong, S. Lee, Microcellular foaming of silicone rubber with supercritical carbon dioxide, Korean J. Chem. Eng. 31 (1) (2014) 166–171.

[45] X. Liao, H. Xu, S. Li, C. Zhou, G. Li, C.B. Park, The effects of viscoelastic properties on the cellular morphology of silicone rubber foams generated by supercritical carbon dioxide, RSC Adv. 5 (129) (2015) 106981–106988.

[46] M. Tebboth, Q. Jiang, A. Kogelbauer, A. Bismarck, Inflatable elastomeric macroporous polymers synthesized from medium internal phase emulsion templates, ACS Appl. Mater. Interfaces 7 (34) (2015) 19243–19250.

[47] Q. Yang, H. Yu, L. Song, Y. Lei, F. Zhang, A. Lu, et al., Solid-state microcellular high temperature vulcanized (HTV) silicone rubber foam with carbon dioxide, J. Appl. Polym. Sci. 134 (20) (2017).

[48] A.S. Alex, D. Thomas, S.K. Manu, N. Sreenivas, V. Sekkar, C. Gouri, Addition-cure, room temperature vulcanizing silicone elastomer based syntactic foams with glass and ceramic microballoons, Polym. Bull. 75 (2) (2018) 747–767.

[49] B. Xiang, Y. Jia, T. Liu, S. Luo, Preparation of silicone rubber foams with bi-modal cells, Gongneng Cailiao/J. Funct. Mater. 49 (9) (2018) 09195–201 and 206.

[50] P. Mazurek, B.E.F. Ekbrant, F.B. Madsen, L. Yu, A.L. Skov, Glycerol-silicone foams—tunable 3-phase elastomeric porous materials, Eur. Polym. J. 113 (2019) 107–114.

[51] R. Verdejo, F. Barroso-Bujans, M.A. Rodriguez-Perez, J.A. de Saja, M. Arroyo, M.A. Lopez-Manchado, Carbon nanotubes provide self-extinguishing grade to silicone-based foams, J. Mater. Chem. 18 (33) (2008) 3933–3939.

[52] R. Verdejo, C. Saiz-Arroyo, J. Carretero-Gonzalez, F. Barroso-Bujans, M.A. Rodriguez-Perez, M.A. Lopez-Manchado, Physical properties of silicone foams filled with carbon nanotubes and functionalized graphene sheets, Eur. Polym. J. 44 (9) (2008) 2790–2797.

[53] R. Verdejo, F.J. Tapiador, L. Helfen, M.M. Bernal, N. Bitinis, M.A. Lopez-Manchado, Fluid dynamics of evolving foams, Phys. Chem. Chem. Phys. 11 (46) (2009) 10860–10866.

[54] M. Moniruzzaman, K.I. Winey, Polymer nanocomposites containing carbon nanotubes, Macromolecules 39 (16) (2006) 5194–5205.

[55] J. Bustillos, C. Zhang, B. Boesl, A. Agarwal, Three-dimensional graphene foam-polymer composite with superior deicing efficiency and strength, ACS Appl. Mater. Interfaces 10 (5) (2018) 5022–5029.

[56] E. Piperopoulos, L. Calabrese, E. Mastronardo, S.H. Abdul Rahim, E. Proverbio, C. Milone, Assessment of sorption kinetics of carbon nanotube-based composite foams for oil recovery application, J. Appl. Polym. Sci. (14) (2019) 136.

[57] E. Piperopoulos, L. Calabrese, E. Mastronardo, E. Proverbio, C. Milone, Synthesis of reusable silicone foam containing carbon nanotubes for oil spill remediation, J. Appl. Polym. Sci. 135 (14) (2018).

[58] F. Cellini, S.D. Peterson, M. Porfiri, Highly compressible fluorescent particles for pressure sensing in liquids, Appl. Phys. Lett. 110 (22) (2017).

[59] J.E. Dusek, M.S. Triantafyllou, J.H. Lang, Piezoresistive foam sensor arrays for marine applications, Sensors Actuators A Phys. 248 (2016) 173–183.

[60] B. Hao, L. Mu, Q. Ma, S. Yang, P.C. Ma, Stretchable and compressible strain sensor based on carbon nanotube foam/polymer nanocomposites with three-dimensional networks, Compos. Sci. Technol. 163 (2018) 162–170.

[61] Y. Luo, Q. Xiao, B. Li, A stretchable pressure-sensitive array based on polymer matrix, Sensors 17 (7) (2017).

[62] A. Rinaldi, A. Tamburrano, M. Fortunato, M.S. Sarto, A flexible and highly sensitive pressure sensor based on a PDMS foam coated with graphene nanoplatelets, Sensors 16 (12) (2016).

[63] R. Xu, D. Wang, H. Zhang, N. Xie, S. Lu, K. Qu, Simultaneous detection of static and dynamic signals by a flexible sensor based on 3d graphene, Sensors (Basel) 17 (5) (2017).

This page intentionally left blank

CHAPTER 7

Thermal, electrical, and sensing properties of rubber nanocomposites

Héctor Aguilar-Bolados[a], Mehrdad Yazdani-Pedram[b], Raquel Verdejo[c]
[a]Faculty of Physical Sciences and Mathematics, University of Chile, Santiago, Chile
[b]Faculty of Chemical and Pharmaceutical Sciences, University of Chile, Santiago, Chile
[c]Institute of Polymer Science and Technology (ICTP-CSIC), Madrid, Spain

Contents

1 Introduction

Few materials have gained such importance as elastomer composites. Elastomer compounds are present in almost all human activities. Indeed, elastomer pieces and parts are used in countless devices, instruments, equipment and machines in the household, industrial, biomedical, technological and scientific fields. The importance of these materials rests on their excellent balance of useful properties, the most important being elasticity and resilience, good electrical insulation and thermal stability, among others. Elastomers have been traditionally filled with a number of fillers, such as silica or carbon black, chemical reagents such as crosslinking agents, accelerators or degradation retardants, to obtain the desired properties. The advent of nanotechnology has broadened the understanding of the nature of the elastomer properties and has enabled the development of new types of elastomer composites. Likewise, new types of fillers have been developed as a consequence of the advance in new syntheses routes and characterization of different organic and inorganic nanoparticles. Among them, the carbon-based nanoparticles, i.e. fullerenes, nanotubes, graphene materials and nano-diamond have taken the prominent position as functional fillers in elastomer matrices. The outstanding mechanical, electrical and thermal properties of these carbon-based nanoparticles are the main reason of the current interests of the scientific community.

Several polymorph structures can be arranged by carbon, which is attributed to the fact that carbon atoms can present three hybridization states of their valence orbitals, sp^3, sp^2 and sp. In the literature, numerous structures of carbon are referred or classified as carbon allotropes. However, this terminology (allotrope) should be used in a thermodynamic sense. Meanwhile, the type of hybridization of the valence orbitals should be described as carbon polymorphs. Only three types of carbon polymorphs are composed exclusively by atoms that present the same valence orbitals hybridization, i.e. (i) diamond, composed by sp^3-hybridized carbon; (ii) graphite, composed by sp^2-hybridized carbon, and (iii) Carbyne, composed by sp-hybridized carbon. In this context, R.B. Heimann and co-workers have suggested a classification scheme based on valence orbital hybridization (Fig. 1). The scheme consists in a triangle in which each vertex corresponds to a valence orbital hybridization. Along each side of the triangle, the transition phases are arranged, while those polymorphs that have contribution from the three types of valence orbital hybridization are displayed inside of the triangle.
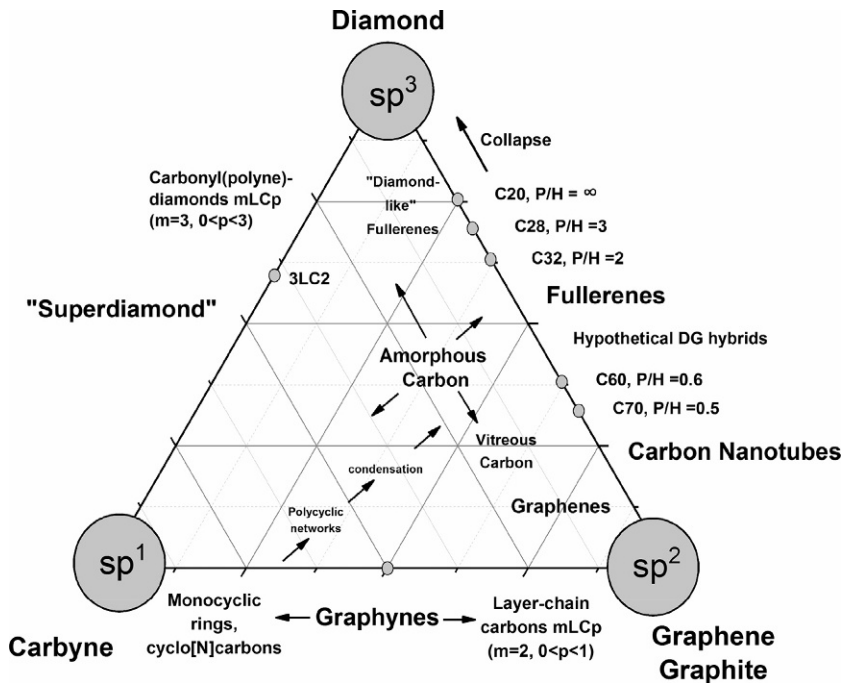
Fig. 1 Ternary "Phase" diagram of carbon allotropes. *Reprinted from R.B. Heimann, S.E. Evsvukov, Y. Koga, Carbon allotropes: a suggested classification scheme based on valence orbital hybridization, Carbon 35(10–11) (1997) 1654–1658, Copyright (1997), with permission from Elsevier.*

The type of hybridization of the valence orbitals not only has an effect on the crystallography of the polymorph, but also on their bulk properties. For instance, the hardness and thermal and electrical conductivity of sp^3 polymorphs are different from those of sp^2 polymorphs; diamond is among the hardest known materials while graphite is among the softest, to name an example.

From a general point of view, the electronic band structure of solids has an impact on the electronic properties of these materials. Namely, the energy difference between the lowest point of conduction band and the highest point of valence band, which is known as bandgap, defines if a material is metalic, semimetalic, semiconductor or insulating [1]. In metals and semimetallic materials, the valence and conduction bands overlap, but the overlapping area in semimetals is smaller than in metal. Semiconductor materials have a small band gap so that electrons can be easily promoted from one state to another by thermal or optical excitation. Meanwhile, insulating materials

have a much greater band gap restricting the transition of electrons to the conduction band. In carbon–based nanomaterials, the energy gap differs depending on the type of valence orbital hybridization.

2 Electronic structure and properties of sp^2 and sp^3 hybridized carbon based-nanomaterials

Most of the studies on carbon-based materials/elastomer nanocomposites are aimed at obtaining materials with superior transport properties. Hence, the most relevant fillers to confer such functionalities to elastomer nanocomposites are carbon–based materials; in particular, graphene materials, carbon nanotubes and CVD diamond nanoparticles. These nanofillers present outstanding properties where their structure plays a crucial role.

2.1 Graphene

Graphene is a sp^2-hybridized carbon structure, which presents several outstanding properties. Among them are its high charge mobility at room temperature, of the order of $200,000 \, cm^2 \, V^{-1} \, s^{-1}$ [2], and its high thermal conductivity, with values between 2000 and $4000 \, Wm^{-1} \, K^{-1}$ [3–6]. Although these properties have been measured only a few years ago, graphene has been a hot topic of research among theoretical physicist for several decades. The first research related to graphene was carried out in 1947, when Phillip Russell Wallace reported a model for graphite [7]. Nevertheless, the graphene was experimentally isolated in 2004 by physicists Konstantin Novoselov and Andre Geim [8].

Graphene unit cell is composed of two carbon atoms, which can be viewed as formed by two sub-lattices (See Fig. 2A and B). In these sub-lattices two of six atoms that are positioned at apexes of hexagons are located, which constitute the hexagonal long-range graphene network [9, 10]. These carbon atoms are linked to each other by three σ bonds, which has trigonal disposition. The σ bondings are formed by sp^2 hybrid orbitals, which are composed by the superposition of s, p$_x$ and p$_y$ orbitals. The unhybridized p$_z$ orbital remains perpendicular to those sp^2 hybrid orbitals and overlaps with other p$_z$ orbitals of the neighboring carbon atoms to form π bonds. These bonds form a π system that leads to the delocalization of electrons, similar to aromatic systems such as benzene, naphthalene, anthracene or pyrene.

The band structure of graphene can be described by a simple tight-binding approximation of π bands, where sigma bands have a negligible
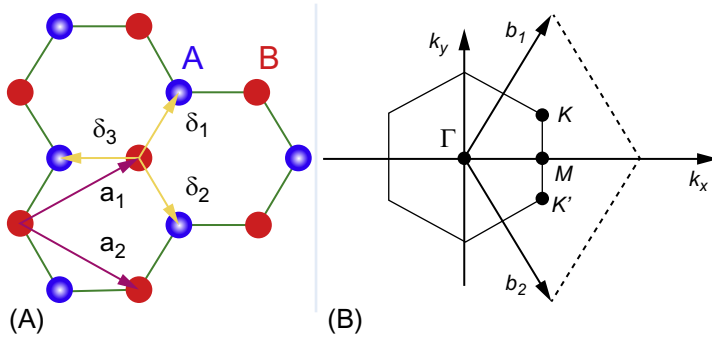
Fig. 2 (A) Honeycomb structure of graphene [3]. (B) Brillouin zone corresponding to each graphene unit. *Reprinted from J. Wang, F. Ma, W. Liang, M. Sun, Electrical properties and applications of graphene, hexagonal boron nitride (h-BN), and graphene/ h-BN heterostructures. Mater. Today Phys. 2 (2017) 6–34, Copyright (2017), with permission from Elsevier.*
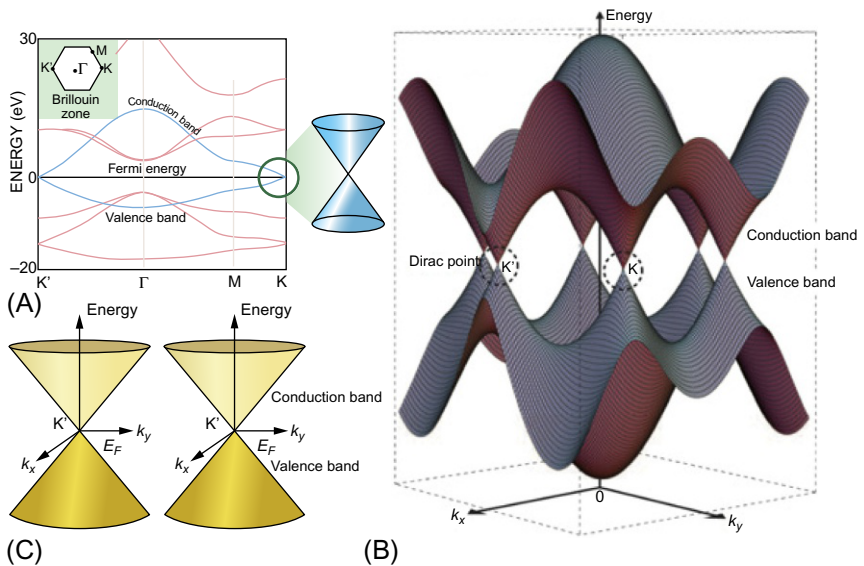
Fig. 3 Band structure near the Fermi level of graphene. (A) 2D schematic diagram, (B) 3D schematic diagram, and (C) Dirac cone of K and K_0, which correspond to the Fermi level of (B). *Reprinted from J. Wang, F. Ma, W. Liang, M. Sun, Electrical properties and applications of graphene, hexagonal boron nitride (h-BN), and graphene/h-BN heterostructures. Mater. Today Phys. 2 (2017) 6–34, Copyright (2017), with permission from Elsevier.*

influence on the electronic properties of graphene, since they are completely filled and have a large difference of energy with the Fermi level (Fig. 3). Thus, the unusual electronic structure is dominated by the long-range

graphene network. At a corner of the hexagonal first Brillouin zone, the π conduction band and π valence band are in contact but not overlap. These points, denoted as K and K′, are referred as Dirac points, since the electronic Hamiltonian that describes the low energy structure of graphene can be expressed using the Dirac equation for massless relativistic particles as $H = v_F \sigma \hbar k$, where v_F is the Fermi velocity in graphene, σ is a spinor-like wavefunction and k the wavevector of the electron. As a consequence, the electrons are free to move as particles of zero mass through the two dimensional electron system. It has been proven that the conductivity of graphene never falls below a minimum value corresponding to the quantum unit of conductance, even when concentrations of charge carriers tend to zero [11]. At room temperature, the carrier mobility in graphene can reach $15{,}000 \, cm^2 V^{-1} \, s$ [12]. It is important to mention that in this two dimensional electron system, the scattering of electrons is hampered; consequently, the average of free path of electron can reach values near $1 \, \mu m$ [13, 14]. The outstanding properties of graphene are undoubtedly the main reason for this material to be the subject of unprecedented interest in many research areas and, in particular, in elastomer composites.

The main challenge that aroused with the discovering of graphene was the development of a reliable method for its production at large scale. While several synthetic methods have been reported in the literature [15–19], the thermal reduction of graphene oxide has become one of the most feasible methods for the production of graphene, since it is easy to handle and to scale up [20]. This method consists in the thermal reduction and expansion of graphene oxide, which is obtained by the oxidation of graphite. The classical chemical processes to obtain graphene oxide are the Brödie's, Tour's and Hummers' methods [21–23], where the latter is considered as the most reliable method due to its simplicity, speed and unrestricted access to reagents necessary for the oxidation reaction. Furthermore, different functionalizations of the graphene surface [24–48] such as N-doped or halogenation have expanded the array of properties to tailor the materials for specific applications.

2.2 Carbon nanotubes

Carbon nanotubes (CNTs) can be classified as intermediate carbon forms, since the sp^2 hybridized valence orbitals of their carbon atoms presents a partial sp^3 character. Carbon nanotubes can be considered as graphene sheets rolled into seamless cylinders; referred either as single or multi-walled CNTs
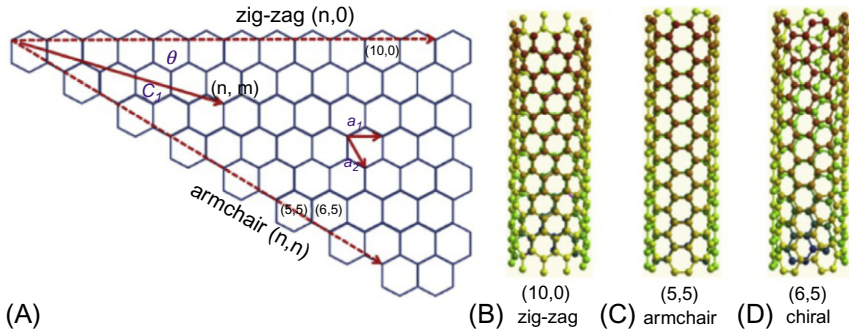
Fig. 4 (A) Unrolled single layer graphene sheet showing the geometry of the SWCNT. (B–D) Examples of the three types of nanotube sidewall; zig-zag, armchair, and chiral. *Reprinted from F. Zhang, P.-X. Hou, C. Liu, H.-M. Cheng, Epitaxial growth of single-wall carbon nanotubes, Carbon 102 (2016) 181–197, Copyright (2016), with permission from Elsevier.*

depending on the number of sheets. Theoretically, the properties of the CNTs depend on the rolling direction of graphene sheet, where $\vec{C}$ is the vector that describes such direction (Eq. 1).

$$\vec{C} = n_1 \hat{a}_1 + n_2 \hat{a}_2 \tag{1}$$

where, n_1 and n_2 are the chiral indexes and $\hat{a}_1$ and $\hat{a}_2$ are the graphene lattice vectors. The chiral vector classifies the CNTs as zigzag if $n_1 = n_2$ or armchair if $n_2 = 0$ (Fig. 4). The cases where $n_1 \neq n_2$ and $n_2 \neq 0$ are classified as chiral carbon nanotubes. The chirality of carbon nanotubes has an effect on their electronic properties, since carbon nanotubes are metallic or semi-metallic if $n_1 - n_2 = 3q$, where q is an integer, and are semi-conductors in all other cases. Experimental values of charge mobility observed in carbon nanotubes has been close to $100,000 \, cm^2 \, V^{-1} \, s^{-1}$ [49] and values of thermal conductivity of up to $6600 \, Wm^{-1} \, K^{-1}$ [50]. The discovering of these carbon polymorphs is attributed to Iijima [51]. As a result of this discovery, several synthetic [52–54] and functionalization routes [55, 56] have been reported.

2.3 Diamond

The diamond is a material composed exclusively of sp^3-type hybridized carbon atoms. Their properties are quite different to those materials where orbital valence has total or partial sp^2 hybridization. The conventional cubic cell of diamond lattice consists of two interpenetrating face-centered cubic Bravais lattices, displaced along the body diagonal of the cubic cell by one quarter of the diagonal's length [7]. The theoretical value of the energy gap

(4.8 eV) agrees with the experimental value of natural diamond (5.42 eV) and it is considered as a semiconducting material. The development of n and p-type doped diamonds has been investigated in order to increase their charge mobility. It has been reported that the Hall charges mobility measured of holes and electron in diamond are around or $>3000\,\mathrm{cm^2\,V^{-1}\,s^{-1}}$ [57]. Previous to the discovery of CNTs and graphene, diamond was considered as the material with the highest thermal conductivity. At room temperature the thermal conductivity of a single-crystal of CVD diamond is around $2200\,\mathrm{Wm^{-1}\,K^{-1}}$ [57]. Other important characteristic of diamond is its reflectance index (2.42), which is the highest known for a non-metallic material [58].

3 Thermal properties of carbon-based materials

As mentioned above, the thermal conductivities of these carbonaceous materials are unique due to their electronic properties. The classical way to define the thermal conductivity is through the Fourier's law, which relates the heat flow and the temperature gradient between two points (Eq. 2).

$$q = -k\nabla T \qquad (2)$$

where q is the heat flow, and k is thermal conductivity, which is considered as a constant for small variations of temperature. In solid materials, the thermal conductivity can be ascribed to two contributions, namely to phonon and electron mobility. While the thermal conductivity of metallic materials is mainly attributed to electron mobility, the thermal conductivity of carbon-based materials is assigned to the acoustic phonons or atom vibration in the crystal lattice. Although the regime of acoustic phonon can be ballistic or dispersive, Fourier's law considers diffusive transport. This diffusive regime occurs only if the phonon mean-free path (Λ) is smaller than the size of the sample (L). Meanwhile, in ballistic regime, phonon mean-free path is larger than the size of the sample $\Lambda > L$. Another important consideration is the fact that the thermal conductivity is considered as intrinsic when the crystal is perfect. In this type of systems the phonon can only be scattered by other phonons. Additionally, phonon scattering can also be considered as an extrinsic effect, via phonon–rough–boundary or phonon-defect scattering.

Carbon-based nanomaterials can present different magnitudes of thermal conductivity, from 0.01 to $3000\,\mathrm{Wm\,K^{-1}}$, which is due to the polymorphism of carbon. Graphitic materials, such as pyrolytic graphite, present

an in-plain thermal conductivity of around $2000\,\mathrm{Wm\,K^{-1}}$; however, this value can decrease by the grain size. Similar to this, the CVD diamond particles present a thermal conductivity that depends on the grain size. Unlike these materials, the thermal transport in carbon nanotubes and graphene are strongly influenced by the intrinsic properties of the sp^2 lattice, which favors their extremely high values.

4 Elastomer nanocomposites filled with carbon-based nanomaterials

Rubbers, or elastomers, are a special class of polymers with specific properties. They are formed by long chains, with high molecular weight and cross-linked at many points giving rise to the formation of a three-dimensional network structure. Elastomers are relatively cheap materials that exhibit rubber-like elasticity. The main characteristic of elastomer compounds is their elastic behavior; they are easily deformable up to 1000% by the application of a relatively low stress, and able to recover its original form once the stress is removed [59]. Due to their flexibility, mechanical strength, and good solvent and oil resistance, elastomers have found multiple applications, among them for insulation of electrical cables and wires or fabrication of personal protective equipment. Besides, elastomers present a wide service temperature and, consequently, they are suitable to be used in a wide temperature range from sub ambient to relatively high temperatures.

5 Methods for the preparation of carbon-based nanoparticles elastomer nanocomposites

The preparation process is key to attain a homogeneous dispersion of the carbon-based nanofillers in the elastomer matrix and, hence, an optimal set of transport properties. The most extended processing methods are the melt mixing or mastication and milling. However, other methods have also been proposed such as polymer solution and latex mixing [60–63]. These methods are applicable depending on the type of elastomer, Fig. 5 shows the most frequently used methods for the preparation of elastomer composites filled with nano–carbon based materials.

5.1 Melt mixing method

Thermoplastic elastomers are materials that combine many of the attributes and features of both vulcanized thermoset rubber and thermoplastic materials.
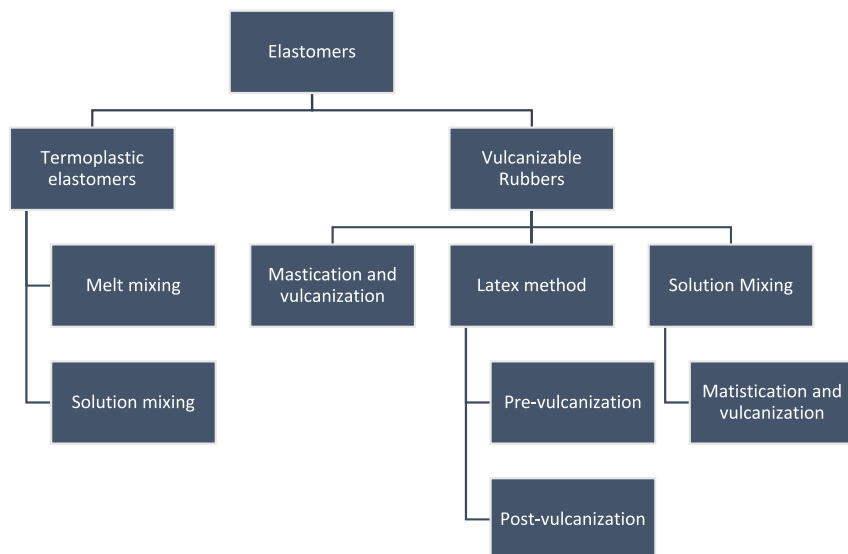
Fig. 5 General scheme of different methods for the preparation of elastomer composites.

Hence, they present an elastomeric behavior while being processed as a thermoplastic polymer. Most thermoplastic elastomers are *co*-polymers having rigid and flexible moieties in their back-bone. The synthesis of these elastomers, either by chain–growth or step–growth polymerization, results in a wide spectra of thermoplastic elastomers. Polystyrene-*block*-poly(ethylene-*ran*-butylene)-block-polystyrene (SEBS) is a thermoplastic elastomer, synthetized by chain–growth polymerization. The two polystyrene blocks placed at the extreme of the polymer chain confers partial rigidity to the back-bone chains and crystallinity to the bulk, while the central block of ethylene-*ran*-butylene confers flexibility to back-bone chain and amorphous domains to the bulk [64]. Meanwhile, thermoplastic elastomers obtained by step-growth polymerization, such as polyurethanes, are composed of short alternating polydisperse blocks of soft and hard segments [65]. The hard segments correspond to aromatic groups, while the oxygenated functions, such as ether, enhance the "free rotation" of the back-bone. The good processability of these thermoplastic elastomers (SEBS and polyurethane thermoplastic elastomer) has promoted their use with carbon–based nanomaterials [66–69]. However, other thermoplastic elastomers such as polyvinyl acetate or SBS, has also been used [70–73].

5.2 Mastication and milling method

The mastication is a mechanical shearing process that significantly reduces the viscosity of elastomers. This mastication process softens the rubber and is needed to mix the vulcanizing reagents, such as accelerators and sulfur. The vulcanization ingredients will tune the crosslink density of elastomers through a careful balance between sulfur and the accelerators. This has an important effect on the resulting mechanical performance of carbon-based elastomer nanocomposites.

Fillers also are added in this stage and, where the filler morphology may be degraded by the high shear process. The percolation thresholds of fillers in composite based on amorphous polymers tend to be higher than those exhibited by composite based on crystalline and semi-crystalline polymers. Fillers in amorphous polymers are homogeneously dispersed in the entire volume, while in semicrystalline polymers they would only be present in the amorphous phase. An additional effect of the nanofillers in vulcanized elastomers is the significant enhancement of the mechanical and electrical properties, due to the interactions that take place between the filler—matrix and filler—filler [74–77].

5.3 Solvent mixing method

Solvent mixing is rarely used to prepare elastomeric nanocomposites since it requires large volumes of apolar solvents and is a lengthy process. The solution mixing method requires the selection of the appropriate solvent for each elastomer. Nevertheless, it should be taken in account that only linear or branched polymer could be dissolved, whereas cross-linked elastomer will only swell when in contact with compatible liquid. The proper solvent can be chosen using the solubility parameters, which are based on a thermodynamic principle that was initially described by Hildebrand [78]. This principle consists in the premise of "*like dissolves like*", which is supported by empiric considerations of mixing enthalpy (ΔH^M). Small values of mixing enthalpy indicate that the solvation of polymer in a determined solvent will take place. As shown in Eq. (3), the enthalpy of mixing is represented as a function of the total volume of the mixture (V_M), the molar fractions (ϕ_i) and the solubility parameters (δ_i) of the components.

$$\Delta H^M = V_M(\delta_1 - \delta_2)^2 \phi_1 \phi_2 \qquad (3)$$

It has been reported that composites based on SBS and MWCNT prepared by solution mixing method presented an electrical percolation

threshold at 0.25 wt% and with only 1.0 wt% of MWCNT the conductivity reached $10^{-4}\,\mathrm{S\,cm^{-1}}$ [79]. Meanwhile, Araby et al. [80] have reported a solution mixing protocol to disperse both graphene and vulcanization agents in SBS polymer matrix, which enable a higher degree of filler dispersion. The electrical percolation threshold was between 5 and 6.5 vol% of filler.

5.4 Latex mixing method

Natural rubber is obtained from its natural source, *Hevea brasiliensis*' tree in form of a latex. Latex is an acceptation borrowed from New Latin of 19th century and it refers to fluids or liquids. In effect, natural rubber corresponds to an aqueous colloidal suspension. *Cis*-1,4-Polyisoprene is the solid that conforms the suspended particles in latex. The particles are stabilized as colloid by the presence of phospholipids on their surface and proteins. As known, cis-1,4-polyisoprene is a polymer that has alkene moieties in its backbone chains. The natural rubber latex with or without the vulcanizing reagents is commercially available. The addition of sulfur, or peroxide, to the latex is known as a pre-vulcanized state, which is then dried and heated to form post-vulcanized rubber. The preparation of carbon nanocomposites using latex mixing method requires the stabilization of hydrophobic carbon-based nanoparticles in an aqueous colloidal suspension, which has been pursued through the use of surfactants. Surfactants refer to a surface active agent to reduce the surface tension [81]. The character of surfactants is amphiphilic, which means that the surfactant molecules have hydrophilic and hydrophobic moieties in their structure [82]. In this regard, stable suspension of carbon-based materials can be obtained by the non–covalent modification using surfactants [60]. Non-covalent modified carbon-based nanomaterials undergo ionic repulsion in aqueous medium if the surfactant is ionic. Non-ionic surfactants promote the stabilization of carbon-based nanomaterials by the occurrence of steric repulsion among the non–covalent modified particles. The addition of aqueous suspension of stabilized carbon-based nanomaterials results in nanocomposites films with homogeneous dispersion of the filler. The low viscosity of natural rubber latex and other polymer lattices, such as SBR or NBR latex, allows the fabrication of these types of composites using laboratory routine equipment [60, 62, 83]. The latex mixing methods also allows other variation such as self-assembly and heterocoagulations, methodologies designed in order to promote the homogeneous dispersion of filler in the rubber matrix [61, 84].

6 Transport properties of carbon-based elastomer nanocomposites

6.1 Electrical conductivity

The first detailed studies on electrically conducting carbon–based particles/ elastomer composites are referred to the use of carbon black as filler [85–88]. In these types of composites, a relevant role on the electrical conductivity is attributed to the morphology of composites and the dispersion of the particles in the polymer matrix. The proximity among particles allows the mobility of electrons by tunneling between adjacent carbon particles and this tunneling effect is improved by thermal fluctuations. Similar considerations have been argued for carbon nanotubes and graphene materials based elastomer composites [89, 90].

A statistical physics model has been used to understand the factors involved in the improved electrical conductivity of polymer composites. This theory known as percolation explains the transition from a local connectivity state to one in which the connections extend indefinitely [91]. A percolation model represents the random connectivity of adjacent sites of hard-core circles in an infinity periodic lattice [92]. This theory is useful for polymer composites, since it considers two different components or phases. Consequently, the electrical conductivity observed in composites based on electrically conducting fillers and insulating polymer matrices is attributed to the formation of a three-dimensional interconnected network of the conductive phase. The critical filler content where the composite becomes electrically conductive is denominated percolation threshold (ϕ_C) [93]. The electrical conductivity in continuum percolation theory is given by Eq. (4) [94].

$$\sigma \propto (\phi - \phi_C)^t \text{ for } \phi > \phi_C \tag{4}$$

where ϕ, ϕ_C and t are the volume fraction of the filler, the percolation threshold and a critical exponent, respectively. Other expression that is used to predict the direct current conductivity (σ_{dc}) and dielectric constant (ε) are Eqs. (5), (6), respectively [95, 96].

$$\sigma_{dc} \propto (\phi_C - \phi)^{-s'} \text{ for } \phi < \phi_C \tag{5}$$

$$\varepsilon(f) \propto \left| \frac{\phi_C - \phi}{\phi_C} \right|^{-s} \text{ for } \phi > \phi_C, \ \phi < \phi_C \tag{6}$$

where, $-s'$ and $-s$ are both known as critical exponents, which are assumed to be universal. The volume fraction of the filler in a polymer composite can be determined by the Eq. (7).

$$\phi = \frac{\dfrac{p}{\rho_f}}{\dfrac{p}{\rho_f} + \dfrac{(1-p)}{\rho_m}} \tag{7}$$

where p and ρ_f are the weight fraction and the density of the filler, and ρ_m is the density of the polymer matrix.

Other important consideration to the percolation in composites was proposed by Balberg et al. [97, 98], who introduced the concept of excluded volume. Excluded volume corresponds to the volume surrounding and including a given object, where other object of similar shape cannot penetrate this volume. Consequently, the excluded volume in the percolation threshold is a dimensional invariant for continuum systems of objects, where the only randomness is in their location in space. The percolation volume will be associated to a critical number density of objects as seen in Eq. (8).

$$\langle V_{ex} \rangle = N_c \langle V \rangle \approx B_c \tag{8}$$

where, $\langle V_{ex} \rangle$ is the total excluded volume, $\langle V \rangle$ is the average excluded volume of an object of volume V_0, N_c is the critical number density of objects at percolation and B_c is a dimensional invariant. Consequently, the percolation threshold can be expressed as seen in Eq. (9) [99].

$$\phi = 1 - \exp\left(-\frac{\langle V_{ex} \rangle V_0}{\langle V \rangle}\right) \tag{9}$$

As a result of these theoretical considerations, the shape of the filler plays an important role on the value of the percolation threshold. For instance, the percolation threshold of cylinder-shaped fillers has been calculated and varies between 0.276% and 5.8% [99], while that of disk-shaped nanofillers varies between 0.487% and 0.765% [100]. Previous to those theoretical considerations, Flandin et al. [101] demonstrated the dominant role of the filler size in the percolation threshold of polyethylene-*co*-octene, a thermoplastic elastomer. In this work, the percolation threshold decreased from 39.5 to 12 vol% using carbon black nanoparticles with diameter of 300 and 21 nm, respectively. Likewise, Das and co-workers, reported a percolation threshold between 2 and 3 wt% of CNTs in styrene butadiene and butadiene rubber [102]. In the case of graphene materials, the dispersion of reduced graphene

oxide in pre-vulcanized natural rubber has shown an electrical percolation threshold between 2.4 phr of filler [60]. Fig. 6 represents the types of filler phases in the elastomer matrix as its contents is increased and its effect on the electrical properties of composites. At low filler content, below percolation threshold, the filler particles are distributed as isolated particles without contact among them. Consequently the increase of electrical conductivity is negligible compared with the polymer matrix. When the filler content reaches the percolation threshold, an interconnected filler percolation network is formed, giving rise to an increase of electrical conductivity (Fig. 6). However, the electrical conductivity reaches a *plateau* at higher content of filler than percolation threshold. The electrical conductivity which is achieved in this *plateau* is inherent of charge transport processes of electrical percolation network and the intrinsic electrical conductivity of the filler.
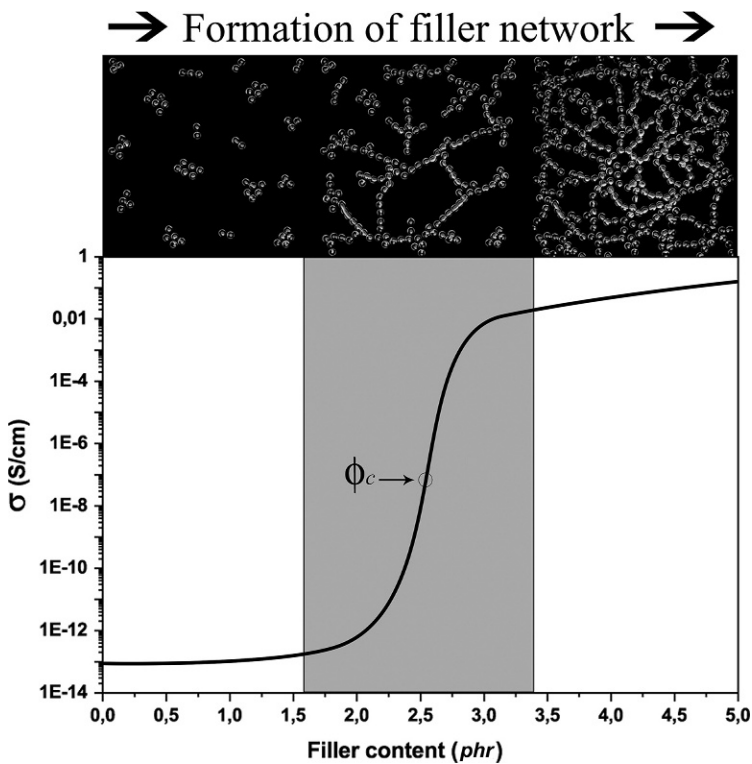
Fig. 6 Scheme of the distribution of filler through elastomer matrix compared with a plot of electrical conductivity as function of filler content.

Since the first studies carried out on the preparation of electrically conducting elastomer composites an evolution of the methods and type of carbonaceous filler has taken place. For instance, A. K. Sircar [86, 87] carried out different studies to investigate the electrical conductivity of carbon black/elastomer composites analyzing the influence of the surface area, structure and porosity. This researcher showed a significant increase of the viscosity with the addition of a conducting carbon black to a blend of highly polar nitrile rubbers with natural rubber, chlorobutyl rubber or EPDM [87]. Styrene-butadiene, acrylonitrile-butadiene, polychloroprene rubber and other matrices were also studied for the preparation of carbon black–based elastomer composites [103–106]. Recently, the addition of MWCNTs or graphene materials by mastication and two roll milling of different rubber such as silicone elastomer, SBR, NR, EPDM, among other, have also been investigated to improve the electrical conductivity [107–117]. In this respect, an important outcome was accomplished by M. Hernandez et al. [114]. The authors showed an increase of the electrical conductivity, acceleration of the cross-linking reaction and an enhancement of the mechanical properties with the addition of 1.0 phr of functionalized graphene sheets to NR. In the case of nano-diamonds the research has been mainly approached to develop elastomer composites with enhanced mechanical properties [118–120], however, there are authors that argument that the nano-diamond can also increase the electrical conductivity [121].

6.2 Thermal conductivity

Current interest for developing thermal interface materials based in elastomers steam from the requirement of lightweight, stretchable, electrically and thermally conducting materials for electronic and optoelectronic applications. The thermal conductivity can be expressed by Eq. (10), which is based on Newton-Laplace equation and the kinetic theory.

$$k \approx \left(\frac{E}{\rho}\right)^{1/2}\left(\frac{C_v \Lambda}{3}\right) \tag{10}$$

Where, E corresponds to the elastic modulus, ρ is the density, C_v is the volumetric heat capacity and Λ is the phonon mean-free path [122]. Consequently, the thermal conductivity in elastomer is relatively low compared to materials such as ceramics or metals. In fact, unfilled polymers possess values of thermal conductivity between 0.17 and 0.35 $\mathrm{Wm\,K^{-1}}$ compared to 247 $\mathrm{Wm\,K^{-1}}$ of aluminum [123]. However, different strategies have been

proposed to enhance the thermal conductivity of elastomers. For instance, the addition of MWCNT provided a significant increase of up to 65% of the thermal conductivity of silicone rubber (PDMS) [124]. The authors argued that the use of grinding method enables the homogeneous dispersion of MWCNT in the polymer matrix. Likewise, J. Hong et al. [125] reported that the functionalization of MWCNTs with oxygen moieties and the preparation of a pre-mix, or masterbatch increased the thermal conductivity of PDMS around 10% with respect to those based on un-functionalized MWCNTs and without pre-mixing. In a similar work [126], they also report that the PDMS composites filled with silica–coated MWCNTs presented a slightly higher thermal conductivity than those filled with un–coated MWCNTs. Nevertheless, the results indicate that the thermal conductivity in these types of composites is conditioned by the thermal conductivity of the polymer matrix. In the case of elastomer composites filled with graphene materials, it has been reported that the addition of 24 vol% of MWCNTs increased three times the thermal conductivity of styrene-butadiene rubber by a solution mixing methods [80]. This graphene composite also showed improvements in its mechanical and electrical properties. Further strategies, such as filler orientation, functionalized carbon–based materials or metal-decorated CNTs have also shown to promote the enhancement of thermal conductivity of elastomers [127–129].

7 Sensing properties of carbon-based elastomer nanocomposites

The development of electrically conducting elastomeric composites has also been analyzed for the potential application as sensor through the combination of rigid conducting fillers and flexible and insulating matrix.

7.1 Strain and damage sensing

Changes in the resistivity, which is the reciprocal of the electrical conductivity, as a result of applied mechanical strain is called piezoresistivity effect, which is a consequence of the decrease or increase of the electrical pathways between conducting filler particles. Hence, the shape, the aspect ratio, the state of the dispersion, and the interaction with the polymer matrix can affect the piezoresistivity response of the composite. However, the theoretical consideration for conventional piezoresistivity materials, such as semiconductors or metals cannot explain the piezoresistivity in carbon-based nanocomposites [130]. In addition, the percolation theory for composites

describes the dependence of the electrical conductivity in polymeric composites and the influence of the filler shape without considering the deformation of the composite. In this respect, S. Kim and co-workers have proposed a three-dimensional percolation theory considering the nonlinear elasticity, strain dependent Poisson's ratio and strain–dependent percolation threshold [131]. These researchers proposed the variation of volume as a result of the deformation, which they expressed in Eqs. (11), (12).

$$\sigma = A \left(\phi_{f1\,or\,f2} - \phi_C \right)^t \tag{11}$$

$$\phi_{f1\,or\,f2} = \frac{V_{filler}}{V_{1\,or\,2}} \tag{12}$$

A and t are a proportionality constant related to the electrical conductivity of fillers and fitting exponent, respectively. Sub-indexes 1 and 2 indicate the initial or deformed state, respectively. $\phi_{f1\,or\,f2}$ correspond to the volume fraction of the filler, which is obtained by the relation between the filler volume (V_{filler}) and composite volume at initial or deformed state (V_1 or V_2). These authors also assumed that the percolation threshold ϕ_C should be corrected at the elongated state. Piezoresistivity sensors are classified as active sensors, since they need specific supply circuits depending on the technology of the transducer [130]. Different studies have addressed sensing strain, compression and damage [63, 132, 133]. Likewise, these materials are appropriate to be used as human motion sensors [134, 135].

7.2 Effect of solvent and oil on sensing properties

The electrical conductivity of elastomer composites filled with carbon-based nanomaterials not only can be affected by deformation, but also can experiment changes as a consequence of their swelling with organic solvents or oils. This is mainly attributed to the fact that the small molecules swell the elastomers and occupy the free volume. This can inhibitive the tunneling of electron between filler nanoparticles. Consequently, the electrical conductivity would decrease significantly. For instance, Pavlovsky and Siegmann have reported that composites based on crosslinked SEBS and carbon black present large reversible changes in conductivity on exposure to various solvents and air drying cycles [136]. They also demonstrated the changes of electrical conductivity as consequence of sorption/desorption of solvent. The reversible swelling of composites allows the occurrence of the breakdown and reconstruction of filler conducting network. The authors observed that the sensing performance mainly depends on solubility parameters of the solvent. In the case of oil, Ponnamma and co-workers

reported that sorption of oil in conducting composites based on isoprene rubber and MWCNT produces a drastic change of resistance [137]. These properties can be useful for environmental purpose such as the detection of oil or organic solvents.

8 Upcoming applications

Currently, electrically conducting rubber composites are being studied to develop new applications of elastomeric materials. For instance, electrically conducting elastomers have applications for EMI shielding purpose, which has significant importance in electronic [138]. Likewise, these materials can be used as protection against lightening, antistatic and electrostatic discharge [139]. The broad range of elastomers and the different composites preparation methods makes it possible to develop a wide number of carbon-based elastomer composites for different purposes. Undoubtedly, carbon-based elastomers are being positioned in different application areas. Therefore, in the near future it will be possible to find devices made with pieces of carbon elastomer composites.

References

[1] J. Heil, A. Böhm, A. Gröger, M. Primke, P. Wyder, P. Keppler, J. Major, H. Bender, E. Schönherr, H. Wendel, B. Wolf, K.U. Würz, W. Grill, H. Herrnberger, S. Knauth, J. Lenzner, Electron focusing in metals and semimetals, Phys. Rep. 323 (5) (2000) 387–455.
[2] K.I. Bolotin, K.J. Sikes, Z. Jiang, M. Klima, G. Fudenberg, J. Hone, P. Kim, H. L. Stormer, Ultrahigh electron mobility in suspended graphene, Solid State Commun. 146 (9) (2008) 351–355.
[3] A.A. Balandin, Thermal properties of graphene and nanostructured carbon materials, Nat. Mater. 10 (8) (2011) 569–581.
[4] S. Chen, Q. Wu, C. Mishra, J. Kang, H. Zhang, K. Cho, W. Cai, A.A. Balandin, R. S. Ruoff, Thermal conductivity of isotopically modified graphene, Nat. Mater. 11 (3) (2012) 203–207.
[5] S. Chen, A.L. Moore, W. Cai, J.W. Suk, J. An, C. Mishra, C. Amos, C.W. Magnuson, J. Kang, L. Shi, R.S. Ruoff, Raman measurements of thermal transport in suspended monolayer graphene of variable sizes in vacuum and gaseous environments, ACS Nano 5 (1) (2011) 321–328.
[6] E. Pop, V. Varshney, A.K. Roy, Thermal properties of graphene: fundamentals and applications, MRS Bull. 37 (12) (2012) 1273–1281.
[7] P.R. Wallace, The band theory of graphite, Phys. Rev. 71 (9) (1947) 622–634.
[8] K.S. Novoselov, A.K. Geim, S.V. Morozov, D. Jiang, Y. Zhang, S.V. Dubonos, I. V. Grigorieva, A.A. Firsov, Electric field effect in atomically thin carbon films, Science 306 (5696) (2004) 666–669.
[9] L.P. Biro, P. Nemes-Incze, P. Lambin, Graphene: nanoscale processing and recent applications, Nanoscale 4 (6) (2012) 1824–1839.

[10] A.K. Geim, K.S. Novoselov, The rise of graphene, Nat. Mater. 6 (2007) 183.

[11] K.S. Novoselov, A.K. Geim, S.V. Morozov, D. Jiang, M.I. Katsnelson, I.V. Grigorieva, S.V. Dubonos, A.A. Firsov, Two-dimensional gas of massless Dirac fermions in graphene, Nature 438 (7065) (2005) 197–200.

[12] J. Wang, F. Ma, W. Liang, M. Sun, Electrical properties and applications of graphene, hexagonal boron nitride (h-BN), and graphene/h-BN heterostructures, Mater. Today Phys. 2 (2017) 6–34.

[13] X. Du, I. Skachko, A. Barker, E.Y. Andrei, Approaching ballistic transport in suspended graphene, Nat. Nanotechnol. 3 (2008) 491.

[14] F. Miao, S. Wijeratne, Y. Zhang, U.C. Coskun, W. Bao, C.N. Lau, Phase-coherent transport in graphene quantum billiards, Science 317 (5844) (2007) 1530.

[15] C. Botas, P. Álvarez, C. Blanco, R. Santamaría, M. Granda, M.D. Gutiérrez, F. Rodríguez-Reinoso, R. Menéndez, Critical temperatures in the synthesis of graphene-like materials by thermal exfoliation–reduction of graphite oxide, Carbon 52 (2013) 476–485.

[16] C. Botas, P. Álvarez, P. Blanco, M. Granda, C. Blanco, R. Santamaría, L.J. Romasanta, R. Verdejo, M.A. López-Manchado, R. Menéndez, Graphene materials with different structures prepared from the same graphite by the Hummers and Brodie methods, Carbon 65 (2013) 156–164.

[17] M.I. Kairi, M. Khavarian, S.A. Bakar, B. Vigolo, A.R. Mohamed, Recent trends in graphene materials synthesized by CVD with various carbon precursors, J. Mater. Sci. 53 (2) (2018) 851–879.

[18] P. Ranjan, S. Agrawal, A. Sinha, T.R. Rao, J. Balakrishnan, A.D. Thakur, A low-cost non-explosive synthesis of graphene oxide for scalable applications, Sci. Rep. 8 (1) (2018)12007.

[19] X. Gao, J. Jang, S. Nagase, Hydrazine and thermal reduction of graphene oxide: reaction mechanisms, product structures, and reaction design, J. Phys. Chem. C 114 (2) (2010) 832–842.

[20] P.V. Kumar, N.M. Bardhan, G.-Y. Chen, Z. Li, A.M. Belcher, J.C. Grossman, New insights into the thermal reduction of graphene oxide: impact of oxygen clustering, Carbon 100 (2016) 90–98.

[21] B.C. Brodie, On the atomic weight of graphite, Philos. Trans. R. Soc. Lond. 149 (1859) 249–259.

[22] W.S. Hummers, R.E. Offeman, Preparation of graphitic oxide, J. Am. Chem. Soc. 80 (6) (1958) 1339.

[23] D.C. Marcano, D.V. Kosynkin, J.M. Berlin, A. Sinitskii, Z. Sun, A. Slesarev, L.B. Alemany, W. Lu, J.M. Tour, Improved synthesis of graphene oxide, ACS Nano 4 (8) (2010) 4806–4814.

[24] F. Lou, M.E.M. Buan, N. Muthuswamy, J.C. Walmsley, M. Ronning, D. Chen, One-step electrochemical synthesis of tunable nitrogen-doped graphene, J. Mater. Chem. A 4 (4) (2016) 1233–1243.

[25] Y. Shang, H. Xu, M. Li, G. Zhang, Preparation of N-doped graphene by hydrothermal method and interpretation of N-doped mechanism, Nano 12 (2) (2016) 1750018.

[26] D. Du, P. Li, J. Ouyang, Nitrogen-doped reduced graphene oxide prepared by simultaneous thermal reduction and nitrogen doping of graphene oxide in air and its application as an electrocatalyst, ACS Appl. Mater. Interfaces 7 (48) (2015) 26952–26958.

[27] A. Navaee, A. Salimi, Efficient amine functionalization of graphene oxide through the Bucherer reaction: an extraordinary metal-free electrocatalyst for the oxygen reduction reaction, RSC Adv. 5 (74) (2015) 59874–59880.

[28] Y. Zhang, Z. Sun, H. Wang, Y. Wang, M. Liang, S. Xue, Nitrogen-doped graphene as a cathode material for dye-sensitized solar cells: effects of hydrothermal reaction and annealing on electrocatalytic performance, RSC Adv. 5 (14) (2015) 10430–10439.

[29] P. Chen, J.-J. Yang, S.-S. Li, Z. Wang, T.-Y. Xiao, Y.-H. Qian, S.-H. Yu, Hydrothermal synthesis of macroscopic nitrogen-doped graphene hydrogels for ultrafast supercapacitor, Nano Energy 2 (2) (2013) 249–256.

[30] H.-L. Guo, P. Su, X. Kang, S.-K. Ning, Synthesis and characterization of nitrogen-doped graphene hydrogels by hydrothermal route with urea as reducing-doping agents, J. Mater. Chem. A 1 (6) (2013) 2248–2255.

[31] B. Jiang, C. Tian, L. Wang, L. Sun, C. Chen, X. Nong, Y. Qiao, H. Fu, Highly concentrated, stable nitrogen-doped graphene for supercapacitors: simultaneous doping and reduction, Appl. Surf. Sci. 258 (8) (2012) 3438–3443.

[32] L.F. Lai, J.R. Potts, D. Zhan, L. Wang, C.K. Poh, C.H. Tang, H. Gong, Z.X. Shen, L.Y. Jianyi, R.S. Ruoff, Exploration of the active center structure of nitrogen-doped graphene-based catalysts for oxygen reduction reaction, Energy Environ. Sci. 5 (7) (2012) 7936–7942.

[33] J.W. Lee, J.M. Ko, J.-D. Kim, Hydrothermal preparation of nitrogen-doped graphene sheets via hexamethylenetetramine for application as supercapacitor electrodes, Electrochim. Acta 85 (2012) 459–466.

[34] J. Long, X. Xie, J. Xu, Q. Gu, L. Chen, X. Wang, Nitrogen-doped graphene nanosheets as metal-free catalysts for aerobic selective oxidation of benzylic alcohols, ACS Catal. 2 (4) (2012) 622–631.

[35] P. Su, H.L. Guo, S. Peng, S.K. Ning, Preparation of nitrogen-doped graphene and its supercapacitive properties, Acta Phys. -Chim. Sin. 28 (11) (2012) 2745–2753.

[36] L. Sun, L. Wang, C.G. Tian, T.X. Tan, Y. Xie, K.Y. Shi, M.T. Li, H.G. Fu, Nitrogen-doped graphene with high nitrogen level via a one-step hydrothermal reaction of graphene oxide with urea for superior capacitive energy storage, RSC Adv. 2 (10) (2012) 4498–4506.

[37] D. Long, W. Li, L. Ling, J. Miyawaki, I. Mochida, S.-H. Yoon, Preparation of nitrogen-doped graphene sheets by a combined chemical and hydrothermal reduction of graphene oxide, Langmuir 26 (20) (2010) 16096–16102.

[38] L.-S. Zhang, X.-Q. Liang, W.-G. Song, Z.-Y. Wu, Identification of the nitrogen species on N-doped graphene layers and Pt/NG composite catalyst for direct methanol fuel cell, Phys. Chem. Chem. Phys. 12 (38) (2010) 12055–12059.

[39] D. Wei, Y. Liu, Y. Wang, H. Zhang, L. Huang, G. Yu, Synthesis of n-doped graphene by chemical vapor deposition and its electrical properties, Nano Lett. 9 (5) (2009) 1752–1758.

[40] I.Y. Jeon, H.J. Choi, M. Choi, J.M. Seo, S.M. Jung, M.J. Kim, S. Zhang, L.P. Zhang, Z.H. Xia, L.M. Dai, N. Park, J.B. Baek, Facile, scalable synthesis of edge-halogenated graphene nanoplatelets as efficient metal-free eletrocatalysts for oxygen reduction reaction, Sci. Rep. 3 (2013) 7.

[41] F. Karlický, K. Kumara Ramanatha Datta, M. Otyepka, R. Zbořil, Halogenated graphenes: rapidly growing family of graphene derivatives, ACS Nano 7 (8) (2013) 6434–6464.

[42] H.L. Poh, P. Šimek, Z. Sofer, M. Pumera, Halogenation of graphene with chlorine, bromine, or iodine by exfoliation in a halogen atmosphere, Chem. Eur. J. 19 (8) (2013) 2655–2662.

[43] F. Karlicky, R. Zboril, M. Otyepka, Band gaps and structural properties of graphene halides and their derivates: a hybrid functional study with localized orbital basis sets, J. Chem. Phys. 137 (3) (2012) 7.

[44] H. Aguilar-Bolados, D. Vargas-Astudillo, M. Yazdani-Pedram, G. Acosta-Villavicencio, P. Fuentealba, A. Contreras-Cid, R. Verdejo, M.A. López-Manchado, Facile and scalable one-step method for amination of graphene using leuckart reaction, Chem. Mater. 29 (16) (2017) 6698–6705.

[45] W. Feng, P. Long, Y. Feng, Y. Li, Two-dimensional fluorinated graphene: synthesis, structures, properties and applications, Adv. Sci. 3 (7) (2016)1500413-n/a.

[46] K. Samanta, S. Some, Y. Kim, Y. Yoon, M. Min, S.M. Lee, Y. Park, H. Lee, Highly hydrophilic and insulating fluorinated reduced graphene oxide, Chem. Commun. 49 (79) (2013) 8991–8993.

[47] J.T. Robinson, J.S. Burgess, C.E. Junkermeier, S.C. Badescu, T.L. Reinecke, F.K. Perkins, M.K. Zalalutdniov, J.W. Baldwin, J.C. Culbertson, P.E. Sheehan, E.S. Snow, Properties of fluorinated graphene films, Nano Lett. 10 (8) (2010) 3001–3005.

[48] H. Aguilar-Bolados, A. Contreras-Cid, M. Yazdani-Pedram, G. Acosta-Villavicencio, M. Flores, P. Fuentealba, A. Neira-Carrillo, R. Verdejo, M.A. López-Manchado, Synthesis of fluorinated graphene oxide by using an easy one-pot deoxyfluorination reaction, J. Colloid Interface Sci. 524 (2018) 219–226.

[49] T. Dürkop, S.A. Getty, E. Cobas, M.S. Fuhrer, Extraordinary mobility in semiconducting carbon nanotubes, Nano Lett. 4 (1) (2004) 35–39.

[50] S. Berber, Y.-K. Kwon, D. Tománek, Unusually high thermal conductivity of carbon nanotubes, Phys. Rev. Lett. 84 (20) (2000) 4613–4616.

[51] S. Iijima, Helical microtubules of graphitic carbon, Nature 354 (6348) (1991) 56–58.

[52] T.W. Ebbesen, P.M. Ajayan, Large-scale synthesis of carbon nanotubes, Nature 358 (1992) 220.

[53] G. Che, B.B. Lakshmi, C.R. Martin, E.R. Fisher, R.S. Ruoff, Chemical vapor deposition based synthesis of carbon nanotubes and nanofibers using a template method, Chem. Mater. 10 (1) (1998) 260–267.

[54] H. Dai, Carbon nanotubes: synthesis, integration, and properties, Acc. Chem. Res. 35 (12) (2002) 1035–1044.

[55] A. Hirsch, O. Vostrowsky, Functionalization of carbon nanotubes, in: A.D. Schlüter (Ed.), Functional Molecular Nanostructures, Springer, Berlin, Heidelberg, 2005, , pp. 193–237.

[56] R.J. Chen, S. Bangsaruntip, K.A. Drouvalakis, N. Wong Shi Kam, M. Shim, Y. Li, W. Kim, P.J. Utz, H. Dai, Noncovalent functionalization of carbon nanotubes for highly specific electronic biosensors, Proc. Natl. Acad. Sci. 100 (9) (2003) 4984.

[57] C.J. Wort, R.S. Balmer, Diamond as an electronic material, Mater. Today 11 (1) (2008) 22–28.

[58] T. Ogata, R. Yagi, N. Nakamura, Y. Kuwahara, S. Kurihara, Modulation of polymer refractive indices with diamond nanoparticles for metal-free multilayer film mirrors, ACS Appl. Mater. Interfaces 4 (8) (2012) 3769–3772.

[59] J.M.G. Cowie, Polymers: Chemistry & Physics of Modern Materials, second ed., Blakkie, London, 1991.

[60] H. Aguilar-Bolados, J. Brasero, M.A. Lopez-Manchado, M. Yazdani-Pedram, High performance natural rubber/thermally reduced graphite oxide nanocomposites by latex technology, Compos. Part B 67 (2014) 449–454.

[61] H. Aguilar-Bolados, M. Yazdani-Pedram, J. Brasero, M. López-Manchado, Influence of the surfactant nature on the occurrence of self-assembly between rubber particles and thermally reduced graphite oxide during the preparation of natural rubber nanocomposites, J. Nanomater. 2015 (2015) 7.

[62] H. Aguilar-Bolados, M.A. Lopez-Manchado, J. Brasero, F. Avilés, M. Yazdani-Pedram, Effect of the morphology of thermally reduced graphite oxide on the mechanical and electrical properties of natural rubber nanocomposites, Compos. Part B 87 (2016) 350–356.

[63] H. Aguilar-Bolados, M. Yazdani-Pedram, A. Contreras-Cid, M.A. López-Manchado, A. May-Pat, F. Avilés, Influence of the morphology of carbon nanostructures on the piezoresistivity of hybrid natural rubber nanocomposites, Compos. Part B 109 (2017) 147–154.

[64] F. Lin, C. Wu, D. Cui, Synthesis and characterization of crystalline styrene-b-(ethylene-co-butylene)-b-styrene triblock copolymers, J. Polym. Sci. A Polym. Chem. 55 (7) (2017) 1243–1249.

[65] A. Burke, N. Hasirci, Polyurethanes in biomedical applications, Adv. Exp. Med. Biol. 553 (2004) 83–101.

[66] S. Pavlovsky, A. Siegmann, Chemical sensing materials. I. Electrically conductive SEBS copolymer systems, J. Appl. Polym. Sci. 113 (5) (2009) 3322–3329.

[67] Y. Li, H. Shimizu, Toward a stretchable, elastic, and electrically conductive nanocomposite: morphology and properties of poly[styrene-b-(ethylene-co-butylene)-b-styrene]/multiwalled carbon nanotube composites fabricated by high-shear, Macromolecules 42 (7) (2009) 2587–2593.

[68] K. Ke, V. Solouki Bonab, D. Yuan, I. Manas-Zloczower, Piezoresistive thermoplastic polyurethane nanocomposites with carbon nanostructures, Carbon 139 (2018) 52–58.

[69] X. Qi, H. Xiu, Y. Wei, Y. Zhou, Y. Guo, R. Huang, H. Bai, Q. Fu, Enhanced shape memory property of polylactide/thermoplastic poly(ether)urethane composites via carbon black self-networking induced co-continuous structure, Compos. Sci. Technol. 139 (2017) 8–16.

[70] P. Costa, J. Silva, V. Sencadas, R. Simoes, J.C. Viana, S. Lanceros-Méndez, Mechanical, electrical and electro-mechanical properties of thermoplastic elastomer styrene-butadiene-styrene/multiwall carbon nanotubes composites, J. Mater. Sci. 48 (3) (2013) 1172–1179.

[71] M. Rahaman, A. Aldalbahi, P. Govindasami, N.P. Khanam, S. Bhandari, P. Feng, T. Altalhi, A new insight in determining the percolation threshold of electrical conductivity for extrinsically conducting polymer composites through different sigmoidal models, Polymers 9 (10) (2017).

[72] L.C. Jia, Z.H. Jiao, D.X. Yan, Z.M. Li, Octadecylamine-grafted graphene oxide helps the dispersion of carbon nanotubes in ethylene vinyl acetate, Polymers 9 (9) (2017).

[73] S. Gaidukovs, E. Zukulis, I. Bochkov, R. Vaivodiss, G. Gaidukova, Enhanced mechanical, conductivity, and dielectric characteristics of ethylene vinyl acetate copolymer composite filled with carbon nanotubes, J. Thermoplast. Compos. Mater. 31 (9) (2018) 1161–1180.

[74] A.R. Payne, The dynamic properties of carbon black–loaded natural rubber vulcanizates. Part I, J. Appl. Polym. Sci. 6 (19) (1962) 57–63.

[75] S. Bhattacharyya, C. Sinturel, O. Bahloul, M.-L. Saboungi, S. Thomas, J.-P. Salvetat, Improving reinforcement of natural rubber by networking of activated carbon nanotubes, Carbon 46 (7) (2008) 1037–1045.

[76] S. Siddabattuni, T.P. Schuman, F. Dogan, Dielectric properties of polymer–particle nanocomposites influenced by electronic nature of filler surfaces, ACS Appl. Mater. Interfaces 5 (6) (2013) 1917–1927.

[77] D. Ponnamma, K.K. Sadasivuni, M. Strankowski, P. Moldenaers, S. Thomas, Y. Grohens, Interrelated shape memory and Payne effect in polyurethane/graphene oxide nanocomposites, RSC Adv. 3 (36) (2013) 16068–16079.

[78] G.H. Brown, Regular solutions. By Joel H. Hildebrand and Robert L. Scott, Inorg. Chem. 2 (2) (1963) 431–432.

[79] L.G. Pedroni, M.A. Soto-Oviedo, J.M. Rosolen, M.I. Felisberti, A.F. Nogueira, Conductivity and mechanical properties of composites based on MWCNTs and styrene-butadiene-styrene block™ copolymers, J. Appl. Polym. Sci. 112 (6) (2009) 3241–3248.

[80] S. Araby, Q. Meng, L. Zhang, H. Kang, P. Majewski, Y. Tang, J. Ma, Electrically and thermally conductive elastomer/graphene nanocomposites by solution mixing, Polymer 55 (1) (2014) 201–210.

[81] J. Gooch, Surfactant, in: J. Gooch (Ed.), Encyclopedic Dictionary of Polymers, Springer, New York, 2011, p. 926.

[82] M.J. Owens, C.H. Bourke, Amphiphilic, in: I.P. Stolerman (Ed.), Encyclopedia of Psychopharmacology, Springer, Berlin, Heidelberg, 2010, p. 78.

[83] J.S. Kim, J.H. Yun, I. Kim, S.E. Shim, Electrical properties of graphene/SBR nanocomposite prepared by latex heterocoagulation process at room temperature, J. Ind. Eng. Chem. 17 (2) (2011) 325–330.

[84] C.F. Matos, F. Galembeck, A.J.G. Zarbin, Multifunctional and environmentally friendly nanocomposites between natural rubber and graphene or graphene oxide, Carbon 78 (2014) 469–479.

[85] A. Voet, J.C. Morawaki, Dynamic mechanical and electrical properties of vulcanizates at elongations up to sample rupture, Rubber Chem. Technol. 47 (4) (1974) 765–777.

[86] A.K. Sircar, T.G. Lamond, Effect of carbon black particle size distribution on electrical conductivity, Rubber Chem. Technol. 51 (1) (1978) 126–132.

[87] A.K. Sircar, Softer conductive rubber compounds by elastomer blending, Rubber Chem. Technol. 54 (4) (1981) 820–834.

[88] E.K. Sichel, J.I. Gittleman, P. Sheng, Electrical properties of carbon-polymer composites, J. Electron. Mater. 11 (4) (1982) 699–747.

[89] C. Li, E.T. Thostenson, T.-W. Chou, Dominant role of tunneling resistance in the electrical conductivity of carbon nanotube–based composites, Appl. Phys. Lett. 91 (22) (2007) 223114.

[90] L. He, S.C. Tjong, Low percolation threshold of graphene/polymer composites prepared by solvothermal reduction of graphene oxide in the polymer solution, Nanoscale Res. Lett. 8 (1) (2013) 132.

[91] J.W. Essam, Percolation theory, Rep. Prog. Phys. 43 (7) (1980) 833.

[92] H. Scher, R. Zallen, Critical density in percolation processes, J. Chem. Phys. 53 (9) (1970) 3759–3761.

[93] E.P. Mamunya, V.V. Davidenko, E.V. Lebedev, Percolation conductivity of polymer composites filled with dispersed conductive filler, Polym. Compos. 16 (4) (1995) 319–324.

[94] S.C. Tjong, Polymer Composites With Carbonaceous Nanofillers: Properties and Applications, Wiley-VCH, Weinheim, Germany, 2012.

[95] I. Webman, J. Jortner, M.H. Cohen, Critical exponents for percolation conductivity in resistor networks, Phys. Rev. B 16 (6) (1977) 2593–2596.

[96] C.W. Nan, Physics of inhomogeneous inorganic materials, Prog. Mater. Sci. 37 (1) (1993) 1–116.

[97] I. Balberg, C.H. Anderson, S. Alexander, N. Wagner, Excluded volume and its relation to the onset of percolation, Phys. Rev. B 30 (7) (1984) 3933–3943.

[98] I. Balberg, Excluded-volume explanation of Archie's law, Phys. Rev. B 33 (5) (1986) 3618–3620.

[99] G.D. Liang, S.C. Tjong, Electrical properties of percolative polystyrene/carbon nanofiber composites, IEEE Trans. Dielectr. Electr. Insul. 15 (1) (2008) 214–220.

[100] W. Lu, H. Lin, D. Wu, G. Chen, Unsaturated polyester resin/graphite nanosheet conducting composites with a low percolation threshold, Polymer 47 (12) (2006) 4440–4444.

[101] L. Flandin, A. Chang, S. Nazarenko, A. Hiltner, E. Baer, Effect of strain on the properties of an ethylene–octene elastomer with conductive carbon fillers, J. Appl. Polym. Sci. 76 (6) (2000) 894–905.

[102] A. Das, K.W. Stöckelhuber, R. Jurk, M. Saphiannikova, J. Fritzsche, H. Lorenz, M. Klüppel, G. Heinrich, Modified and unmodified multiwalled carbon nanotubes in high performance solution-styrene–butadiene and butadiene rubber blends, Polymer 49 (24) (2008) 5276–5283.

[103] B.G. Soares, F. Gubbels, R. Jérôme, E. Vanlathem, R. Deltour, Electrical conductivity of polystyrene-rubber blends loaded with carbon black, Rubber Chem. Technol. 70 (1) (1997) 60–70.

[104] K.P. Sau, T.K. Chaki, D. Khastgir, Electrical and mechanical properties of conducting carbon black filled composites based on rubber and rubber blends, J. Appl. Polym. Sci. 71 (6) (1999) 887–895.

[105] G.T. Mohanraj, T.K. Chaki, A. Chakraborty, D. Khastgir, Effect of some service conditions on the electrical resistivity of conductive styrene-butadiene rubber-carbon black composites, J. Appl. Polym. Sci. 92 (4) (2004) 2179–2188.

[106] S. Salaeh, C. Nakason, Influence of modified natural rubber and structure of carbon black on properties of natural rubber compounds, Polym. Compos. 33 (4) (2012) 489–500.

[107] M.J. Jiang, Z.M. Dang, H.P. Xu, Significant temperature and pressure sensitivities of electrical properties in chemically modified multiwall carbon nanotube/methylvinyl silicone rubber nanocomposites, Appl. Phys. Lett. 89 (18) (2006).

[108] C.H. Liu, S.S. Fan, Nonlinear electrical conducting behavior of carbon nanotube networks in silicone elastomer, Appl. Phys. Lett. 90 (4) (2007).

[109] H. Lorenz, J. Fritzsche, A. Das, K.W. Stöckelhuber, R. Jurk, G. Heinrich, M. Klüppel, Advanced elastomer nano-composites based on CNT-hybrid filler systems, Compos. Sci. Technol. 69 (13) (2009) 2135–2143.

[110] J. Fritzsche, H. Lorenz, M. Klüppel, CNT based elastomer-hybrid-nanocomposites with promising mechanical and electrical properties, Macromol. Mater. Eng. 294 (9) (2009) 551–560.

[111] A.S.A. Reffaee, D.E. El Nashar, S.L. Abd-El-Messieh, K.N. Abd-El Nour, Electrical and mechanical properties of acrylonitrile rubber and linear low density polyethylene composites in the vicinity of the percolation threshold, Mater. Des. 30 (9) (2009) 3760–3769.

[112] Y. Sun, Z.X. Guo, J. Yu, Effect of ABS rubber content on the localization of MWCNTs in PC/ABS blends and electrical resistivity of the composites, Macromol. Mater. Eng. 295 (3) (2010) 263–268.

[113] I. Kang, M.A. Khaleque, Y. Yoo, P.J. Yoon, S.Y. Kim, K.T. Lim, Preparation and properties of ethylene propylene diene rubber/multi walled carbon nanotube composites for strain sensitive materials, Compos. A: Appl. Sci. Manuf. 42 (6) (2011) 623–630.

[114] M. Hernández, M. Bernal, R. Verdejo, T.A. Ezquerra, M.A. López-Manchado, Overall performance of natural rubber/graphene nanocomposites, Compos. Sci. Technol. 73 (1) (2012) 40–46.

[115] A. Das, G.R. Kasaliwal, R. Jurk, R. Boldt, D. Fischer, K.W. Stöckelhuber, G. Heinrich, Rubber composites based on graphene nanoplatelets, expanded graphite, carbon nanotubes and their combination: a comparative study, Compos. Sci. Technol. 72 (16) (2012) 1961–1967.

[116] S.K. Peddini, C.P. Bosnyak, N.M. Henderson, C.J. Ellison, D.R. Paul, Nanocomposites from styrene-butadiene rubber (SBR) and multiwall carbon nanotubes (MWCNT) part 1: morphology and rheology, Polymer 55 (1) (2014) 258–270.

[117] S. Araby, N. Saber, X. Ma, N. Kawashima, H. Kang, H. Shen, L. Zhang, J. Xu, P. Majewski, J. Ma, Implication of multi-walled carbon nanotubes on polymer/graphene composites, Mater. Des. 65 (2015) 690–699.

[118] V.Y. Dolmatov, Polymer-diamond composites based on detonation nanodiamonds. Part 2, J. Superhard Mater. 29 (2) (2007) 65–75.

[119] V.Y. Dolmatov, Composition materials based on elastomer and polymer matrices filled with nanodiamonds of detonation synthesis, Nanotechnol. Russ. 4 (9) (2009) 556.

[120] F.H. Jahromi, A.A. Katbab, Nanodiamond-based PP/EPDM thermoplastic elastomer composites: microstructure, tribo-dynamic, and thermal properties, J. Appl. Polym. Sci. 125 (3) (2012) 1942–1950.

[121] V.N. Mochalin, Y. Gogotsi, Nanodiamond–polymer composites, Diam. Relat. Mater. 58 (2015) 161–171.

[122] M.D. Bartlett, N. Kazem, M.J. Powell-Palm, X. Huang, W. Sun, J.A. Malen, C. Majidi, High thermal conductivity in soft elastomers with elongated liquid metal inclusions, Proc. Natl. Acad. Sci. 114 (9) (2017) 2143.

[123] D.D.L. Chung, Materials for thermal conduction, Appl. Therm. Eng. 21 (16) (2001) 1593–1605.

[124] C.H. Liu, H. Huang, Y. Wu, S.S. Fan, Thermal conductivity improvement of silicone elastomer with carbon nanotube loading, Appl. Phys. Lett. 84 (21) (2004) 4248–4250.

[125] J. Hong, J. Lee, C.K. Hong, S.E. Shim, Effect of dispersion state of carbon nanotube on the thermal conductivity of poly(dimethyl siloxane) composites, Curr. Appl. Phys. 10 (1) (2010) 359–363.

[126] J. Hong, J. Lee, C.K. Hong, S.E. Shim, Improvement of thermal conductivity of poly(dimethyl siloxane) using silica–coated multi-walled carbon nanotube, J. Therm. Anal. Calorim. 101 (1) (2010) 297–302.

[127] H. Huang, C. Liu, Y. Wu, S. Fan, Aligned carbon nanotube composite films for thermal management, Adv. Mater. 17 (13) (2005) 1652–1656.

[128] G. Zhang, F. Wang, J. Dai, Z. Huang, Effect of functionalization of graphene nanoplatelets on the mechanical and thermal properties of silicone rubber composites, Materials 9 (2) (2016).

[129] M. Raja, A.M. Shanmugharaj, S.H. Ryu, J. Subha, Influence of metal nanoparticle decorated CNTs on polyurethane based electro active shape memory nanocomposite actuators, Mater. Chem. Phys. 129 (3) (2011) 925–931.

[130] A.S. Fiorillo, C.D. Critello, A.S. Pullano, Theory, technology and applications of piezoresistive sensors: a review, Sensors Actuators A Phys. 281 (2018) 156–175.

[131] S. Kim, S. Choi, E. Oh, J. Byun, H. Kim, B. Lee, S. Lee, Y. Hong, Revisit to three-dimensional percolation theory: accurate analysis for highly stretchable conductive composite materials, Sci. Rep. 6 (2016)34632.

[132] Y. Tang, Z. Zhao, H. Hu, Y. Liu, X. Wang, S. Zhou, J. Qiu, Highly stretchable and ultrasensitive strain sensor based on reduced graphene oxide microtubes–elastomer composite, ACS Appl. Mater. Interfaces 7 (49) (2015) 27432–27439.

[133] R. Zhang, H. Deng, R. Valenca, J. Jin, Q. Fu, E. Bilotti, T. Peijs, Strain sensing behaviour of elastomeric composite films containing carbon nanotubes under cyclic loading, Compos. Sci. Technol. 74 (2013) 1–5.

[134] K. Suzuki, K. Yataka, Y. Okumiya, S. Sakakibara, K. Sako, H. Mimura, Y. Inoue, Rapid–response, widely stretchable sensor of aligned MWCNT/elastomer composites for human motion detection, ACS Sens. 1 (6) (2016) 817–825.

[135] T. Yamada, Y. Hayamizu, Y. Yamamoto, Y. Yomogida, A. Izadi-Najafabadi, D.N. Futaba, K. Hata, A stretchable carbon nanotube strain sensor for human-motion detection, Nat. Nanotechnol. 6 (2011) 296.

[136] S. Pavlovsky, A. Siegmann, Chemical sensing materials II: Electrically conductive peroxide crosslinked SEBS copolymers systems, J. Appl. Polym. Sci. 114 (3) (2009) 1390–1396.

[137] D. Ponnamma, K.K. Sadasivuni, S. Thomas, I. Krupa, M.A.-A. AlMa'adeed, Flexible oil sensors based on multiwalled carbon nanotube–filled isoprene elastomer composites, Rubber Chem. Technol. 89 (2) (2015) 306–315.

[138] J. Jeddi, A.A. Katbab, The electrical conductivity and EMI shielding properties of polyurethane foam/silicone rubber/carbon black/nanographite hybrid composites, Polym. Compos. 39 (10) (2018) 3452–3460.

[139] M. Izadi, F. Danafar, M.Z.A.A. Kadir, Natural rubber—carbon nanotubes composites, recent advances and challenges for electrical applications, in: Proceedings—2016 IEEE International Conference on Automatic Control and Intelligent Systems, I2CACIS 2016, 2017, pp. 61–65.

Further reading

[140] G. Calzaferri, R. Rytz, The band structure of diamond, J. Phys. Chem. 100 (26) (1996) 11122–11124.

This page intentionally left blank

CHAPTER 8

Testing of rubber nanocomposites for aerospace, automotive and oil and gas applications

A. Alvino, S. Borsini
SERMS srl, Terni, Italy

Contents

1 Introduction

Elastomers are traditionally used in industrial components due to their low cost, flexibility, good processability and light weight solutions as metal parts replacement. Nowadays, some critical aspects remain unsolved mainly if their application in extreme environments is demanded [1–6]; for example the development of high performance elastomeric materials working in high pressure and temperature environments like those of oil and gas extraction environment is still challenging; moreover, in extreme locations where also the extreme conditions such icing problems become hazardous, the extraction activities are limited as well as in transportation where bearing seals

---

mounted on aircraft components are subjected to icing problems, a solution is required [7–11].

Elastomeric applications are subjected to fatigue cracks, blistering, and swelling. Such mechanical and chemical damages limit their original functions and can be a serious issue in terms of safety hazards when the elastomers are used as seals and hoses. The occurrence of the first cracks makes the material susceptible to further damage. For this reason, the first issue that a materials scientist has to take in consideration when designing and realizing elastomers, are the hostile conditions to which they are exposed when operating in extreme environments and the subsequent innovations that have been developed for their use. High performance elastomers in rubber–based fuel line and sealing components that operate in hostile environments in contact with oil and gas are required; the resistance to both high pressure and temperature is a serious technological challenge in such field, since it is difficult to improve significantly both properties.

In oil field applications, elastomers are subjected to dramatic swelling and rapid gas decompression that hinder their stability for long periods of time.

All these applications will require a series of tests in order to evaluate the appropriateness of an elastomeric material generally successfully used for bearing seals and gaskets in automotive applications to be also used in an aeronautical environment. Such tests have been performed at SERMS srl, an Italian environmental tests laboratory, following a specific material characterization program provided by its customer and edited based on the knowledge of the Life Cycle Environmental Profile of its specific application.

2 Cold temperature degradation

Elastomeric gaskets, like those made from nitrile rubber, work because they are flexible. Compressed in a flange, the material fills the gap between joint faces, regardless of how each side moves. When a joint gets cold the gap often grows wider, and the gasket material is expected to recover enough to maintain a good seal. When elastomers become very cold they lose this ability. When choosing gasket material for an application that could see low temperatures it's important to check it has sufficient low temperature flexibility. Nitrile rubber and neoprene gaskets are flexible because they are made from entangled chains of molecules that move over one another. When temperatures drop, contraction limits the movement of these molecules and the material gets stiffer. Eventually, there's no room for any

movement and the material becomes brittle. The "freezing" temperature of an elastomer is termed its glass transition temperature (T_g). Strictly speaking, freezing happens over a range, and the brittle point is several degrees lower than the T_g. What matters for gaskets though is when the material loses any ability to recover. For reliable in-service performance, these values must be lower than the worst conditions the gasket will experience.

2.1 Test description

Scope of this test is to determine the effect of the cold temperature according to the parameters required by the customer: $T = -55\,°C$, 3 min of exposure. To evaluate the effect on the specimens, a Differential Scanning Calorimeter (DSC) has been used. The DSC is a machine that measures temperatures and heat flows associated with thermal transitions in a material. A measurement of the T_g of each specimen has been done before and after the cold temperature test. Four specimens, having dimensions 50×25 mm coming from the same batch, have been inspected. Two specimens have been used to evaluate the original glass transition temperature value and two specimens have been used to evaluate the glass transition temperature value after the cold temperature test. Below, the results of the DSC test (glass transition temperature) will be shown. To evaluate the glass transition temperature, a TA Instrument DSC has been used. The samples have been exposed to a thermal cycle with a temperature gradient of $10\,°C/min$ in the range from $-80\,°C$ to $20\,°C$. The thermal cycle is made of three phases: first heating, cooling and second heating. The glass transition temperature value has been evaluated during second heating. In this section, the glass transition temperature value of two samples taken from the same batch of the samples that will be exposed to cold temperature are summarized. The values are summarized on a table and the graph (heat flow vs temperature) for each sample are shown in Table 1.

The two samples were exposed to the test environment with the following parameters:
- temperature: $-55\,°C \pm 2\,°C$
- exposure time: 3 min

Table 1 Glass transition temperature of the original samples (pre) and exposed (post) to cold temperature

Samples ID	T_g (pre) (°C)	T_g (post) (°C)
CR1	−55.27	−54.63
CR2	−54.02	−54.41

The final glass transition temperature values of two samples, taken from the same batch, exposed to cold temperature are reported. The values are summarized on a table and the graphs (heat flow vs. temperature) for each sample are shown in Table 1.

3 UV degradation

Another dominant factor in selecting a material for outdoor application like elastomeric gasket is UV degradation. The UV interacts with the carbon bonds in the molecular chains of the elastomer. This produces free radicals which then react with oxygen to produce carbonyl groups, in other words a stress–induced chemical attack. The earliest sign on exposed surfaces of elastomer gaskets will be discoloration, with excessive exposure in prone materials leading to subsequent cracking and, in extreme cases, disintegration.

3.1 Test description

Scope of this test is to determine the Xenotest resistance according to the ASTM G 155 cycle 2 for a total of 240 h. To evaluate the Xenotest resistance of the specimens, a differential scanning calorimeter (DSC) has been used. A measurement of the T_g of each specimen has been done before and after the Xenotest Resistance. Four specimens having dimensions 130×40 mm coming from the same have been used. Two specimens have been used to evaluate the original glass transition temperature value. Two specimens have been used to evaluate the glass transition temperature value after the Xenotest. Photos of each samples have been taken at the beginning and after the Xenotest exposure in order to visually examine the specimens to assess the presence of any damage or discolor. In this section, the results of the Xenotest resistance (visual examination) and the DSC test (glass transition temperature) will be shown.

In this section, the glass transition temperature values of two samples, taken from the same batch, exposed to Xenotest are reported. The values are summarized on a Table 2. The graphs (heat flow vs. temperature) have been omitted in order to avoid making the chapter too cumbersome.

The two samples were exposed to the test environment with the following parameters:
- Cycle: 2 ASTM G 155
- Filter: daylight
- Irradiance: 0.35 W/m^2/nm
- Wavelength: 340 nm

Table 2 Glass transition temperatures of the samples before (second column) and after (third column) the exposition to Ozone Xeno-test (in accordance with to the standard ASTM G 155)

Samples ID	T_g (°C)	T_g (°C)
UV1_DSC	−54.78	−55.19
UV2_DSC	−55.42	−54.74

– Exposure cycle: 102 min light at 63 (62.5) °C; black panel temperature 18 min light and water spray; 6 h dark at 95(64) %RH, at 24 (62.5) °C black panel temperature

The final glass transition temperature values of two samples, taken from the same batch, exposed to Xenotest are reported. The values are summarized on a table.

4 Fluid resistance

Elastomeric gaskets may be exposed to oils, greases, fuels, and other fluids during service. The exposure may be continuous or intermittent and may occur over wide temperature ranges. Properties of rubber articles deteriorate during exposure to these liquids, affecting the performance of the rubber part, which can result in partial failure. The fluid resistance test attempts to simulate service conditions through controlled accelerated testing and to evaluate the change in physical properties such as tensile strength, elongation at break, hardness and volume change after exposure of the test item to a variety of fluids for which they may be exposed during their lifetime.

The main fluids come from environments encountered in the aeronautical, automotive and military sectors and are classified by family:

- fuels
- solvents and cleaning liquid
- de–icing liquid

4.1 Test description

To evaluate the ability of rubber to withstand the effect of liquids the test specimens have been exposed to the influence of liquids under definite conditions of temperature and time. The resulting deterioration is determined by measuring the changes in physical properties, such as stress/strain

properties, hardness, and changes in mass, volume before and after immersion in the test liquid.

Two set of specimens have been used: Dumbbell–shaped specimens used to evaluate the tensile strength and the elongation at breaks and rectangular specimens (50×25 mm) to evaluate the hardness (shore A) and the change in mass and volume. In the next figure the dimensions of the Dumbbell–shaped specimens are shown.

A minimum number of three Dumbbell–shaped specimens and rectangular specimens have been used for each fluid (Fig. 1).

For every fluid, specimens have been immersed in the appropriate fluid for a minimum 70 h at the temperature indicated in Table 3. Then the physical properties (tensile strength, elongation at breaks, hardness and change in mass and volume) have been evaluated and compared with the original value of the specimens before the immersion period. The original values of the physical properties of the specimens have been evaluated in ambient conditions ($20\,°C$).
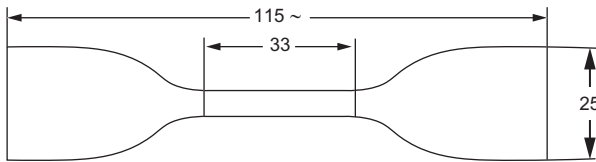
Fig. 1 Dumbbell-shaped specimens for the evaluation of the tensile strength and elongation at breaks.

Table 3 Classes of test fluids and fluid temperature

Class of contaminating fluid	Test fluid	Fluid temperature (°C)
Fuel	Fuel jet A1	40
Hydraulic fluids	Aeroshell fluid 41 (mineral based)	80
	Aeroshell fluid 31 (synthetic fluid)	70
Solvent and cleaning fluids	Isopropyl alcohol	50
	Denatured alcohol	23
	Fulcron	23
	Trans 1–2dichloroethylene	23
De–icing fluids	Ethylene glycol	50
	Propylene glycol	50

At the end of the required immersion period, the specimens have been removed and cooled to room temperature for 60 min. Then each specimen has been quickly dipped in acetone and blotted lightly with filter paper. Then the physical properties have been evaluated.

4.2 Tensile strength and elongation at breaks

To evaluate the tensile strength a Lloyd INSTRUMENT dynamometer has been used (Fig. 2).

The tensile strength and elongation at breaks on the dumbbell–shaped specimens have been evaluated after they have been exposed for 70 h on each fluids of Table 3. In Table 4 the results of the liquid effects are shown as a percentage of the change in each physical property, calculated as follow

$$DP\% = [(P_i - P_o)/Po] \times 100$$

where

  DP % = change in property (tensile strength and elongation at breaks) after immersion (%)

  P_i = Property (value evaluated in the test of the tested specimens) after immersion

  P_o = original property before immersion (average value evaluated from the test on the original specimens, not been exposed to any environmental conditions)
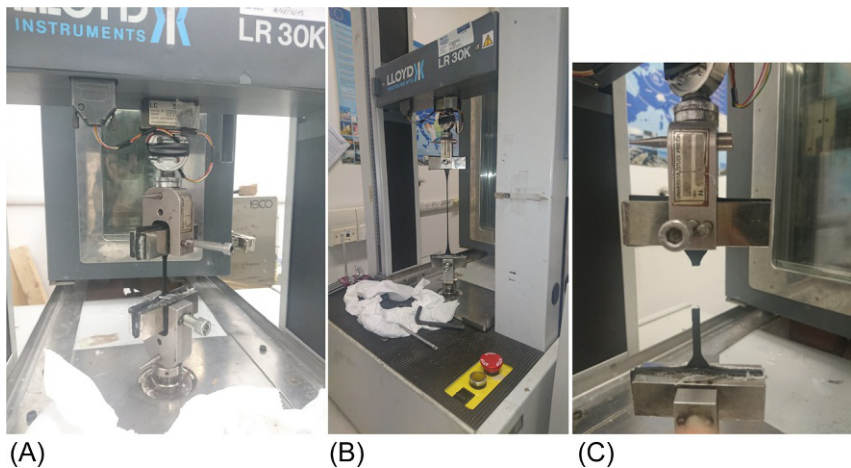
Fig. 2 (A) Tensile strength and elongation at breaks—details of the set up. (B) Tensile strength and elongation at breaks—details of the test. (C) Tensile strength and elongation at breaks—details specimen broken.

Table 4 Tensile strength and elongation at breaks—effects of exposition to different fluids

Test fluid	Original value		Post-immersion test (mean value)		Percentage of the change (mean value)	
	Elongation at breaks (%)	Tensile strength (MPa)	Elongation at breaks (%)	Tensile strength (MPa)	Tensile strength (MPa)	Elongation at breaks (%)
Ethylene glycol	326	15.56	363.80	14.05	−9.72	11.60
Fuel jet A1	326	15.56	372.03	14.76	−5.15	14.12
Propylene glycol	326	15.56	386.85	13.99	−10.10	18.67
Denatured alcohol	326	15.56	340.86	13.39	−13.96	4.56
Fulcron	326	15.56	325.06	12.64	−18.78	−0.29
Aeroshell fluid 31	326	15.56	338.17	14.32	−7.98	3.74
Isopropyl alcohol	326	15.56	310.99	12.49	−19.74	−4.60
Aeroshell fluid 41	326	15.56	257.69	11.70	−24.82	−20.95
Trans 1–2dichloroethylene	326	15.56	135.81	6.091	−60.86	−58.34

4.3 Hardness strength

To evaluate the hardness an O.M.A.G. hardness tester model n° art 13 have been used (Fig. 3).

   The hardness (Shore A) has been evaluated on the rectangular specimens after they have been exposed for 70 h on each fluids of Table 3. In Table 5
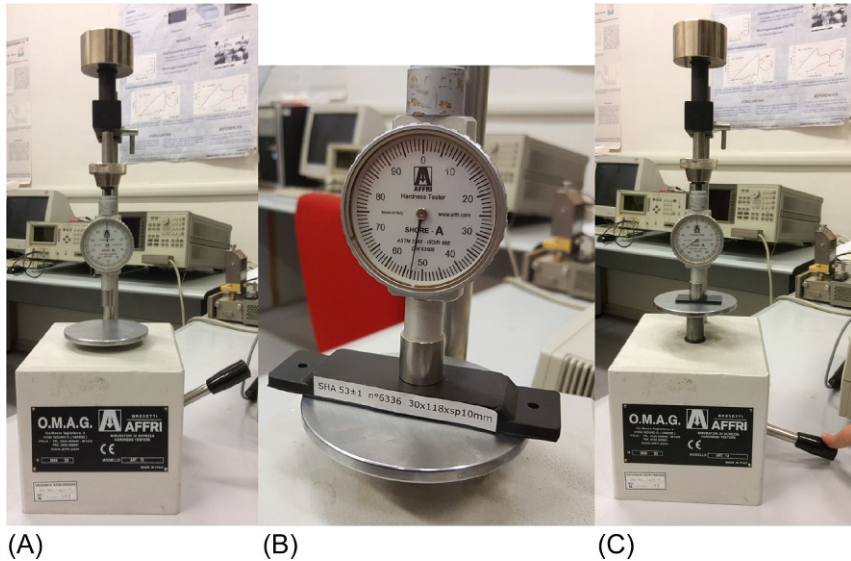
Fig. 3 (A) Hardness tester used to evaluate the hardness (shore A) of the specimens. (B) Hardness tester used to evaluate the hardness (shore A) of the specimens— details of the calibration done using a calibrated specimen. (C) Hardness tester used to evaluate the hardness (shore a) of the specimens—details of the test.

Table 5 Hardness strength—effects of explosion to different fluids

Test fluid	Original hardness value— (Shore A)	Post immersion hardness— (Shore A)	Hardness variation
Ethylene glycol	65.6	69	3.4
Fuel jet A1	65.6	64	−1.6
Propylene glycol	65.6	69	3.4
Denatured alcohol	65.6	65	−0.6
Fulcron	65.6	61	−4.6
Aeroshell fluid 31	65.6	63	−2.6
Isopropyl alcohol	65.6	62	−3.6
Aeroshell fluid 41	65.6	56	−9.6
Trans 1–2dichloroethylene	65.6	51	−14.6

the results of the liquid effects are shown as a hardness change, calculated as follow

$$DH = H_i - H_o$$

where

DH = hardness change after immersion, in hardness unit

H_i = hardness after immersion, in hardness unit

H_o = original value (average value evaluated from the test on the original specimens, not been exposed to any environmental conditions)

4.4 Change in mass and volume

To evaluate the mass and volume a Mettler–Toledo analytical scale model AB135–S/FACT has been used.

The mass and volume have been evaluated on the rectangular specimens after they have been exposed for 70 h on each fluids of Table 3. In Table 6 the results of the liquid effects are shown as percentage change, calculated as follow

$$\Delta M\% = (M_2 - M_1)/M_1 * 100$$
$$\Delta V\% = (V_2 - V_1)/V_1 * 100$$

where

ΔM = change in mass (%)

M_1 = initial mass of specimen in air, g

M_2 = mass of specimen in air after immersion, g

ΔV = change in volume (%)

V_1 = initial volume of specimen, cm^3

V_2 = volume of specimen after immersion, cm^3

5 Compression set test

Compression set test is intended to measure the ability of rubber compounds to retain elastic properties after prolonged action of compressive stresses. This test is applicable to the rubber used in machinery mounting, vibration dampers and seals.

5.1 Test description

The specimens are compressed under a constant deflection and maintained under this condition for a specified time and at a specified temperature.

Table 6 Change in mass and volume—effects of explosion to different fluids

Fluid	Original value		Post immersion value		Percentage variation	
	Weight (g)	Volume (cm^3)	Weight (g)	Volume (cm^3)	Weight (%)	Volume (%)
Ethylene glycol	3.70798	3.70544	3.58696	3.58380	−3.26	−3.28
Fuel jet A1	3.64476	3.64276	3.72450	3.72144	2.19	2.16
Propylene glycol	3.64255	3.64030	3.45547	3.45160	−5.14	−5.18
Denatured alcohol	3.69508	3.69264	3.74962	3.72968	1.48	1.00
Fulcron	3.66837	3.66668	3.59710	3.58218	−1.94	−2.30
Aeroshell fluid 31	3.68016	3.67798	3.94058	3.93524	7.08	6.99
Isopropyl alcohol	3.68604	3.68406	3.71748	3.71410	0.85	0.82
Aeroshell fluid 41	3.56797	3.56598	4.39206	4.38716	23.10	23.03
Trans 1–2dichloroethylene	3.60971	3.60792	6.05762	5.95626	67.81	65.09

The specimens have been used are cylindrical disk with the following dimensions:

- Thickness, mm: 6.0±0.2
- Diameter, mm: 13.0±0.2

The compression device consisted of two flat steel plates between the parallel faces of which the specimens will be compressed (see Fig. 4).

Steel spacers (thickness 4.50±0.01 mm) have been placed on each side of the rubber specimens to control their thickness while compressed (see Figs. 5–7).

The assembled device has been placed in a climatic chamber and it remained at 100°C for 22h. At the end of the test period, the device has been taken from the climatic chamber and the test specimens have been removed. The specimens have been placed on a wood surface for 30 min before making the measurement of the final thickness. In Table 7 the initial thickness measurements and the final ones are shown. The compression set will be expressed as a percentage of the deflection as follows:

$$CB = [(t_0 - t_i)/(t_0 - t_n)] \times 100$$

where

CB = compression set expressed as percentage of the original deflection

t_0 = original thickness of the specimen

t_i = final thickness of the specimen

t_n = thickness of the spacer bar used

6 Conclusions

Common challenges for developing materials in extreme environment promote the opportunities to discover crossover solutions; for example, sealing
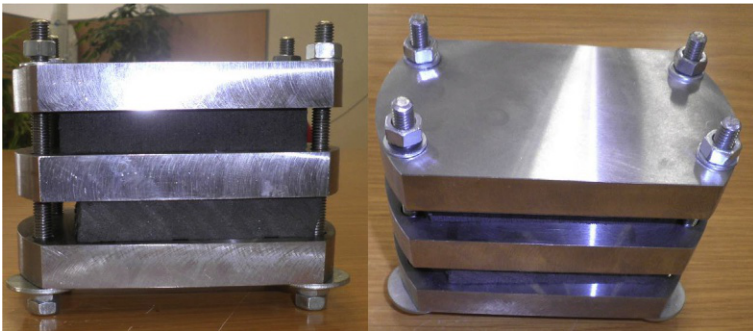
Fig. 4 Device for compression set test under constant deflection, test method B.
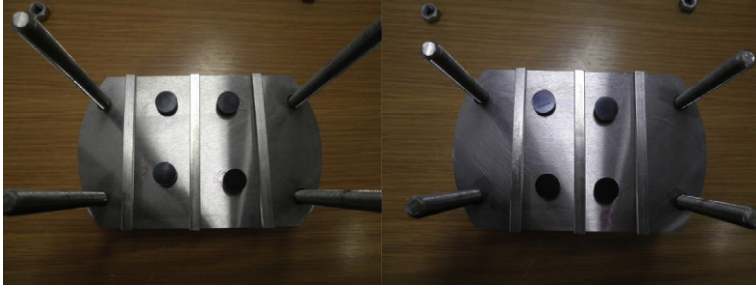
Fig. 5 Compression set test—test set up.
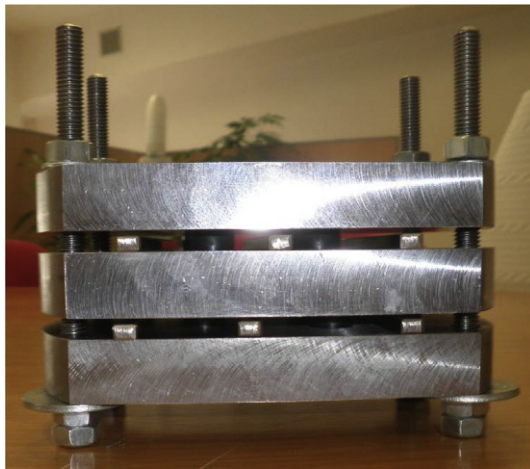
Fig. 6 Compression set test—assembled device.

Fig. 7 Compression set test—details of the deflection.

Table 7 Specimens thickness pre and post test and compression set value

Sample no.	Original thickness (mm)	Thickness after test (mm)	Compression set (%)
1	5.95	5.780	12.03
2	5.95	5.800	10.34
3	5.95	5.750	13.79
4	5.94	5.790	10.42
5	5.97	5.820	10.20
6	5.93	5.780	10.49
7	5.97	5.810	10.88
8	5.96	5.810	10.27

materials being developed in the energy sector for ultra–high–temperature applications are generating interest in aerospace. These new technologies will have an impact on several areas by increasing the competitiveness of European industry through the use of customized elastomeric nanocomposites to be used in extreme environments. Hence, helping Industry to become leader in graphitic materials technologies supporting worldwide customers with specialized, value-added, groundbreaking solutions for their advanced applications in several sectors (oil and gas, automotive, aeronautics); enabling a more widespread use of a high % of ethanol in petrol through the validation of a new generation of ethanol resistant vehicle components. The widespread diffusion of high percentage (>10%) ethanol blended gasoline is connected to their capability to lower CO_2 emissions, on the other hand, a market barrier is the risk to damage plastic and rubber components in cars and handheld products. Low permeation rate and a reduced interaction with the solvent (lower swelling) leads to the competitiveness of such polymers with new biofuels and finally opening the market to new products i.e. advanced sealings, corrosion resistant hoses. Thus, the development of reliable, high–performing elastomeric materials will continue to have a crucial role for industrial players.

References

[1] T. Baird, T. Fields, R. Drummond, D. Mathison, B. Langseth, A. Martin, et al., High-pressure, high-temperature well logging, perforating and testing, Oilfield Rev. 10 (1998) 50–67.
[2] C. Baudet, J.C. Grandidier, L. Cangémi, A damage model for the blistering of polyvinylidene fluoride subjected to carbon dioxide decompression, J. Mech. Phys. Sol. 59 (2011) 1909–1926.

[3] K. Bertoldi, P.M. Reis, S. Willshaw, T. Mullin, Negative Poisson's ratio behavior induced by an elastic instability, Adv. Mater. 22 (2010) 361–366.

[4] R.P. Campion, Durability review of elastomers for severe fluid duties, Rubber Chem. Technol. 76 (2003) 719–746.

[5] M.K. Chaudhury, K.H. Kim, Shear-induced adhesive failure of a rigid slab in contact with a thin confined film, Eur. Phys. J. 23 (2007) 175–183.

[6] M. Endo, T. Noguchi, M. Ito, K. Takeuchi, T. Hayashi, Y.A. Kim, et al., Extreme-performance rubber nanocomposites for probing and excavating deep oil resources using multi-walled carbon nanotubes, Adv. Funct. Mater. 18 (2008) 3403–3409.

[7] L. Valentini, S. Bittolo Bon, M.A. Lopez-Manchado, R. Verdejo, L. Pappalardo, A. Bolognini, et al., Synergistic effect of graphene nanoplatelets and carbon black in multifunctional EPDM nanocomposites, Compos. Sci. Technol. 128 (2016) 123–130.

[8] L. Valentini, S. Bittolo Bon, N.M. Pugno, Graphene and carbon nanotube auxetic rubber bionic composites with negative variation of the electrical resistance and comparison with their nonbionic counterparts, Adv. Funct. Mater. 27 (2017)1606526.

[9] Y. Vega-Cantú, R. Hauge, L. Norman, W.E. Billups, Enhancement of the chemical resistance of nitrile rubber by direct fluorination, J. Appl. Polym. Sci. 89 (2003) 971–979.

[10] K.E. Prasad, B. Das, U. Maitra, U. Ramamurty, C.N.R. Rao, Extraordinary synergy in the mechanical properties of polymer matrix composites reinforced with 2 nanocarbons, Proc. Natl. Acad. Sci. U. S. A. 1060 (2009) 13186–13189.

[11] S. Rooj, A. Das, G. Heinrich, Tube-like natural halloysite/fuoroelastomer nanocomposites with simultaneous enhanced mechanical, dynamic mechanical and thermal properties, Eur. Polym. J. 47 (2011) 1746–1755.

This page intentionally left blank

CHAPTER 9

Analytical solutions for monoclinic/trigonal structures replicating multi-wall carbon nano-tubes for applications in composites with elastomeric/polymeric matrix

A. Cutolo[a], A.R. Carotenuto[a], F. Carannante[a], N. Pugno[b,c,d,e], M. Fraldi[a,b]
[a]Department of Structures for Engineering and Architecture, University of Napoli "Federico II", Napoli, Italy
[b]Laboratory of Bio-Inspired and Graphene Nanomechanics, University of Trento, Trento, Italy
[c]Ket Lab, Edoardo Amaldi Foundation, Rome, Italy
[d]Department of Civil, Environmental and Mechanical Engineering and Laboratory of Bio-inspired and Graphene Nanomechanics, University of Trento, Trento, Italy
[e]School of Engineering and Materials Science, Queen Mary University of London, London, United Kingdom

Contents

1 Introduction

Structures like MWCNTs can be idealized as composite cylinders constituted by a selected number (the *walls*) of layers with overall monoclinic/trigonal elastic behavior. This typology falls in the wide class of non–homogeneous

composite materials represented by Functionally Graded Materials (FGMs), frequently observed also in biological tissues at different scale levels and met in some man–made media, classically constituted by a continuous or piece–wise assembling of two or more basic components arranged along a prescribed direction (an example being represented by classical laminates). Within this wide class of composites, multi-phase cylinders constituted by $n \in \mathbb{N}$ hollow layers enveloping a central core (*n*–plies Functionally Graded Material Cylinders, n–FGMCs, see Fig. 1) have been extensively studied in recent literature works because their geometry is often encountered in several situations of engineering interest. Indeed, with the aim to catch the mechanical response of these structures that also include thermal as well as other inelastic effects, analytical solutions have been developed in the last decades by considering both isotropic and laminated composite plates and shells.

In particular, Liew et al. [1] obtained analytical solutions for a functionally graded circular cylinder, by a novel limiting process that employs the solutions of homogeneous circular hollow cylinders, whereas Shao [2] derived analytical solutions for mechanical stresses of a functionally graded circular cylinder with finite length, finding mechanical and thermal stresses for the two-dimensional thermoelastic problems, where the cylinder is assumed to be composed of *n* homogeneous fictitious layers in the radial direction. Mian and Spencer [3] determined some results for isotropic laminated FGMs with specific variation of the elastic moduli in the direction of the axis of the object. Importantly, Fraldi and Cowin [4] obtained further new results for non-homogeneous and anisotropic materials, including FGMs, by using a *Stress-Associated Solution* theorem. Also, Alshits and Kirkhner [5] derived some elastic solutions for radially inhomogeneous and cylindrically anisotropic circular cylinders, where no variations of the stresses along the axis of the cylinder are assumed. Exact analytical solutions for the elastic response of a solid circular cylinder composed by the assembly of a central core and *n* surrounding hollow phases –all made of different homogeneous elastic materials, under de Saint Venant load conditions- have been developed by Fraldi et al. [6], specifying strategies to write the behavior of the whole object into an equivalent one-dimensional homogenized beam model. In this framework, the analytical solution for FGM cylinders constituted of *n* monoclinic phases is illustrated in the following sections of this Chapter. This is of particular interest because the generic monoclinic external hollow phase of the FGMC can be associated in a straightforward manner to the elastic behavior of helically arranged fibers as well as to the microstructure of MWCNTs, that exhibit orthotropic symmetry in the helicoidal local system, by means of standard geometric transformations. As a result, the analytical solution permits
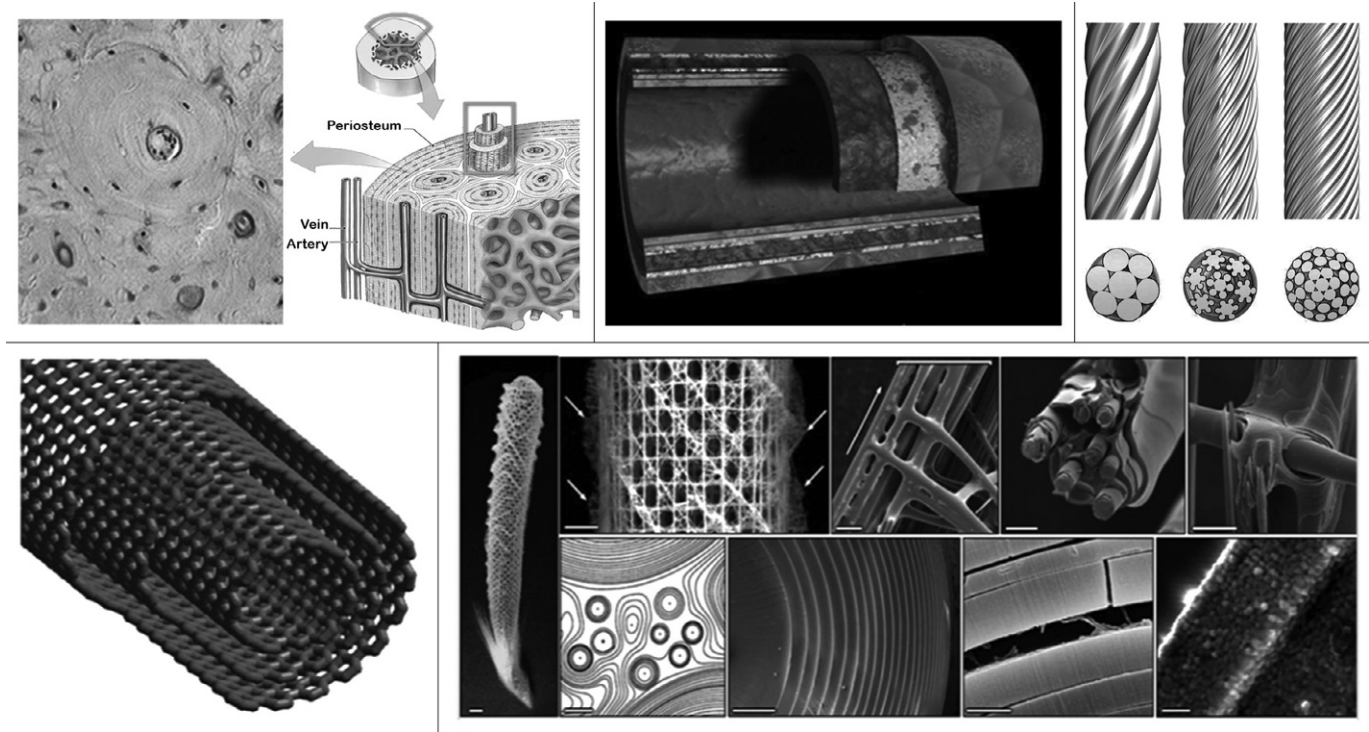
Fig. 1 Selected examples of Functionally Graded Materials: osteon microstructure (top-left); arterial walls (top-central); Hierarchical strands (top-right); multi-wall carbon nanotubes (bottom-left); diatomee microstructures (bottom-right).

to obtain the continuum characterization of complex hierarchical structures such as generic multi-strands constituted by helically arranged orthotropic fibers wrapping with different angles. A complete correspondence between the strand model and the continuum multi-layer monoclinic cylinder, thanks to standard homogenization techniques, can shade the light on important axial-torsional coupling occurring within these particular structures that, in the most of continuum models, is often neglected, with the except of some recent studies such as, for example, the elongation-torsional effect due to the radial inhomogeneity of cords, built up with wire bundles helically arranged around a central fiber or bundle, studied by Fraldi et al. [6a]. In this paper, the authors in fact described the overall stress–strain behavior of the arrangement, by capturing the unpredicted nonlinear and post-elastic features of hierarchical strands. Similar approach will be partially used in this Chapter and then, with in mind MWCNTs, generalized to investigate the role of the coupling between torsion and tensile loads. Other interesting results for laminated composite tubes were obtained by Chouchaoui and Ochoa [7], Chen et al. [8], Tarn [9], and Tarn and Wang [10]. In particular, these last two authors, by employing the so-called *state space approach*, starting from some results obtained by Lekhnitskii [11] and involving an original rearrangement of the field equations that yields to isolate new *state variables*, built up analytical solutions for elastic problems in which the stresses do not vary along the axis of the composite tube. Although under the hypothesis of *generalized plane strain and torsion*, this strategy offers the possibility to find exact solutions for laminated composite tube under extension, torsion, shearing and pressuring, by assuming cylindrically anisotropy for each phase. Huang and Dong [12] presented a procedure for the analysis of stresses and deformations in a laminated circular cylinder of perfectly bonded materials with the most general form of cylindrically anisotropy and Ting [13] furnishes an useful strategy for uncoupling equations in cylindrically anisotropic cylinders, explicitly utilized in the follows. In what follows, we will make reference to a $n + 1$-*phases* layered circular cylinder constituted by n hollow anisotropic homogeneous phase and a central isotropic core, here named *n-plies* Functionally Graded Material Cylinder (*n*-FGMCs).

2 Cylindrically monoclinic materials

If the internal structure of a material possesses a symmetry of any kind, then this symmetry can be observed in its elastic properties. This will occur because the elastic properties are identical to the directions of symmetry that develop in the body (the equivalent directions).

F. Neumann introduced a principle for crystals that establishes the connection between symmetries of construction and elastic symmetries. This principle can be formulated in the following way: a generic material, regard to any of its physical properties, has the same kind of symmetry as its crystallographic form. This principle can be expanded to include bodies which are not crystalline, but which possess a structural symmetry (such as wood or plywood). However, elastic symmetry is usually more extensive than geometric symmetry; in addition to the equivalent directions that coincide with the symmetric directions of the structure, other directions exist for which the elastic properties are identical.

If an anisotropic body possesses an elastic symmetry, then the equations of the generalized Hooke's law are simplified. As known, linear elasticity in Euler's three-dimensional space connects the second-rank Cauchy stress tensor $\mathbf{T}$ to the second-rank strain tensor $\mathbf{E}$ through a relation of direct proportionality mediated by the fourth-order stiffness tensor $\mathbf{C}$, i.e. $\mathbf{T} = \mathbf{C} : \mathbf{E}$. For a generically anisotropic body, the elasticity of the material as well as equilibrium and geometric considerations set the maximum number of independent stiffness constants to 21 (triclinic material). As well-known, however, the occurrence of possible material symmetries can reduce this number up to two sole independent moduli (in case of isotropic materials).

We find these simplifications by applying the following method: we refer the body to a first coordinate system x_1, x_2, x_3 and then to a second coordinate system x'_1, x'_2, x'_3. For the first coordinate system x_1, x_2, x_3 with base vectors $\{\mathbf{e}_1, \mathbf{e}_2, \mathbf{e}_3\}$, the elastic strain potential is

$$V = \frac{1}{2}(\mathbf{C} : \mathbf{E})^T : \mathbf{E} = \frac{1}{2} C_{ijhk} \varepsilon_{ij} \varepsilon_{hk} \qquad (1)$$

and, for the second coordinate system x'_1, x'_2, x'_3 with base vectors $\{\mathbf{e}'_1, \mathbf{e}'_2, \mathbf{e}'_3\}$, it reads:

$$V = \frac{1}{2}(\mathbf{C}' : \mathbf{E}')^T : \mathbf{E}' = \frac{1}{2} C'_{ijhk} \varepsilon'_{ij} \varepsilon'_{hk} \qquad (2)$$

Since the expressions of the elastic potentials have to coincide, one has:

$$\frac{1}{2}(\mathbf{C} : \mathbf{E})^T : \mathbf{E} = \frac{1}{2}(\mathbf{C}' : \mathbf{E}')^T : \mathbf{E}' \qquad (3)$$

We shall express the components ε'_{ij} of the strain tensor $\mathbf{E}'$ in terms of the components ε_{ij} by using the well transformation law of second order tensor tensors, i.e. $\mathbf{E}' = \mathbf{Q} \mathbf{E} \mathbf{Q}^T$, with $\mathbf{Q} = \mathbf{e}'_i \otimes \mathbf{e}_j$ representing an orthogonal transformation matrix. Then, from Eq. (3) one finds that the stiffness components transform between the two systems as $C'_{ijhk} = Q_{ip} Q_{jq} Q_{hr} Q_{ks} C_{pqrs}$. If the directions considered identify axes of structural symmetry, also material

symmetry will occur and equivalent elastic properties are expected with respect to those directions of internal symmetries. Therefore, the greater is the number of symmetries that occur in the internal structure of the material, the simpler is the structure of the stiffness tensor. Each case of symmetry leads to the invariance of the stiffness constants with respect to specific system transformations, which can be rotations about a prescribed axis ($\mathbf{Q} \in Orth^{+}$, i.e. $\mathbf{Q}^{T}\mathbf{Q}=\mathbf{I}$ and $|\mathbf{Q}|=1$) or reflections with respect to a given plane of symmetry (in this case $\mathbf{Q} \in Orth^{-}$, i.e. $\mathbf{Q}^{T}\mathbf{Q}=\mathbf{I}$ and $|\mathbf{Q}|=-1$). The invariance of the stiffness constants due to symmetric transformations requires that:

$$C_{ijhk} = Q_{ip} Q_{jq} Q_{hr} Q_{ks} C_{pqrs} \qquad (4)$$

We conclude that certain coefficients C_{ijhk} are equal to zero, and other coefficients are connected by definite relations. As a result, it turns out that bodies possessing elastic symmetry have a smaller number of independent elastic constants than 21.

If a material has one plane of reflective symmetry and, equivalently, of elastic symmetry, then independent elastic constants reduce to 13. This material is said to possess a monoclinic anisotropy. Let us assume that through each point of a body we draw a plane possessing the property that any two directions symmetric with respect to this plane are equivalent with respect to the elastic properties. As an example, by taking the x_1-axis as normal direction to the plane of elastic symmetry, we have to verify the relations (4) with respect to the reflection matrix $\mathbf{Q}=\mathbf{I}-2\mathbf{e}_1 \otimes \mathbf{e}_1$ and, after some passages, we obtain that $C_{ij1k}=-C_{ij1k}=C_{ijk1}=0$ for $k \neq 1$. Thus, the following equations of the generalized Hooke's law can be written as:

$$\begin{bmatrix} \sigma_{11} \\ \sigma_{22} \\ \sigma_{33} \\ \sigma_{23} \\ \sigma_{13} \\ \sigma_{12} \end{bmatrix} = \begin{bmatrix} c_{11} & c_{12} & c_{13} & c_{14} & 0 & 0 \\ c_{12} & c_{22} & c_{23} & c_{24} & 0 & 0 \\ c_{13} & c_{23} & c_{33} & c_{34} & 0 & 0 \\ c_{14} & c_{24} & c_{34} & c_{44} & 0 & 0 \\ 0 & 0 & 0 & 0 & c_{55} & c_{56} \\ 0 & 0 & 0 & 0 & c_{56} & c_{66} \end{bmatrix} \cdot \begin{bmatrix} \varepsilon_{11} \\ \varepsilon_{22} \\ \varepsilon_{33} \\ \varepsilon_{23} \\ \varepsilon_{13} \\ \varepsilon_{12} \end{bmatrix} \qquad (5)$$

where the Voigt notation has been employed.

3 Transformation of the elastic stiffness tensor from helicoidal to cylindrical coordinate system

Let us consider the helicoidal coordinate system (r, t, c) characterized by unit vector $(\mathbf{e}_r, \mathbf{e}_t, \mathbf{e}_c)$. This coordinate system has unit vector $\mathbf{e}_t$ that tangent to

helix; the unit vector $\mathbf{e}_r$ is perpendicular to $\mathbf{e}_t$; and unit vector $\mathbf{e}_c$ is perpendicular to plane definite by axis "r" and "t".

Let us consider a new coordinate system characterized by cylindrical system (r, φ, x_3). The unit vector of the cylindrical system are denote by $(\mathbf{e}_r, \mathbf{e}_\varphi, \mathbf{e}_3)$.

If cylindrical system has the same origin of the helicoidal system, then the unit vector $\mathbf{e}_r$ is coincident into two coordinate systems. The angle between two versor $\mathbf{e}_t$ and $\mathbf{e}_\varphi$ is identified by θ, that equal to angle between two versor $\mathbf{e}_c$ and $\mathbf{e}_3$.

Euler's theorem on the representation of rigid body rotations has many forms. The theorem concerns the characterization of a three-dimensional rotation by an angle θ about a specific axis, here indicated by the unit vector $\mathbf{p}$. This theorem is represented by the formula [14, 15]:

$$Q = I + P\sin\theta + (1 - \cos\theta)P^2 \tag{6}$$

where $\mathbf{I}$ is the three-dimensional identity tensor, while the three-dimensional skew-symmetric tensor $\mathbf{P}$ with components P_{ij} is introduced to represent the unit vector $\mathbf{p}$,

$$\mathbf{P} = \begin{bmatrix} 0 & -p_3 & p_2 \\ p_3 & 0 & -p_1 \\ -p_2 & p_1 & 0 \end{bmatrix} \quad \text{or} \quad P_{ij} = e_{ijk}p_k \tag{7}$$

where e_{ijk} is the Levi-Civita permutation symbol. It is easy to show that $\mathbf{P}$ has the following properties:

$$\mathbf{P} = -\mathbf{P}^T, \quad \mathbf{P}\mathbf{p} = 0, \quad \mathbf{P}^2 = \mathbf{p} \otimes \mathbf{p} - \mathbf{I}, \quad \mathbf{P}^3 = -\mathbf{P}. \tag{8}$$

The transformation law between cylindrical and helicoidal coordinate system is characterized by a rotation about the radial axis. In this case, the vector $\mathbf{p} = \{1, 0, 0\}$ and skew-symmetric tensor $\mathbf{P}$ becomes:

$$\mathbf{P} = \begin{bmatrix} 0 & 0 & 0 \\ 0 & 0 & -1 \\ 0 & 1 & 0 \end{bmatrix} \tag{9}$$

By substituting the tensor (9) in Eq. (6), we obtain the rotation matrix

$$\mathbf{Q} = \begin{bmatrix} 1 & 0 & 0 \\ 0 & \cos\theta & -\sin\theta \\ 0 & \sin\theta & \cos\theta \end{bmatrix} \tag{10}$$

and the transformation law between helicoidal and cylindrical coordinate systems reads:

$$
\begin{bmatrix} \mathbf{e}_r \\ \mathbf{e}_\varphi \\ \mathbf{e}_z \end{bmatrix} = \begin{bmatrix} 1 & 0 & 0 \\ 0 & \cos\theta & -\sin\theta \\ 0 & \sin\theta & \cos\theta \end{bmatrix} \cdot \begin{bmatrix} \mathbf{e}_r \\ \mathbf{e}_t \\ \mathbf{e}_c \end{bmatrix} = \mathbf{Q} \cdot \begin{bmatrix} \mathbf{e}_r \\ \mathbf{e}_t \\ \mathbf{e}_c \end{bmatrix} \tag{11}
$$

In a space of six dimensions, the representation of a three-dimensional rotation by an angle θ about a specific axis with direction $\mathbf{p}$ is represented by a six-dimensional orthogonal tensor by the formula:

$$
\hat{\mathbf{Q}} = \hat{\mathbf{I}} + \hat{\mathbf{P}}\sin\theta + (1 - \cos\theta)\hat{\mathbf{P}}^2 + \frac{1}{3}\sin\theta(1 - \cos\theta)\left(\hat{\mathbf{P}} + \hat{\mathbf{P}}^3\right)
$$
$$
+ \frac{1}{6}(1 - \cos\theta)^2 \left(\hat{\mathbf{P}}^2 + \hat{\mathbf{P}}^4\right) \tag{12}
$$

Where $\hat{\mathbf{I}}$ is the six-dimensional identity tensor and the skew-symmetric tensor $\hat{\mathbf{P}}$ with components

$$
\hat{\mathbf{P}} = \begin{bmatrix} 0 & 0 & 0 & 0 & \sqrt{2}p_2 & -\sqrt{2}p_3 \\ 0 & 0 & 0 & -\sqrt{2}p_1 & 0 & \sqrt{2}p_3 \\ 0 & 0 & 0 & \sqrt{2}p_1 & \sqrt{2}p_2 & 0 \\ 0 & \sqrt{2}p_1 & -\sqrt{2}p_1 & 0 & p_3 & p_2 \\ -\sqrt{2}p_2 & 0 & \sqrt{2}p_2 & -p_3 & 0 & p_1 \\ \sqrt{2}p_3 & -\sqrt{2}p_3 & 0 & p_2 & -p_1 & 0 \end{bmatrix} \tag{13}
$$

satisfies the conditions

$$
\hat{\mathbf{P}} = -\hat{\mathbf{P}}^T, \quad \hat{\mathbf{P}}^5 + 5\hat{\mathbf{P}}^3 + 4\hat{\mathbf{P}} = \mathbf{0}, \quad \hat{\mathbf{P}}^6 + 5\hat{\mathbf{P}}^4 + 4\hat{\mathbf{P}}^2 = \mathbf{0} \tag{14}
$$

Matrices of six-dimensional tensors have been here distinguished from three-dimensional ones by using hat notation. The rotation matrix (12) is of particular interest in anisotropic elasticity because the elastic tensor can be expressed as a second rank tensor in six dimensions [16], as well as in its more traditional representation as a fourth-rank tensor in three dimensions. In particular, formula (12) helpfully connects the geometric operation in three dimensions to the matrix algebra of six dimensions. Since the tensor transformation rules for a second-rank tensor rather than a fourth-rank tensor apply, transformations of the reference coordinate system for the elasticity tensor may be accomplished in a very straightforward fashion using matrix multiplication.

The anisotropic form of Hooke's law is often written in indicial notation as $\sigma_{ij} = C_{ijkm}\varepsilon_{km}$, where the C_{ijkm} are the components of the three-dimensional fourth order stiffness tensor.

There are three important symmetric restrictions on the components C_{ijkm} of the fourth rank tensor, which make the components with the subscripts $ijkm$, $jikm$ and $kmij$ be equal. Specifically, the major symmetry, which derives from requiring that no work is produced by an elastic material in a

closed loading cycle, gives that $\mathbf{C} = \mathbf{C}^T$ or $C_{ijkm} = C_{kmij}$, while the minor symmetry property, following from the symmetry of the strain tensor and from the equilibrium-derived symmetry of the stress tensor, implies that $C_{ijkm} = C_{jikm} = C_{jimk}$.

Written as a linear transformation in six dimensions, Hooke's law has the representation $\mathbf{T} = \mathbf{c}\mathbf{E}$ or

$$
\begin{bmatrix} \sigma_{11} \\ \sigma_{22} \\ \sigma_{33} \\ \sigma_{23} \\ \sigma_{13} \\ \sigma_{12} \end{bmatrix} = \begin{bmatrix} c_{11} & c_{12} & c_{13} & c_{14} & c_{15} & c_{16} \\ c_{12} & c_{22} & c_{23} & c_{24} & c_{25} & c_{26} \\ c_{13} & c_{23} & c_{33} & c_{34} & c_{35} & c_{36} \\ c_{14} & c_{24} & c_{34} & c_{44} & c_{45} & c_{46} \\ c_{15} & c_{25} & c_{35} & c_{45} & c_{55} & c_{56} \\ c_{16} & c_{26} & c_{36} & c_{46} & c_{56} & c_{66} \end{bmatrix} \cdot \begin{bmatrix} \varepsilon_{11} \\ \varepsilon_{22} \\ \varepsilon_{33} \\ 2\varepsilon_{23} \\ 2\varepsilon_{13} \\ 2\varepsilon_{12} \end{bmatrix} \tag{15}
$$

In Voigt notation, the coefficients $c_{\alpha\beta}$ are related to the components C_{ijkm} through

$$
\alpha = \begin{cases} i & \text{if } i=j \\ 9-(i+j) & \text{if } i \neq j \end{cases} \quad \text{and} \quad \beta = \begin{cases} k & \text{if } k=m \\ 9-(k+m) & \text{if } k \neq m \end{cases} \tag{16}
$$

The matrix $\mathbf{c}$ in Eq. (15) is not a matrix of tensor components in six dimensions, although it is formed by the components of a three-dimensional fourth-rank tensor.

Six-dimensional vector base and notations are introduced so that the stress and strain second-rank tensors in three-dimensional Cartesian reference systems can be expressed as vectors in a six-dimensional vector space. In particular, the six-dimensional vectors of stress and strain are denoted by $\hat{\mathbf{T}}$ and $\hat{\mathbf{E}}$, respectively, whereas the three-dimensional second-rank tensors of stress and strain are denoted by $\mathbf{T}$ and $\mathbf{E}$, respectively. The direct relationship between the components of $\hat{\mathbf{T}}$ and $\mathbf{T}$, and $\hat{\mathbf{E}}$ and $\mathbf{E}$, are dual representations given by

$$
\hat{\mathbf{T}} = \begin{bmatrix} \hat{\sigma}_1 \\ \hat{\sigma}_2 \\ \hat{\sigma}_3 \\ \hat{\sigma}_4 \\ \hat{\sigma}_5 \\ \hat{\sigma}_6 \end{bmatrix} = \begin{bmatrix} \sigma_{11} \\ \sigma_{22} \\ \sigma_{33} \\ \sqrt{2}\sigma_{23} \\ \sqrt{2}\sigma_{13} \\ \sqrt{2}\sigma_{12} \end{bmatrix}, \quad \hat{\mathbf{E}} = \begin{bmatrix} \hat{\varepsilon}_1 \\ \hat{\varepsilon}_2 \\ \hat{\varepsilon}_3 \\ \hat{\varepsilon}_4 \\ \hat{\varepsilon}_5 \\ \hat{\varepsilon}_6 \end{bmatrix} = \begin{bmatrix} \varepsilon_{11} \\ \varepsilon_{22} \\ \varepsilon_{33} \\ \sqrt{2}\varepsilon_{23} \\ \sqrt{2}\varepsilon_{13} \\ \sqrt{2}\varepsilon_{12} \end{bmatrix} \tag{17}
$$

where the shear components of these new six-dimensional stress and strain vectors are the shear components of the three-dimensional stress and strain tensors multiplied by $\sqrt{2}$. This $\sqrt{2}$ factor ensures that the scalar product of the two six-dimensional vectors is equal to the trace of the product of the

corresponding second rank tensors, i.e. $\hat{\mathbf{T}} \cdot \hat{\mathbf{E}} = tr\mathbf{T} \cdot \mathbf{E}$. Therefore, the Eq. (15) can be rewritten in the form:

$$\hat{\mathbf{T}} = \hat{\mathbf{c}}\hat{\mathbf{E}} \tag{18}$$

where $\hat{\mathbf{c}}$ is a new six-by-six matrix given by:

$$
\begin{bmatrix}
\sigma_{11} \\
\sigma_{22} \\
\sigma_{33} \\
\sqrt{2}\sigma_{23} \\
\sqrt{2}\sigma_{13} \\
\sqrt{2}\sigma_{12}
\end{bmatrix}
=
\begin{bmatrix}
c_{11} & c_{12} & c_{13} & \sqrt{2}c_{14} & \sqrt{2}c_{15} & \sqrt{2}c_{16} \\
c_{12} & c_{22} & c_{23} & \sqrt{2}c_{24} & \sqrt{2}c_{25} & \sqrt{2}c_{26} \\
c_{13} & c_{23} & c_{33} & \sqrt{2}c_{34} & \sqrt{2}c_{35} & \sqrt{2}c_{36} \\
\sqrt{2}c_{14} & \sqrt{2}c_{24} & \sqrt{2}c_{34} & 2c_{44} & 2c_{45} & 2c_{46} \\
\sqrt{2}c_{15} & \sqrt{2}c_{25} & \sqrt{2}c_{35} & 2c_{45} & 2c_{55} & 2c_{56} \\
\sqrt{2}c_{16} & \sqrt{2}c_{26} & \sqrt{2}c_{36} & 2c_{46} & 2c_{56} & 2c_{66}
\end{bmatrix}
\cdot
\begin{bmatrix}
\varepsilon_{11} \\
\varepsilon_{22} \\
\varepsilon_{33} \\
\sqrt{2}\varepsilon_{23} \\
\sqrt{2}\varepsilon_{13} \\
\sqrt{2}\varepsilon_{12}
\end{bmatrix}
\tag{19}
$$

or

$$
\begin{bmatrix}
\hat{\sigma}_{11} \\
\hat{\sigma}_{22} \\
\hat{\sigma}_{33} \\
\hat{\sigma}_{23} \\
\hat{\sigma}_{13} \\
\hat{\sigma}_{12}
\end{bmatrix}
=
\begin{bmatrix}
\hat{c}_{11} & \hat{c}_{12} & \hat{c}_{13} & \hat{c}_{14} & \hat{c}_{15} & \hat{c}_{16} \\
\hat{c}_{12} & \hat{c}_{22} & \hat{c}_{23} & \hat{c}_{24} & \hat{c}_{25} & \hat{c}_{26} \\
\hat{c}_{13} & \hat{c}_{23} & \hat{c}_{33} & \hat{c}_{34} & \hat{c}_{35} & \hat{c}_{36} \\
\hat{c}_{14} & \hat{c}_{24} & \hat{c}_{34} & \hat{c}_{44} & \hat{c}_{45} & \hat{c}_{46} \\
\hat{c}_{15} & \hat{c}_{25} & \hat{c}_{35} & \hat{c}_{45} & \hat{c}_{55} & \hat{c}_{56} \\
\hat{c}_{16} & \hat{c}_{26} & \hat{c}_{36} & \hat{c}_{46} & \hat{c}_{56} & \hat{c}_{66}
\end{bmatrix}
\cdot
\begin{bmatrix}
\hat{\varepsilon}_{11} \\
\hat{\varepsilon}_{22} \\
\hat{\varepsilon}_{33} \\
\hat{\varepsilon}_{23} \\
\hat{\varepsilon}_{13} \\
\hat{\varepsilon}_{12}
\end{bmatrix}
\tag{20}
$$

The relationship between the non-tensorial Voigt notation $\mathbf{c}$ and six-dimensional second rank tensor components $\hat{\mathbf{c}}$ is easily constructed from Eq. (19), a table of this relationship being reported by Mehrabadi and Cowin [16].

Also, the symmetric matrix $\hat{\mathbf{c}}$ in Eq. (20) can be shown to represent the components of a second rank tensor in a six-dimensional space, whereas the components of the matrix $\mathbf{c}$ appearing in Eq. (15) do not form a tensor [16].

Importantly, it is easy to prove that if the material has rhombic syngony in the helicoidal system, then the material exhibits a monoclinic anisotropy in the cylindrical coordinate system. The monoclinic crystal system has exactly one plane of reflective symmetry [14, 17–19]. In particular, we show that, in the cylindrical coordinate, the plane of elastic symmetry is $\theta - x_3$. Since $\mathbf{p} = \{1, 0, 0\}$, the tensor $\hat{\mathbf{P}}$ in Eq. (13) becomes:

$$
\hat{\mathbf{P}} =
\begin{bmatrix}
0 & 0 & 0 & 0 & 0 & 0 \\
0 & 0 & 0 & -\sqrt{2} & 0 & 0 \\
0 & 0 & 0 & \sqrt{2} & 0 & 0 \\
0 & \sqrt{2} & -\sqrt{2} & 0 & 0 & 0 \\
0 & 0 & 0 & 0 & 0 & 1 \\
0 & 0 & 0 & 0 & -1 & 0
\end{bmatrix}
\tag{21}
$$

The six-dimensional orthogonal tensor $\hat{\mathbf{Q}}$ is instead equal to:

$$
\hat{\mathbf{Q}} = \begin{bmatrix}
1 & 0 & 0 & 0 & 0 & 0 \\
0 & \cos^2\theta & \sin^2\theta & -\dfrac{\sqrt{2}}{2}\sin 2\theta & 0 & 0 \\
0 & \sin^2\theta & \cos^2\theta & \dfrac{\sqrt{2}}{2}\sin 2\theta & 0 & 0 \\
0 & \dfrac{\sqrt{2}}{2}\sin 2\theta & -\dfrac{\sqrt{2}}{2}\sin 2\theta & \cos 2\theta & 0 & 0 \\
0 & 0 & 0 & 0 & \cos\theta & \sin\theta \\
0 & 0 & 0 & 0 & -\sin\theta & \cos\theta
\end{bmatrix}
\tag{22}
$$

In the helicoidal coordinate system, according to Eq. (19), the orthotropic stiffness matrix can be written as:

$$
\mathbf{c}^{hel} = \begin{bmatrix}
c_{11}^{hel} & c_{12}^{hel} & c_{13}^{hel} & 0 & 0 & 0 \\
c_{12}^{hel} & c_{22}^{hel} & c_{23}^{hel} & 0 & 0 & 0 \\
c_{13}^{hel} & c_{23}^{hel} & c_{33}^{hel} & 0 & 0 & 0 \\
0 & 0 & 0 & 2c_{44}^{hel} & 0 & 0 \\
0 & 0 & 0 & 0 & 2c_{55}^{hel} & 0 \\
0 & 0 & 0 & 0 & 0 & 2c_{66}^{hel}
\end{bmatrix}
\tag{23}
$$

in which the stiffness constants c_{ij}^{hel} are linked with elastic moduli of a locally orthotropic material E_{rr}, E_{tt}, E_{cc}, ν_{rt}, ν_{tc}, ν_{rc}, G_{rt}, G_{tc}, G_{rc}. Also, by virtue of linearity, the stress vector is obtained by multiplying the matrix $\mathbf{c}^{hel}$ by the strain vector, in Voigt notation, as seen in Eq. (19). By using Eq. (12) and by remembering that $\hat{\mathbf{c}}$ transforms as a second-order tensor in a six-dimensional space, i.e. [17]

$$
\hat{\mathbf{c}}' = \hat{\mathbf{Q}} \cdot \hat{\mathbf{c}} \cdot \hat{\mathbf{Q}}^T
\tag{24}
$$

the elastic constant matrix in the cylindrical coordinate system becomes:

$$
\mathbf{c}^{cyl} = \begin{bmatrix}
c_{11}^{cyl} & c_{12}^{cyl} & c_{13}^{cyl} & 2c_{14}^{cyl} & 0 & 0 \\
c_{12}^{cyl} & c_{22}^{cyl} & c_{23}^{cyl} & 2c_{24}^{cyl} & 0 & 0 \\
c_{13}^{cyl} & c_{23}^{cyl} & c_{33}^{cyl} & 2c_{34}^{cyl} & 0 & 0 \\
c_{14}^{cyl} & c_{24}^{cyl} & c_{34}^{cyl} & 2c_{44}^{cyl} & 0 & 0 \\
0 & 0 & 0 & 0 & 2c_{55}^{cyl} & c_{56}^{cyl} \\
0 & 0 & 0 & 0 & c_{56}^{cyl} & 2c_{66}^{cyl}
\end{bmatrix}
\tag{25}
$$

The constant c_{ij}^{cyl} are in explicit related to the constants c_{ij}^{hel} and the angle θ of the helix by virtue of the relation (24), in which Eqs. (23), (12) have been substituted:

$$
\begin{aligned}
&c_{11}^{cyl} = c_{11}^{hel}, \quad c_{12}^{cyl} = c_{12}^{hel}\cos^2\theta + c_{13}^{hel}\sin^2\theta, \quad c_{13}^{cyl} = c_{13}^{hel}\cos^2\theta + c_{12}^{hel}\sin^2\theta, \\
&c_{14}^{cyl} = \left(c_{12}^{hel} - c_{13}^{hel}\right)\frac{\sin 2\theta}{2}, \\
&c_{22}^{cyl} = c_{22}^{hel}\cos^4\theta + 2\left(c_{23}^{hel} + 2c_{44}^{hel}\right)\cos^2\theta\sin^2\theta + c_{33}^{hel}\sin^4\theta, \\
&c_{23}^{cyl} = c_{23}^{hel}\cos^2 2\theta + \frac{1}{4}\left(c_{22}^{hel} + 2c_{23}^{hel} + c_{33}^{hel} - 4c_{44}^{hel}\right)\sin^2 2\theta, \\
&c_{24}^{cyl} = \frac{1}{4}\left[c_{22}^{hel} - c_{33}^{hel} + \left(c_{22}^{hel} - 2c_{23}^{hel} + c_{33}^{hel} - 4c_{44}^{hel}\right)\cos 2\theta\right]\sin 2\theta, \\
&c_{33}^{cyl} = c_{33}^{hel}\cos^4\theta + 2\left(c_{23}^{hel} + 2c_{44}^{hel}\right)\cos^2\theta\sin^2\theta + c_{22}^{hel}\sin^4\theta, \\
&c_{34}^{cyl} = \frac{1}{4}\left[c_{22}^{hel} - c_{33}^{hel} + \left(4c_{44}^{hel} - c_{33}^{hel} + 2c_{23}^{hel} - c_{22}^{hel}\right)\cos 2\theta\right]\sin 2\theta, \\
&c_{44}^{cyl} = c_{44}^{hel}\cos^2 2\theta + \frac{1}{4}\left(c_{22}^{hel} - 2c_{23}^{hel} + c_{33}^{hel}\right)\sin^2 2\theta, \\
&c_{55}^{cyl} = c_{55}^{hel}\cos^2\theta + c_{66}^{hel}\sin^2\theta, \quad c_{56}^{cyl} = \left(c_{66}^{hel} - c_{55}^{hel}\right)\frac{\sin 2\theta}{2}, \\
&c_{66}^{cyl} = c_{55}^{hel}\sin^2\theta + c_{66}^{hel}\cos^2\theta
\end{aligned}
\tag{26}
$$

4 General theory of linear elastostatic problems in cylindrical coordinates

With reference to the cylindrical coordinate system $\{r, \vartheta, x_3\}$ and for quasi-static problems, the equilibrium equations, in the absence of body forces, are:

$$
\begin{aligned}
&\sigma_{rr,r} + r^{-1}\sigma_{r\vartheta,\vartheta} + \sigma_{r3,3} + r^{-1}\left(\sigma_{rr} - \sigma_{\vartheta\vartheta}\right) = 0 \\
&\sigma_{r\vartheta,r} + r^{-1}\sigma_{\vartheta\vartheta,\vartheta} + \sigma_{\vartheta3,3} + 2r^{-1}\sigma_{r\vartheta} = 0 \\
&\sigma_{r3,r} + r^{-1}\sigma_{\vartheta3,\vartheta} + \sigma_{33,3} + r^{-1}\sigma_{r3} = 0
\end{aligned}
\tag{27}
$$

in which comma is used hereinafter for indicating partial derivatives. In the framework of the analysis of n-FGMCs, due to the cylindrical geometry of the phases, it results extremely useful to adopt the formalism introduced by Ting [13], which yields to rewrite the equilibrium equations (27) in vector form. One can hence introduce the "emerging" stresses (e.g. tractions on the boundary surface of a single phase) as follows:

$$
\left(r\mathbf{t}_r\right)_{,r} + \left(\mathbf{t}_\vartheta\right)_{,\vartheta} + r\,\mathbf{t}_{3,3} + \mathbf{K}\,\mathbf{t}_\vartheta = 0
\tag{28}
$$

where

$$
\mathbf{t}_r = \begin{bmatrix} \sigma_{rr} \\ \sigma_{r\vartheta} \\ \sigma_{r3} \end{bmatrix}, \quad
\mathbf{t}_\vartheta = \begin{bmatrix} \sigma_{\vartheta r} \\ \sigma_{\vartheta\vartheta} \\ \sigma_{\vartheta3} \end{bmatrix}, \quad
\mathbf{t}_3 = \begin{bmatrix} \sigma_{3r} \\ \sigma_{3\vartheta} \\ \sigma_{33} \end{bmatrix},
\tag{29}
$$

represent the traction vectors on the surfaces at $r = const.$, $\vartheta = const.$ and $x_3 = const.$, respectively, and $\mathbf{K}$ is a 3×3 matrix given by

$$\mathbf{K} = \begin{bmatrix} 0 & -1 & 0 \\ 1 & 0 & 0 \\ 0 & 0 & 0 \end{bmatrix} \tag{30}$$

The compatibility equations $\mathbf{E} = \mathrm{sym}\,(\mathbf{u} \otimes \nabla)$ relating the strain components ε_{ij} to the displacement vector $\mathbf{u} = \{u_r, u_\vartheta, u_3\}$ are:

$$\begin{aligned} \varepsilon_{rr} &= u_{r,r}, \quad \varepsilon_{\vartheta\vartheta} = r^{-1}(u_{\vartheta,\vartheta} + u_r), \quad \gamma_{r\vartheta} = 2\varepsilon_{r\vartheta} = r^{-1}(u_{r,\vartheta} + r u_{\vartheta,r} - u_\vartheta) \\ \varepsilon_{33} &= u_{3,3}, \quad \gamma_{r3} = 2\varepsilon_{r3} = u_{3,r} + u_{r,3}, \quad \gamma_{\vartheta 3} = 2\varepsilon_{\vartheta 3} = r^{-1}(u_{3,\vartheta} + r\, u_{\vartheta,3}), \end{aligned} \tag{31}$$

Under the assumption of cylindrical anisotropy and by identifying $(1,2,3) \equiv (r, \vartheta, x_3)$, the stress-strain law $\sigma_{ij} = C_{ijhk}\varepsilon_{hk}$ leads to write

$$\begin{aligned} (\mathbf{t}_r)_j &= \sigma_{rj} = C_{1jhk}\varepsilon_{hk} \\ &= C_{1j11}\varepsilon_{rr} + C_{1j22}\varepsilon_{\vartheta\vartheta} + C_{1j33}\varepsilon_{33} + C_{1j12}\gamma_{r\vartheta} + C_{1j13}\gamma_{r3} + C_{1j23}\gamma_{\vartheta 3} \end{aligned} \tag{32}$$

Similar equations hold for $(\mathbf{t}_\vartheta)_j$ and for $(\mathbf{t}_3)_j$. By making use of Eq. (31), it can be shown that:

$$\begin{aligned} \mathbf{t}_r &= \mathbf{Q}_{rr}\, \mathbf{u},_r + r^{-1}\mathbf{Q}_{r\vartheta}(\mathbf{u},_\vartheta + \mathbf{K}\,\mathbf{u}) + \mathbf{Q}_{r3}\,\mathbf{u},_3 \\ \mathbf{t}_\vartheta &= \mathbf{Q}_{r\vartheta}^T\mathbf{u},_r + r^{-1}\mathbf{Q}_{\vartheta\vartheta}(\mathbf{u},_\vartheta + \mathbf{K}\,\mathbf{u}) + \mathbf{Q}_{\vartheta 3}\,\mathbf{u},_3 \\ \mathbf{t}_3 &= \mathbf{Q}_{r3}^T\,\mathbf{u},_r + r^{-1}\mathbf{Q}_{\vartheta 3}^T(\mathbf{u},_\vartheta + \mathbf{K}\,\mathbf{u}) + \mathbf{Q}_{33}\mathbf{u},_3 \end{aligned} \tag{33}$$

where superscript T denotes the transposition, while $\mathbf{Q}_{rr}$, $\mathbf{Q}_{r\vartheta}$, $\mathbf{Q}_{r3}$, $\mathbf{Q}_{\vartheta\vartheta}$, $\mathbf{Q}_{\vartheta 3}$, $\mathbf{Q}_{33}$ are 3×3 matrices given by:

$$\mathbf{Q}_{rr} = \begin{bmatrix} c_{11} & c_{16} & c_{15} \\ c_{16} & c_{66} & c_{56} \\ c_{15} & c_{56} & c_{55} \end{bmatrix}, \quad \mathbf{Q}_{r\vartheta} = \begin{bmatrix} c_{16} & c_{12} & c_{14} \\ c_{66} & c_{26} & c_{46} \\ c_{56} & c_{25} & c_{45} \end{bmatrix}, \quad \mathbf{Q}_{r3} = \begin{bmatrix} c_{15} & c_{14} & c_{13} \\ c_{56} & c_{46} & c_{36} \\ c_{55} & c_{45} & c_{35} \end{bmatrix},$$

$$\mathbf{Q}_{\vartheta\vartheta} = \begin{bmatrix} c_{66} & c_{26} & c_{46} \\ c_{26} & c_{22} & c_{24} \\ c_{46} & c_{24} & c_{44} \end{bmatrix}, \quad \mathbf{Q}_{\vartheta 3} = \begin{bmatrix} c_{56} & c_{46} & c_{36} \\ c_{25} & c_{24} & c_{23} \\ c_{45} & c_{44} & c_{34} \end{bmatrix}, \quad \mathbf{Q}_{33} = \begin{bmatrix} c_{55} & c_{45} & c_{35} \\ c_{45} & c_{44} & c_{34} \\ c_{35} & c_{34} & c_{33} \end{bmatrix} \tag{34}$$

It is worth to notice that the elastic constants C_{ijhk} and the corresponding $c_{\alpha\beta}$ are here referred to the cylindrical coordinate system (the superscript *cyl* has been omitted). In particular, by starting from a *cylindrically anisotropic*

material, the matrices $\mathbf{Q}_{hk}$ $h,\ k\in\{r,\theta,3\}$ are constant. Differently, the matrices $\mathbf{Q}_{hk}$ $h,\ k\in\{r,\vartheta,3\}$ will result not constant for materials that are even homogeneous in a Cartesian reference system. Substitution of Eq. (33) in Eq. (28) leads to a differential vector equation in terms of the unknown $\mathbf{u}$:

$$
\begin{aligned}
&\mathbf{Q}_{rr}\,\mathbf{u}_{,rr}+\mathbf{Q}_{33}\,\mathbf{u}_{,33}+\left(\mathbf{Q}_{r3}+\mathbf{Q}_{r3}^{T}\right)\mathbf{u}_{,r3}+r^{-2} \\
&\left[\mathbf{Q}_{\vartheta\vartheta}\mathbf{u}_{,\vartheta\vartheta}+\mathbf{K}\mathbf{Q}_{\vartheta\vartheta}\mathbf{K}\mathbf{u}+(\mathbf{Q}_{\vartheta\vartheta}\mathbf{K}+\mathbf{K}\mathbf{Q}_{\vartheta\vartheta})\mathbf{u}_{,\vartheta}\right]+ \\
&+r^{-1}\left[\begin{array}{l}\left(\mathbf{Q}_{r\vartheta}+\mathbf{Q}_{r\vartheta}^{T}\right)\mathbf{u}_{,r\vartheta}+\left(\mathbf{Q}_{\vartheta3}+\mathbf{Q}_{\vartheta3}^{T}\right)\mathbf{u}_{,\vartheta3}+\left(\mathbf{Q}_{r\vartheta}\mathbf{K}+\mathbf{K}\mathbf{Q}_{r\vartheta}^{T}+\mathbf{Q}_{rr}\right)\mathbf{u}_{,r}+ \\ +\left(\mathbf{K}\mathbf{Q}_{\vartheta3}+\mathbf{Q}_{\vartheta3}^{T}\mathbf{K}+\mathbf{Q}_{r3}\right)\mathbf{u}_{,3}\end{array}\right]=\mathbf{0}
\end{aligned}
$$

$$(35)$$

By considering an initially orthotropic material in helicoidal coordinates, described by the stiffness matrix (23), the transformation into cylindrical coordinates ruled by Eq. (26) implies that the matrices $\mathbf{Q}_{hk}$ explicitly depend on the helix angle θ. Eq. (26) imply that the material becomes monoclinic when reported in cylindrical coordinates, with the plane of elastic symmetry being $\vartheta-x_3$. Also, with reference to n-FGMCs, the linearly elastic constitutive relations (15) can be particularized for each $j-th$ phase. In the Voigt notation, they read:

$$
\sigma_{\alpha}^{(j)}=c_{\alpha\beta}^{(j)}\varepsilon_{\beta}^{(j)}
$$

$$(36)$$

where $j=1,\ldots,n$ and the stress and strain vectors and the elasticity matrix are respectively given by:

$$
\left[\sigma_{k}^{(j)}\right]=\begin{bmatrix}\sigma_{rr}^{(j)}\\ \sigma_{\vartheta\vartheta}^{(j)}\\ \sigma_{33}^{(j)}\\ \tau_{r\vartheta}^{(j)}\\ \tau_{\vartheta3}^{(j)}\\ \tau_{r3}^{(j)}\end{bmatrix},\ \left[\varepsilon_{j}^{(i)}\right]=\begin{bmatrix}\varepsilon_{rr}^{(j)}\\ \varepsilon_{\vartheta\vartheta}^{(j)}\\ \varepsilon_{33}^{(j)}\\ \gamma_{r\vartheta}^{(j)}\\ \gamma_{\vartheta3}^{(j)}\\ \gamma_{r3}^{(j)}\end{bmatrix},\ \mathbf{c}^{(i)}=\begin{bmatrix}c_{11}^{(j)}&c_{12}^{(j)}&c_{13}^{(j)}&c_{14}^{(j)}&0&0\\ c_{12}^{(j)}&c_{22}^{(j)}&c_{23}^{(j)}&c_{24}^{(j)}&0&0\\ c_{13}^{(j)}&c_{23}^{(j)}&c_{33}^{(j)}&c_{34}^{(j)}&0&0\\ c_{14}^{(j)}&c_{24}^{(j)}&c_{34}^{(j)}&c_{44}^{(j)}&0&0\\ 0&0&0&0&c_{55}^{(j)}&c_{56}^{(j)}\\ 0&0&0&0&c_{56}^{(j)}&c_{66}^{(j)}\end{bmatrix}
$$

$$(37)$$

and the superscript (j) denotes the generic j-th phase of the n-FGMC. As a consequence, also the matrices $\mathbf{Q}_{hk}$ are written for each monoclinic layer as:

$$
\mathbf{Q}_{rr}^{(j)} = \begin{bmatrix} c_{11}^{(j)} & 0 & 0 \\ 0 & c_{66}^{(j)} & c_{56}^{(j)} \\ 0 & c_{56}^{(j)} & c_{55}^{(j)} \end{bmatrix}, \quad
\mathbf{Q}_{r\vartheta}^{(j)} = \begin{bmatrix} 0 & c_{12}^{(j)} & c_{14}^{(j)} \\ c_{66}^{(j)} & 0 & 0 \\ c_{56}^{(j)} & 0 & 0 \end{bmatrix}, \quad
\mathbf{Q}_{r3}^{(j)} = \begin{bmatrix} 0 & c_{14}^{(j)} & c_{13}^{(j)} \\ c_{56}^{(j)} & 0 & 0 \\ c_{55}^{(j)} & 0 & 0 \end{bmatrix},
$$

$$
\mathbf{Q}_{\vartheta\vartheta}^{(j)} = \begin{bmatrix} c_{66}^{(j)} & 0 & 0 \\ 0 & c_{22}^{(j)} & c_{24}^{(j)} \\ 0 & c_{24}^{(j)} & c_{44}^{(j)} \end{bmatrix}, \quad
\mathbf{Q}_{\vartheta3}^{(j)} = \begin{bmatrix} c_{56}^{(j)} & 0 & 0 \\ 0 & c_{24}^{(j)} & c_{23}^{(j)} \\ 0 & c_{44}^{(j)} & c_{34}^{(j)} \end{bmatrix}, \quad
\mathbf{Q}_{33}^{(j)} = \begin{bmatrix} c_{55}^{(j)} & 0 & 0 \\ 0 & c_{44}^{(j)} & c_{34}^{(j)} \\ 0 & c_{24}^{(j)} & c_{33}^{(j)} \end{bmatrix},
$$

(38)

Under the hypothesis of axis–symmetry of both geometry of the object (n-FGMC) and load conditions, the displacement field is independent from the coordinate ϑ, and the equilibrium equation (35) takes the form:

$$
\mathbf{Q}_{rr}^{(j)}\,\mathbf{u}^{(j)}{}_{,rr} + \mathbf{Q}_{33}^{(j)}\,\mathbf{u}^{(j)}{}_{,33} + \left(\mathbf{Q}_{r3}^{(j)} + \left(\mathbf{Q}_{r3}^{(j)}\right)^T\right)\mathbf{u}^{(j)}{}_{,r3} + r^{-2}\mathbf{K}\mathbf{Q}_{\vartheta\vartheta}^{(j)}\mathbf{K}\mathbf{u}^{(j)}
$$

$$
+ r^{-1}\left[\begin{array}{l} \left(\mathbf{Q}_{r\vartheta}^{(j)}\mathbf{K} + \mathbf{K}\left(\mathbf{Q}_{r\vartheta}^{(j)}\right)^T + \mathbf{Q}_{rr}^{(j)}\right)\mathbf{u}^{(j)}{}_{,r} \\ + \left(\mathbf{K}\mathbf{Q}_{\vartheta3}^{(j)} + \left(\mathbf{Q}_{\vartheta3}^{(j)}\right)^T\mathbf{K} + \mathbf{Q}_{r3}^{(j)}\right)\mathbf{u}^{(j)}{}_{,3} \end{array}\right] = \mathbf{0}
$$

(39)

These equilibrium equations can be then rearranged in a compact way as follows:

$$
\mathbf{A}_1^{(j)}\,\mathbf{u}^{(j)}{}_{,rr} + \mathbf{A}_2^{(j)}\,\mathbf{u}^{(j)}{}_{,33} + \mathbf{A}_3^{(j)}\mathbf{u}^{(j)}{}_{,r3} + r^{-1}\left[\mathbf{A}_4^{(j)}\,\mathbf{u}^{(j)}{}_{,r} + \mathbf{A}_5^{(j)}\,\mathbf{u}^{(j)}{}_{,3}\right]
$$
$$
+ r^{-2}\mathbf{A}_6^{(j)}\,\mathbf{u}^{(j)} = \mathbf{0}
$$

(40)

where

$$
\mathbf{A}_1^{(j)} = \mathbf{Q}_{rr}^{(j)}, \quad \mathbf{A}_2^{(j)} = \mathbf{Q}_{33}^{(j)}, \quad \mathbf{A}_3^{(j)} = \mathbf{Q}_{r3}^{(j)} + \left(\mathbf{Q}_{r3}^{(j)}\right)^T,
$$
$$
\mathbf{A}_4^{(j)} = \mathbf{Q}_{r\vartheta}^{(j)}\mathbf{K} + \mathbf{K}\left(\mathbf{Q}_{r\vartheta}^{(j)}\right)^T + \mathbf{Q}_{rr}^{(j)},
$$
$$
\mathbf{A}_5^{(j)} = \mathbf{K}\mathbf{Q}_{\vartheta3}^{(j)} + \left(\mathbf{Q}_{\vartheta3}^{(j)}\right)^T\mathbf{K} + \mathbf{Q}_{r3}^{(j)}, \quad \mathbf{A}_6^{(j)} = \mathbf{K}\mathbf{Q}_{\vartheta\vartheta}^{(j)}\mathbf{K},
$$

(41)

4.1 Exact solution for the generic hollow phase

We consider the generic case in which an assembled functionally graded circular cylinder is constituted by a central *core*, denoted by (c), and n arbitrary *cladding* phases, represented by hollow cylinders that exhibit monoclinic

elastic behavior. The displacement solution for the j-th generic phase of the $(n + 1)$-FGMC is:

$$u_r^{(j)} = u_r^{(j)}(r, x_3), \quad u_\vartheta^{(j)} = u_\vartheta^{(j)}(r, x_3), \quad u_3^{(j)} = u_3^{(j)}(r, x_3), \quad R^{(j-1)} < r < R^{(j)} \quad (42)$$

By applying the compatibility equations (31), the stress vector becomes:

$$
\begin{bmatrix}
\sigma_{rr}^{(j)} \\
\sigma_{\vartheta\vartheta}^{(j)} \\
\sigma_{33}^{(j)} \\
\sigma_{\vartheta3}^{(j)} \\
\sigma_{r3}^{(j)} \\
\sigma_{r\vartheta}^{(j)}
\end{bmatrix}
=
\begin{bmatrix}
c_{11}^{(j)} & c_{12}^{(j)} & c_{13}^{(j)} & c_{14}^{(j)} & 0 & 0 \\
c_{12}^{(j)} & c_{22}^{(j)} & c_{23}^{(j)} & c_{24}^{(j)} & 0 & 0 \\
c_{13}^{(j)} & c_{23}^{(j)} & c_{33}^{(j)} & c_{34}^{(j)} & 0 & 0 \\
c_{14}^{(j)} & c_{24}^{(j)} & c_{34}^{(j)} & c_{44}^{(j)} & 0 & 0 \\
0 & 0 & 0 & 0 & c_{55}^{(j)} & c_{56}^{(j)} \\
0 & 0 & 0 & 0 & c_{56}^{(j)} & c_{66}^{(j)}
\end{bmatrix}
\begin{bmatrix}
u_{r,r}^{(j)} \\
u_r^{(j)}/r \\
u_{3,3}^{(j)} \\
u_{\vartheta,3}^{(j)} \\
u_{r,3}^{(j)} + u_{3,r}^{(j)} \\
u_{\vartheta,r}^{(j)} - u_\vartheta^{(j)}/r
\end{bmatrix}
\quad (43)
$$

By requiring that the stress components are independent of the x_3 variable, the following differential equations can be obtained:

$$u_{r,r3}^{(j)} = 0, \quad u_{r,3}^{(j)} = 0, \quad u_{3,33}^{(j)} = 0, \quad u_{\vartheta,33}^{(j)} = 0, \quad u_{r,33}^{(j)} + u_{3,r3}^{(j)} = 0, \quad u_{\vartheta,r3}^{(j)} + \frac{u_{\vartheta,3}^{(j)}}{r} = 0, \quad (44)$$

The displacements that satisfy equation (44) have the expression

$$
\begin{aligned}
u_r^{(j)} &= p_1^{(j)}(r), \\
u_\vartheta^{(j)} &= p_2^{(j)}(r) + \phi^{(j)} r x_3, \\
u_3^{(j)} &= p_3^{(j)}(r) + \varepsilon_0^{(j)} x_3,
\end{aligned}
\quad (45)
$$

where $p_1^{(j)}(r)$, $p_2^{(j)}(r)$, $p_3^{(j)}(r)$ are unknown functions of the sole radial coordinate. By substituting the displacement field (45) into the Navier-Cauchy equilibrium equations (40) and by virtue of relations (41), the following ODE system is finally derived:

$$
\begin{cases}
c_{11}^{(j)}\left(p_{1,r}^{(j)} + r p_{1,rr}^{(j)}\right) - c_{22}^{(j)} p_1^{(j)} + \left(c_{13}^{(j)} - c_{23}^{(j)}\right)\varepsilon_0^{(j)} r + \left(2c_{14}^{(j)} - c_{24}^{(j)}\right)\phi^{(j)} r^2 = 0 \\
c_{56}^{(j)}\left(2 r p_{3,r}^{(j)} + r^2 p_{3,rr}^{(j)}\right) + c_{66}^{(j)}\left(r^2 p_{2,rr}^{(j)} + r p_{2,r}^{(j)} - p_2^{(j)}\right) = 0 \\
c_{55}^{(j)}\left(p_{3,r}^{(j)} + r p_{3,rr}^{(j)}\right) + c_{56}^{(j)} r p_{2,rr}^{(j)} = 0
\end{cases}
\quad (46)
$$

The function $p_1^{(j)}(r)$ is found by integrating the Eq. $(46)_1$, that is

$$p_1^{(j)}(r) = C_1^{(j)}\left(r^{\lambda^{(j)}} + r^{-\lambda^{(j)}}\right) + i C_2^{(j)}\left(r^{\lambda^{(j)}} - r^{-\lambda^{(j)}}\right) + h_1^{(j)} \varepsilon_0^{(j)} r + h_2^{(j)} \phi^{(j)} r^2 \quad (47)$$

where $h_1^{(j)} = \dfrac{c_{23}^{(j)} - c_{13}^{(j)}}{c_{11}^{(j)} - c_{22}^{(j)}}$, $h_2^{(j)} = \dfrac{c_{24}^{(j)} - 2c_{14}^{(j)}}{4c_{11}^{(j)} - c_{22}^{(j)}}$ and $\lambda^{(j)} = \sqrt{\dfrac{c_{22}^{(j)}}{c_{11}^{(j)}}}$.

The functions $p_2^{(j)}(r)$ and $p_3^{(j)}(r)$ are instead obtained by integrating the coupled equations $(46)_{2-3}$, i.e.:

$$p_2^{(j)}(r) = h_4^{(j)} C_4^{(j)} - \frac{h_3^{(j)} C_3^{(j)}}{r}$$

$$p_3^{(j)}(r) = \frac{h_4^{(j)} C_3^{(j)}}{r} + h_5^{(j)} C_4^{(j)} \log r$$

(48)

where $h_3^{(j)} = \frac{c_{55}^{(j)}}{2\left(c_{56}^{(j)2} - c_{55}^{(j)} c_{66}^{(j)}\right)}$, $h_4^{(j)} = \frac{c_{56}^{(j)}}{\left(c_{56}^{(j)2} - c_{55}^{(j)} c_{66}^{(j)}\right)}$, $h_5^{(j)} = \frac{c_{66}^{(j)}}{\left(c_{56}^{(j)2} - c_{55}^{(j)} c_{66}^{(j)}\right)}$.

Then, the displacement solution is:

$$u_r^{(j)} = C_1^{(j)} \left(r^{\lambda^{(j)}} + r^{-\lambda^{(j)}}\right) + i C_2^{(j)} \left(r^{\lambda^{(j)}} - r^{-\lambda^{(j)}}\right) + h_1^{(j)} \varepsilon_0^{(j)} r + h_2^{(j)} \phi^{(j)} r^2$$

$$u_\vartheta^{(j)} = \phi^{(j)} r x_3 + h_4^{(j)} C_4^{(j)} - \frac{h_3^{(j)} C_3^{(j)}}{r}$$

(49)

$$u_3^{(j)} = \varepsilon_0^{(j)} x_3 + \frac{h_4^{(j)} C_3^{(j)}}{r} + h_5^{(j)} C_4^{(j)} \log r$$

The internal core phase is assumed to be isotropic. For this reason, the terms that diverge at $r=0$ must vanish in a way that the displacement solution for the core phase (c) is given by:

$$u_r^{(c)} = C_0^{(c)} r$$

$$u_\vartheta^{(c)} = \phi^{(c)} r x_3$$

(50)

$$u_3^{(c)} = \varepsilon_0^{(c)} x_3$$

By particularizing the Hooke's law (43) to the special case of isotropic stiffness constants and by therein substituting the solutions (50) the stresses in the core result:

$$\sigma_{rr}^{(c)} = \left(c_{11}^{(c)} + c_{12}^{(c)}\right) C_0^{(c)} + c_{12}^{(c)} \varepsilon_0^{(c)}$$

$$\sigma_{\vartheta\vartheta}^{(c)} = \left(c_{11}^{(c)} + c_{12}^{(c)}\right) C_0^{(c)} + c_{12}^{(c)} \varepsilon_0^{(c)}$$

(51)

$$\sigma_{33}^{(c)} = 2 c_{12}^{(c)} C_0^{(c)} + c_{11}^{(c)} \varepsilon_0^{(c)}$$

$$\sigma_{\vartheta 3}^{(c)} = \left(c_{11}^{(c)} - c_{12}^{(c)}\right) \phi^{(c)} r$$

On the other hand, for the cylindrically monoclinic hollow layers, the use of Eqs. (43), (49) returns the following stress components:

$$
\begin{bmatrix} \sigma_{rr}^{(j)} \\ \sigma_{\vartheta\vartheta}^{(j)} \\ \sigma_{33}^{(j)} \\ \sigma_{\vartheta 3}^{(j)} \\ \sigma_{r3}^{(j)} \\ \sigma_{r\vartheta}^{(j)} \end{bmatrix} =
\begin{bmatrix}
\left(k_{11}^{(j)} r^{\lambda^{(j)}-1} + k_{12}^{(j)} r^{-\left(\lambda^{(j)}+1\right)} \right) & i\left(k_{13}^{(j)} r^{\lambda^{(j)}-1} + k_{14}^{(j)} r^{-\left(\lambda^{(j)}+1\right)} \right) & 0 & 0 & k_{15}^{(j)} & k_{16}^{(j)} r \\
\left(k_{21}^{(j)} r^{\lambda^{(j)}-1} + k_{22}^{(j)} r^{-\left(\lambda^{(j)}+1\right)} \right) & i\left(k_{23}^{(j)} r^{\lambda^{(j)}-1} + k_{24}^{(j)} r^{-\left(\lambda^{(j)}+1\right)} \right) & 0 & 0 & k_{25}^{(j)} & k_{26}^{(j)} r \\
\left(k_{31}^{(j)} r^{\lambda^{(j)}-1} + k_{32}^{(j)} r^{-\left(\lambda^{(j)}+1\right)} \right) & i\left(k_{33}^{(j)} r^{\lambda^{(j)}-1} + k_{34}^{(j)} r^{-\left(\lambda^{(j)}+1\right)} \right) & 0 & 0 & k_{35}^{(j)} & k_{36}^{(j)} r \\
\left(k_{41}^{(j)} r^{\lambda^{(j)}-1} + k_{42}^{(j)} r^{-\left(\lambda^{(j)}+1\right)} \right) & i\left(k_{43}^{(j)} r^{\lambda^{(j)}-1} + k_{44}^{(j)} r^{-\left(\lambda^{(j)}+1\right)} \right) & 0 & 0 & k_{45}^{(j)} & k_{46}^{(j)} r \\
0 & 0 & 0 & -r^{-1} & 0 & 0 \\
0 & 0 & -r^{-2} & 0 & 0 & 0
\end{bmatrix}
\begin{bmatrix} C_1^{(j)} \\ C_2^{(j)} \\ C_3^{(j)} \\ C_4^{(j)} \\ \varepsilon_0^{(j)} \\ \phi^{(j)} \end{bmatrix}
\tag{52}
$$

in which

$$k_{11}^{(j)} = k_{13}^{(j)} = c_{12}^{(j)} + c_{11}^{(j)}\lambda^{(j)}, \quad k_{12}^{(j)} = -k_{14}^{(j)} = c_{12}^{(j)} - c_{11}^{(j)}\lambda^{(j)},$$

$$k_{15}^{(j)} = k_{25}^{(j)} = \frac{c_{23}^{(j)}\left(c_{11}^{(j)} + c_{12}^{(j)}\right) - c_{13}^{(j)}\left(c_{12}^{(j)} + c_{22}^{(j)}\right)}{c_{11}^{(j)} - c_{22}^{(j)}},$$

$$k_{26}^{(j)} = 2k_{16}^{(j)} = \frac{2c_{24}^{(j)}\left(2c_{11}^{(j)} + c_{12}^{(j)}\right) - 2c_{14}^{(j)}\left(2c_{12}^{(j)} + c_{22}^{(j)}\right)}{4c_{11}^{(j)} - c_{22}^{(j)}},$$

$$k_{21}^{(j)} = k_{23}^{(j)} = c_{22}^{(j)} + c_{12}^{(j)}\lambda^{(j)}, \quad k_{22}^{(j)} = -k_{24}^{(j)} = c_{22}^{(j)} - c_{12}^{(j)}\lambda^{(j)},$$

$$k_{31}^{(j)} = k_{33}^{(j)} = c_{23}^{(j)} + c_{13}^{(j)}\lambda^{(j)}, \quad k_{32}^{(j)} = -k_{34}^{(j)} = c_{23}^{(j)} - c_{13}^{(j)}\lambda^{(j)}, \tag{53}$$

$$k_{35}^{(j)} = c_{33}^{(j)} - \frac{c_{13}^{(j)2} - c_{23}^{(j)2}}{c_{11}^{(j)} - c_{22}^{(j)}}, \quad k_{36}^{(j)} = c_{34}^{(j)} + \frac{\left(c_{24}^{(j)} - 2c_{14}^{(j)}\right)\left(c_{23}^{(j)} + 2c_{13}^{(j)}\right)}{4c_{11}^{(j)} - c_{22}^{(j)}},$$

$$k_{41}^{(j)} = k_{43}^{(j)} = c_{24}^{(j)} + c_{14}^{(j)}\lambda^{(j)}, \quad k_{42}^{(j)} = -k_{44}^{(j)} = c_{24}^{(j)} - c_{14}^{(j)}\lambda^{(j)},$$

$$k_{45}^{(j)} = c_{34}^{(j)} - \frac{\left(c_{14}^{(j)} + c_{24}^{(j)}\right)\left(c_{13}^{(j)} - c_{23}^{(j)}\right)}{c_{11}^{(j)} - c_{22}^{(j)}}, \quad k_{46}^{(j)} = c_{44}^{(j)} + \frac{c_{24}^{(j)2} - 4c_{14}^{(j)2}}{4c_{11}^{(j)} - c_{22}^{(j)}}$$

The results obtained until now satisfy the equilibrium and compatibility equations inside each generic *j*-th phase of a composite circular cylinder subjected to axis-symmetrical strains. Under both the hypothesis of linear elastic behavior of the materials and the assumption of perfect bond at the cylindrical interfacial boundaries (no de-lamination or friction phenomena are taken into consideration), we have now to guarantee both the equilibrium and the compatibility equations at the boundary surfaces between two generic adjacent phases.

To this aim, suitable interface and boundary conditions have to be introduced. The total unknown parameters to be determined are:

$$C_0^{(c)}, \phi^{(c)}, \varepsilon_0^{(c)}$$
$$C_1^{(j)}, C_2^{(j)}, C_3^{(j)}, C_4^{(j)}, \phi^{(j)}, \varepsilon_0^{(j)} \quad j \in \{1, 2, \dots, n\} \tag{54}$$

where the three coefficients in $(54)_1$ represent the unknowns of the core, while the *6n* coefficients in $(54)_2$ are the unknowns of every circular hollow cylinder, the last two coefficients physically representing the unit angle warping and the axial strain of each layer, respectively.

Hence, the total number of unknowns is $(6n + 3)$, which has to match the number of algebraic equations to be solved. More precisely, we consider $6n$ interface conditions and 3 external boundary conditions, written at the outermost cylindrical surface and at the ends of the FGMC. The first $6n$ equilibrium and compatibility equations require the continuity of displacement and stresses at the each interface, that is:

$$
\begin{cases}
u_r^{(j)}\left(r = R^{(j)}\right) = u_r^{(j+1)}\left(r = R^{(j)}\right) \\
u_\vartheta^{(j)}\left(r = R^{(j)}\right) = u_\vartheta^{(j+1)}\left(r = R^{(j)}\right) \\
u_3^{(j)}\left(r = R^{(j)}\right) = u_3^{(j+1)}\left(r = R^{(j)}\right) \\
\sigma_{rr}^{(j)}\left(r = R^{(j)}\right) = \sigma_{rr}^{(j+1)}\left(r = R^{(j)}\right) \\
\sigma_{r3}^{(j)}\left(r = R^{(j)}\right) = \sigma_{r3}^{(j+1)}\left(r = R^{(j)}\right) \\
\sigma_{r\vartheta}^{(j)}\left(r = R^{(j)}\right) = \sigma_{r\vartheta}^{(j+1)}\left(r = R^{(j)}\right)
\end{cases}
\quad j \in \{0, 1, \dots, n-1\} \qquad (55)
$$

where $R^{(j)}$ is the outer radius of the j-th phase and $j = 0$ denotes the internal core. Furthermore, the respect of the equations $(55)_{2,3,5,6}$ implies that:

$$
\phi^{(c)} = \phi^{(j)} = \phi, \quad \varepsilon_0^{(c)} = \varepsilon_0^{(j)} = \varepsilon_0, \quad C_3^{(j)} = C_4^{(j)} = 0, \quad \forall j \in \{0, 1, \dots, n-1\},
$$
$$(56)$$

By recalling Eq. (56), the system (55) reduces to:

$$
\begin{cases}
u_{rr}^{(j)}\left(r = R^{(j)}\right) = u_{rr}^{(j+1)}\left(r = R^{(j)}\right) \\
\sigma_{rr}^{(j)}\left(r = R^{(j)}\right) = \sigma_{rr}^{(j+1)}\left(r = R^{(j)}\right)
\end{cases}
\quad j \in \{0, 1, \dots, n-1\} \qquad (57)
$$

Eq. (57) can be written in explicit form as

$$
\begin{cases}
\left(C_1^{(j)} - C_1^{(j+1)}\right)\left(R^{(j)\lambda^{(j)}} + R^{(j)-\lambda^{(j)}}\right) \\
+ i\left(C_2^{(j)} - C_2^{(j+1)}\right)\left(R^{(j)\lambda^{(j)}} - R^{(j)-\lambda^{(j)}}\right) + \left(h_1^{(j)} - h_1^{(j+1)}\right)\varepsilon_0 R^{(j)} \\
+ \left(h_2^{(j)} - h_2^{(j+1)}\right)\phi R^{(j)2} + R^{(j)} C_0^{(0)} \delta_{0j} = 0 \\
\left(C_1^{(j)} k_{11}^{(i)} - C_1^{(j+1)} k_{11}^{(j+1)}\right) R^{(j)\lambda^{(j)}-1} + \left(C_1^{(j)} k_{12}^{(j)} - C_1^{(j+1)} k_{12}^{(j+1)}\right) R^{(j)-\lambda^{(j)}-1} \\
+ \left(k_{15}^{(j)} - k_{15}^{(j+1)} + \dfrac{E \nu \delta_{0j}}{1 - \nu - 2\nu^2}\right)\varepsilon_0 + \\
i\left(C_2^{(j)} k_{13}^{(j)} - C_2^{(j+1)} k_{13}^{(j+1)}\right) R^{(j)\lambda^{(j)}-1} + i\left(C_2^{(j)} k_{14}^{(j)} - C_2^{(j+1)} k_{14}^{(j+1)}\right) \\
R^{(j)-\lambda^{(j)}-1} + \left(k_{16}^{(j)} - k_{16}^{(j+1)}\right)\phi R^{(j)} + \dfrac{E C_0 \delta_{0j}}{1 - \nu - 2\nu^2} = 0
\end{cases}
$$
$$(58)$$

where δ_{0j} is the Kronecker symbol and the isotropic Lamé moduli $c_{11}^{(c)} = \dfrac{E(1-\nu)}{1-\nu-2\nu^2}$ and $c_{12}^{(c)} = \dfrac{E\nu}{1-\nu-2\nu^2}$ have been additionally taken into account

for the central core, E and ν being the Young modulus and the Poisson's ratio.

The Cauchy equilibrium equations on the external surface of the cylinder $(j=n)$ imposes vanishing radial stresses in absence of lateral pressure:

$$\sigma_{rr}^{(n)}\left(r=R^{(n)}\right)=0 \tag{59}$$

This gives

$$C_1^{(n)}\left(k_{11}^{(n)}R^{(n)\lambda^{(j)}-1}+k_{12}^{(n)}R^{(n)-\lambda^{(j)}-1}\right)+iC_2^{(n)}\left(k_{13}^{(n)}R^{(n)\lambda^{(j)}-1}+k_{14}^{(n)}R^{(n)-\lambda^{(j)}-1}\right)$$
$$+k_{15}^{(n)}\varepsilon_0+k_{16}^{(n)}\phi R^{(n)}=0 \tag{60}$$

Finally, it remains to consider the conditions at the basis of the compound cylinder. In a *force-prescribed* case, it is sufficient to write the (translational and rotational) equilibrium equations in the x_3 direction on one of the bases. Therefore, without loss of generality, at $x_3=0$ we can impose that

$$\int_0^{2\pi}\int_0^{R^{(0)}}\sigma_{33}^{(0)}(x_3=0)r\,dr\,d\vartheta+\sum_{j=1}^n\int_0^{2\pi}\int_{R^{(j-1)}}^{R^{(j)}}\sigma_{33}^{(j)}(x_3=0)\,r\,dr\,d\vartheta=F_3,$$
$$\int_0^{2\pi}\int_0^{R^{(0)}}\sigma_{\vartheta 3}^{(0)}(x_3=0)r^2\,dr\,d\vartheta+\sum_{j=1}^n\int_0^{2\pi}\int_{R^{(j-1)}}^{R^{(j)}}\sigma_{\vartheta 3}^{(j)}(x_3=0)\,r^2\,dr\,d\vartheta=\mathfrak{M}_t, \tag{61}$$

where F_3 $\mathfrak{M}_t$ are the total axial force and the twisting moment applied at $x_3=0$, respectively.

In order to solve the algebraic system constituted by Eqs. (58), (60), (61), it is convenient to re-arrange the whole $(2n+3)\times(2n+3)$ algebraic system according to a matrix-based procedure. Indeed, we can collect the known terms in the *loads* vector $\mathbf{L}$

$$\mathbf{L}^T=\{0,0,\ldots,0,F_3,\mathfrak{M}_t\} \tag{62}$$

and the unknown parameters in the vector $\mathbf{X}$ with components

$$\mathbf{X}^T=\left\{C_0^{(0)},C_1^{(1)},C_2^{(1)},C_1^{(2)},C_2^{(2)},\ldots,C_1^{(i)},C_2^{(i)},\ldots,C_1^{(n)},C_2^{(n)},\varepsilon_0,\phi\right\} \tag{63}$$

so that the set of Eqs. (58), (60), (61), reads as

$$\mathbb{P}\cdot\mathbf{X}=\mathbf{L} \tag{64}$$

where $\mathbb{P}$ is a $(2n+3) \times (2n+3)$ square matrix containing the coefficients $P_{h/m}$, which are functions of both the radii and the elastic moduli of the phases. The expressions of the coefficients $P_{h/m}$ are reported in detail in the Appendix.

Finally, being the system (64) of linear and algebraic type and provided that $\det \mathbb{P} \neq 0$,[a] it is possible to write the solution by exploiting the Cramer rule:

$$\mathbf{X} = \mathbb{P}^{-1}\mathbf{L} = \frac{1}{\det \mathbb{P}}\mathrm{adj}\,[\mathbb{P}]\mathbf{L} = \frac{1}{\det \mathbb{P}}\widetilde{\mathbb{P}}\mathbf{L}, \quad X_m = \frac{1}{\det \mathbb{P}}\sum_{h=1}^{m=2n+3}\widetilde{P}_{h/m}L_h,$$

(65)

where $\mathrm{adj}\,[\mathbb{P}] = \widetilde{\mathbb{P}}$ is the adjoint matrix of $\mathbb{P}$.

In presence of a linear elastostatic problem with displacement boundary conditions the Eq. (61) must be replaced by analogous kinematic conditions. At the base $x_3 = L$, we write:

$$\begin{cases} u_3^{(j)}(x_3 = L) = W_0 \\ u_9^{(j)}(x_3 = L) = \varphi_0 r \end{cases} \quad \forall j \in \{0, 1, \dots n\}$$

(66)

where L is the total length of the cylinder, W_0 is a prescribed displacement value, φ_0 is a prescribed twisting angle (the rotation around the x_3 axis). By solving the conditions (66), we obtain the uniform longitudinal deformation ε_0 and unit angle of rotation ϕ as function of W_0 and φ_0:

$$\begin{aligned} \varepsilon_0 L = W_0 &\Rightarrow \varepsilon_0 = \frac{W_0}{L} \\ \phi L r = \varphi_0 r &\Rightarrow \phi = \frac{\varphi_0}{L} \end{aligned}$$

(67)

Then, being ε_0 and ϕ assigned, the displacement-prescribed problem can be solved by considering interface conditions analogous to Eq. (58), i.e.:

---

[a] The possibility to invert the matrix $\mathbb{P}$ is ensured by invoking the uniqueness of the linear elastic solution, due to Kirchhoff's theorem. This could appear not immediately evident if one directly tries to see the actual form of $\mathbb{P}$. However, as we will show in the next section, when the proposed strategy is applied to a three-phase composed cylinder, an analytical proof that the algebraic problem is well-posed is also given by utilizing the *Mathematica* code [20], where the command *RowReduce* is employed. This command performs a version of Gaussian elimination, adding multiples of rows together so as to produce zero elements when possible. The final matrix is in reduced row echelon form. If is a non-degenerate square matrix, as well as our case, RowReduce [$\mathbb{P}$] gives the *IdentityMatrix* [Length[$\mathbb{P}$]].

$$\begin{cases} \left(C_1^{(i)} - C_1^{(i+1)} \right) \left(R^{(i)\lambda^{(j)}} + R^{(i)-\lambda^{(j)}} \right) + i \left(C_2^{(i)} - C_2^{(i+1)} \right) \\[4pt] \left(R^{(i)\lambda^{(j)}} - R^{(i)-\lambda^{(j)}} \right) + R^{(j)} C_0^{(0)} \delta_{0j} \\[4pt] = \dfrac{1}{L} \left[\left(h_1^{(i+1)} - h_1^{(i)} \right) W_0 R^{(i)} + \left(h_2^{(i+1)} - h_2^{(i)} \right) \varphi_0 R^{(i)2} \right] \\[8pt] \left(C_1^{(i)} k_{11}^{(i)} - C_1^{(i+1)} k_{11}^{(i+1)} \right) R^{(i)\lambda^{(j)}-1} + \left(C_1^{(i)} k_{12}^{(i)} - C_1^{(i+1)} k_{12}^{(i+1)} \right) R^{(i)-\lambda^{(j)}-1} \\[4pt] + i \left(C_2^{(i)} k_{13}^{(i)} - C_2^{(i+1)} k_{13}^{(i+1)} \right) R^{(i)\lambda^{(j)}-1} + \\[4pt] + i \left(C_2^{(i)} k_{14}^{(i)} - C_2^{(i+1)} k_{14}^{(i+1)} \right) R^{(i)-\lambda^{(j)}-1} + \dfrac{E C_0 \delta_{0j}}{1 - \nu - 2\nu^2} = \\[4pt] = \dfrac{1}{L} \left[\left(k_{16}^{(i+1)} - k_{16}^{(i)} + \dfrac{E\nu \delta_{0j}}{1 - \nu - 2\nu^2} \right) \varphi_0 R^{(i)} + \left(k_{15}^{(i+1)} - k_{15}^{(i)} \right) W_0 \right] \end{cases} \tag{68}$$

Similarly, the lateral boundary condition (60) becomes

$$C_1^{(n)} \left(k_{11}^{(n)} R^{(n)\lambda^{(j)}-1} + k_{12}^{(n)} R^{(n)-\lambda^{(j)}-1} \right) + i C_2^{(n)} \left(k_{13}^{(n)} R^{(n)\lambda^{(j)}-1} + k_{14}^{(n)} R^{(n)-\lambda^{(j)}-1} \right)$$
$$= -\dfrac{1}{L} \left[k_{15}^{(n)} W_0 + k_{16}^{(n)} \varphi_0 R^{(n)} \right] \tag{69}$$

Also Eqs. (68), (69) can be helpfully re-arranged by following a matrix-based procedure. Indeed, we can collect the known terms in the *displacements* vector **D** of dimensions $2n + 1$

$$\mathbf{D} = \dfrac{1}{L} \begin{bmatrix} h_1^{(1)} R^{(0)} & h_2^{(1)} R^{(0)2} \\[4pt] k_{15}^{(1)} & k_{16}^{(1)} R^{(0)} + E\nu (2\nu^2 + \nu - 1)^{-1} \\[4pt] \vdots & \vdots \\[4pt] \left(h_1^{(j+1)} - h_1^{(j)} \right) R^{(j)} & \left(h_2^{(j+1)} - h_2^{(j)} \right) R^{(j)2} \\[4pt] k_{15}^{(j+1)} - k_{15}^{(j)} & \left(k_{16}^{(j+1)} - k_{16}^{(j+1)} \right) R^{(j)} \\[4pt] \vdots & \vdots \\[4pt] \left(h_1^{(n)} - h_1^{(n-1)} \right) R^{(n-1)} & \left(h_2^{(n)} - h_2^{(n-1)} \right) R^{(n-1)2} \\[4pt] k_{15}^{(n)} - k_{15}^{(n-1)} & \left(k_{16}^{(n)} - k_{16}^{(n-1)} \right) R^{(n-1)} \\[4pt] -k_{15}^{(n)} & -k_{16}^{(n)} R^{(n)} \end{bmatrix} \cdot \begin{bmatrix} W_0 \\[4pt] \varphi_0 \end{bmatrix} \tag{70}$$

The unknowns are instead ordered in the vector **Y** with the same dimension.

$$\mathbf{Y}^T = \left\{ C_0^{(0)}, C_1^{(1)}, C_2^{(1)}, C_1^{(2)}, C_2^{(2)}, ..., C_1^{(i)}, C_2^{(i)}, ..., C_1^{(n)}, C_2^{(n)} \right\} \quad (71)$$

This leads to re-organize the system in the matrix form

$$\mathbb{Q} \cdot \mathbf{Y} = \mathbf{D} \quad (72)$$

Herein $\mathbb{Q}$ is a $(2n+1) \times (2n+1)$ square matrix containing the coefficients $Q_{h/m}$ that depend on geometric and elastic parameters.

Provided that $\det\mathbb{Q} \neq 0$, the linear algebraic system (72) can be inverted according to the Cramer rule in order to find the unknown parameters

$$\mathbf{Y} = \mathbb{Q}^{-1}\mathbf{D} = \frac{\text{adj}[\mathbb{Q}]}{\det\mathbb{Q}}\mathbf{D} = \frac{\widetilde{\mathbb{Q}}}{\det\mathbb{Q}}\mathbf{D}, \quad Y_m = \frac{1}{\det\mathbb{Q}} \sum_{h=1}^{m=2n+1} \widetilde{Q}_{h/m}D_h, \quad (73)$$

where $\text{adj}[\mathbb{Q}] = \widetilde{\mathbb{Q}}$ is the adjoint matrix of $\mathbb{Q}$.

4.2 Example applications for FGMCs with three phases
4.2.1 3-FGMC subjected to axial force

We consider the case that the FGMC solid is constituted by a central core and two hollow cylinder phases (1) and (2). The three phases have the same volume equal to π and the solid is loaded by axial force F_3 applied on its basis (see Fig. 2).

We assume that the two hollow phases are transversally isotropic in the helicoidal coordinate system and the plane of the isotropy is $r-c$, but the central core is made of isotropic material. Moreover, we introduce the following relationship between the helicoidal elastic constants for the sake of simplicity:

$$E_{rr} = E_{cc} = E, \quad E_{tt} = \eta E, \quad \nu_{rt} = \nu_{tc} = \nu_{rc} = \nu$$
$$G_{rt} = G_{tc} = \frac{\eta E}{2(1+\nu)}, \quad G_{rc} = \frac{E}{2(1+\nu)} \quad (74)$$

The relationships (74) show that a common Poisson's coefficient has been utilized while $\eta = E_{tt}/E_{cc}$ is the ratio between the longitudinal and transverse Young moduli measured in the helicoidal system. Transverse isotropy allows to write the following stiffness constants as:

$$c_{11}^{hel} = c_{33}^{hel} = \frac{E(\nu^2 - \eta)}{(1+\nu)[\eta(\nu-1) + 2\nu^2]}, c_{22}^{hel} = \frac{E\eta^2(\nu-1)}{\alpha(\nu-1) + 2\nu^2},$$
$$c_{13}^{hel} = -\frac{E\nu(\nu+\eta)}{(1+\nu)[\eta(\nu-1) + 2\nu^2]}, \quad c_{12}^{hel} = c_{23}^{hel} = -\frac{\eta\nu E}{\eta(\nu-1) + 2\nu^2}, \quad (75)$$
$$c_{44}^{hel} = c_{66}^{hel} = \frac{\eta E}{2(1+\nu)}, \quad c_{55}^{hel} = \frac{E}{2(1+\nu)}$$
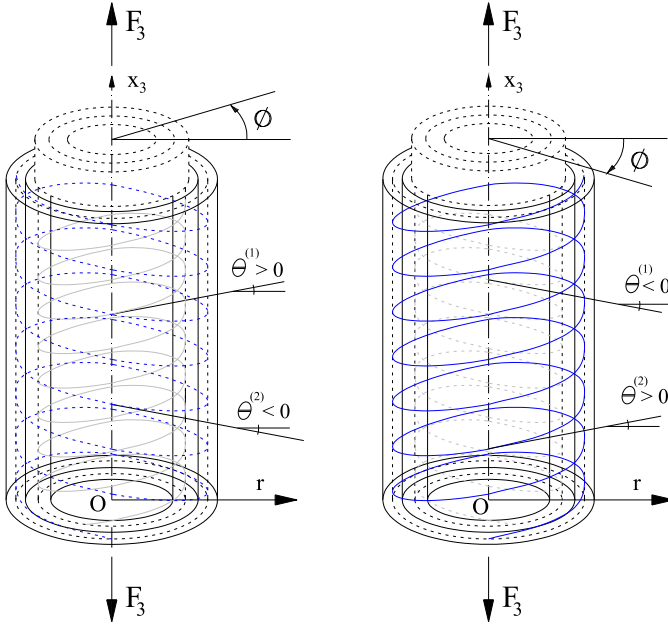
Fig. 2 Schematic representation of a three-phase FGMC subjected to end-point forces and exhibiting different wrapping angles of the fibers.

Substituting the Eq. (75) into Eq. (26), we obtained the connection between the elastic constant assigned in the helicoidal system and the ones in the associated cylindrical system:

$$c_{11}^{cyl} = \frac{E(\nu^2 - \eta)}{(1+\nu)[\eta(\nu-1)+2\nu^2]}, \quad c_{12}^{cyl} = -\frac{E\nu[\nu + \eta(2+\nu) + (\eta-1)\nu\cos 2\theta]}{2(1+\nu)[\eta(\nu-1)+2\nu^2]},$$

$$c_{13}^{cyl} = -\frac{E\nu\left[(\eta+\nu)\cos^2\theta + \eta(1+\nu)\sin^2\theta\right]}{(1+\nu)[\eta(\nu-1)+2\nu^2]}, \quad c_{14}^{cyl} = -\frac{E\nu^2(\eta-1)\sin 2\theta}{2(1+\nu)[\eta(\nu-1)+2\nu^2]},$$

$$c_{22}^{cyl} = \frac{E\left[\eta^2(\nu^2-1)\cos^4\theta + 2\eta(\nu-1)(\alpha+\nu)\sin^2 2\theta\cos^2 2\theta + (\nu^2-\eta)\sin^4\theta\right]}{(1+\nu)[\eta(\nu-1)+2\nu^2]},$$

$$c_{23}^{cyl} = \frac{E\left\{\left[\eta(\eta-1) - 2\eta(1+\eta)\nu + \nu^2(1+\eta(\eta-6))\right]\sin^2 2\theta - 4\eta\nu(\nu)\cos^2 2\theta\right\}}{4(1+\nu)[\eta(\nu-1)+2\nu^2]},$$

$$c_{24}^{cyl} = \frac{E(\eta-1)\left[\nu^2 + \eta(\nu^2-1) + (\eta(\nu-1)^2 - \nu^2)\cos 2\theta\right]\sin 2\theta}{4(1+\nu)[\eta(\nu-1)+2\nu^2]},$$

$$c_{33}^{cyl} = \frac{E\left[(\nu^2-\eta)\cos^4\theta + 2\eta(\nu-1)(\eta+\nu)\sin^2 2\theta\cos^2 2\theta + \eta^2(\nu^2-1)\sin^4\theta\right]}{(1+\nu)[\eta(\nu-1)+2\nu^2]},$$

$$c_{34}^{cyl} = -\frac{E(\eta-1)\left[\eta - (1+\eta)\nu^2 + (\eta(\nu-1)^2 - \nu^2)\cos 2\theta\right]\sin 2\theta}{4(1+\nu)[\eta(\nu-1)+2\nu^2]},$$

$$c_{44}^{cyl} = \frac{E\eta\left[2\nu^2 + \eta(\nu-1)\right](1+\cos 4\theta) + E\left\{(1+\eta)\left[\nu^2(1+\eta)-\eta\right] + 2\nu\eta\right\}\sin^2 2\theta}{4(1+\nu)[\eta(\nu-1)+2\nu^2]},$$

$$(76)$$

We assume that the helix slope is equal to θ in the phase (1) and is $-\theta$ in the phase (2) (as shown in Fig. 2). This determines the following relationship between the cylindrical elastic constants of the two hollow layers:

$$
\begin{aligned}
&c_{11}^{(1)} = c_{11}^{(2)}, \; c_{12}^{(1)} = c_{12}^{(2)}, \; c_{13}^{(1)} = c_{13}^{(2)}, \\
&c_{22}^{(1)} = c_{22}^{(2)}, \; c_{23}^{(1)} = c_{23}^{(2)}, \; c_{33}^{(1)} = c_{33}^{(2)}, \\
&c_{44}^{(1)} = c_{44}^{(2)}, \; c_{55}^{(1)} = c_{55}^{(2)}, \; c_{66}^{(1)} = c_{66}^{(2)}, \\
&c_{14}^{(1)} = -c_{14}^{(2)}, \; c_{24}^{(1)} = -c_{24}^{(2)}, \; c_{34}^{(1)} = -c_{34}^{(2)}, \; c_{56}^{(1)} = -c_{56}^{(2)},
\end{aligned}
\tag{77}
$$

Moreover, it is easy to verify other relationship between the constants $k_{ij}^{(1)}$ and $k_{ij}^{(2)}$:

$$
\begin{aligned}
&\lambda^{(1)} = \lambda^{(2)}, \; h_1^{(1)} = h_1^{(2)}, \; h_2^{(1)} = h_2^{(2)}, \\
&k_{ij}^{(1)} = k_{ij}^{(2)} \; \forall j \in \{1, \ldots, 5\}, \; and \; k_{i6}^{(1)} = -k_{i6}^{(2)} \; \forall i \in \{1, 2, 3\} \\
&k_{4j}^{(1)} = -k_{4j}^{(2)} \; \forall j \in \{1, \ldots, 5\}, \; and \; k_{46}^{(1)} = k_{46}^{(2)}
\end{aligned}
\tag{78}
$$

Recalling the Eqs. (58), (60), (61), we identify the 7 unknowns parameter $C_0^{(c)}$, ϕ, ε_0, $C_1^{(1)}$, $C_2^{(1)}$, $C_1^{(2)}$, $C_2^{(2)}$ and determine the coefficient of the matrix $\mathbb{P}$:

$$p_{11} = R^{(0)}, \; p_{12} = -R^{(0)-\lambda_1}\left(1 + 2R^{(0)2\lambda_1}\right), \; p_{13} = -i\left(R^{(0)\lambda_1} - R^{(0)-\lambda_1}\right), \; p_{14} = 0,$$

$$p_{15} = 0, \; p_{16} = -h_1^{(1)}R^{(0)}, \; p_{17} = -h_2^{(1)}R^{(0)2}, \; p_{21} = \frac{E}{1 - \nu - 2\nu^2},$$

$$p_{22} = -R^{(0)-(1+\lambda_1)}\left(k_{12}^{(1)} + k_{11}^{(1)}R^{(0)2\lambda_1}\right), p_{23} = -iR^{(0)-(1+\lambda_1)}\left(k_{14}^{(1)} + k_{13}^{(1)}R^{(0)2\lambda_1}\right),$$

$$p_{24} = 0, \; p_{25} = 0, \; p_{26} = -k_{15}^{(1)} + \frac{E\nu}{1 - \nu - 2\nu^2}, p_{27} = -k_{16}^{(1)}R^{(0)},$$

$$p_{32} = 2^{-\lambda_1/2}R^{(0)-\lambda_1}\left(1 + 2^{\lambda_1}R^{(0)2\lambda_1}\right), p_{33} = -i2^{-\lambda_1/2}R^{(0)-\lambda_1}\left(-1 + 2^{\lambda_1}R^{(0)2\lambda_1}\right),$$

$$p_{34} = -2^{-\lambda_1/2}R^{(0)-\lambda_1}\left(1 + 2^{\lambda_1}R^{2\lambda_1}\right), p_{35} = -i2^{-\lambda_1/2}R^{(0)-\lambda_1}\left(1 + 2^{\lambda_1}R^{(0)2\lambda_1}\right),$$

$$p_{36} = 0, \; p_{37} = 4h_2^{(1)}R^{(0)2}, \; p_{41} = 0,$$

$$p_{42} = 2^{-(\lambda_1 + 1)/2}R^{(0)-(1+\lambda_1)}\left(k_{12}^{(1)} + 2^{\lambda_1}k_{11}^{(1)}R^{(0)2\lambda_1}\right),$$

$$p_{43} = -i2^{-(\lambda_1 + 1)/2}R^{(0)-(1+\lambda_1)}\left(k_{14}^{(1)} + 2^{\lambda_1}k_{13}^{(1)}R^{(0)2\lambda_1}\right),$$

$$p_{44} = -2^{-(\lambda_1 + 1)/2}R^{(0)-(1+\lambda_1)}\left(k_{12}^{(1)} + 2^{\lambda_1}k_{11}^{(1)}R^{2\lambda_1}\right),$$

$$p_{45} = -i2^{-(\lambda_1 + 1)/2}R^{(0)-(1+\lambda_1)}\left(k_{14}^{(1)} + 2^{\lambda_1}k_{13}^{(1)}R^{(0)2\lambda_1}\right),$$

$$p_{46} = 0, \; p_{47} = 2\sqrt{2}k_{16}^{(1)}R^{(0)}, \; p_{51} = 0, \; p_{52} = 0, \; p_{53} = 0,$$

$$p_{54} = 3^{-(1+\lambda_1)/2}R^{-(1+\lambda_1)}\left(k_{12}^{(1)} + 3^{\lambda_1}k_{11}^{(1)}R^{(0)2\lambda_1}\right),$$

$$p_{55} = i3^{-(1+\lambda_1)/2}R^{-(1+\lambda_1)}\left(k_{14}^{(1)} + 3^{\lambda_1}k_{13}^{(1)}R^{(0)2\lambda_1}\right),$$

$$p_{56} = k_{15}^{(1)}, \quad p_{57} = -\sqrt{3}k_{16}^{(1)}R^{(0)}, \quad p_{61} = \frac{2E\pi\nu R^{(0)2}}{1-\nu-2\nu^2},$$

$$p_{62} = \frac{2^{1-\lambda_1/2}\pi R^{(0)1-\lambda_1}\left[\begin{array}{c}2^{\lambda_1/2}\left(2^{(1+\lambda_1)/2}-1\right)(\lambda_1-1)k_{31}^{(1)}R^{(0)2\lambda_1}\\ -\left(\sqrt{2}-2^{\lambda_1/2}\right)(1+\lambda_1)k_{32}^{(1)}\end{array}\right]}{\lambda_1^2-1},$$

$$p_{63} = \frac{i2^{1-\lambda_1/2}\pi R^{(0)1-\lambda_1}\left[\begin{array}{c}2^{\lambda_1/2}\left(2^{(1+\lambda_1)/2}-1\right)(\lambda_1-1)k_{33}^{(1)}R^{(0)2\lambda_1}\\ -\left(\sqrt{2}-2^{\lambda_1/2}\right)(1+\lambda_1)k_{34}^{(1)}\end{array}\right]}{\lambda_1^2-1},$$

$$p_{64} = \frac{\pi R^{(0)1-\lambda_1}\left[\left(2^{(3-\lambda_1)/2}-2\,3^{(1-\lambda_1)/2}\right)k_{32}^{(1)} - 2\left(2^{(1+\lambda_1)/2}-3^{(1+\lambda_1)/2}\right)k_{31}^{(1)}R^{(0)2\lambda_1}\right]}{\lambda_1-1},$$

$$p_{65} = \frac{i2^{1-\lambda_1/2}3^{-\lambda_1/2}\pi R^{(0)1-\lambda_1}\left[\begin{array}{c}6^{\lambda_1/2}\left(2^{(1+\lambda_1)/2}-3^{(1+\lambda_1)/2}\right)(\lambda_1-1)k_{33}^{(1)}R^{(0)2\lambda_1}\\ +\left(\sqrt{3}2^{\lambda_1/2}-\sqrt{2}3^{\lambda_1/2}\right)(1+\lambda_1)k_{34}^{(1)}\end{array}\right]}{\lambda_1^2-1},$$

$$p_{66} = \frac{\pi R^{(0)2}\left[E(\nu-1)+2k_{35}^{(1)}\left(2\nu^2+\nu-1\right)\right]}{2\nu^2+\nu-1}, \quad p_{67} = \frac{2}{3}\left(4\sqrt{2}-3\sqrt{3}-1\right)k_{36}^{(1)}\pi R^{(0)3},$$

$$p_{71} = 0, \quad p_{72} = \frac{2^{1-\lambda_1/2}\pi R^{(0)2-\lambda_1}\left[\begin{array}{c}2^{\lambda_1/2}\left(2^{1+\lambda_1/2}-1\right)(\lambda_1-2)k_{41}^{(1)}R^{(0)2\lambda_1}\\ +\left(2^{\lambda_1/2}-2\right)(2+\lambda_1)k_{42}^{(1)}\end{array}\right]}{\lambda_1^2-4},$$

$$p_{73} = \frac{i2^{1-\lambda_1/2}\pi R^{(0)2-\lambda_1}\left[\begin{array}{c}2^{\lambda_1/2}\left(2^{1+\lambda_1/2}-1\right)(\lambda_1-2)k_{43}^{(1)}R^{(0)2\lambda_1}\\ +\left(2^{\lambda_1/2}-2\right)(2+\lambda_1)k_{44}^{(1)}\end{array}\right]}{\lambda_1^2-1},$$

$$p_{74} = \frac{2^{1-\lambda_1/2}3^{-\lambda_1/2}\pi R^{(0)2-\lambda_1}\left[\begin{array}{c}6^{\lambda_1/2}\left(2^{1+\lambda_1/2}-3^{1+\lambda_1/2}\right)(\lambda_1-2)k_{41}^{(1)}R^{(0)2\lambda_1}\\ +\left(3\,2^{\lambda_1/2}-2\,3^{\lambda_1/2}\right)(2+\lambda_1)k_{42}^{(1)}\end{array}\right]}{\lambda_1^2-4},$$

$$p_{75} = \frac{i2^{1-\lambda_1/2}3^{-\lambda_1/2}\pi R^{(0)2-\lambda_1}\left[\begin{array}{c}6^{\lambda_1/2}\left(2^{1+\lambda_1/2}-3^{1+\lambda_1/2}\right)(\lambda_1-2)k_{43}^{(1)}R^{(0)2\lambda_1}\\+\left(3 2^{\lambda_1/2}-2\,3^{\lambda_1/2}\right)(2+\lambda_1)k_{44}^{(1)}\end{array}\right]}{\lambda_1^2-4},$$

$$p_{76} = \frac{2}{3}\left(4\sqrt{2}-3\sqrt{3}-1\right)k_{45}^{(1)}\pi R^{(0)3}, \quad p_{77} = \pi R^{(0)4}\left(\frac{E}{2(1+\nu)}+4k_{46}^{(1)}\right) \tag{79}$$

Finally, the *loads* vector $\mathbf{L}$ is $\mathbf{L}^T = \{0, 0, \ldots, 0, F_3, 0\}$ and the solution (65) can be found.

4.2.2 3-FGMC subjected to a twisting moment

We consider the same 3-FGMC of the previous example loaded by couple torque $\mathfrak{M}_t$ on its bases. The unknowns parameter are $C_0^{(e)}$, ϕ, ε_0, $C_1^{(1)}$, $C_2^{(1)}$, $C_1^{(2)}$, $C_2^{(2)}$ and the coefficients of the matrix $\mathbb{P}$ correspond to those ones given in Eq. (79), while the *loads* vector $\mathbf{L}$ becomes $\mathbf{L}^T = \{0, 0, \ldots, 0, 0, \mathfrak{M}_t\}$.

4.2.3 3-FGMC with prescribed twisting angle

The 3-FGMC of Section 4.2.1 is subjected to prescribed displacement conditions at its bases. In particular, we first considered null vertical displacement W_0 and a nonzero angle of rotation φ_0, for numerical needs assumed to be equal to 0.1 radiants, and the solution (73) can be constructed by implementing Eqs. (67), (68), (69). The analysis of the nonzero stress components, i.e. σ_{rr}, $\sigma_{\vartheta\vartheta}$, σ_{33} and $\sigma_{\vartheta3}$ has been shown in Figs. 4–7, respectively.

4.2.4 3-FGMC with imposed displacement in x_3 direction

The last example deals with the 3-FGMC subjected to a sole nonzero vertical displacement W_0. In this way, the solution can be calculated as in the previous case by properly changing the displacement vector of Eq. (70). Results in terms of internal Cauchy stresses are reported in Figs. 8–11, respectively, in which the value of applied displacement was set equal to 0.1 mm. The axial force and the torque couple that develop under the action of the two applied displacement is finally shown in Fig. 12.

4.3 Strategies for obtaining overall elasticity tensors: The Voigt estimation

The overall mechanical response of the generic $(n+1)$-FGMC can be studied by means of well-known homogenization strategies [21], which allow to calculate the effective properties of the composite structure. To this aim, we

consider a volume V bounded by ∂V, which constituted by n elastic cylindrical hollow phases with volume $V^{(i)}$ and an elastic cylindrical central core $V^{(0)}$. Any hollow phase has elasticity tensors $\mathbf{C}^{(i)}(i=1,2,\dots,n)$ and the central core has elasticity tensor $\mathbf{C}^{(0)}$. All the phases of the cylindrical solid are homogeneous and assumed to be linearly elastic, this implying that the overall response of the solid is linearly elastic, too. Perfect bond is also assumed between adjacent phases. By considering an isotropic central core and monoclinic external layers, the overall response of the solid may be anisotropic: this depends on the geometry and arrangement of the phases. Therefore, the overall elasticity tensors of the cylindrical solid, denoted by $\overline{\mathbf{C}}$, has to be evaluated. To do this, we calculate the average value of the strain field over each phase as:

$$\overline{\mathbf{E}}^{(i)} = \left\langle \mathbf{E}^{(i)}(\mathbf{x}) \right\rangle = \frac{1}{V^{(i)}} \int_{V^{(i)}} \mathbf{E}^{(i)}(\mathbf{x}) dV \tag{80}$$

and the average value of the stress field:

$$\overline{\mathbf{T}}^{(i)} = \left\langle \mathbf{T}^{(i)}(\mathbf{x}) \right\rangle = \frac{1}{V^{(i)}} \int_{V^{(i)}} \mathbf{T}^{(i)}(\mathbf{x}) dV \tag{81}$$

Since each phase is homogeneous, we can write:

$$\overline{\mathbf{T}}^{(i)} = \mathbf{C}^{(i)} : \overline{\mathbf{E}}^{(i)} \tag{82}$$

and for cylindrical central core

$$\overline{\mathbf{T}}^{(0)} = \mathbf{C}^{(0)} : \overline{\mathbf{E}}^{(0)} \tag{83}$$

Therefore, the average elasticity tensor by starting from

$$\overline{\mathbf{T}} = \overline{\mathbf{C}} : \overline{\mathbf{E}} = f_0 \overline{\mathbf{T}}^{(0)} + \sum_{i=1}^{n} f_i \overline{\mathbf{T}}^{(i)} = f_0 \mathbf{C}^{(0)} \overline{\mathbf{E}}^{(0)} + \sum_{i=1}^{n} f_i \mathbf{C}^{(i)} \overline{\mathbf{E}}^{(i)} \tag{84}$$

where $f^{(i)} = \frac{V^{(i)}}{V}$ is the volume fraction of the $i-th$ cylindrical hollow phase, $f^{(0)} = \frac{V^{(0)}}{V}$ is the volume fraction of the cylindrical central core, while $\overline{\mathbf{T}}$ and $\overline{\mathbf{E}}$ are the average stress and strain tensor of the entire cylindrical solid, respectively, which correspond to the weighted summation of the average stress and strain fields in each layer with volume fraction $f^{(i)}$. In the case of a prescribed macrostrain, we have that $\overline{\mathbf{E}} = \overline{\mathbf{E}}^{(0)} = \overline{\mathbf{E}}^{(i)}$, and Eq. (84) gives the expression of the Voigt elasticity tensor:

$$\overline{\mathbf{C}} = f_0 \mathbf{C}^{(0)} + \sum_{i=1}^{n} f_i \mathbf{C}^{(i)} \tag{85}$$

In general, the elastic response of the cylindrical multiphase solid is dependent on the sign of the helix angles $\theta^{(i)}$ developing in its phases. The presented cases let to examine the global response of a three-phase solid composed by helicoidal fibers under the contemporary action of axial forces and torsion. The phase 0 is assumed isotropic, while the phase 1 is constituted by fibers that have the slope $\theta^{(1)} = \theta$ and the phase 2 is constituted by counter-wrapped fibers having slope $\theta^{(2)} = -\theta$. Therefore, in this model, the orientation of the helicoidal fibers influence the global mechanical behavior. In particular, if a traction force F_3 is applied and $\theta > 0$ ($\theta^{(1)} > -\theta^{(2)} = \theta$), then we obtain a positive axial deformation (i.e. elongation: $\varepsilon_{33} = \varepsilon_0 > 0$) and a positive unitary twist angle (counter-clockwise: $\phi > 0$). Conversely, if $F_3 > 0$ but $\theta < 0$ (where $\theta^{(1)} > -\theta^{(2)} = \theta$), the cylinder still elongates but the unitary twist angle is negative (clockwise: $\phi < 0$), the phases wrapping in an opposite sense (see Fig. 2).

If the applied twist couple $\mathfrak{M}_t$ is counter-clockwise (positive) and $\theta > 0$ (where $\theta^{(1)} > -\theta^{(2)} = \theta$), then the unitary twisted angle and the axial strain are positive ($\phi > 0$ and $\varepsilon_{33} = \varepsilon_0 > 0$). Instead, if $\theta < 0$, ($\theta^{(1)} > -\theta^{(2)} = \theta$), the unitary twisted angle ϕ is positive but the axial strain negative and contraction occurs ($\varepsilon_{33} = \varepsilon_0 < 0$, see Fig. 3).
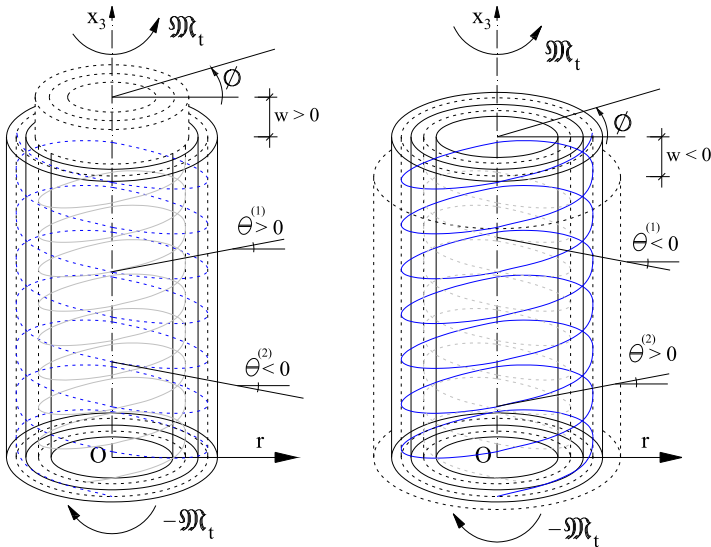
Fig. 3 Schematic representation of a three-phase FGMC subjected to end-point twisting couple and exhibiting different wrapping angles of the fibers.
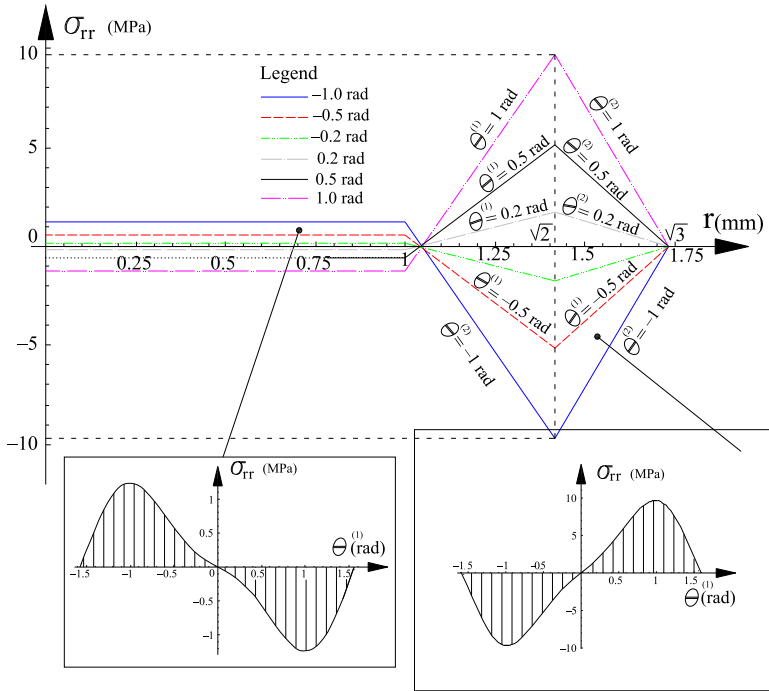
Fig. 4 The stress component σ_{rr} as function of the radius and slope of the fibers under a prescribed torsion angle $\varphi_0 = 0.1\,rad$.
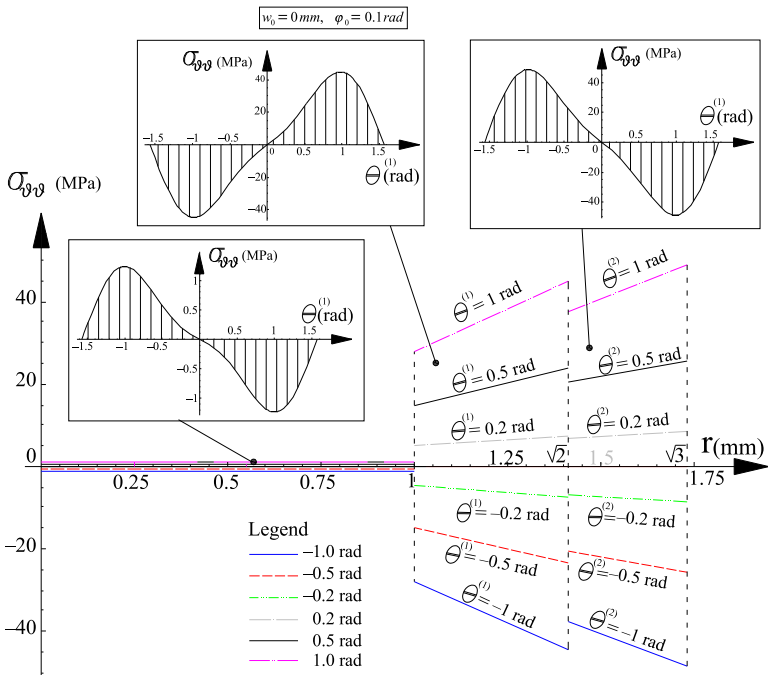
Fig. 5 The stress component $\sigma_{\vartheta\vartheta}$ as function of the radius and slope of the fibers under a prescribed torsion angle $\varphi_0 = 0.1\,rad$.
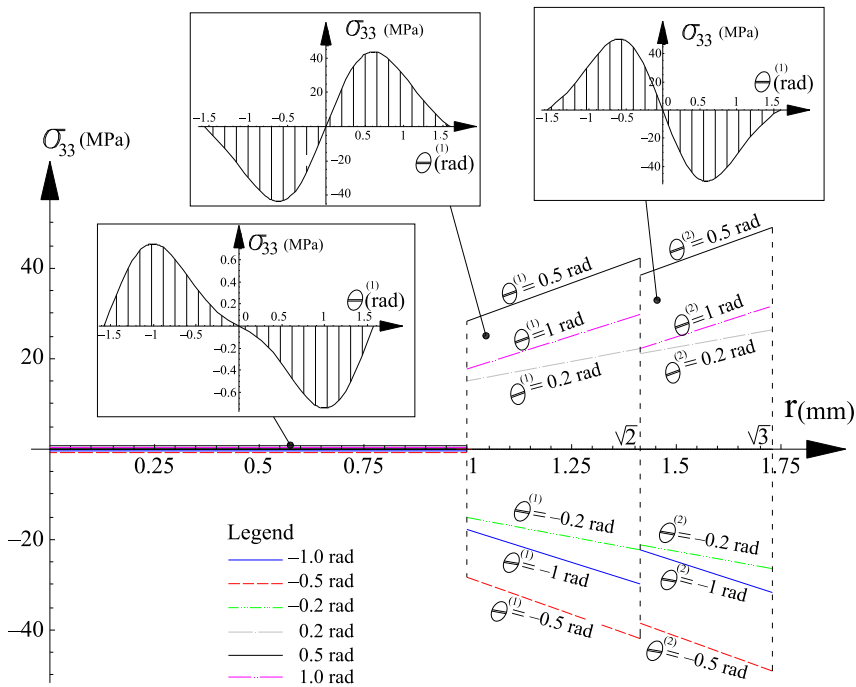
Fig. 6 The stress component σ_{33} as function of the radius and slope of the fibers under a prescribed torsion angle $\varphi_0 = 0.1\, rad$.
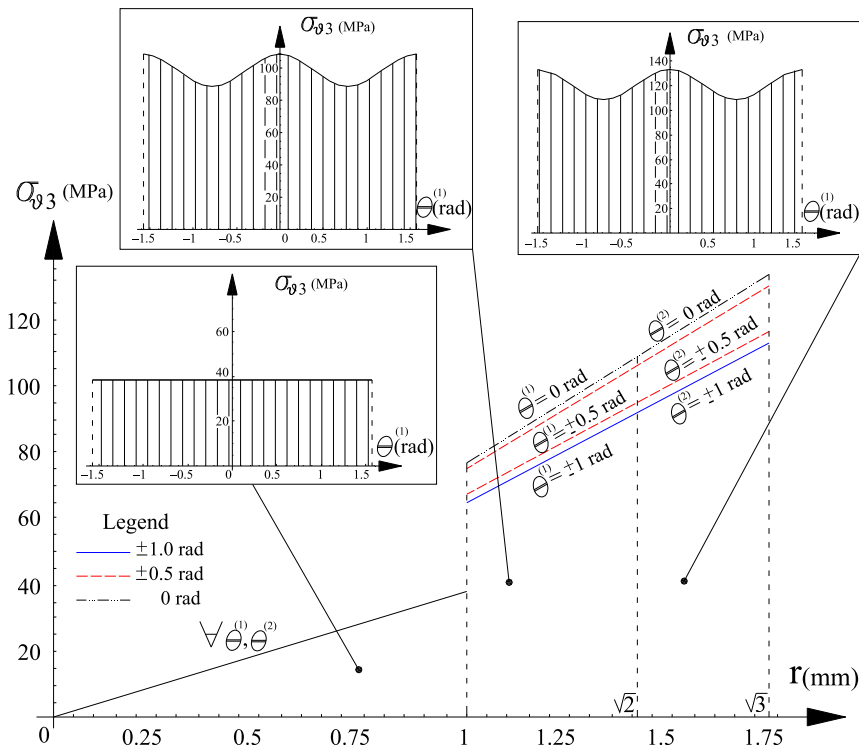
Fig. 7 The stress component $\sigma_{\vartheta 3}$ as function of the radius and slope of the fibers under a prescribed torsion angle $\varphi_0 = 0.1\, rad$.
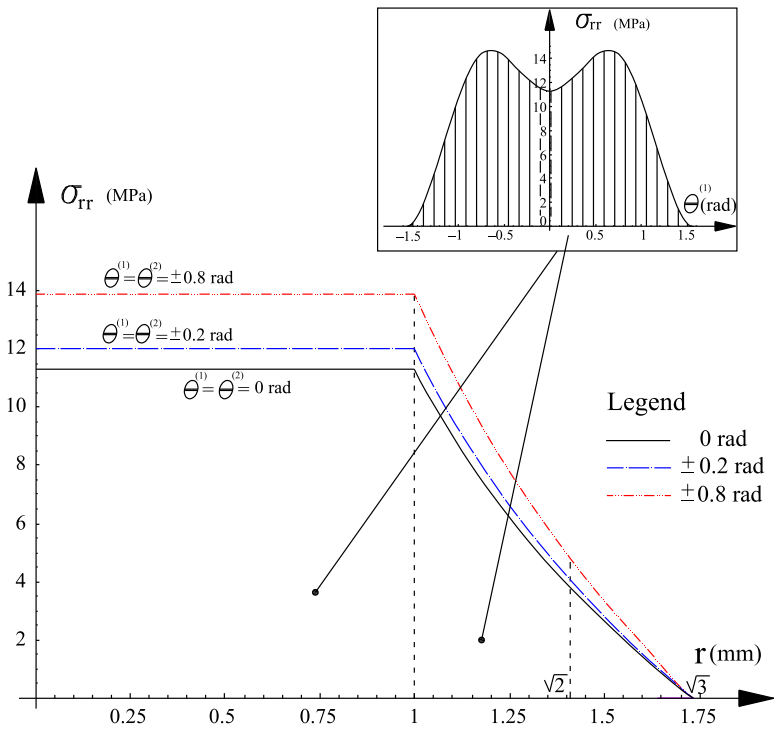
Fig. 8 The stress component σ_{rr} as function of the radius and slope of the fibers under a prescribed displacement $W_0 = 0.1\,\text{mm}$.
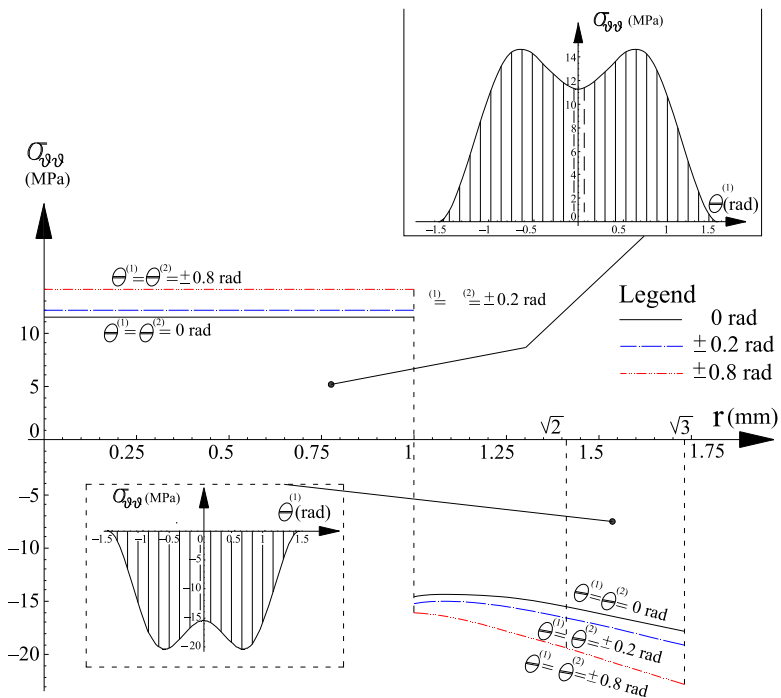
Fig. 9 The stress component $\sigma_{\vartheta\vartheta}$ as function of the radius and slope of the fibers under a prescribed displacement $W_0 = 0.1\,\text{mm}$.
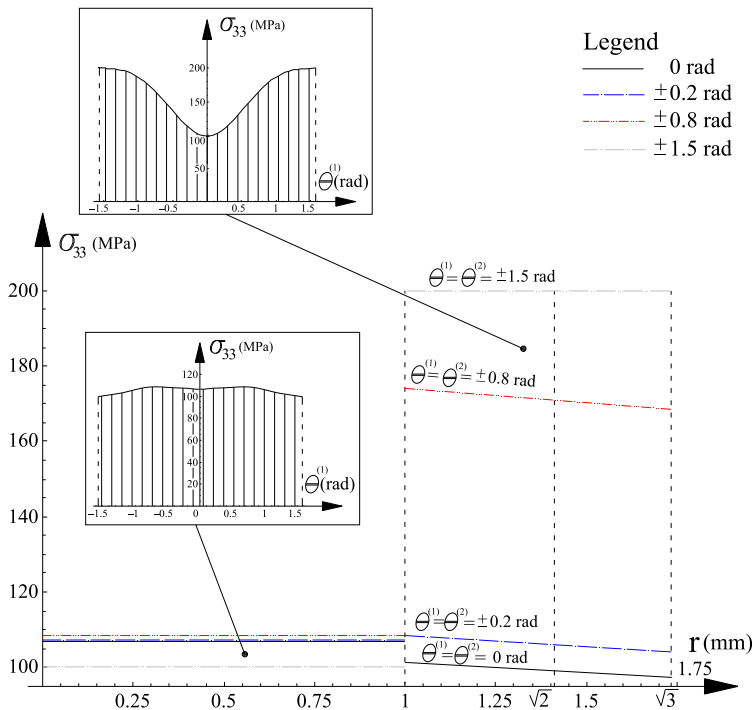
Fig. 10 The stress component σ_{33} as function of the radius and slope of the fibers under a prescribed displacement $W_0 = 0.1$ mm.
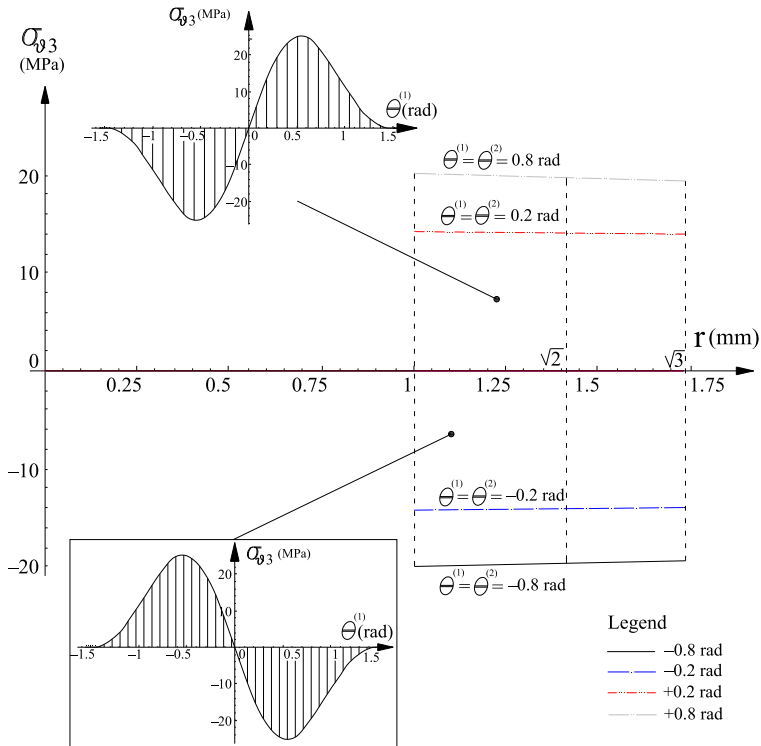
Fig. 11 The stress component $\sigma_{\vartheta 3}$ as function of the radius and slope of the fibers under a prescribed displacement $W_0 = 0.1$ mm.
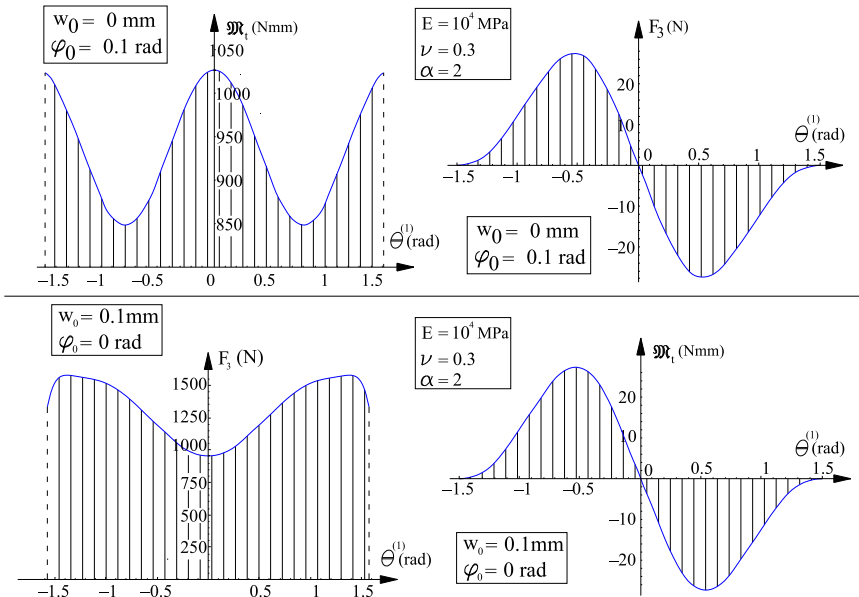
Fig. 12 The axial force and couple torque reaction on basis of the solid for imposed displacements. We reported the diagram of the $\mathfrak{M}_t$ and F_3 as function of slope of the fibers.

5 Conclusions

In this chapter, with in mind MWCNT, a particular class of heterogeneous materials, namely the Functionally Graded Materials (FGM), has been in depth investigated. In particular, attention has been paid on the development of fully analytical solutions for generic FGM cylinders constituted of n monoclinic phases and a central isotropic core $((n+1)$-FGMC) under de Saint Venant load conditions. The generic monoclinic external phase of the FGMC can be directly associated to the elastic behavior of helically arranged fibers that exhibit orthotropic symmetry in the helicoidal local system. Therefore, the developed solution permits to describe, at the continuum level, the mechanical response of any compound cylinder constituted by layers with helically arranged structures characterized by different angles and/or other micro-geometrical parameters, in a way to put in light the overall axial-torsional coupling and the related stress fields in these particular structures. Exact solutions also permit to obtain effective mechanical properties by using standard homogenization techniques, in fact utilized at the end of the work for highlighting the power of the adopted method and the relevance of the results for applications in the analysis of composites reinforced with MWCNTs.

Acknowledgments

Appendix

A.1 Explicit expression of the coefficients $P_{h/m}$ of the matrix $\mathbb{P}$ for n arbitrary phases

For the case of circular composite cylinders constituted by a central core and n hollow phases, the elastic axis-symmetrical solutions for the above described load conditions are related to the solution of the algebraic linear system (1.64), where the $(6n+4) \times (6n+4)$ matrix $\mathbf{P}$ is

$$\mathbf{P} = \begin{bmatrix} P_{1/1} & P_{1/2} & \cdots & P_{1/6i-5} & P_{1/6i-4} & \cdots & P_{1/6i} & \cdots & P_{1/6n+1} & \cdots & P_{1/6n+4} \\ P_{2/1} & P_{2/2} & \cdots & P_{2/6i-5} & P_{2/6i-4} & \cdots & P_{2/6i} & \cdots & P_{2/6n+1} & \cdots & P_{2/6n+4} \\ \cdots & \cdots & \cdots & \cdots & \cdots & \cdots & \cdots & \cdots & \cdots & \cdots & \cdots \\ P_{6i-5/1} & P_{6i-5/2} & \cdots & P_{6i-5/6i-5} & P_{6i-5/6i-4} & \cdots & P_{6i-5/6i} & \cdots & P_{6i-5/6n+1} & \cdots & P_{6i-5/6n+4} \\ P_{6i-4/1} & P_{6i-4/2} & \cdots & P_{6i-4/6i-5} & P_{6i-4/6i-4} & \cdots & P_{6i-4/6i} & \cdots & P_{6i-4/6n+1} & \cdots & P_{6i-4/6n+4} \\ \cdots & \cdots & \cdots & \cdots & \cdots & \cdots & \cdots & \cdots & \cdots & \cdots & \cdots \\ P_{6i/1} & P_{6i/2} & \cdots & P_{6i/6i-5} & P_{6i/6i-4} & \cdots & P_{6i/6i} & \cdots & P_{6i/6n+1} & \cdots & P_{6i/6n+4} \\ \cdots & \cdots & \cdots & \cdots & \cdots & \cdots & \cdots & \cdots & \cdots & \cdots & \cdots \\ P_{6n+1/1} & P_{6n+1/2} & \cdots & P_{6n+1/6i-5} & P_{6n+1/6i-4} & \cdots & P_{6n+1/6i} & \cdots & P_{6n+1/6n+1} & \cdots & P_{6n+1/6n+4} \\ \cdots & \cdots & \cdots & \cdots & \cdots & \cdots & \cdots & \cdots & \cdots & \cdots & \cdots \\ P_{6n+4/1} & P_{6n+4/2} & \cdots & P_{6n+4/6i-5} & P_{6n+4/6i-4} & \cdots & P_{6n+4/6i} & \cdots & P_{6n+4/6n+1} & \cdots & P_{6n+4/6n+4} \end{bmatrix} \tag{A.1}$$

and:

$$P_{1/1} = -\frac{R^{(0)}}{\mu^{(0)}}, \quad P_{1/4} = \frac{1}{2\mu^{(1)}R^{(0)}}, \quad P_{1/6} = \frac{R^{(0)}}{\mu^{(1)}}, P_{1/2} = P_{1/3} = P_{1/5} = 0,$$

$$P_{1/k} = 0 \quad \forall k \in \{7, 8, \ldots, 6n+4\}$$

$$P_{2/2} = -\frac{2R^{(0)}}{\mu^{(0)}}, \quad P_{2/5} = \frac{1}{\mu^{(1)}R^{(0)}}, \quad P_{2/7} = \frac{2R^{(0)}}{\mu^{(1)}},$$

$$P_{2/1} = P_{2/3} = P_{2/4} = P_{2/6} = 0, \quad P_{2/k} = 0, \quad \forall k \in \{8, 9, \ldots, 6n+4\}$$

$$P_{3/2} = \frac{R^{(0)2}\left(\mu^{(0)} + \lambda^{(0)}\right)}{\mu^{(0)2}}, \quad P_{3/3} = -\frac{2\left(2\mu^{(1)} + \lambda^{(1)}\right)}{\mu^{(1)}\left(\mu^{(1)} + \lambda^{(1)}\right)}\log R^{(0)},$$

$$P_{3/5} = -\frac{\log R^{(0)}}{\mu^{(0)} + \lambda^{(0)}}, \quad P_{3/7} = -\frac{R^{(0)}\left(\mu^{(1)} + \lambda^{(1)}\right)}{\mu^{(1)2}}, \quad P_{3/8} = -1,$$

$$P_{3/6n+4} = -\frac{R^{(0)2}\left(\mu^{(1)}\lambda^{(0)} - \mu^{(0)}\lambda^{(1)}\right)}{4\mu^{(0)}\mu^{(1)}}, P_{3/1} = P_{3/4} = P_{3/6} = 0,$$

$$P_{3/k} = 0, \quad \forall k \in \{9, 10, \ldots, 6n+3\}$$

$$P_{4/1} = -\frac{2\left(\lambda^{(0)} + \mu^{(0)}\right)}{\mu^{(0)}}, \quad P_{4/4} = -\frac{1}{R^{(0)2}}, \quad P_{4/6} = \frac{2\left(\lambda^{(1)} + \mu^{(1)}\right)}{\mu^{(1)}},$$

$$P_{4/6n+3} = \lambda^{(0)} - \lambda^{(1)}, P_{4/2} = P_{4/3} = P_{4/5} = 0,$$

$$P_{4/k} = 0, \quad \forall k \in \{7, 8, \ldots, 6n+2, 6n+4\}$$

$$P_{5/2} = -\frac{4\left(\lambda^{(0)} + \mu^{(0)}\right)}{\mu^{(0)}}, P_{5/5} = -\frac{2}{R^{(0)2}}, P_{5/7} = \frac{4\left(\lambda^{(1)} + \mu^{(1)}\right)}{\mu^{(1)}},$$

$$P_{5/6n+4} = \lambda^{(0)} - \lambda^{(1)}, P_{5/1} = P_{5/3} = P_{5/4} = P_{5/6} = 0,$$

$$P_{5/k} = 0, \quad \forall k \in \{8, 9, \ldots, 6n+3\}$$

$$P_{6/2} = \frac{2R^{(0)}\lambda^{(0)}}{\mu^{(0)}}, \quad P_{6/3} = -\frac{2\left(2\mu^{(1)} + \lambda^{(1)}\right)}{R^{(0)2}\left(\lambda^{(1)} + \mu^{(1)}\right)}, \quad P_{6/5} = \frac{\lambda^{(1)}}{R^{(0)}\left(\lambda^{(1)} + \mu^{(1)}\right)},$$

$$P_{6/7} = -\frac{2R^{(0)}\lambda^{(1)}}{\mu^{(1)}}, \quad P_{6/6n+4} = \frac{1}{2}R^{(0)}\left(2\mu^{(0)} + \lambda^{(0)} - 2\mu^{(1)} - \lambda^{(1)}\right),$$

$$P_{6/1} = P_{6/4} = P_{6/6} = 0, \quad P_{6/k} = 0, \quad \forall k \in \{8, 9, \ldots, 6n+3\}$$

$$P_{6i-5/6i-8} = -\frac{1}{2R^{(i)}\mu^{(i)}}, P_{6i-5/6i-6} = -\frac{R^{(i)}}{\mu^{(i)}}, P_{6i-5/6i-2} = \frac{1}{2R^{(i)}\mu^{(i+1)}},$$

$$P_{6i-5/6i} = \frac{R^{(i)}}{\mu^{(i+1)}}, \quad \forall i \in \{2, \ldots, n-1\}$$

$$P_{6i-5/k} = 0, \quad \forall k \in \{1, 2, \ldots, 6n+4\} - \{6i-8, 6i-6, 6i-2, 6i\}$$

$$P_{6i-4/6i-7} = -\frac{1}{R^{(i)}\mu^{(i)}}, \ \ P_{6i-4/6i-5} = -\frac{2R^{(i)}}{\mu^{(i)}}, \ \ P_{6i-4/6i-1} = \frac{1}{R^{(i)}\mu^{(i+1)}},$$

$$P_{6i-4/6i+1} = \frac{2R^{(i)}}{\mu^{(i+1)}}, \forall i \in \{2, \ldots, n-1\}$$

$$P_{6i-4/k} = 0 \ \ \forall k \in \{1, 2, \ldots, 6n+4\} - \{6i-7, 6i-5, 6i-1, 6i+1\}$$

$$P_{6i-3/6i-9} = \frac{2\log R^{(i)}\left(2\mu^{(i)} + \lambda^{(i)}\right)}{\mu^{(i)}\left(\mu^{(i)} + \lambda^{(i)}\right)}, \ \ P_{6i-3/6i-7} = \frac{\log R^{(i)}}{\mu^{(i)} + \lambda^{(i)}},$$

$$P_{6i-3/6i-5} = \frac{R^{(i)2}\left(\mu^{(i)} + \lambda^{(i)}\right)}{\mu^{(i)2}}, \ \ P_{6i-3/6i-4} = 1,$$

$$P_{6i-3/6i-3} = -\frac{2\log R^{(i)}\left(2\mu^{(i+1)} + \lambda^{(i+1)}\right)}{\mu^{(i+1)}\left(\mu^{(i+1)} + \lambda^{(i+1)}\right)}, \ \ P_{6i-3/6i-1} = -\frac{\log R^{(i)}}{\mu^{(i+1)} + \lambda^{(i+1)}},$$

$$P_{6i-3/6i+1} = -\frac{R^{(i)2}\left(\mu^{(i+1)} + \lambda^{(i+1)}\right)}{\mu^{(i+1)2}},$$

$$P_{6i-3/6i+2} = 1, \ P_{6i-3/6n+4} = \frac{R^{(i)2}\left(\mu^{(i)}\lambda^{(i+1)} - \lambda^{(i)}\mu^{(i+1)}\right)}{4\mu^{(i)}\mu^{(i+1)}}, \forall i \in \{2, \ldots, n-1\}$$

$$P_{6i-3/k} = 0 \ \ \forall k \in \{1, 2, \ldots, 6n+3\}$$

$$- \{6i-9, 6i-7, 6i-5, 6i-4, 6i-3, 6i-1, 6i+1, 6i+2, 6n+4\}$$

$$P_{6i-2/6i-8} = \frac{1}{R^{(i)2}}, \ \ P_{6i-2/6i-6} = -\frac{2\left(\mu^{(i)} + \lambda^{(i)}\right)}{\mu^{(i)}}, \ \ P_{6i-2/6i-2} = -\frac{1}{R^{(i)2}},$$

$$P_{6i-2/6i} = \frac{2\left(\mu^{(i+1)} + \lambda^{(i+1)}\right)}{\mu^{(i+1)}}, \ \ P_{6i-2/6n+3} = \lambda^{(i)} - \lambda^{(i+1)}, \forall i \in \{2, \ldots, n-1\}$$

$$P_{6i-2/k} = 0 \ \ \forall k \in \{1, 2, \ldots, 6n+4\} - \{6i-8, 6i-6, 6i-2, 6i, 6n+3\}$$

$$P_{6i-1/6i-7} = \frac{2}{R^{(i)2}}, \ P_{6i-1/6i-5} = -\frac{4\left(\mu^{(i)} + \lambda^{(i)}\right)}{\mu^{(i)}},$$

$$P_{6i-1/6i-1} = -\frac{2}{R^{(i)2}}, P_{6i-1/6i+1} = \frac{4\left(\mu^{(i+1)} + \lambda^{(i+1)}\right)}{\mu^{(i+1)}},$$

$$P_{6i-1/6n+4} = \lambda^{(i)} - \lambda^{(i+1)}, \ \forall i \in \{2, ..., n-1\},$$

$$P_{6i-1/k} = 0, \ \ \forall k \in \{1, 2, ..., 6n+4\} - \{6i-7, 6i-5, 6i-1, 6i+1, 6n+4\}$$

$$P_{6i/6i-9} = \frac{2\left(2\mu^{(i)} + \lambda^{(i)}\right)}{R^{(i)}\left(\mu^{(i)} + \lambda^{(i)}\right)}, \ \ P_{6i/6i-7} = -\frac{\lambda^{(i)}}{R^{(i)}\left(\mu^{(i)} + \lambda^{(i)}\right)},$$

$$P_{6i/6i-5} = \frac{2R^{(i)}\lambda^{(i)}}{\mu^{(i)}}, P_{6i/6i-3} = -\frac{2\left(2\mu^{(i+1)} + \lambda^{(i+1)}\right)}{R^{(i)}\left(\mu^{(i+1)} + \lambda^{(i+1)}\right)},$$

$$P_{6i/6i-1} = \frac{\lambda^{(i+1)}}{R^{(i)}\left(\mu^{(i+1)} + \lambda^{(i+1)}\right)}, \ \ P_{6i/6i+1} = -\frac{2R^{(i)}\lambda^{(i+1)}}{\mu^{(i+1)}},$$

$$P_{6i/6n+4} = \frac{R^{(i)}\left(2\mu^{(i+1)} + \lambda^{(i+1)} - 2\mu^{(i)} - \lambda^{(i)}\right)}{2}, \ \ \forall i \in \{2, ..., n-1\}$$

$$P_{6i/k} = 0 \ \ \forall k \in \{1, 2, ..., 6n+4\}$$

$$- \{6i-9, 6i-7, 6i-5, 6i-3, 6i-1, 6i+1, 6n+4\},$$

$$P_{6n+1/6n-2} = \frac{1}{R^{(n)2}}, \ \ P_{6n+1/6n} = -\frac{2\left(\mu^{(n)} + \lambda^{(n)}\right)}{\mu^{(n)}}, \ \ P_{6n+1/6n+3} = \lambda^{(n)},$$

$$P_{6n+1/k} = 0, \ \ \forall k \in \{1, 2, ..., 6n+4\} - \{6n-2, 6n, 6n+3\},$$

$$P_{6n+2/6n-1} = \frac{2}{R^{(n)2}}, P_{6n+2/6n+1} = -\frac{4\left(\mu^{(n)} + \lambda^{(n)}\right)}{\mu^{(n)}}, P_{6n+2/6n+4} = \lambda^{(n)},$$

$$P_{6n+2/k} = 0, \ \ \forall k \in \{1, 2, ..., 6n+3\} - \{6n\pm1\},$$

$$P_{6n+3/6n-3} = \frac{2\left(2\mu^{(n)} + \lambda^{(n)}\right)}{R^{(n)}\left(\mu^{(n)} + \lambda^{(n)}\right)}, \ \ P_{6n+3/6n-1} = -\frac{\lambda^{(n)}}{R^{(n)}\left(\mu^{(n)} + \lambda^{(n)}\right)},$$

$$P_{6n+3/6n+1} = \frac{2R^{(s)}\lambda^{(s)}}{\mu^{(s)}}, \ \ P_{6n+3/6n+4} = -\frac{R^{(n)}\left(2\mu^{(n)} + \lambda^{(n)}\right)}{2},$$

$$P_{6n+3/k} = 0, \ \ \forall k \in \{1, 2, \ldots, 6n+3\} - \{6n-3, 6n\pm1\},$$

$$P_{6n+4/1} = -\frac{2\pi\lambda^{(0)}R^{(0)2}}{\mu^{(0)}}, P_{6n+4/6i} = \frac{2\pi\lambda^{(i)}\left(R^{(i-1)2} - R^{(i)2}\right)}{\mu^{(i)}} \ , \ \ \forall i \in \{1, 2, \ldots, n-1\},$$

$$P_{6n+4/6n+3} = \pi\left[\sum_{i=0}^{n-1}R^{(i)2}\left(2\mu^{(i)} + \lambda^{(i)} - 2\mu^{(i+1)} - \lambda^{(i+1)}\right) + R^{(n)2}\left(2\mu^{(n)} + \lambda^{(n)}\right)\right],$$

$$P_{6n+4/k} = 0, \ \ \forall k \in \{2, \ldots, 6n+4\} - \{1, 6i, 6n+3\}.$$

References

[1] K.M. Liew, S. Kitipornchai, X.Z. Zhang, C.W. Lim, Analysis of the thermal stress behaviour of functionally graded hollow circular cylinders, Int. J. Solids Struct. 40 (2003) 2355–2380.

[2] Z.S. Shao, Mechanical and thermal stresses of a functionally graded circular hollow cylinder with finite length, Int. J. Pres. Ves. Pip. 82 (2005) 155–163.

[3] M.,.A. Mian, A.J.M. Spencer, Exact solutions for functionally graded and laminated elastic materials, J. Mech. Phys. Solids 46 (12) (1998) 2283–2295.

[4] M. Fraldi, S.C. Cowin, Inhomogeneous elastostatic problem solutions constructed from stress-associated homogeneous solutions, J. Mech. Phys. Solids 52 (2004) 2207–2233.

[5] V.I. Alshits, O.K. Kirchner, Cylindrically anisotropic, radially inhomogeneous elastic materials, Proc. R. Soc. A 457 (2001) 671–693.

[6] M. Fraldi, F. Carannante, L. Nunziante, Analytical solutions for n-phase functionally graded material cylinders under de saint Venant load conditions: homogenization and effects of Poisson ratios on the overall stiffness, Compos. Part B Eng. 45 (2013) 1310–1324.

[6a] M. Fraldi, et al., A hybrid deterministic-probabilistic approach to model the mechanical response of helically arranged hierarchical strands, J. Mech. Phys. Solids 106 (2017) 338–352.

[7] C.S. Chouchaoui, O.O. Ochoa, Similitude study for a laminated cylindrical tube under tensile, torsion, bending, internal and external pressure. Part I: governing equations, Compos. Struct. 44 (1999) 221–229.

[8] T. Chen, C.T. Chung, W.L. Lin, A revisit of a cylindrically anisotropic tube subjected to pressuring, shearing, torsion, extension and a uniform temperature change, Int. J. Solids Struct. 37 (2000) 5143–5159.

[9] J.Q. Tarn, Exact solutions for functionally graded anisotropic cylinders subjected to thermal and mechanical loads, Int. J. Solids Struct. 38 (2001) 8189–8206.

[10] J.Q. Tarn, Y.M. Wang, Laminated composite tubes under extension, torsion, bending, shearing and pressuring: a state space approach, Int. J. Solids Struct. 38 (2001) 9053–9075.

[11] S.G. Lekhnitskii, Theory of Elasticity of an Anisotropic Body, Mir, Moscow, 1981.

[12] C.H. Huang, S.B. Dong, Analysis of laminated circular cylinders of materials with the most general form of cylindrical anisotropy. I. Axially symmetric deformations, Int. J. Solids Struct. 38 (2001) 6163–6182.

[13] T.C.T. Ting, Anisotropic Elasticity-Theory and Applications, Oxford University Press, 1996.

[14] M.E. Gurtin, The Linear Theory of Elasticity, Handbbuch der Physik, Springer, Berlin, 1972.

[15] C. Truesdell, R. Toupin, S. Flugge (Ed.), The Classical Field Theories, Encyclopedia of Physics, Springer Verlag, Berlin, 1960. vol. 3(1).

[16] M. Mehrabadi, S.C. Cowin, Eigentensors of linear anisotropic elastic materials, Q. J. Mech. Appl. Math. 43 (1990) 15–41.

[17] S.C. Cowin, Continuum Mechanics of Anisotropic Materials, Springer, 2013.

[18] S.C. Cowin, M.M. Mehrabadi, On the identification of material symmetry for anisotropic elastic materials, Q. J. Mech. Appl. Math. 40 (4) (1987) 451–476.

[19] S.G. Lekhnitskii, Theory of Elasticity of an Anisotropic Elastic Body, Holden-Day, San Francisco, 1963.

[20] Wolfram Research, I, Mathematica, 2015. Wolfram Research, Inc.

[21] S. Nemat-Nasser, M. Hori, Micromechanics: Overall properties of heterogeneous materials, second ed., North Holland series in Applied Mathematics, vol. 37, Elsevier, 1998.

Further reading

[22] ANSYS, Inc, ANSYS Mechanical User's Guide, release 15.0 Edition (November) (2013).

[23] F. Blouin, A. Cardou, A study of helically reinforced cylinders under axially symmetric loads mathematical modelling, Int. J. Solids Struct. 25 (2) (1989) 189–200.

[24] J.A. Crossley, A.H. England, A.J.M. Spencer, Bending and flexure of cylindrically monoclinic elastic cylinders, Int. J. Solids Struct. 40 (2003) 6999–7013.

[25] D. Elata, R. Eshkenazy, M.P. Weiss, The mechanical behaviour of a wire rope with an independent wire rope core, Int. J. Solids Struct. 41 (5) (2004) 1157–1172.

[26] M. Fraldi, S.C. Cowin, Chirality in the torsion of cylinders with trigonal symmetry, J. Elast. 69 (2002) 121–148.

[27] S.R. Ghoreishi, T. Messager, P. Catraud, P. Davies, Validity and limitations of linear analytical models for steel wire strands under axial loading, using 3D FE model, Int. J. Mech. Sci. 49 (2007) 1251–1261.

[28] R.E. Hobbs, Interwire Slippage and Fatigue Prediction in Stranded Cables for LTP Tethers, Behaviour of Offshore Structure, vol. 2, Hemisphere publishing/ McGraw-Hill, New York, 1982.

[29] F.H. Hruska, Calculation of stresses in wire ropes, Wire Wire Prod. 26 (9) (1951) 766–767.

[30] F.H. Hruska, Radial forces in wire ropes, Wire Wire Prod. 27 (5) (1952) 459–463.

[31] F.H. Hruska, Tangential forces in wire ropes, Wire Wire Prod. 28 (5) (1953) 455–460.

[32] C. Jolicoeur, A. Cardou, Semicontinuous mathematical model for bending of multilayered wire strands, J. Eng. Mech. 122 (7) (1996) 643–650.

[33] R.H. Knapp, Nonlinear analysis of a helically armored cable with nonuniform mechanical properties in tension and torsion, in: Proceeding of IEEE/MTS Conference of Engineering in the Ocean Environment, San Diego, 1975, pp. 55–164.

[34] K. Kumar, J.E. Cochran Jr., Closed-form analyses for elastic deformations of multilayered strand, J. Appl. Mech. 54 (1987) 898–903.

[35] M. Labrosse, Contribution à l'étude du rôle du frottement sur le comportement et la durée de vie des câbles monocouches (Ph.D. thesis), Ecole Centrale de Nantes, France, 1998.

[36] S. Leelavanichkul, A. Cherkaev, Elastic cylinder with helicoidal orthotropy: Theory and application, Int. J. Eng. Sci. 47 (2009) 1–20.

[37] A.E.H. Love, A Treatise on the Mathematical Theory of Elasticity, fourth ed., Dover Publications, New York, 1944.

[38] S. Machida, A.J. Durelli, Response of a strand to axial and torsional displacement, J. Mech. Eng. Sci. 15 (1973) 241–251.

[39] K.G. McConnell, W.P. Zemeke, A model to predict the coupled axial torsion properties of ACSR electrical conductors, Exp. Mech. 22 (7) (1982) 237–244.

[40] C. McManus, Left Hand, Right Hand—The Origins of Asymmetry in Brains, Bodies. Atoms and Cultures, Harvard, Cambridge, MA, 2002.

[41] A. Nawrocki, M. Labrosse, A finite element model for simple straight wire rope strand, Comput. Struct. 77 (2000) 345–369.

[42] W.F. Neumann, N.W. Neumann, The Chemical Dynamics of Bone Mineral, Univ. Chicago Press, Chicago, 1958.

[43] A.J. Pons, A. Karma, Helical crack-front instability in mixed-mode fracture, Nature 464 (2010) 85–89.

[44] H. Ramsey, A theory of thin rods with application to helical constituent wires in cables, Int. J. Mech. Sci. 30 (1988) 559–570.

[45] M. Raoof, I. Kraincanic, Analysis of large diameter steel ropes, J. Eng. Mech. 121 (6) (1995) 667–675.

[46] S. Sathikh, M.B.K. Moorthy, M. Krishnan, A symmetric linear elastic model for helical wire strands under axisymmetric loads, J. Strain Anal. Eng. Des. 31 (5) (1996) 389–399.

[47] C.K. Shield, G.A. Costello, The effect of wire rope mechanics on the material properties of cord composites: an elasticity approach, J. Appl. Mech. 61 (1994) 1–8.

[48] S.L. Sokolov, Prediction of the fatigue life of pneumatic tires, J. Mach. Manuf. Reliab. 39 (5) (2010) 66–73.

[49] W. Thompson, Lord Kelvin, Baltimore Lectures on Molecular Dynamics and the Wave Theory of Light, 1904. London.

[50] J.L. Turner, J.L. Ford, Interply behavior exhibited in complimentary composite laminates, Rubber Chem. Technol. 55 (1982) 1079–1094.

[51] Z. Wang, L. Zhang, J. Song, G. Cao, X. Liu, A novel approach for modeling simulation of helix twisting structure based on mass-spring model, Adv. Mech. Eng. 2013 (2013) 1–10.

CHAPTER 10

Conductive elastomer engineering in extreme environments

Luca Valentini[a], Miguel Angel Lopez-Manchado[b]
[a]Civil and Environmental Engineering Department, University of Perugia, INSTM Research Unit, Strada di Pentima, Terni, Italy
[b]Institute of Polymer Science and Technology, ICTP-CSIC, Madrid, Spain

Contents

1 Conductive elastomers: Materials point of view

Acrylonitrile–butadiene rubber (NBR) is commonly considered the work-horse of the industrial and automotive rubber products industries because of its good mechanical properties (Table 1), its resistance to lubricants and greases and its relatively low cost; finished products are found in the market place as compression molded products [1–3]. The physical and chemical resistance properties of NBR materials are determined by the acrylonitrile content (ACN) of the base polymer which can vary between 18% and 50%. By selecting an elastomer with the appropriate acrylonitrile content in balance with other properties, NBR is used in fuel and oil handling hose, seals and grommets, and water handling applications. Lower ACN content ensures good flexibility at low temperatures, but offers limited resistance to oils and fuels. As the ACN content increases, the low temperature flexibility reduces and the resistance to oil and fuels improves. Nevertheless, it has been

Table 1 Typical physical properties of NBR, HNBR, FKM, TPV

Material	Shore A hardness	Tensile stress at break [MPa]	Elongation at break [%]	Compression set [%]	Service temperature [°C]	Abrasion rating (1) worst to (10) best	Cost [Euro/Kg]
NBR	74	15.3	328	23.6 @ 100°C	−40/+107	1.9	5
HNBR	88	12.4	100	25 @ 100°C	−40/+160	1.4	25
FKM/ TPV	92	19.4	100	7 @ 200°C	−15/+200	1	75–250

found that wide application of such materials as intake manifold etc., suffers of several limitations due to the limited physical properties of NBR elastomers such as very aggressive corrosion against bio-fuels. NBR is generally not resistant to aromatic and chlorinated hydrocarbons, fuels with a high aromatic content, polar solvents, glycol-based brake fluids and non-flammable hydraulic fluids. NBR has also low resistance to ozone and aging (Table 2). HNBR is obtained by partially or fully hydrogenation of NBR. The media resistance compares to that of NBR (Tables 1 and 2). Fluorinated elastomers (FKM) (typically containing 65% fluorine) and more recently perfluoroelastomers FFKM (typically containing 71% fluorine) provide materials with excellent high temperature and chemical resistance. FKM is of critical importance in solving problems in aerospace, automotive, chemical and petroleum industries. In particular, FKM materials are noted for their high resistance to heat and a wide variety of chemicals (see Table 2) and they are usually extruded [4, 5]. Other key benefits include excellent resistance to aging and ozone, very low gas permeability and the fact that the materials are self-extinguishing. FKM materials are generally not resistant to hot water, steam, polar solvents, glycol-based brake fluids and low molecular weight organic acids. Fluorine containing thermoplastic vulcanizate (TPV) elastomers on fluorocarbon polymers consist of a continuous thermoplastic fluorocarbon resin phase and a dispersed amorphous vulcanized fluorine containing elastomer phase, which is useful as a melt formable material having rubber elasticity and processable by injection molding. Injection molded components can find use as seals and gaskets in applications where high temperatures and harsh chemical environments are common, for example in certain types of automotive applications.

Table 2 Basic properties of NBR, HNBR, FKM, TPV

Basic properties	NBR	HNBR	FKM/TPV
Compression set	◆	◆	◆
Abrasion resistance	▪	▪	▪/□
Aging resistance	▼	▪	◆
Ozone resistance	▼	▪	◆
Resistance to oil and grease	▪	▪	◆
Fuel resistance	▼	□	▪
Resistance to hot water	80 °C	100 °C	80 °C
Resistance to steam	●	●	●

Very good, (◆); good, (▪); average, (□); poor, (▼); not recommended, (●).

More in general, the standard classification system for rubber compo-
nents in automotive applications (ASTM D2000) offers a guidance on the
types of materials available to indicate what level of performance can be
expected from the materials and to offer a means of providing a "line
call-out" designation for materials as reported below. The materials are iden-
tified initially by type, which is an indication of heat resistance, and by class,
which is based on oil resistance (Fig. 1).

The main drawback of the NBR/HNBR and FKM/TPV when oper-
ating in severe conditions relies on:

(a) *Swelling and blistering* caused by ethanol permeation through the thick-
ness of the elastomeric material. The elastomeric material tends to swell
when immersed in a solvent, e.g. bio–fuel. Fuel lines used in the vehicle
combustion system are made up mostly of elastomers, and undergo a
strong degradation that changes their properties when exposed to
bio–fuel.

(b) *Poor organic solvent compatibility, lack of resistance to hot water, steam, polar
solvent, glycol based brake fluids and low molecular weight organic acids.*

(c) *Weight (+26%) and volume change (+34%)*

(d) *Poor thermal conductivity* (in the range of 0.20–0.40 W/mK)
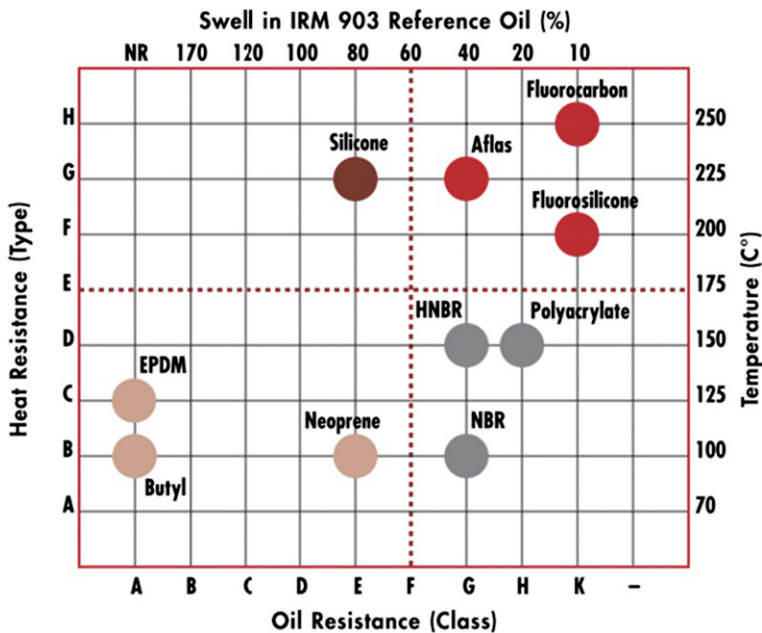
Fig. 1 Standard classification for rubber in automotive applications.

(e) *Low damping properties* ($<10\,G$) and changing with the temperature

(f) *Low explosive decompression resistance*

(g) *Lack of elasticity, poor strength, low elongation at break*

The industrial mass production of sp^2 hybridized carbon nanostructured materials (carbon nanotubes, graphite nanoplatelets, graphene) make them very strong candidates for the fabrication of elastomeric nanocomposites to be used in extreme environments like those in contact with wet ethanol and subjected to harsh operating conditions such as elevated temperatures, extreme mechanical loading and vibrations [6–9]. The natural abundance and the relatively low cost of graphitic–based fillers makes them very promising for use in the manufacturing process of a large number of elastomer composites. Graphitic compounds (CNTs, GNPs and graphene), compared to other conventional types of fillers, exhibit a significant ability to enhance mechanical and other functional properties of a rubber–like matrix, especially in the case of fine dispersion in the host medium, which in favor of the interfacial interaction.

Fine dispersion of graphitic inclusions is critical since it is directly correlated to the efficient occurrence of their multi–functional behavior: improvement of mechanical and tribological properties, thermal stability of the component, increase in thermal and electrical conductivity and gas barrier properties, etc. [10–13].

The thickness, the diameter and the surface area of the sheet–formed graphitic fillers, which affect the most the properties of the composite, can be tuned by various techniques, such as intercalation, oxidation, heat treatment and ultrasonic treatment [14]. In recent studies, it has been demonstrated that the reinforcing particle size and shape dramatically affects the functional behavior of rubber composites [15, 16]. In the case of NBR, tuning of the above parameters can manipulate the friction coefficient, the energy absorption capacity and the wear resistance of the material ("large" particles are in favor of low friction, "small" particles favor low wear) [17, 18]. Modification of the graphitic fillers is also a very important issue: i.e. functionalized GNPs (aiming to greater specific surface area) can modify NBR–based composites to exhibit a significant decrease in the fatigue crack growth under dynamic loading [19]. Nowadays, it is possible to combine traditional NBR (or HNBR) and TPV with carbon–based fillers (CNTs, GNPs) already available on the market, as well as with (modified or not) inclusions that can be fabricated in lab–scale within the project. It is well known that the presence of polar groups in polymer molecules generally reduces the permeability of the polymers, whereas there will be, an opposite effect with the presence of

double bonds. It has been demonstrated that the utilization of CNTs/GNPs reduces the permeability in HNBR elastomers due to the formation of a strong matrix-filler networks [20]. HNBR, having an ACN content, is polar in nature and has intermolecular dipole interactions with CNTs in the rubber matrix This interaction increases the density of the polymer chain matrix and, thereby, decreases the free volume in the rubber matrix. This resulted in a highly impermeable surface due to closer spacing between the filler and the rubber chain molecules.

The combined effect of CNTs/GNPs hybrid filler *tested at laboratory level*, exhibited astonishing improvements (see Fig. 2):

(a) *Improvement of the mechanical properties >50%.* For what concern the mechanical properties, thanks to the use of GNPs it was possible not only to improve the modulus 100% of 20% in a HNBR compound, but also to increase the storage modules at low and high temperature.

(b) *Thermal conductivity >4 W/mK.*

(c) *Healing efficiencies at least 90%* of the mechanical properties of the GNPs composite for the elastic modulus and the tensile strength, respectively CNTs/GNPs composites had better dispersibility, higher conductivity, lower percolation threshold, and better thermal conductivity, which may be attributed to a unique 2-D laminar structure of the GNPs and its homogeneous dispersion in the rubber matrix. The CNTs are incorporated into laminar GNPs to prevent GNPs aggregating in the rubber forming a 2-D homogeneous dispersion system, which improved the conductivity of the composites and made more GNPs firmly bound to the SR crosslinked network. Meanwhile, due to its high special surface area, the GNPs nanosheets can contact with polymer chains improving the mechanical properties.

2 Elastomeric conductive composites with high strain recovery and anti-corrosive properties

Electrically conductive materials capable of substantial elastic stretch and bending are needed for the applications reported in the previous chapter [8, 21–26] (Fig. 3). Different approaches involving CNTs, GNPs and elastic polymers have been suggested for the fabrication of conductive elastic composites. Sekitani et al. [27] developed rubber-like conductive composites by mixing millimeter-long single–walled carbon nanotubes (SWNTs), an ionic liquid, and a fluorinated copolymer, while Cao et al. [28] fabricated flexible electrodes by incorporating SWNT networks in plastics consisting of
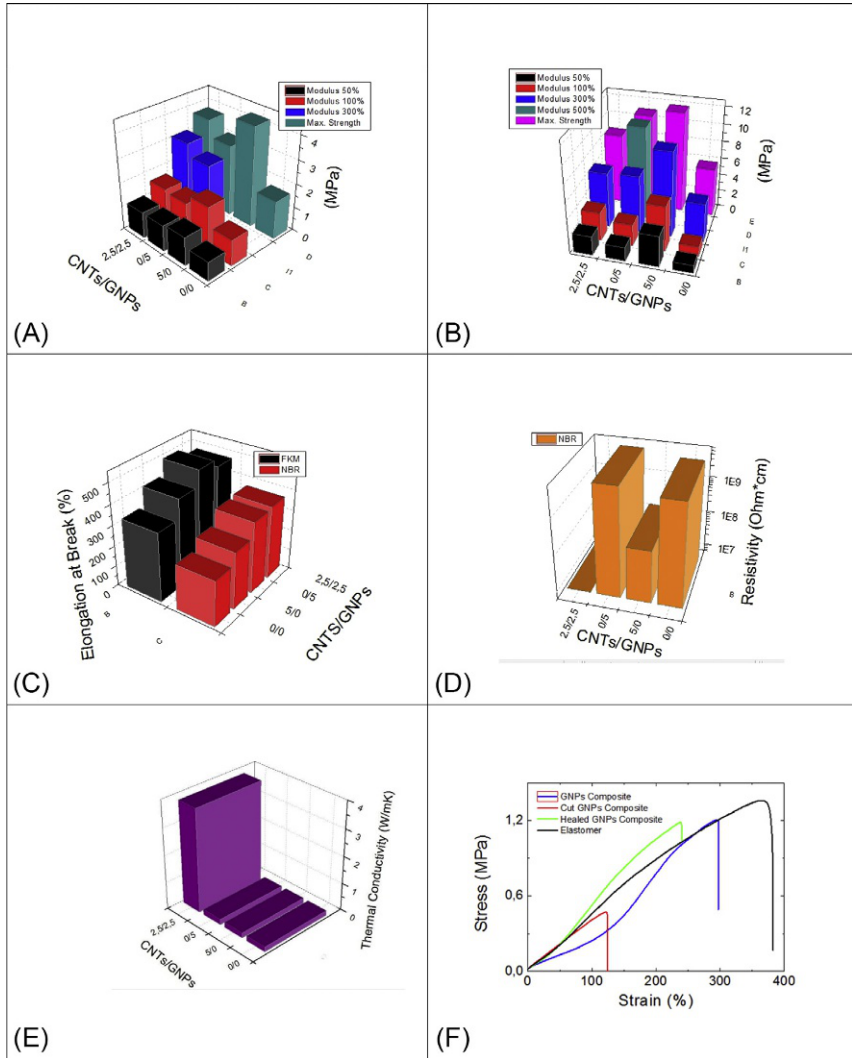
Fig. 2 Mechanical properties of (A) NBR/CNTs/GNPs composites. (B) FKM/CNTs/GNPs composites. (C) Elongation at break of NBR and FKM composites. (D) Electrical resistivity and (E) thermal conductivity of NBR/CNTs/GNPs composites. (F) Stress-strain curves demonstrating the self-healing of rubber/GNPs nanocomposites.

polyimide, polyurethane, and polyamic acid films. Although quite success–ful, these studies indicated that high loading of CNTs (or other conductive additive) was necessary to obtain a highly conducting composite. On the other hand, incorporation of high concentrations of CNTs into an elastic
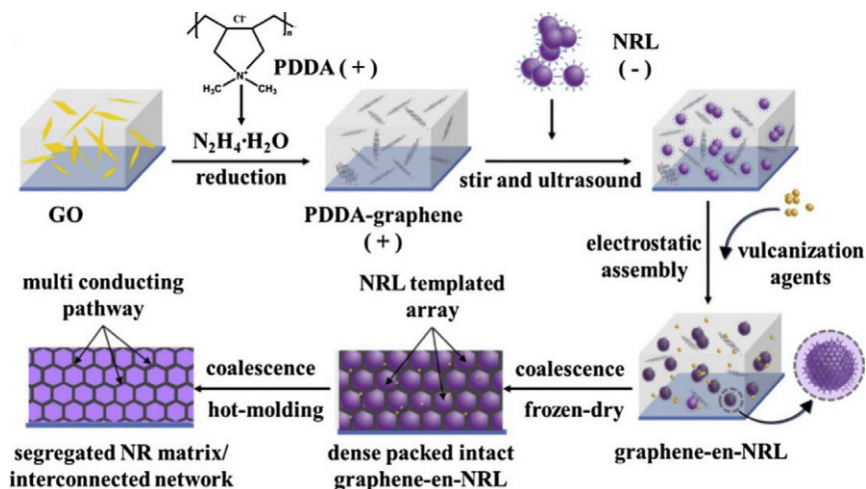
Fig. 3 Schematic description of a multi-step process for the preparation of graphene-filled natural rubber nanocomposites [8].

polymer increases the stiffness of the resulting composite and decreases its stretchability [29]. M.K. Shin et al. [30] found that a combination of high stretchability and high electrical conductivity can be obtained for composites prepared from three–dimensional CNT structures, such as CNT forests (vertically aligned arrays of CNTs). Unlike previous methods involving casting CNT/polymer dispersions as a film, these composites were prepared by the direct infiltration of multiwalled carbon nanotube (MWNT) forests with a polyurethane (PU) solution.

The developed preparation procedure appears scalable for material fabrication on an industrial scale, though transition from present batch based forest growth processes to continuous forest growth processes would be needed for applications that are price sensitive and depend on sheet weight, rather than the area of elastomeric sheet.

Highly stretchable fluoroelastomers (FKM, typically containing 65% fluorine) with stretch ratios $\lambda > 6$ (where $\lambda =$ final length/initial length, or Lf/Li) are of critical importance in solving problems in aerospace, automotive, chemical and petroleum industries [31, 32]. In particular, FKM materials are noted for their high resistance to heat and a wide variety of chemicals, other key benefits include excellent resistance to aging and ozone and very low gas permeability.

However, FKM materials are generally not resistant to ethanol, methanol and glycols fluids. Hence, new products of FKMs with enhanced

performance are needed. The specific challenge in this regard is a quantified target that consists in the optimization of elastomeric-like nanocomposites with multifunctional properties like monitoring the FKM strain with electrical resistance variation and anti-corrosion properties for the compatibility of such materials with high percentage of ethanol blended gasoline and with improved resistance to solvents.

Since the main factors that affect the composite properties are the particle size and the mode of interactions with the matrix materials, the nano-scale dimensions of 2D graphitic nanoinclusions such graphene nanoplatelets (GNPs) result in a huge benefit thanks to a better shape factor, larger contact surface and higher mechanical strength. It was found that the use of GNPs ensures very good dispersion into the polymer phase and improves the most the mechanical and electrical properties of the composite, by enhancing the interface between the filler and the host medium [33, 34].

GNPs are very effective in improving the barrier properties of a polymer nanocomposite, by inhibiting the molecular diffusion through the matrix also resulting to enhanced corrosion resistance and low permeability [35, 36]. Valentini et al. [37] reported a novel method that consists in the lamination of hydrophobic Parafilm containing graphene nanoplatelets on fluoroelastomer substrate (Fig. 4). Parafilm is a soft, solvent-proof and self-sealant thermoplastic material obtained by blending paraffin wax and polyolefin and that displays irreversible elongational thinning as the material is stretched. They used a lamination process to transfer GNPs on self-adherent Parafilm substrate and they show that a high-strain state of such conductive Parafilm/GNPs film is reversible when the film is transferred by lamination to a fluoroelastomer (FKM) substrate. The stretching of GNP network stuck on viscoelastic Parafilm gave rise to regions of high and low GNP concentrations with increasing the electrical resistance upon stretching. Upon relaxation from a high strain state, the composite film on FKM substrate maintains the initial electrical conductive state. It was also shown the reduction of the ethanol corrosion action in terms of swelling and mechanical performance of the neat FKM when the Parafilm/GNPs film is used for its packaging.

3 Elastomeric conductive composites for aerospace applications

Pyroshock (also called pyrotechnic shock) testing is designed to simulate the high-frequency, high-magnitude shock pulse that a product may experience
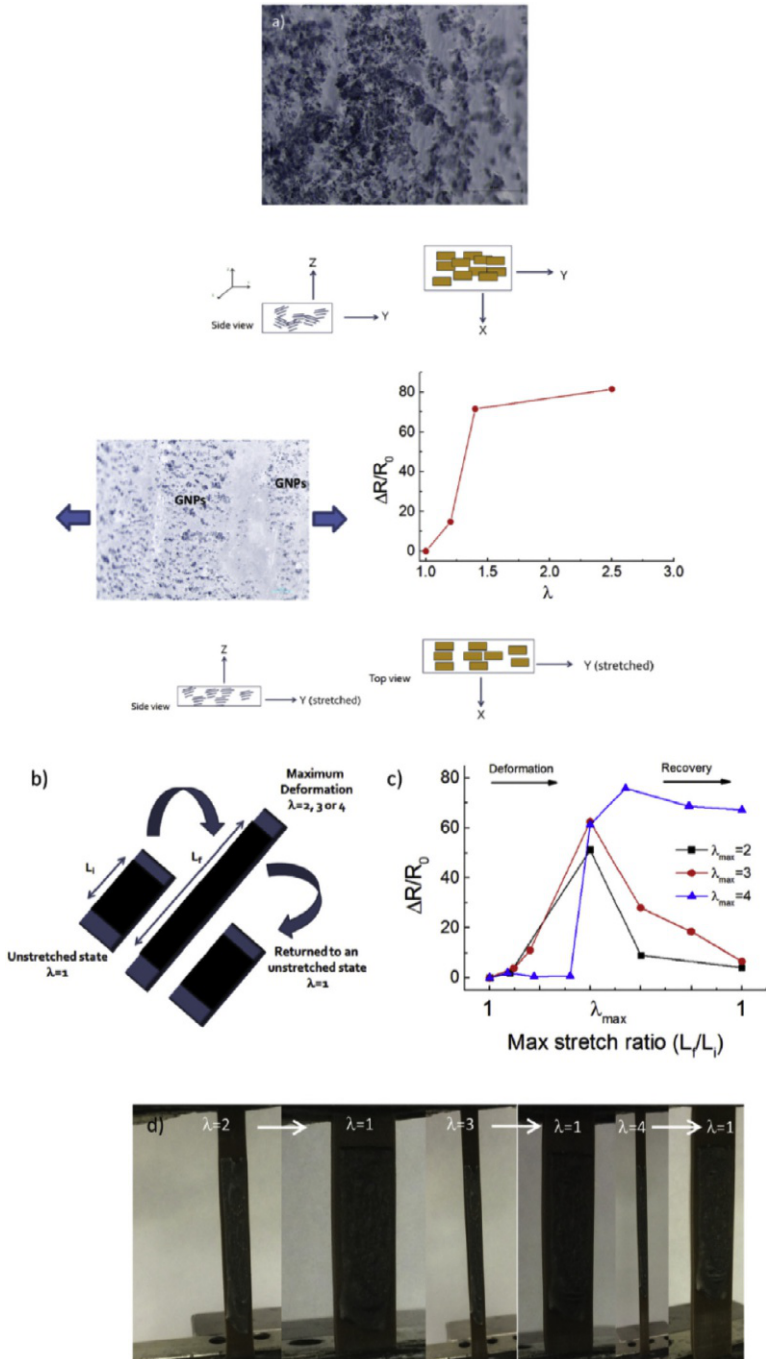
(see figure legend on opposite page)

as the result of an explosive event such as the separation of the booster rockets on the space shuttle or an explosive impact on military structural components [38–41].

In aerospace missions, pyroshocks occur due to controlled explosions of ordnance devices enabling the functionality of space modules. These shocks result from deployment mechanisms or opening solar sails and can cause failures of electronic devices and structures. Components made of composite materials are of crucial importance for assuring the reliability of aero–space modules and pyroshock tests for the completion of strict requirements have to be met. Consequently, it is significant to predict the pyroshock responses on composite materials. The pyroshock prediction is still a complex prediction but one of the most challenging issue in composite science and technology.

The weight saving offered by structural composites make them highly attractive not only to the military, but also to the aerospace and automotive industries. Failures in these structures are mainly attributed to the dynamic loading conditions such as fatigue and vibrations.

High vibration levels often generate excessive noise and leads to cyclic fatigue damage. Polymer damping materials have long been used to reduce vibration levels [42–46]. The vibration isolation property of polymer materials depends significantly on environmental conditions such as temperature, vibration frequency, dynamic load, etc.

These existing damping materials have offered improved damping performance for structural components and systems. But there is a need to develop advanced materials for damping applications, that can overcome these limitations. Researches efforts in this direction have been much focused on the development of polymer damping materials based on

---

Fig. 4, cont'd (A) Optical micrographs and schematic side/top view of GNP platelets embedded in Parafilm matrix in unstretched and stretched state (i.e. the arrows indicate the strain direction), respectively. The initial side/top view shows an interconnected electrical path of GNPs, GNPs then separate during stretching, thus raising the sheet electrical resistance. (B) Schematic representation of stretch mechanism before the stretch at $\lambda=1$, during the stretch at different stretching ratios and after relaxing to an unstretched state $\lambda=1$ of Parafilm/GNPs coupled with fluoroelastomer. (C) Electrical resistance variations to initial resistance values of Parafilm/GNPs coupled with fluoroelastomer substrate through the stretching cycles from $\lambda=1$ to $\lambda_{max}=2$, 3 or 4, then returned to a relaxed state ($\lambda_{max} \rightarrow 1$). (D) Photographs of Parafilm/GNPs coupled with fluoroelastomer substrate through stretching cycle from $\lambda=2$, 3, 4 to a relaxed state (right panels) [37].

nanocomposites in which nanotubes, nanofibers or nanoparticles are embedded in polymer substrates and much promising results have been established [47–49]. The research on rubber nanocomposites can be both fundamental and applied, and has attracted growing attention. Numerous studies have demonstrated that the uniform distribution of nanoscaled filler particles into a rubber matrix, with reasonably good interfacial bonding strength, could lead to a rubber nanocomposite with significantly improved properties [50–59]. Rubber is an important commercial material widely being used not only for automobile and industrial applications but also for space components [60]. Since rubber for space application requires good reinforcement at the minimum possible filler loading, incorporation of few percentage of graphene nanoplatelets is a viable alternative to obtain low density high performance composites. The mechanical properties of such matrix containing equal amount of graphene nanoplatelets and carbon black was the optimum compared to those containing either graphene nanoplatelets or carbon black [61, 62]. It is known that rubbers or elastomers generally have a low thermal conductivity. Consequently, when such materials are used as packaging for electronic circuit, they store the generated heat that in turn raises the temperature of the device itself, thereby promoting heat deterioration of the electronic component. To achieve this goal, the heat conduction capability of a rubber may be improved by compounding a rubber with a filler having a heat conductivity higher than that of the rubber. High filler loadings (>30 vol%) or traditional metallic materials were typically necessary to develop functional elastomers with appropriate level of thermal conductivity [63, 64]. The employment of high filler loading makes difficult the processing, such as possibility to be extruded and injection molded, while traditional metallic materials with the highest thermal conductivity are too heavy and subjected to corrosion. Moreover the reinforcing capacity is deteriorated after some certain value of filler amount.

When a dramatic increase in properties, such as mechanical and thermal properties can be achieved when two different fillers both with saturate amount are added in rubber matrix synchronously, this is suggestive of synergistic effect [61]. When a part of CB with GNPs was replaced to produce ethylene–propylene diene terpolymer rubber (EPDM) based nanocomposites; a proper combination of GNPs lead to synergistic effect in improving the thermal conductivity, damping and mechanical properties of the nanocomposites (see Fig. 5).
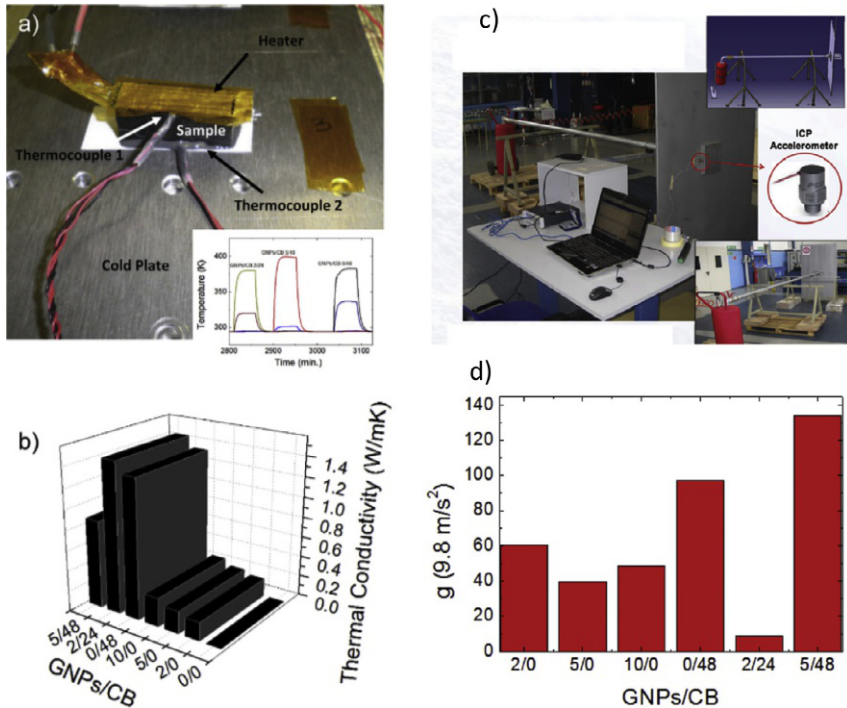
Fig. 5 (A) Set up of the thermal conductivity measurements. (B) Thermal conductivity values as a function of the GNPs/CB content. (C) Set-up of the impact test. The impact area is a metallic plate where the sample to be tested has been fastened to. The sample was hit by a percussion which excites the vibration. A shock accelerometer positioned in the back plate is thus excited and the response is recorded and digitalized via high performance data acquisition system. (D) Peak acceleration measured by the accelerometer in the impact test of the prepared samples [61].

4 End of life of elastomeric conductive composites

Automotive rubber components are easy to dismantle and have consolidated recycling markets. Electrically conducting rubber nano-composites in combination with carbon black and carbon fibers can be integrated into concrete obtaining electrically conductive concrete inside building applications. Electrically conductive concrete, forming floor plates, slabs and walls can be used in industrial buildings as well as in dwelling houses replacing contemporary unsafe heating systems (having numerous pipes, connections and liquid agents and utilizing tons of copper metal). Copper production is environmentally unclean; thousands tons of CO_2 emissions will be reduced, minimizing climate changes.

There are more than 242 million scrap tires generated each year in the United States creating a significant disposal problem. This is the reason why interest to rubber modified concrete is high [65–71]. At the same time question is still under investigation. The advantages of the rubber modified concrete (RMC) are: (a) The toughness and ductility of RMC are usually higher than that of regular concrete, which makes it suitable for many applications; (b) The density of RMC is lower than the density of regular concrete. Different size nano-modified rubber particles addition to the concrete is leading to shrinkage micro- cracks arrest and bridging at the concrete maturing stage (when concrete elastic modulus is low). Matured concrete with rubber particles has higher damping properties. Micro and nano-modified rubber particles addition to the fiberconcrete is leading to hierarchical, different size scale reinforcement formation in the concrete matrix; simultaneously, concrete structure external surfaces frictional properties are increasing. Concrete and fiberconcrete with rubber particles can be used for sound insulation walls elements along noisy traffic roads, as industrial building floors elements, roads and yards pavements etc. [72–76].

Layered fiberconcrete is very promising direction in building technologies exploiting reinforced concrete as loads bearing material [77–79]. Short and long fibers, polymeric matrix composite fibers in combination with nano-modified rubber particles exhibit higher material integrity (according to micro and nano cracks opening mitigation), better sound and heat insulating properties. Nano-modified rubber particles can be introduced into asphalt exploiting "dry" or "wet" technologies. Modified rubber particles mixing with bitumen, pellets like sub product can be obtained [80, 81]. Sub product is easy to use and to store. Rubber modified asphalt reduces the occurrence of cracking because of its bridging behavior. Rubber particles in combination with short synthetic fibers in asphalt can greatly reduce crack occurrence and evolution increasing road durability and exploitation time. Generally, roads paved with conventional asphalt require maintenance every few years because asphalt may lose some elasticity or resiliency through oxidation. Because of the resistance to cracking and aging exhibited by rubber-modified asphalt, roads paved with rubber-modified asphalt applications generally experience longer service lives before maintenance is required as well as particles and fibers are mitigating cracks evolution in it. Low oxygen permeability of rubber nanocomposites could reduce oxidative aging. The pavement materials are also subjected to repeated stresses from expansion and contraction due to temperature changes, and cracks begin to appear; thermally conductive rubberized asphalt generally resists

the formation of these cracks better than conventional asphalt. Electrically conducting rubber nanocomposites can be also integrated in such asphalt with anti–icing properties. In transportation, bearing seals mounted on air-craft components are subjected to icing problems that require a solution. More in general, the removal of accreted ice remains an expensive daily and industrially concern across the globe [82, 83].

Different chemical and physical methods have been developed to remove ice once formed, e.g. heaters, hot water/glycol mixtures, vibrators, pneumatic boots on aircrafts, or to prevent the water wettability, e.g. nanostructured ice-phobic coatings [84–90]. In general, the adhesion of ice on stiff substrate with-out interfacial defects is hard to be separated. However, if one of the solids is deformable, then they can be separated imposing a differential deformation. Kim et al. [91] found that polymeric films of low modulus and low surface energy do promote easy release and demonstrated that the critical shear stress of fracture decreases with the shear modulus of an elastomeric surface. Thus, when ice adhered to a low cross-link elastomer experiences a shear stress, the ice detaches from the ice-elastomer interface at low applied loads [86]. For elas-tomers, it is known that the modulus is related to the cross-link density that can be calculated by the well-known Flory formula [92]; durable organogel antii-cing material via swelling cross-linked poly(dimethylsiloxane) with liquid par-affin was reported [89] while Golovin et al. [93] recently predicted the icephobicity of different types of polymers by filling a polymer with oil. Recently, Park et al. [94, 95] demonstrated that the hybrid filler provided sig-nificant enhancement of mechanical properties, such as flexural strength, flex-ural modulus, and fracture toughness. In particular, the epoxy composite containing graphene hybrid exhibited a stronger mechanical behavior. Spon-taneous change of adhesion of solidifying liquid on surfaces is of significant importance in materials technology where it finds applications such as anti-icing components operating in extreme environments like those of seals. In this work, nitrile butadiene rubber (NBR) composites reinforced with graphene, carbon nanotubes, and a mix of them after immersion in several fluids, expe-rienced both a swelling and a reduction of the cross-link density that reduces ice adhesion, being this effect more evident for graphene containing samples.

5 Conclusion and perspectives

Common challenges for developing materials in extreme environment pro-mote the opportunities to discover crossover solutions; for example, sealing materials being developed in the energy sector for ultra–high-temperature

applications are generating interest in aerospace. These new technologies will have an impact on several areas by:

– Increasing the competitiveness of European industry through the use of CNTs and GNPs for a new generation of customized elastomeric nano-composites to be used in extreme environments, thus paving the way to deeper knowledge and hands-on expertise in cost-effective mass-scale nanostructured carbon production. Hence, helping European Industry to become leader in graphitic materials technologies supporting world-wide customers with specialized, value-added, ground breaking solutions for their advanced applications in several sectors (oil and gas, automotive, aeronautics).

– Developing new tools for the design of high-performing elastomeric nanocomposites, which will allow to increase efficiency of production processes.

– Enabling a more widespread use of a high % of ethanol in petrol through the validation of a new generation of ethanol resistant vehicle components.

– The widespread diffusion of high percentage ($>10\%$) ethanol blended gasoline is connected to their capability to lower CO_2 emissions, on the other hand, a market barrier is the risk to damage plastic and rubber components in cars and handheld products. Low permeation rate and a reduced interaction with the solvent (lower swelling) leads to the competitiveness of such polymers with new biofuels.

– Opening the market to new products i.e. advanced sealings, corrosion resistant hoses made of GNP/CNT-containing premixes, will reduce number of failures in mineral processing operations. Thus the development of new composites based on the use of grapheme intercalated compounds will support and strengthen the oil and gas extraction industry as it faces increasing technical challenges to sustain the growing worldwide demand for energy. Thus the development of reliable, high–performing elastomeric materials will continue to have a crucial role for industrial players.

Acknowledgments

References

[1] C.H. Hepburn, C.M. Blow (Eds.), Rubber Technology and Manufacture, second ed., Buttenvorths, 1982.

[2] A.K. Bhowmick (Ed.), Rubber Products Manufacturing Technology, Marcel Dekker, 1994.

[3] J.E. Mark, B. Erman, F.R. Eirich (Eds.), Science and Technology of Rubber, Academic Press, 1994.

[4] M. Morton (Ed.), Rubber Technology, Springer, 1999.

[5] Y. Ikeda, A. Kato, S. Kohjiya, Y. Nakajima (Eds.), Rubber Science: A Modern Approach, Springer, 2017.

[6] K.L. Sadasivumi, D. Ponnamma, S. Thomas, Y. Grohens, Evolution from graphite to graphene elastomer composites, Prog. Polym. Sci. 39 (2014) 449–780.

[7] S. Arabi, Q.S. Meng, L.Q. Zhang, I. Zaman, P. Majewski, J. Ma, Elastomeric composites based on carbon nanomaterials, Nanotechnology 26 (2015)112001.

[8] D.C. Papageorgious, I.A. Kinloch, R.J. Young, Graphene/elastomer nanocomposites, Carbon 95 (2015) 460–484.

[9] Z.H. Tang, B.C. Guo, L.Q. Zhang, D.M. Jia, Graphene/rubber nanocomposites, Acta Polym. Sin. 7 (2014) 865–877.

[10] L. Bokobza, Multiwall carbon nanotube elastomeric composites. A review, Polymer 48 (2007) 4907–4920.

[11] B. Mensah, K.C. Gupta, H. Kim, W. Wang, K.U. Jeong, C. Nah, Graphene-reinforced elastomeric nanocomposite. A review, Polym. Test. 68 (2018) 160–184.

[12] R. Verdejo, M.A. Lopez-Manchado, L. Valentini, J.M. Kenny, Carbon nanotubes/elastomer nanocomposites, in: S. Thomas, R. Stephen (Eds.), Rubber Nanocomposites: Preparation, Properties and Applications, vol. 6, Wiley, 2009, , pp. 147–168.

[13] Y. Liu, L.Y. Wang, L.F. Zhao, H.F. He, X.Y. Shao, G.B. Fang, Z.G. Wan, R.C. Zeng, Research progress of graphene-based rubber nanocomposites, Polym. Compos. 39 (2018) 1006–1022.

[14] A. Pazat, C. Barres, F. Bruno, C. Janin, E. Beyou, Preparation and properties of elastomer composites containing "graphene" based filler: a review, Polym. Rev. 58 (2018) 403–443.

[15] Y. Wang, X. Qiu, J. Zheng, Effect of the sheet size on the thermal stability of silicone rubber-reduced graphene oxide nanocomposites, J. Appl. Polym. Sci. 136 (2019) 47034.

[16] X. Wu, T.F. Lin, Z.H. Tang, B.C. Guo, G.S. Huang, Natural rubber/graphene oxide composites: effect of sheet size on mechanical properties and strain induced crystallization behavior, Express Polym. Lett. 9 (2015) 672–685.

[17] Y.Q. Li, Q.H. Wang, T.M. Wang, G.Q. Pan, Preparation and tribological properties of graphene/oxide/nitrile rubber nanocomposites, J. Mater. Sci. 47 (2012) 730–738.

[18] L.L. Wang, L.Q. Zhang, M. Tian, Mechanical and tribological properties of acrylonitrile-butadiene rubber filled with graphite and carbon black, Mater. Des. 39 (2012) 450–457.

[19] A. Frick, M. Borm, V. Maralidharam, Influence of fillers on the mechanical and tribological properties of acrylo-nitrile-butadiene-vulcanisates (NBR), KGK-Kautsch. Gummi Kunstst. 71 (2018) 23–31.

[20] L. Valentini, S. Bittolo Bon, M. Hernandez, M.A. Lopez-Manchado, N.M. Pugno, Nitrile butadiene rubber composites reinforced with reduced graphene oxide and carbon nanotubes show superior mechanical, electrical and icephobic properties, Compos. Sci. Technol. 166 (2018) 109–114.

[21] M. Fihn, The challenges of commercializing flexible displays, Solid State Technol. 49 (2006) 43.

[22] S.P. Lacour, J. Jones, Z. Suo, S. Wagner, Design and performance of thin metal film interconnects for skin-like electronic circuits, IEEE Electron Device Lett. 25 (2004) 179–181.

[23] J.M. Engel, N. Chen, K. Ryu, S. Pandya, C. Tucker, Y. Yang, C. Liu, in: L. Spangler, T.W. Kenny (Eds.), Solid State Sensors, Actuators, and Microsystems Workshop, Transducer Research Foundation, San Diego, CA, 2006, p. 316.

[24] L. Johnson, F.K. Perkins, T. O'Hearn, P. Skeath, C. Merritt, J. Frieble, S. Sadda, M. Humayun, D. Scribner, Electrical stimulation of isolated retina with microwire glass electrodes, J. Neurosci. Methods 137 (2004) 265–273.

[25] R. Pelrine, R. Kornbluh, Q.B. Pei, J. Joseph, High-speed electrically actuated elastomers with strain greater than 100%, Science 287 (2000) 836–839.

[26] R. Pelrine, R. Kornbluh, G. Kofod, High-strain actuator materials based on dielectric elastomers, Adv. Mater. 12 (2000) 1223–1225.

[27] T. Sekitani, Y. Noguchi, K. Hata, T. Fukushima, T. Aida, T. Someya, A rubberlike stretchable active matrix using elastic conductors, Science (12) (2008) 1468–1472.

[28] Q. Cao, H.S. Kim, N. Pimparkar, J.P. Kulkarni, C. Wang, M. Shim, K. Roy, M.A. Alam, J.A. Rogers, Medium-scale carbon nanotube thin-film integrated circuits on flexible plastic substrates, Nature 454 (2008) 495–500.

[29] V.K. Rangari, M. Yousuf, S. Jeelani, M.X. Pulikkathara, V.N. Khabashesku, Alignment of carbon nanotubes and reinforcing effects in nylon-6 polymer composite fibers, Nanotechnology 19 (2008)245703.

[30] M.K. Shin, J. Oh, M. Lima, M.E. Kozlov, S.J. Kim, R.H. Baughman, Elastomeric conductive composites based on carbon nanotube forests, Adv. Mater. 22 (2010) 2663–2667.

[31] S. Rooj, A. Das, G. Heinrich, Tube-like natural halloysite/fluoroelastomer nanocomposites with simultaneous enhanced mechanical, dynamic mechanical and thermal properties, Eur. Polym. J. 47 (2011) 1746–1755.

[32] M.A. Kader, M.Y. Lyu, C. Nah, A study on melt processing and thermal properties of fluoroelastomer nanocomposites, Compos. Sci. Technol. 66 (2006) 1431–1443.

[33] T. Kuilla, S. Bhadra, D. Yao, N.H. Kim, S. Bose, J.H. Lee, Recent advances in graphene based polymer composites, Prog. Polym. Sci. 35 (2010) 1350–1375.

[34] R. Verdejo, M.M. Bernal, L.J. Romasanta, M.A. Lopez-Manchado, Graphene filled polymer nanocomposites, J. Mater. Chem. 21 (2011) 3301–3310.

[35] A.M. Pinto, J. Cabral, D.A. Pacheco Tanaka, A.M. Mendes, F.D. Magalhaes, Effect of incorporation of graphene oxide and graphene nanoplatelets on mechanical and gas permeability properties of poly(lactic acid) films, Polym. Int. 62 (2012) 33–40.

[36] B.M. Yoo, H.J. Shin, H.W. Yoon, H.B. Park, Graphene and graphene oxide and their uses in barrier polymers, J. Appl. Polym. Sci. 131 (2014) 39628–39634.

[37] L. Valentini, S. Bittolo Bon, M.A. Lopez-Manchado, L. Mussolin, N.M. Pugno, Development of conductive paraffin/graphene films laminated on fluoroelastomers with high strain recovery and anti-corrosive properties, Compos. Sci. Technol. 149 (2017) 254–261.

[38] N. Davie, V. Bateman, Shock and Vibration Handbook, McGraw-Hill, 1995.

[39] M.L. Lai, A. Soom, Statistical energy analysis for the time-integrated transient response of vibrating systems, J. Vib. Acoust. 112 (1990) 206–213.

[40] P. Shi, Simulation of impact involving an elastic rod, Comput. Methods Appl. Mech. Eng. 151 (1998) 497–499.

[41] Y. Mao, H. Huang, Y. Yan, Numerical techniques for predicting pyroshock responses of aerospace structures, Adv. Mater. Res. 108 (2010) 1043–1048.

[42] S.T. Latibari, M. Mehrali, L. Mottahedin, A. Fereidoon, H.S.C. Metselaar, Investigation of interfacial damping nanotube-based composite, Compos. Part B Eng. 50 (2013) 354–361.

[43] J.B. Kosmatka, S.L. Liguore, Review of methods for analyzing constrained layer damping structures, J. Aerosp. Eng. 6 (1993) 268–283.

[44] A. Baz, J. Ro, The concept and performance of active constrained layer damping treatments, J. Sound Vib. 28 (1994) 18–21.

[45] W.H. Liao, K.W. Wang, On the analysis of viscoelastic materials for active constrained layer damping treatments, J. Sound Vib. 207 (1997) 319–334.

[46] V. Spitas, C. Spitas, P. Michelis, Modeling of the elastic damping response of a carbon nanotube–polymer nanocomposite in the stress-strain domain using an elastic energy release approach based on stick-slip, Mech. Adv. Mater. Struct. 20 (2013) 791–800.

[47] A. Buldum, J.P. Lu, Atomic scale sliding and rolling of carbon nanotubes, Phys. Rev. Lett. 83 (1999) 5050–5053.

[48] C.Q. Ru, Effect of van der Waals forces on axial buckling of a double-walled carbon nanotube, J. Appl. Phys. 87 (2000) 7227–7231.

[49] J. Suhr, N. Koratkar, P. Keblinski, P. Ajayan, Viscoelasticity in carbon nanotube composites, Nat. Mater. 4 (2005) 134–137.

[50] G.R. Hamed, Rubber reinforcement and its classification, Rubber Chem. Technol. 80 (2007) 533–544.

[51] G. Mertz, F. Hassouna, P. Leclère, A. Dahoun, V. Toniazzo, D. Ruch, Correlation between (nano)-mechanical and chemical changes occurring during photo-oxidation of filled vulcanised styrene butadiene rubber (SBR), Polym. Degrad. Stab. 97 (2012) 2195–2201.

[52] M.A. Bashir, M. Shahid, R.A. Alvi, A.G. Yahya, Effect of carbon black on curing behavior, mechanical properties and viscoelastic behavior of natural sponge rubber-based nano-composites, Key Eng. Mater. 510 (2012) 532–539.

[53] J. Ma, P. Xiang, Y. Mai, L. Zhang, A novel approach to high performance elastomer by using clay, Macromol. Rapid Commun. 25 (2004) 1692–1696.

[54] J.F. Fu, L.Y. Chen, H. Yang, Q.D. Zhong, L.Y. Shi, W. Deng, X. Dong, Y. Chen, G.Z. Zhao, Mechanical properties, chemical and aging resistance of natural rubber filled with nano-Al_2O_3, Polym. Compos. 33 (2012) 404–411.

[55] M. Arroyo, M.A. Lopez-Manchado, B. Herrero, Organo-montmorillonite as substitute of carbon black in natural rubber compounds, Polymer 44 (2003) 2447–2453.

[56] M.A. Lopez-Manchado, J. Biagiotti, L. Valentini, J.M. Kenny, Dynamic mechanical and Raman spectroscopy studies on interaction between single-walled carbon nanotubes and natural rubber, J. Appl. Polym. Sci. 92 (2004) 3394–3400.

[57] M. Hernandez, M.M. Bernal, R. Verdejo, T.A. Ezquerra, M.A. Lopez-Manchado, Overall performance of natural rubber/graphene nanocomposites, Compos. Sci. Technol. 73 (2012) 40–46.

[58] H. Aguilar-Bolados, J. Brasero, M.A. Lopez-Manchado, M. Yazdani-Pedram, High performance natural rubber/thermally reduced graphite oxide nanocomposites by latex technology, Compos. Part B 67 (2014) 449–454.

[59] H. Aguilar-Bolados, M.A. Lopez-Manchado, J. Brasero, F. Aviles, M. Yazdani-Pedram, Effect of the morphology of thermally reduced graphite oxide on the mechanical and electrical properties of natural rubber nanocomposites, Compos. Part B 87 (2016) 350–356.

[60] E. Narayanan, S.S. Bhagawan, B. John, A.K. Bhaskaran, Space quality rubber products: case study with nitrile/butadiene rubber based engine gimbal control system bladder, Plastics 27 (1998) 337–340.

[61] L. Valentini, S. Bittolo Bon, M.A. Lopez-Manchado, R. Verdejo, L. Pappalardo, A. Bolognini, A. Alvino, S. Borsini, A. Berardo, N.M. Pugno, Synergistic effect of graphene nanoplatelets and carbon black in multifunctional EPDM nanocomposites, Compos. Sci. Technol. 128 (2016) 123–130.

[62] L. Valentini, A. Bolognini, A. Alvino, S. Bittolo Bon, M. Martin-Gallego, M.A. Lopez-Manchado, Pyroshock testing on graphene based EPDM nanocomposites, Compos. Part B 60 (2014) 479–484.

[63] S. Araby, I. Zaman, Q. Meng, N. Kawashima, A. Michelmore, H.C. Kuan, P. Majewski, J. Ma, L. Zhang, Melt compounding with graphene to develop functional, high-performance elastomers, Nanotechnology 24 (2013) 165601.

[64] Z. Han, A. Fina, Thermal conductivity of carbon nanotubes and their polymer nano-composites: a review, Prog. Polym. Sci. 36 (2011) 914–944.

[65] K. Bisht, P.V. Ramana, Waste to resource conversion of crumb rubber for production of sulphuric acid resistant concrete, Constr. Build. Mater. 194 (2019) 276–286.

[66] S. Ramdani, A. Guettala, M.L. Benmalek, J.B. Aguilar, Physical and mechanical performance of concrete made with waste rubber aggregate, glass powder and silica sand powder, J. Build. Eng. 21 (2019) 302–311.

[67] H. Zhu, J. Liang, J. Xu, M.X. Bio, J.J. Li, B. Tang, Research on anti-chloride ion penetration property of crumb rubber concrete at different ambient temperatures, Constr. Build. Mater. 189 (2018) 42–53.

[68] N.F. Medina, R. Garcia, I. Hajirasouliha, K. Pilakoutas, M. Guadagnini, S. Raffoul, Composites with recycled rubber aggregates: properties and opportunities in construction, Constr. Build. Mater. 188 (2018) 884–897.

[69] S. Mohammad, L. Jie, Investigation of the mechanical properties and carbonation of construction and demolition materials together with rubbers, J. Clean. Prod. 202 (2018) 553–560.

[70] M. Yazi, L. Tung-Chai, M. Kim Hung, Recycling of wastes for value-added applications in concrete blocks: an overview, Resour. Conserv. Recycl. 138 (2018) 298–312.

[71] B.S. Thomas, S. Kumar, P. Mehra, R.C. Gupta, M. Joseph, L.J. Csetenyi, Abrasion resistance of sustainable green concrete containing waste tire rubber particles, Constr. Build. Mater. 124 (2016) 906–909.

[72] S. Hirakawa, C. Hopkins, Experimental determination of transient structure-borne sound power from heavy impact sources on heavyweight floors with floating floors using an inverse form of transient statistical energy analysis, Appl. Acoust. 140 (2018) 74–82.

[73] R. Jongkwan, S. Hansal, K. Yonghee, Effect of the suspended ceiling with low-frequency resonant panel absorber on heavyweight floor impact sound in the building, Build. Environ. 139 (1–7) (2018).

[74] Y.P. Fei, W. Fang, M.Q. Zhang, J.M. Jin, P. Fan, J.T. Yang, Z.D. Fei, F. Chen, T.R. Kwang, Morphological, structure, rheological behavior, mechanical properties and sound insulation performance of thermoplastic rubber composites reinforced by different inorganic fillers, Polymers 10 (2018) 276.

[75] B. Zhang, C.S. Poon, Sound insulation properties of rubberized lightweight aggregate concrete, J. Clean. Prod. 172 (2018) 3176–3185.

[76] A.C. Corredor-Bedoya, R.A. Zoppi, A.L. Serpa, Composites of scrap tire rubber particles and adhesive mortar—noise insulation potential, Cem. Concr. Compos. 82 (2017) 45–66.

[77] V. Lusis, A. Krasnikovs, O. Kononova, V.A. Lapsa, R. Stonys, A. Macanovskis, A. Lukasenoks, Effect of short fibers orientation on mechanical properties of composite material-fiber reinforced concrete, J. Civ. Eng. Manag. 23 (2017) 1091–1099.

[78] A.C. Bordelon, J.R. Roesler, Spatial distribution of synthetic fibers in concrete with X-ray computed tomography, Cem. Concr. Compos. 53 (2014) 35–43.

[79] T. Ponikiewski, J. Gołaszewski, M. Rudzki, M. Bugdolb, Determination of steel fibres distribution in self-compacting concrete beams using X-ray computed tomography, Arch. Civ. Mech. Eng. 15 (2015) 558–568.

[80] D. Lo Presti, M.A. Izquierdo, A. Carrion, A. Jimenez del Barco, Towards storage stable high-content recycled tyre rubber modified bitumen, Constr. Build. Mater. 172 (2018) 106–111.

[81] M.A. Franesqui, J. Yepes, C. Garcia-Gonzalez, J. Gallego, Sustainable low-temperature asphalt mixtures with marginal porous volcanic aggregates and crumb rubber modified bitumen, J. Clean. Prod. 207 (2019) 44–56.

[82] N.D. Mulherin, R.B. Haehnel, Ice Engineering: Progress in Evaluating Surface Coatings for Icing Control at Corps Hydraulic Structures, US Army Engineer Research and Development Center, 2003.

[83] V. Hejazi, K. Sobolev, M. Nosonovsky, From superhydrophobicity to icephobicity: forces and interaction analysis, Sci. Rep. 3 (2013) 2194–2196.

[84] J. Chen, R. Dou, D. Cui, Q. Zhang, Y. Zhang, F. Xu, X. Zhou, J. Wang, Y. Song, L. Jiang, Robust prototypical anti-icing coatings with a self-lubricating liquid water layer between ice and substrate, ACS Appl. Mater. Interfaces 5 (2013) 4026–4030.

[85] R. Dou, J. Chen, Y. Zhang, X. Wang, D. Cui, Y. Song, L. Jiang, J. Wang, Anti-icing coating with an aqueous lubricating layer, ACS Appl. Mater. Interfaces 6 (2014) 6998–7003.

[86] K. Golovin, S.P.R. Kobaku, D.H. Lee, E.T. DiLoreto, J.M. Mabry, A. Tuteja, Designing durable icephobic surfaces, Sci. Adv. 2 (2016) 1501496–1501512.

[87] P. Kim, T.S. Wong, J. Alvarenga, M.J. Kreder, W.E. Adorno-Martinez, J. Aizenberg, Liquid-infused nanostructured surfaces with extreme anti-ice and anti-frost performance, ACS Nano 6 (2012) 6569–6577.

[88] C. Urata, G.J. Dunderdale, M.W. England, A. Hozumi, Self-lubricating organogels (SLUGs) with exceptional syneresis-induced anti-sticking properties against viscous emulsions and ices, J. Mater. Chem. 3 (2015) 12626–12630.

[89] Y. Wang, X. Yao, J. Chen, Z. He, J. Liu, Q. Li, J. Wang, L. Jiang, Organogel as durable anti-icing coatings, Sci. China Mater. 58 (2015) 559–565.

[90] L. Zhu, J. Xue, Y. Wang, Q. Chen, J. Ding, Q. Wang, Ice-phobic coatings based on silicon-oil-infused polydimethylsiloxane, ACS Appl. Mater. Interfaces 5 (2013) 4053–4062.

[91] M.K. Chaudhury, K.H. Kim, Shear-induced adhesive failure of a rigid slab in contact with a thin confined film, Eur. Phys. J. E Soft Matter 23 (2007) 175–183.

[92] P.J. Flory, Principles of Polymer Chemistry, Cornell Univ Press, Ithaca, NY, 1953 (Chapter 11).

[93] K. Golovin, A. Tuteja, A predictive framework for the design and fabrication of icephobic polymers, Sci. Adv. 3 (2017) 1701617–1701619.

[94] Y. Zhang, K.Y. Rhee, S.J. Park, Nanodiamond nanocluster-decorated graphene oxide/epoxy nanocomposites with enhanced mechanical behavior and thermal stability, Compos. Part B 114 (2017) 111–120.

[95] Y. Zhang, K.Y. Rhee, D. Hui, S.J. Park, A critical review of nanodiamond based nanocomposites: synthesis, properties and applications, Compos. Part B 143 (2018) 19–27.

This page intentionally left blank

Index

Note: Page numbers followed by *f* indicate figures and *t* indicate tables.

HIGH-PERFORMANCE ELASTOMERIC MATERIALS REINFORCED BY NANO-CARBONS

MULTIFUNCTIONAL PROPERTIES AND INDUSTRIAL APPLICATIONS

EDITED BY: LUCA VALENTINI AND MIGUEL ANGEL LOPEZ MANCHADO

High-Performance Elastomeric Materials Reinforced by Nano-Carbons: Multifunctional Properties and Industrial Applications supports the development of advanced rubber nanocomposites, with multifunctional properties, for use in state-of-the-art applications in challenging industrial environments.

The book begins by introducing the materials in question, studying the classification of rubber and nano-carbons, as well as the functionalization methods for carbon nanotubes and graphene for rubber systems. This is followed by in-depth sections on processing methods and on properties of advanced rubber nanocomposites. Smart aspects, such as electrically conductive rubbers and end-of-life considerations, are then considered.

The detailed information provided facilitates the work of all those researching, or working with, elastomeric materials. This includes academic researchers, scientists, and postgraduate students working with advanced rubber nanocomposites, or across materials science, polymer chemistry, polymer physics, and chemical engineering. The book is also of great interest to engineers and research scientists using elastomeric materials in the design or manufacture of high-performance products for application in harsh environments.

ABOUT THE EDITORS

Luca Valentini is an associate professor of materials science and technology at the Civil and Environmental Engineering Department of the University of Perugia, Italy. He received his master's degree in physics from the University of Perugia, and his PhD degree in materials science from the University of Napoli "Federico II" in 2001. He was an assistant professor at the University of Perugia from 2006 to 2015. His current research topics include functional properties of polymer nanocomposites, bionicomposites based on nano-carbons, electrical, mechanical, and optical properties of thin films based on nano-carbons.

Miguel Angel Lopez-Manchado is a research professor at the Instituto de Ciencia y Tecnología de Polímeros, ICTP-CSIC, Spain. He received his PhD degree in chemical sciences from the University Complutense of Madrid in 1997. His current research topics involve processing and characterization of composite materials and nanocomposites, and evaluation of structure-property relationships.

Key Features

- Enables the reader to understand the latest advanced applications of high-performance elastomers reinforced by nano-carbons.
- Unlocks the door to essential properties for harsh environments, such as thermal conductivity, oil resistance, permeability, deicing, and cracking resistance.
- Covers the processability of elastomers reinforced by nano-carbons, including extrusion, compression, molding methods, and techniques.

Technology and Engineering / Material Science

ELSEVIER

elsevier.com/books-and-journals